UNIVERSITÉ DE STRASBOURG

ÉCOLE DOCTORALE DE PHYSIQUE ET CHIMIE-PHYSIQUE

Institut Pluridisciplinaire Hubert Curien (IPHC), UMR 7178

THÈSE présentée par :

Yongzhen HOU

soutenue le : **15 Mai 2024**

pour obtenir le grade de : **Docteur de l'université de Strasbourg**

Discipline/ Spécialité : Physique

Study of light and heavy-flavour jet production and correlations with ALICE at the LHC

THÈSE dirigée par :

M. MAIRE Antonin	Chargé de recherche, IPHC, Université de Strasbourg
M. KUHN Christian	Directeur de recherche, IPHC, Université de Strasbourg
Mme MAO Yaxian	Professeur, IOPP, Central China Normal University

RAPPORTEURS :

Mme YI Li	Professeur, IFIS, Shangdong University
M. QIN Guangyou	Professeur, IOPP, Central China Normal University

---

AUTRES MEMBRES DU JURY :

Mme HUANG Mei	Professeur, IHPEP, University of Chinese Academy of Sciences
M. GUERNANE Rachid	Chargé de recherche, LPSC, Université Grenoble Alpes
M. ZHOU Daicui	Professeur, IOPP, Central China Normal University

Dissertation

Study of light and heavy-flavour jet production and correlations with ALICE at the LHC

By

Yongzhen HOU

Supervisors: Christian Kuhn, Antonin Maire, Yaxian Mao

Specialty: Particle Physics and Nuclear Physics

Research Area: High Energy Nuclear Physics

College of Physical Science and Technology
Central China Normal University
Hubert Curien pluridisciplinary Institute
University of Strasbourg

May. 2024

Abstract

What is the essence of the universe, what is it made of and how did it evolve towards its present observable structure? Such questions has compelled humanity to persistently contemplate, deduce, and validate, culminating in the Big Bang Theory widely accepted by contemporary scientists. Rewinding time, the theory guided by General Relativity and the Standard Model of Particle Physics, tells us how the universe and its content evolved during 13.7 billion years from a state of extreme high energy density. In its very early phase, approximately between 10^{-12} seconds to 10^{-6} seconds following the start of the known evolution, matter existed first in a structureless state of extreme temperatures and high energy densities named the quark−gluon plasma (QGP). In this state, quarks and gluons, the presently thought building blocs of matter, roam freely over large distances, they are said to be deconfined. Investigating the formation, characteristics, and properties of the QGP state will help us understand the formation and evolution of the universe and the interactions of matter.

To address the crucial scientific challenge for recreating and observing this primordial state of matter, physicists exploit particle colliders, such as the Relativistic Heavy Ion Collider (RHIC) at the Brookhaven National Laboratory (BNL) in the United States and the Large Hadron Collider (LHC) at the European Council for Nuclear Research (CERN). These two international facilities provide currently the world's largest environment for conducting heavy-ion experiments at ultrarelativistic energies. At LHC, A Large Hadron Collider Experiment (ALICE) has been designed and optimized for such physics studies. Its objective is to investigate the physics of strongly interacting matter under the most extreme conditions of energy density and temperatures ever achieved in the laboratory and adequate for the formation of the quark-gluon plasma, as predicted by lattice quantum chromodynamics (QCD).

Due to the fleetingly short lifetime of the QGP under laboratory conditions, the state cannot be observed directly, necessitating to rely on the observation of the late final hadronic stage of the collision to infer information on the QGP. A diversity of probes to address QGP properties are continuously proposed and exercised among which the most commonly exploited are jet quenching, heavy-flavor hadron spectra, collective flow, and strangeness enhancement. In high-energy nucleon-nucleon collisions, first chance hard scattering processes occur when two partons, the nucleon constituents, collide involving a large momentum transfer. The back-to-back scattered partons pair fragments then on a short time scale, through the hadronisation process, into stable hadrons forming two observable back-to-back jets, i.e. collimated sprays of final-state hadrons. In heavy-ion collisions, hard scattered partons are produced simultaneously with the formation of the quark−gluon plasma. When these high-p_{T} partons traverse and interact

with the QGP medium due to strong interactions they radiate soft gluons (low transverse momentum gluons) leading to a significant suppression or even quenching of the transverse momentum of the hard-scattered partons. This results in the suppression of high-p_{T} final-state hadron spectra and an increase in low-p_{T} final-state hadron yields produced by the fragmentation of the parton jet. This phenomenon is referred to as "jet quenching". Jet quenching manifests as a significant suppression of the yield of final-state hadrons in the high-p_{T} range relative to the yield in proton-proton (pp) collisions, known as the nuclear modification factor R_{AA}. The nuclear modification factor in a nuclear collision environment is an important observable for searching the QGP effects in RHIC and LHC experiments. Due to jet quenching effects, the production and structure of final-state jets are modified such as yield suppression of hadrons and high transverse momentum jets, medium-induced yield enhancement of low-p_{T} jets, modification of jet internal substructure, and deflection of jet centroids (medium-induced acoplanarity). Therefore, jet measurements and correlation analyses between jets and hadrons are essential tools for studying the "jet quenching" effect and the response of the hot and dense medium to jets. In the LHC energy regime, jet yields are significantly enhanced, making them an important probe for studying quark matter.

In proton-proton (pp) collisions, studying the production and correlation properties of jets serves as a test for perturbative quantum chromodynamics (pQCD) calculations and can also provide a reference baseline for heavy-ion collisions. Investigating jets in different collision systems (pp, proton-nucleus (p–A), and nucleus-nucleus (A–A)) allows for a better understanding of heavy-ion collisions. The current experimental observations do not provide adequate evidence to establish the formation of the quark-gluon plasma state in small systems, including proton-proton and proton-nucleus (p–A) collisions. However, experimental measurements in small systems are mandatory to test predictions of pQCD calculations and provide an essential baseline for the heavy-ion collision measurements. Comparing measurements in pp and p–A collisions provide crucial information on cold-matter modification of the fragmentation function, while comparing measurements in pp and A–A collisions unveil the hot nuclear matter effects. These different system comparisons offer in particular valuable insights into the QGP density, its degrees of freedom and the transport of hard scattered partons inside the QGP medium, contributing to the understanding of the evolution and characteristics of the QGP state.

Recently, several QGP-like observations were unexpectedly made with small collision systems, in particular high multiplicity pp and p–A collisions. They exhibit effects in various so called collective observable qualitatively similar to the ones observed in A–A collisions and attributed to the formation of the QGP. The most notorious one is the observation in high-multiplicity pp events of long range cor-

relations among hadrons a signature of collective flow in the hadronic final-state. In the light of these discoveries, it naturally prompts us to wonder whether a strongly interacting QGP can also be produced in high energy pp collisions and if so, what is its formation mechanism and what does it imply for QGP in heavy-ion collisions. To contribute answering these questions, we have studied the jet production in high multiplicity pp collisions searching for eventual jet quenching effects that would enrich the set of observable in favour of the formation of the QGP state.

For the present thesis, we have analyzed experimental data and investigated properties of the QGP exploiting, through the investigation of jet yields and their correlation characteristics, the Run2 data collected during 2015-2018 by the ALICE experiment at the LHC. The multiplicity dependence of the charged-particle jet production has been first studied in pp collisions at the centre-of-mass energy of $\sqrt{s} = 13$ TeV with data collected by ALICE. Jets are reconstructed from charged particles using the anti-k_{T} algorithm with resolution parameters R varying from 0.2 to 0.7. Jets are measured in the pseudorapidity range $|\eta_{\mathrm{jet}}| < 0.9 - R$ and in the transverse momentum range $5 < p_{\mathrm{T,jet}}^{\mathrm{ch}} < 140$ GeV/c. The multiplicity intervals are categorised by the ALICE forward detector V0 reducing the correlations between event selection and the jet observable. The p_{T} differential cross section of inclusive charged-particle jets are reported and compared to leading order (LO) and next-to-leading order (NLO) pQCD calculations. It is found that the data are better described by the NLO calculation, although the NLO prediction overestimates the jet cross section below 20 GeV/c. The inclusive cross-section ratios for different R values are also measured and compared to model calculations. These measurements provide insights into the angular dependence of jet fragmentation. The jet yield as function of multiplicity then is presented, it increases with increasing self-normalised charged-particle multiplicity. This increase shows only a weak dependence on jet transverse momentum and resolution parameter at the highest multiplicity. While such behaviour is qualitatively described by the present version of PYTHIA, quantitative description may require implementing new mechanisms for multi-particle production in hadronic collisions.

To study the fragmentation properties of jets, complete jet reconstruction is required. Currently, this method still has certain limitations in heavy-ion collisions, especially in high-energy nucleus-nucleus collisions, where there is significant contamination from initial-state radiation, multiple parton interactions (MPI), and background particles originating from projectile and target fragmentation. The contribution of these background particles restricts effective jet reconstruction, particularly for studies involving low transverse momentum ($p_{\mathrm{T}} < 30$ GeV/c) jets. Therefore, continuous innovation in algorithms and particle reconstruction methods is necessary for better measurements of final-state hadronic jets.

When it is not feasible to reconstruct low transverse momentum jets event-by-event significantly affected by the underlying event (UE), trigger particle correlation analysis becomes an effective method for studying the hot dense matter effects on jets. This involves measuring the correlation between trigger particles and recoil jets to study the yield of recoil jets. New measurements of the semi-inclusive distribution of charged-particle jets recoiling from a high-p_{T} hadron ("h+jet") in pp and Pb–Pb collisions at $\sqrt{s} = 5.02$ TeV are studied. Trigger-normalized recoil jet yields as a function of jet p_{T} and $\Delta\varphi$ are reported for jet resolution parameters $R = 0.2$, 0.4, and 0.5 in the range $7 < p_{\mathrm{T,jet}}^{\mathrm{ch}} < 140$ GeV/c and $\pi/2 < \Delta\varphi < \pi$, where $\Delta\varphi$ is the azimuthal angular separation between hadron trigger and recoil jet. The results are compared to predictions from PYTHIA 8, POWHEG, JETSCAPE, JEWEL and the Hybrid Model calculations. In general, the models describe the recoil jet yields well within uncertainties. The low $p_{\mathrm{T,jet}}^{\mathrm{ch}}$ reach of the measurement explores unique phase space for studying jet quenching and the interaction of jets with the quark–gluon plasma generated in high-energy nuclear collisions. Comparison of $p_{\mathrm{T,jet}}^{\mathrm{ch}}$ distributions from pp and central Pb–Pb collisions allows us to probe medium-induced jet energy loss and intra-jet broadening. Additionally, comparing their acoplanarity distributions between hadron trigger and recoil jet helps us explore in-medium jet scattering and the medium's response. These measurements are then compared to theoretical calculations that incorporate jet quenching.

Heavy-flavour (charm and beauty) quarks are abundantly produced in hard scatterings at the initial stage of a collision, but, due to their heavy mass, thermal production from the QGP state is negligible. They traverse the medium and lose part of their energy via collisional and radiative processes. Therefore, heavy quarks are ideal tomographic probes of the QGP, allowing extraction of the medium transport properties. Studies of production properties of heavy-flavour jets in pp collisions can also set additional constraints on the heavy-quark energy loss mechanism and the medium properties as they provide insight into how the energy is lost and dissipated in the medium. The feasibility studies on the identification and tagging measurements of charm quark jets along such lines have been addressed.

In conclusion, the main purpose of this thesis is to study the properties of the quark-gluon plasma through the jet quenching effect. Therefore, we first investigate whether there is a jet quenching effect in small systems, and then we effectively control the complex background in heavy-ion collisions using hadron-jet correlation method to study the jet quenching in a wide kinematic range and large radius jets. Finally, we further explore the shape and composition of jets, as well as the hadronization mechanism of baryons and mesons, using the correlation between jets and heavy-flavor hadrons. Therefore, this thesis first reports on the measurements of charged jet cross-sections in minimum bias (MB) events in proton-proton collisions at $\sqrt{s} = 13$ TeV with ALICE, as well as the multiplicity dependence of jet yields. Comparing

the charged jet cross-sections with different resolution parameters with model calculations, the results of NLO perturbative quantum chromodynamics calculations show better agreement with experimental results in the higher transverse momentum range. It was also observed that the jet yield increases with increasing multiplicity. However, comparison of jet yields between different multiplicity events and MB events, it is found that this increase has weak dependence on jet transverse momentum and resolution parameters. Subsequently, we conducted a study on the measurement of semi-inclusive recoil jet yields in proton-proton collisions via hadron-jet correlations. The distribution of recoil jet yields as a function of transverse momentum and azimuthal angle was obtained, and they were compared with different model calculations, revealing consistency within uncertainties. Comparing the physical results from proton-proton collisions with those from central Pb–Pb collisions, we found, within the current measurement precision, for the first time, enhancement of jet yields and medium-induced acoplanarity broadening effects at low transverse momentum intervals, as well as suppression effects in the higher transverse momentum range. Comparing different model calculations with experimental results suggests that the medium-induced acoplanarity broadening mechanisms may be related to jet scattering from QGP quasi-particles, medium-induced wake effects, and jet fragmentation. Finally, we present performance plots of the azimuthal correlation between D^0 and charged-particle jets, mainly including the invariant mass distributions of D^0.

Keywords: Quark gluon plasma; Heavy-ion; ALICE; Hadron; Jets; Hadronization; Energy loss; Jet quenching; Small system; Heavy quarks

Résumé

Quelle est la nature de la matière de l'Univers, comment la la matière a-t-elle évolué depuis sa structure d'origine jusqu'à sa structure actuelle ? Telles sont les questions, parmi tant d'autres, auxquelles les scientifiques tentent de répondre sans relâche. La théorie du Big-Bang, la théorie de l'histoire de l'Univers largement reconnue aujourd'hui par la communauté scientifique, s'appuyant sur les deux piliers de la physique que sont la Relativité Générale et le Modèle Standard de la Physique des Particules, offre une description de l'évolution de l'Univers et de son contenu pendant les 13.7 milliards depuis son origine connue, un état de densité énergétique extrêmement élevée. Dans sa toute première phase, approximativement entre les 10^{-12} secondes et 10^{-6} premières secondes de son histoire, la matière existait d'abord dans un état sans structure, à des températures extrêmes et des densités d'énergie élevées, appelé plasma de quarks et de gluons (QGP). Dans cet état, les quarks et les gluons, actuellement considérés comme les éléments constitutifs de la matière, se déplacent librement sur de grandes distances, supérieures à la taille du proton ; on dit alors que les particules élémentaires sont déconfinées, c'est-à-dire ne sont pas encore liées pour former des particules composites. Ainsi, étudier la formation, les caractéristiques et les propriétés de l'état QGP contribue à une meilleure compréhension de la formation et de l'évolution de la matière dans l'Univers, de la matière primordiale à la matière actuelle.

Pour relever ce défi scientifique et recréer l'état primordial de la matière, les physiciens exploitent les accélérateurs de particules, tels ceux actuellement opérationnels, le collisionneur d'ions lourds relativistes (RHIC) au Brookhaven National Laboratory (BNL) aux États-Unis et le grand collisionneur de hadrons (LHC) au Conseil Européen pour la Recherche Nucléaire (CERN). Ces deux installations internationales offrent actuellement un environnement unique au monde pour réaliser des expériences mettant en jeu des collisions d'ions lourds à des énergies ultrarelativistes. Au LHC, l'expérience ALICE (A Large Hadron Collider Experiment) a été conçue et optimisée pour l'étude du plasma de quarks et de gluons. Son objectif plus général est d'étudier la physique de la matière en interaction forte dans les conditions les plus extrêmes de densité d'énergie et de températures adéquates pour la formation du plasma de quarks et de gluons, prévue par la chromodynamique quantique sur réseau (QCD), la théorie de l'interaction forte.

En raison de la courte durée de vie du plasma de quarks et de gluons dans les conditions de laboratoire, cet état ne peut être observé directement. On ne peut que s'appuyer sur l'observation de la phase hadronique, produit final et observable de la collision, pour déduire de précieuses informations sur le plasma de quarks et de gluons. Diverses sondes permettant d'en étudier les propriétés sont constam-

ment élaborées et testées. Citons, entre autres, la suppression des jets, la production de hadrons de saveur lourde, la formation d'un écoulement collectif des hadrons et l'augmentation de l'étrangeté. Lors de collisions nucléon-nucléon à haute énergie, des diffusions, dites dures de première chance, se produisent entre partons, les constituants du nucléon, deux-à-deux, entraînant un important transfert de quantité de mouvement. Chacun des deux partons ainsi diffusés dos à dos rapidement se fragmente, par le processus d'hadronisation, en hadrons stables. La topologie des hadrons ainsi produits forme deux jets parfaitement identifiables et émis dos-à-dos. Dans les collisions entre ions lourds, ces diffusions dures sont simultanées à la formation du plasma de quarks et de gluons et les partons diffusées sont amenés à traverser le plasma. Lors de le leur cheminement, ils interagissent par interaction forte avec le plasma perdant de l'énergie par rayonnement de gluons mous (gluons à faible moment transverse): Cette perte d'énergie se manifeste par une suppression significative, voire totale, du moment transverse des partons diffusés. Ce phénomène se traduit par une modification observable des spectres de section efficace de production des hadrons: une baisse significative de production à grand impulsion transverse compensée par une augmentation de la production à faible impulsion. Cet effet est appelée "suppression du jet" (jet quenching en anglais). L'observable adaptée à la mise en évidence de cet effet est connue sous le nom de facteur de modification nucléaire R_{AA}. Cette observable compare les spectres de production de hadrons mesurés dans les collisions proton-proton de biais minimum et les les mêmes spectes mesurés dans les collisions entre ions-lourds, généralement en fonction du paramètre d'impact de la collision. L'effet suppression de jet a également pour conséquence la modification de la structure interne des jets et la modification de la géométrie dos-à-dos créant une acoplanarité entre jets. Mettre en évidence ces effets, nécessite des analyses de corrélation entre les jets.

Etudier la production de jets et leurs corrélations dans les collisions proton-proton (pp), est un préalable nécessaire aux études similaires réalisées dans les collisions entre ions lourds. Cela permet, d'un côté, de tester les prédictions des modèles s'appuyant sur les calculs d'approximation pertubative de chromodynamique quantique(pQCD). D'un autre côté, cela fournit la référence indispensable pour identifier les effets dus à la formation du plasma de quark et de gluon, supposant que cet état n'est pas formé dans les collisions pp. Compléter ces études par des mesures dans les collisions proton-noyau (p–A) est une étape intéressante permettant de mieux cerner les conditions de formation du plasma. Ainsi, la comparaison des mesures réalisées dans les collisions pp et p–A permet d'évaluer les modifications de la fonction de fragmentation dans matière nucléaire froide, tandis que la comparaison entre les collisions pp et A–A permet d'évaluerles effets dus à la matière nucléaire chaude. De ces comparaisons on pourra ainsi tirer de précieuses informations sur la densité du QGP, la nature de ses degrés de liberté et les propriétés de transport des partons à travers le QGP.

Récemment, de manière inattendue, plusieurs observations, similaires à celles généralement attribuées dans les collisions entre ions lourds à la formation du QGP, ont été faites avec des collisions pp et p–A pour des événements à haute multiplicité de l'état final. Citons, en particulier, l'observation, dans les événements pp à haute multiplicité, de corrélations à longue portée entre les hadrons, considérés généralement comme une signature d'un flux collectif de l'ensemble des hadrons dans l'état final. À la lumière de ces découvertes, il est légitime de s'interroger si un QGP peut être produit dans ces collisions, dites de petits systèmes. Si cela est le cas, il faut comprendre quel en est le mécanisme de formation et quelles sont les implications pour l'étude du QGP dans les collisions entre ions lourds. Pour apporter des éléments de réponse à ces questions essentielles, nous avons étudié la phénoménologie de la production de jet dans les collisions pp à haute multiplicité et déceler d'éventuelles effets qui pourraient être attribués à la formation du QGP.

Nous avons analysé les données collectées, lors du Run2, entre 2015 et 2018, pour des collisions pp à l'énergie du centre de masse de $\sqrt{s} = 13$ TeV, par l'expérience ALICE au LHC. Nous avons étudié la production des jets ainsi que leurs corrélations. Nous avons ainsi établi pour la première fois la dépendancede la production de jets de particules chargées avec la multiplicité de hadrons dans l'événement. Les jets chargés sont reconstruits uniquement à partir des particules chargées à l'aide de l'algorithme anti-k_{T} et avec des paramètres de résolution R variant entre 0.2 et 0.7. L'intervalle de pseudorapidité couvert par la mesure est tel que $|\eta_{\mathrm{jet}}| < 0.9 - R$ et l'intervalle de moment transverse $5 < p_{\mathrm{T,jet}}^{\mathrm{ch}} < 140$ GeV/c. La multiplicité hadronique de l'événement est déterminé à l'aide des informations fournies par le détecteur V0 situé à l'avant de l'expérience ALICE, à grande pseudo-rapidité, permettant de décorréler la mesure de multiplicité de la mesure des jets.

Nous présentons le spectre en p_{T} de la section efficace différentielle de production inclusive de jets chargés et comparons nos mesures aux calculs pQCD au premier ordre(Leading Order, en anglais) et d'ordre supérieur (Next to Leading Order, en anglais). Nous constatons que nos résultats sont le mieux décrits par le calcul NLO, même si la prédiction NLO surestime notre mesure dans la région d'impulsion transverse en-dessous de 20 GeV/c. Pour estimer la topologie de la fragmentation des jets, nous avons mesuré la section efficace de production inclusive des jets pour différentes valeurs de R et avons comparé les rapports aux prédictions des modèles. Nous présentons ensuite la production de jets en fonction de la multiplicité hadronique des événements : la production augmente avec la multiplicité indépendemment du moment transverse du jet et du paramètre de résolution sauf à la plus haute multiplicité où la dépendance reste cependant faible. Bien que ce comportement soit qualitativement décrit par la version actuelle du modèle PYTHIA, une description quantitative nécessite l'implémentation de nouveaux

mécanismes décrivant la production multi-particules dans les collisions hadroniques.

Pour étudier les propriétés de fragmentation des jets, une reconstruction complète des jets est requise. Les méthodes actuellement disponibles ne sont pas encore optimisées pour être appliquées à l'environnement hadronique créé dans les collisions entre ions lourds à haute énergie où il faut tenir compte d'une importante contamination due au rayonnement de l'état initial, aux interactions multiples de partons (Multiple Parton Interaction, en anglasi) et aux particules provenant de la fragmentation du projectile et de la cible. Ces contaminations limitent la reconstruction effective des jets, particulièrement ceux à faible moment transverse ($p_{\mathrm{T}} < 30$ GeV/c). Pour pallier à ce défaut, on peut soit chercher à améliorer les algorithmes de reconstruction soit sélectionner les jets à l'aide d'une analyse de corrélation. Une telle analyse revient à mesurer la corrélation entre des particules individuelles de grande impulsion transverse et des jets emis en coincidence dos-à-dos. Nous avons ainsi réalisé des mesures originales de la distribution semi-inclusive des jets chargés étiquetés par un hadron à haut-p_{T} ("h+jet") dans les collisions pp et Pb–Pb à $\sqrt{s} = 5.02$ TeV.

Nous présentons la mesure de la production de jets étiquetés en fonction du moment transverse du jet et de l'angle azimuthal relatif entre l'axe du jet et du hadron individuel pour des paramètres de résolution de jet $R = 0.2$, 0.4, et 0.5 dans l'intervalle $7 < p_{\mathrm{T,jet}}^{\mathrm{ch}} < 140$ GeV/c et $\pi/2 < \Delta\varphi < \pi$,. Nous comparons nos résultats aux prédictions de PYTHIA8, POWHEG, JETSCAPE, JEWEL et aux calculs de Hybrid Model. En général, les modèles décrivent de façon satisfaisante la production des jets dans la limite des incertitudes de mesure. La possibilité d'identifier ainsi les jets de basse impulsion transverse permet d'explorer un domaine de l'espace de phase autrement hors de portée pour l'étude de la suppression des jets et de leur interaction avec le plasma quark-gluon. En comparant les distributions de $p_{\mathrm{T,jet}}^{\mathrm{ch}}$ obtenues dans les collisions pp et Pb–Pb nous pouvons explorer les modifications subies par les jets (perte d'énergie et élargissement intra-jet) suite aux interactions avec le milieu traversé. De plus, de la comparaison de l'acoplanarité entre le hadron et le jet nous pouvons tirer des informations, d'un côté, sur la diffusion des partons dans le milieu et, d'un autre côté, sur la réponse du milieu à l'nteraction avec le jet. Nous comparons nos résultats aux prédictions théoriques des modèles qui incorporent des mécanismes d'interation jet-matière.

Les quarks de saveur lourde (charme et beauté) sont abondamment produits principalement dans des diffusions dures au stade initial d'une collision, étant donné qu'en raison de leur masse élevée la production thermique à partir de l'état QGP reste négligeable. Ils traversent le milieu et perdent une partie de leur énergie par processus collisionnels et radiatifs. Les quarks lourds peuvent ainsi être considérés comme une sonde tomographique idéale du QGP. Nous avons réalisé un travail préliminaire pour étudier

la faisabilité de l'identification des jets de quarks lourd ainsi que de l'étiquetage de jets de quark charmé.

Mots-clés: Plasma de quarks et de gluons; Ions lourds; ALICE, Hadron; Jets; Hadronisation; Perte d'énergie; Jet quenching; Petit système; Quarks lourds

Contents

List of Figures

List of Tables

1 Introduction

In this chapter introducing the physics motivating the ALICE scientific program, we will provide a concise yet essential overview of the fundamental knowledge in high-energy nuclear and particle physics. We first introduce the fundamental particles of the Standard Model and their interactions. We then describe the specific characteristics of these particles and the properties that define them. We continue with a concise introduction to Quantum Chromodynamics (QCD), emphasising two critical aspects of QCD: quark confinement and asymptotic freedom. We then delve into the concept of a new deconfined QCD matter known as the quark-gluon plasma and the use of jets to learn about it. Subsequently, we elaborate on the main characteristics of heavy-ion collisions and their space-time evolution. Finally, we present the QGP probes in heavy-ion collisions and the QGP-like behaviours observed in small systems, with a focus on the jet quenching effect in hard probes associated with the jets that are the main object of this thesis.

Experimental evidence has been put forward at the Large Hadron Collider and the Relativistic Heavy-Ion Collider prooving the formation of the quark–gluon plasma (QGP) state of matter in high-energy heavy-ion collisions. This state of matter is the one of primordial matter as it supposedly existed during the very early stage of the universe, thus motivating research to investigate it in the laboratory. Due to the remarkably brief lifespan of the QGP state, direct observation remains unattainable with our current technological capabilities. Therefore, we must rely on the distinctive characteristics of suitable observable probes to infer the formation and properties of the QGP. In high-energy experiments, QGP probes can be categorized into three main groups: soft probes, hard probes and electroweak probes. Soft probes include for example collective flow of low p_{T} hadrons, enhanced production of strange particles, while the hard probes include mainly heavy quarks, high p_{T} hadrons and jets. electroweak probes include photons, leptons or Z/W bosons measurements. It came as a surprise that several features interpreted in heavy-ion collisions as a signature of the QGP formation have been also observed in smaller collision systems, including p–Pb and pp collisions at LHC energies. These observations, which raise questions about the known particle production mechanisms, are briefly discussed at the end of this chapter.

1.1 The Standard Model of Particle Physics

Since the 1930s, the collective work and discoveries shared by thousands of physicists have unveiled the fundamental structure of matter: all known matter in the universe is composed of a mere handful of elementary building blocks known as fundamental particles interacting through four fundamental forces

[39]. The four forces are the gravitational force, the electromagnetic force, the weak force and the strong force. Each force is characterized by a typical range and strength. The strong force is the strongest one, acting on a small range of the order of 1 fm. The electromagnetic force is about 100 times weaker than the strong force, but has an infinite range. The weak force is 1 million times weaker than the strong force and with a shorter range of the order of 10^{-3} fm. The gravitational force is significantly weaker than the other fundamental forces (about 10^{39} times weaker) and has an infinite range.

The Standard Model (SM) of particle physics provides an exhaustive description of elementary particles and their interactions including three out of the four fundamental forces (gravity is excluded, because it is the weakest of all forces by several orders of magnitude and can be neglected in the context of particle physics) [40]. Developed in the early 1970s, this theory has not only adeptly accounted for nearly all experimental findings to date but has also made precise predictions spanning a wide range of phenomena. With precision experiments performed at previous and current accelerators, the SM can be considered as a physics theory well tested to highest precision at the quantum level.

The standard model considers 17 elementary particles, as illustrated in Figure 1.1. Different colors differentiate the various particle types: quarks, leptons, and bosons. The provided numerical values represent their mass (top), electrical charge (middle), and spin (bottom). They are six quarks, six leptons, four force-carrying particles and one Higgs boson. The matter-building blocks, called fermions, quarks and leptons are further categorized in six types, called flavors. The force carriers, called bosons, are associated with the three nuclear forces. Fermions carry half-integer spin and obey the Fermi-Dirac statistics; bosons carry integer spin and obey the Bose-Einstein statistics.

Quarks carry a color charge (therefore interact with the strong force) and an electric charge (therefore interact also with the electromagnetic force) and come in six flavors: up (u), down (d), charm (c), strange (s), top (t), and bottom (b). Quarks form either triplets or doublets, giving rise to composite particles. Specifically, the combination of three different quarks results in the formation of baryons, while doublets (two quarks) give rise to mesons. Collectively, baryons and mesons belong to the category of hadrons. Baryons can be further subdivided into nucleons and hyperons. Nucleons refer to protons and neutrons, which form the atomic nucleus. Hyperons are characterized by the presence of at least one strange quark among their constituents. Leptons carry no color charge (do not interact with the strong force) and an electric charge and come in three families: electron (e), muon (μ), and tau (τ) each associated with its respective neutrino (ν_e, ν_μ, ν_τ).

Neutrinos are the particles associated to the weak interaction. They have very little mass (of the or-

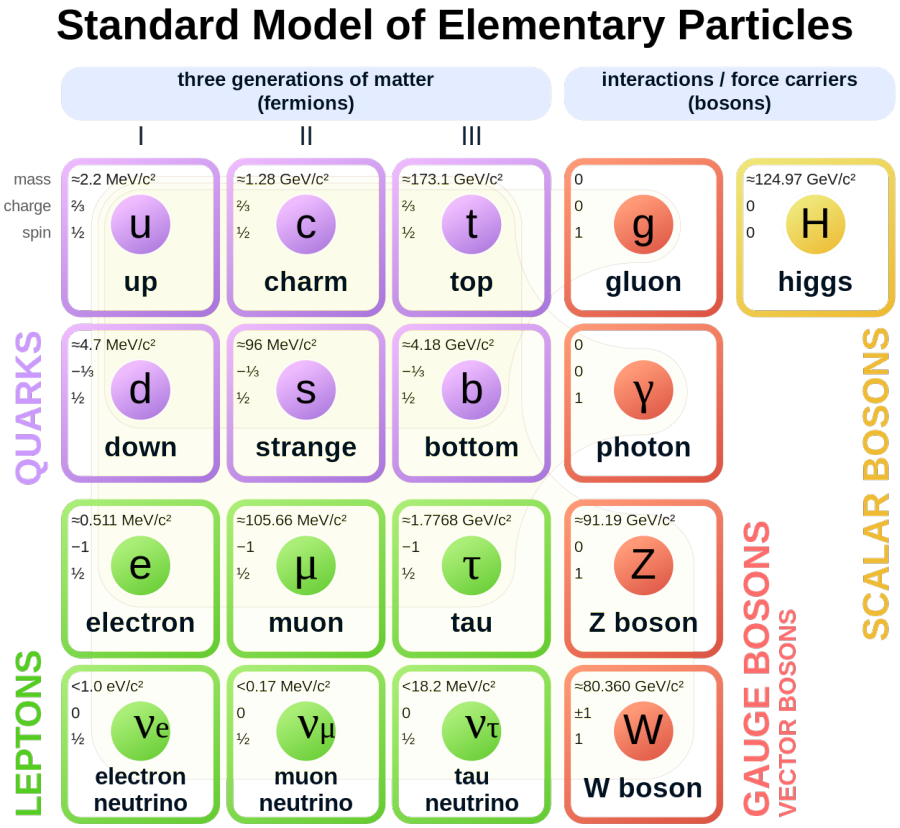

Figure 1.1: Diagram of the Standard Model of particle physics, illustrating the fundamental particles and their interactions through the exchange of force-carrying particles. Figure from Ref. [1].

der of eV not yet firmly established experimentally) and interact so weakly with matter that they are exceptionally difficult to detect.

In quantum field theory, the interaction between fermions is described by the exchange of boson force carriers: gluon for the strong interaction, photon for the electromagnetic interaction and *W* and *Z* bosons for the weak interaction. The bosons mediators are listed in the forth column of Fig. 1.1. Each force operates between particles based on specific charges carried by the particles: such as color charge for the strong force, electric charge for electromagnetic interaction, and weak charge for the weak interaction.

The most recent addition to the SM of Physics is the Higgs boson, it is a spin 0, electrically neutral scalar particle and carries no color charge. Its existence was experimentally confirmed in 2012 by the CERN experiments. It is theorized that the Higgs boson is produced by the quantum excitation of the Higgs field which is responsible for the mass of all elementary particles which are predicted to be massless according to the symmetries defining the interactions.

1.2 Quantum Chromodynamics

In fundamental physics, the smallest fundamental unit of an element that retains its chemical characteristics is the atom, comprising positively charged nuclei encircled by negatively charged electrons. The nucleus is composed of protons and neutrons, collectively referred to as nucleons. Each atomic nucleus contains at least one nucleon. The force between nuclei and electrons is the electromagnetic force that is described by quantum electrodynamics (QED) [41]. Protons and neutrons, in turn, consist of quarks, giving rise to the notion that a nucleon is a composite particle formed of quarks. A proton has two up quarks and a down quark (uud), and a neutron has an up quark and two down quarks (udd). Quantum ChromoDynamics (QCD) is a non-Abelian gauge theory describing the strong interaction among quarks and gluons. It is based on the $SU(3)$ gauge symmetry group. The charges responsible for strong interactions are color charges, they are the internal degrees of freedom of the QCD theory [42, 43]. In total, six color charges are considered. A quark can carry one out of three colors: red, green and blue; an antiquark carries one out of the corresponding anti-colors: anti-red, anti-green and anti-blue. The mediator gluon carries a color charge and an anti-color which gives them the possibility to interact with other gluons.

The QCD Lagrangian [43] is

$$\mathcal{L}_{\mathrm{QCD}} = \sum_q \bar{\psi}_{q,k} \left(i\gamma^\mu D_{\mu,kl} - m_q \, \delta_{kl} \right) \psi_{q,l} - \frac{1}{4} F^a_{\mu\nu} F^{\mu\nu}_a \tag{1.1}$$

where $D_{\mu,kl}$ is the covariant gauge derivative that introduces the interaction between quarks and gluons, and it is expressed as follows

$$D_{\mu,kl} = \partial_\mu \delta_{kl} - i g_s A^a_\mu T^a_{kl}, \tag{1.2}$$

Substituting equation (1.2) into equation (1.1), the Lagrangian transforms into

$$\mathcal{L}_{\mathrm{QCD}} = \sum_q \bar{\psi}_{q,k} \left(i\gamma^\mu \partial_\mu \delta_{kl} - g_s \gamma^\mu A^a_\mu T^a_{kl} - m_q \, \delta_{kl} \right) \psi_{q,l} - \frac{1}{4} F^a_{\mu\nu} F^{\mu\nu}_a \tag{1.3}$$

The two fundamental parameters of QCD are the quark mass m_q and the dimensionless coupling parameter g_s. The quantity g_s is related to the strong coupling constant as $\alpha_s = \frac{g_s^2}{4\pi}$. Both m_q and α_s are determined by experiments. The sum runs over the six quark flavours, $\bar{\psi}_{q,k}$ and $\psi_{q,k}$ is the quark field of flavor are the quark-field spinors with flavors q and color k. γ^μ are the Dirac γ-matrices. A^a_μ describes the gluon gauge fields of the 8 different gluons, T^a_{kl} corresponds to the eight 3×3 generator matrices of the $SU(3)$ group, and $a \in \{1, 2, \ldots 8\}$ indexes the $SU(3)$ gauge group. $F^a_{\mu\nu}$ is the gluon field strength tensor and can be defined as

$$F^a_{\mu\nu} = \partial_\mu A^a_\nu - \partial_\nu A^a_\mu - g_s f^{abc} A^b_\mu A^c_\nu \tag{1.4}$$

where f^{abc} correspond to the structure constants of the $SU(3)$-group Lie algebra. Since the $SU(3)$ group is non-Abelian, the structure constants are not null, and in addition to vertices between a quark, an antiquark, and a gluon, vertices among three and four gluons are possible. The presence of gluon self-interactions implies that the colour force is a short-range interaction even if gluons are massless particles.

In general, equation (1.3) consists of four distinct terms, each with its specific role. The first term represents the dynamics of free quarks, the second term accounts for quark-gluon interactions and is regulated by the quark-gluon interaction strength, denoted as g_s. The third term introduces the mass of a quark of flavor q with mass m_q. Lastly, the fourth term, which involves the gluon kinetic term for the gauge gluon field, incorporates the gluon field tensor $F^a_{\mu\nu}$, as defined in Eq. (1.4). This gluon field tensor is analogous to the electromagnetic tensor in QED, but with an additional term to account for the gluon carrying a color charge.

The running coupling constant of the strong interaction exhibits the two characteristic properties of the strong interaction: asymptotic freedom at high energies and color confinement at low energy. The coupling g_s depends on the energy scale of an interaction, due to screening and antiscreening from loop diagrams that increasingly appear with higher resolution scale. The running of the coupling as $\alpha_s = \frac{g_s^2}{4\pi}$ at leading order in perturbative QCD (pQCD) for a given momentum transfer Q turns out to be given by

$$\alpha_s(Q) = \frac{2\pi}{\left(11 - \frac{2}{3}n_f\right) log\left(\frac{Q}{\Lambda_{\text{QCD}}}\right)} \tag{1.5}$$

where n_f is the number of quark flavors, Λ_{QCD} (≈ 200 MeV) is a non-perturbative QCD scale parameter [43]. Fig. 1.2 shows the experimental measurements of energy dependence of the coupling constant α_s as a function of the momentum transfer Q. The value of the QCD running coupling constant at the Z boson mass is 0.1179 ± 0.0010.

As illustrated in this Fig. 1.2, the strength of the coupling constant α_s decreases with increasing Q, and two different regimes can be distinguished: **asymptotic freedom** and **colour confinement** [44]. At high energy $Q \to \infty$ (small distance scales), α_s is closer to 0 and asymptotic freedom is reached. This means the quarks and gluons are very weakly interacting or free when distance between them become shorter or the energy density gets higher. In this case the pQCD calculations of scattering amplitudes based on a perturbative expansion in α_s are applicable. Often, only the first, second, or third orders in α_s, referred to as Leading Order (LO), Next to Leading Order (NLO), and Next to Next to Leading Order (NNLO) respectively, are computed. At low energy $Q \to 0$ (large distance scales), α_s is becoming very large and quarks and gluons are confined within a hadron to be neutral in color charge, that is color confinement.

This is why we cannot observe quarks and gluons as free particle. However, at high energy densities, it is expected that quarks can move freely over distances larger than the size of a hadron, such a condition defines the QGP state.

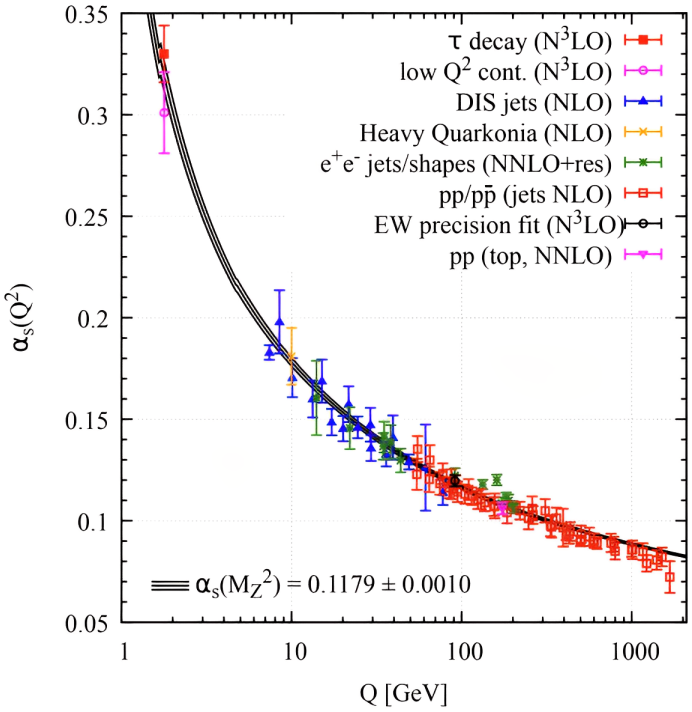

Figure 1.2: Summary of experimental measurements of the QCD coupling constant α_s as a function of the transferred momentum Q. The brackets carry the respective degree of perturbative QCD theory used in the extraction of α_s. Figure from Ref. [2].

1.3 Hard scattering and jet production

As discussed in Section 1.2, the hard (high Q^2) and soft (low Q^2) processes in high energy collisions occur on different length and time scales. While the hard processes can be treated in perturbative QCD, soft processes cannot. The concept of QCD factorization consists in the separation of hard processes and soft processes, essentially separating the non-perturbative initial state, described by a Parton Distribution Function (PDF), from the perturbative hard scattering, and from the non-perturbative final state, described by the Fragmentation Function (FF). The three parts are considered independent.

For example, a particularly relevant QCD calculation to this thesis is the one for the production cross-section for inclusive jets (jet+X) (jets will be described in Section 3.2) in proton-proton collisions. It can be factorized, in the limit of sufficiently small jet cone sizes, as shown in Equation 1.6 from Ref. [45] and Fig. 1.3. Each of the individual terms of this equation will be described below, where ⊗ represents

the convolution over the parton momentum fractions.

$$\frac{d\sigma^{pp\to jet+X}}{dp_T d\eta} = \sum_{ab} f_a(x_a, Q^2) \otimes f_b(x_b, Q^2) \otimes (\sum_c \hat{\sigma}_{ab\to c}(z, \mu) \otimes J_c) \tag{1.6}$$

where partons a, b within a proton scatter into an outgoing jet c plus anything else. $f_a(x_a, Q^2)$ and $f_b(x_b, Q^2)$ represent the probability of finding inside the proton a parton with a momentum fraction $p_{\text{parton,i}}/p_{\text{proton}}$ at given a momentum transfer Q^2. Note that the PDF depends on Q^2 since with a higher resolution scale, one sees more loop diagrams to scatter from.

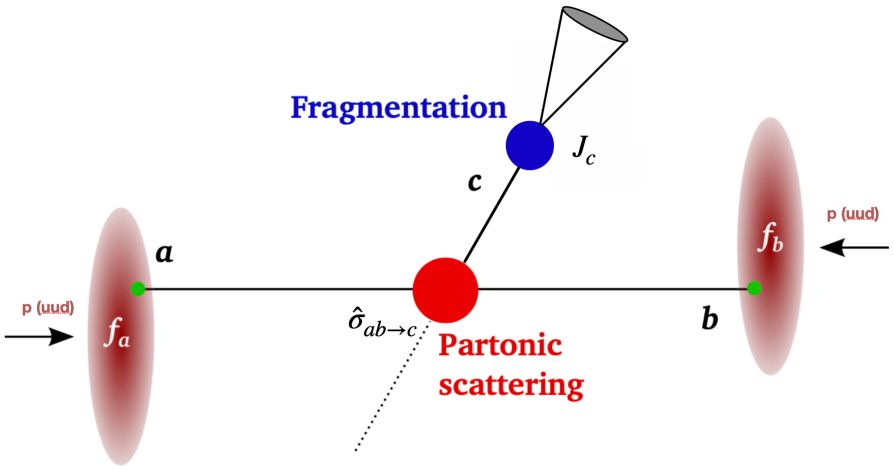

Figure 1.3: The factorization of the jet production cross section as expressed in Equation 1.6.

The momentum transfer Q^2 determines the resolution scale with which we probe the proton. At low Q^2 values, which correspond to a coarse resolution scale, the PDF is dominated by the three valence quarks, each carrying $\approx 1/3$ of the proton momentum. As Q^2 increases, we probe the short-range structure of the proton and the softer contributions of sea quarks and gluons increases. At very low x values, the PDF is dominated by soft gluons. This can be understood since at a coarse resolution scale, we may see only a propagating quark, but as we zoom in, we will see numerous soft gluon radiations from the quark, which carry part of the quark's momentum (resulting in a strong enhancement of the parton population at low-x). Accordingly the pp cross section increases with $\sqrt{s}$, as the PDFs contain more gluons that are likely to interact.

The Parton Distribution Function is a non-perturbative object, and cannot be calculated directly (although lattice QCD attempts are progressing). However, given a PDF at one scale, one can calculate it at another scale through the perturbative evolution equations known as the Dokshitzer-Gribov-Lipatov-Altarelli-Parisi (DGLAP) evolution equations [46–48]. The PDF can be measured as a function of x

and Q in deep inelastic scattering (DIS) experiments where high-energy electrons are scattered off a hadron. Fig. 1.4 shows the proton PDF at $Q = 3.2$ GeV and $Q = 100$ GeV. At very low values of x, the gluon PDF is dominant whereas at high values of x the valence quark PDFs (particularly u and d quarks) dominate, indicating that the soft contributions to a nucleon tend to come from gluons and the hard contributions tend to come from quarks. Eventually, at very low x, the gluon PDF is expected to saturate, forming a state called a Color Glass Condensate (CGC) [49]. Understanding saturation effects, and their role in the collisions of high-energy hadrons and nuclei, is one of the main physics goals of the upcoming Electron-Ion Collider (EIC) [50].

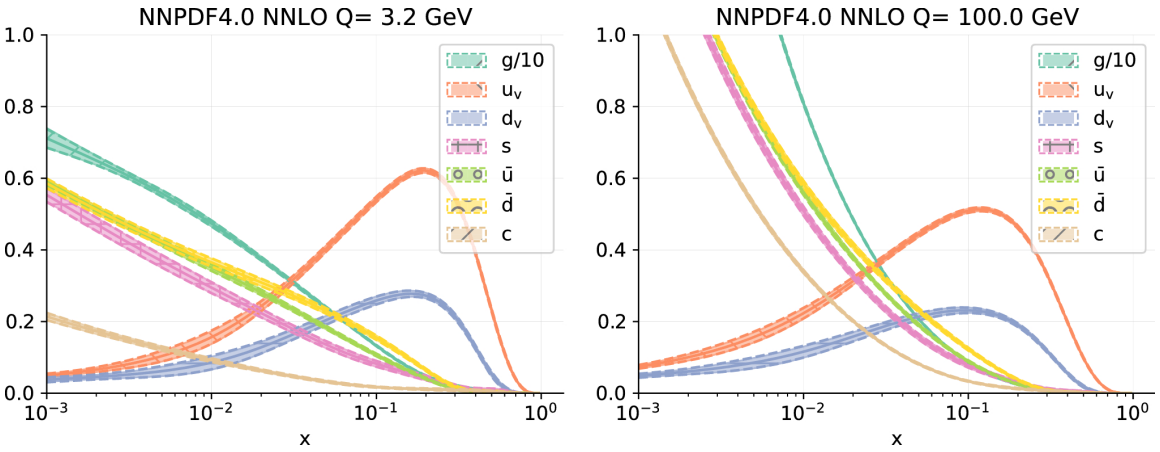

Figure 1.4: PDFs as a function of x calculated at NNLO for $Q = 3.2$ GeV (left) and $Q = 100GeV$ (right). Figure from Ref. [3].

$\hat{\sigma}_{ab\to c}(z,\mu)$ in Equation 1.6 represents the production of a parton c in the hard scattering $(a + b \to c)$ of two partons a and b at a hard-scattering scale $\mu \sim p_{\mathrm{T}}$ with $z = p_{\mathrm{T,c}}/p_{\mathrm{T}}$. This can be calculated perturbatively at different orders in α_s. J_c in Equation 1.6, referred to as the jet function, is the term that describes the formation of the jet from the parton c. The DGLAP evolution equations can be used to evolve jet functions from the scale of the jet mass to the scale of the hard scattering. The jet formation is calculated from the Fragmentation Function (FF), which is also a non-perturbative object and cannot be described from fundamental QCD, but as the PDFs it can be evolved perturbatively from one scale to another. The FF can only be determined experimentally. It involves a parton shower, which is a perturbative process governed by the QCD splitting function fragmenting hard partons into soft partons, followed by a non-perturbative fragmentation and hadronization mechanism. There are several phenomenological models of hadronization, such as the Lund string model or cluster fragmentation models (see Section 2.4.1 for details).

As mentioned above, non-perturbative techniques become mandatory when α_s is on the $O(1)$ at very low

Q. Several methods exist for performing **non-perturbative calculations**, with Lattice QCD (LQCD) being the most prominent. Lattice QCD is a lattice gauge theory formulated on a grid/lattice in space and time, where quarks occupy lattice sites and gluons represent the links. The lattice spacing depends on the energy scale. When the spacing (a) is zero and the size of the lattice (L) is taken infinitely large, the continuum is recovered. Lattice QCD calculations are often invoked to calculate the QCD phase diagram, typically for $\mu_B = 0$. For lattice calculations where $\mu_B \neq 0$, other techniques are employed.

Another technique for non-perturbative QCD calculations is Anti-de Sitter/Conformal Field Theory (AdS/CFT), based on a supposed correspondence between AdS theories of quantum gravity and CFTs. This correspondence relies on a weak-strong duality, making calculations that are challenging in strongly-coupled gauge theories more manageable in a semi-classical gravitational picture. Additional information about AdS/CFT correspondence can be found in [51]. A third method for non-perturbative QCD calculations is Soft Collinear Effective Theory (SCET). SCET is an effective field theory for soft or collinear particles, utilized for non-perturbative QCD calculations involving interactions between particles of different energies, such as high-energy quarks with soft gluons. For further details about SCET, refer to [52].

1.4 A new phase of matter

According to the Big Bang model, primordial matter in the early Universe is predicted to have existed in a state composed of deconfined quarks and gluons – the Quark-Gluon Plasma (QGP) [53, 54]. As the Universe expanded and cooled down, the QGP underwent a transition towards hadronic matter, the present state of matter. Similar conditions extreme in energy density and temperature can be created at much smaller scales in the laboratory by colliding beams of heavy ions. Such collisions release substantial energy into confined space of the size of a nucleus, resulting in the extremely high energy densities required for the formation of matter in the state of deconfined quarks and gluons – the QGP.

The strong dependence of the α_s value on Q points to the existence of distinct phases of the strongly-interacting matter, depending on the average momentum exchanged in the interactions between its constituents. The properties of strongly-interacting matter can be studied through lattice QCD calculations as a function of the system temperature T and baryon chemical potential μ_B [55, 56], which is defined as the energy needed to increase the total baryon number by one unit and is proportional to the net baryon density.

Fig. 1.5 shows the QCD phase diagram as a function of T and μ_B, and the regions probed by different accelerator facilities are indicated. At low temperature and low baryon density, quarks and gluons are

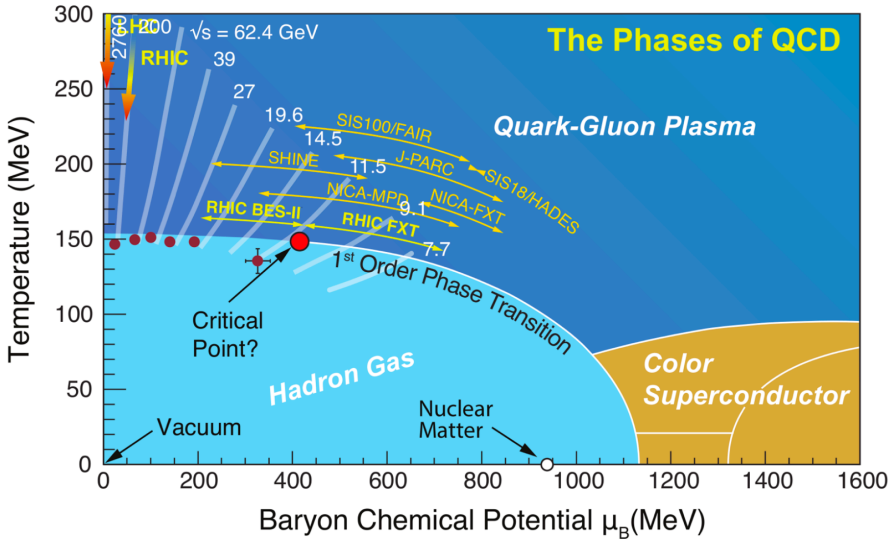

Figure 1.5: A schematic QCD phase diagram in the temperature (T) and baryonic chemical potential (μ_B) plane. Figure from Ref. [4].

confined into hadrons. The matter can be described as an hadronic gas. The ordinary nuclear matter predominantly exists in the region where the temperature (T) is approximately $T \approx 0$, and the baryon chemical potential is approximately $\mu_B \approx 1$ GeV, the mass of the nucleon. At larger values of the baryon chemical potential goes higher, the temperature remaining low, nuclear matter can be described as a degenerate gas of neutrons with a structure similar to the one of the atomic nucleus. This type of matter is expected to constitute the core of neutron stars. As the μ_B continues to increase, a low-temperature gaseous state emerges, wherein quarks are no longer confined within hadrons but begin to form color Cooper pairs, a state referred to as a color-superconductive state [57]. Nuclear matter converts into a hadron gas at high temperatures, and above $T \approx 100 - 150$ MeV, it is expected to undergo a transition towards the quark-gluon plasma (QGP). The QGP is a state of strongly-interacting matter in which the colour degrees of freedom are not confined in colour-singlet hadrons, and quarks and gluons are free to move over a volume larger than the size of hadrons. The nature of the transition from hadronic matter to QGP state can be investigated using lattice QCD calculations. At very high temperatures and very small down to zero μ_B, lattice QCD predicts a continuous crossover between the two phases and simultaneously the chiral-symmetry is restored [58]. This condition of high temperature and vanishing net baryon density is thought to be the analogous situation of the early universe and can be reproduced by colliding heavy ions at ultra-relativistic energies. Depending on the assumptions about the studied systems, lattice QCD predicted critical temperature T_c is approximately 155 MeV, corresponding to an energy density of 1 GeV/fm^3 [59]. At higher μ_B and finite temperatures, a phase transition of the first

order from hadronic matter to deconfined QCD matter is predicted to occur, implicating the presence of a critical point marking the endpoint of the phase boundary of the first-order phase transition line. The existence or the exact location of the phase boundary and the critical point is still under investigation.

1.5 High energy heavy-ion collisions

To analyze QCD properties and probe the hot dense quark-gluon plasma, we experimentally utilize large accelerators for high-energy collisions. Collisions include nucleon–nucleon collisions, nucleon–nucleus collisions and nucleus–nucleus collisions. Nucleon–nucleon or more precisely proton–proton collisions are conceptually the easiest reaction type. Through QCD interaction, partons inside the protons interact through quasi-elastic scattering and produce a great number of new particles. The likelihood of QGP formation in these collisions is expected to be minimal. In contrast, nucleus–nucleus collisions involve heavy atomic nuclei like gold (Au) or lead (Pb), making them more complex than nucleon–nucleon collisions. Beyond the processes in nucleon–nucleon collisions, effects arising from collision geometry and the QGP medium must be considered. Nucleus–nucleus collisions cannot simply be described as an incoherent superposition of nucleon–nucleon collisions. Nucleon–nucleus collisions, as proton–proton collisions, are also expected to have a low likelihood of QGP formation. However, these collisions occur in a nuclear environment, making them ideal candidates for addressing cold nuclear matter effects to be distinguished from hot nuclear matter effects. For more information on collisions, see Section 2.4.

Presently, two facilities are dedicated to high-energy heavy-ion collisions: the Relativistic Heavy Ion Collider (RHIC) at Brookhaven National Lab and the Large Hadron Collider (LHC) at CERN. The LHC, situated at CERN (the European Organization for Nuclear Research, Conseil Europeen pour la Recherche Nucléaire) in Switzerland, is the world's largest and most powerful particle accelerator. It has been primarily build to search for the Higgs boson and explore possible physics beyond the Standard Model physics. It allows in addition a vigourous physics program for the in-depth study of the quark-gluon plasma properties. RHIC hosts the STAR and PHENIX experiments, while the LHC hosts the ALICE, ATLAS, CMS, and LHCb experiments. The first evidence for the formation of the QGP was claimed on 2000 by the CERN heavy-ion program at the Super Proton Synchrotron (SPS) accelerator [16]. In 2001, RHIC officially claimed to have created deconfined QCD matter in Pb–Pb collisions [60]. This section provides an overview of the space-time evolution and experimental variables of high-energy hadron collisions.

1.5.1 Space-time evolution

Fig. 1.6 presents a schematic diagram of the space-time evolution of relativistic nucleus-nucleus collisions, both with and without a deconfined state. If the energy density and temperature generated in these collisions do not reach the critical values required for quark-gluon plasma formation, it is depicted in the left side of Fig. 1.6, the system is left with hadronic degrees of freedom only. Just after the collisions a pre-hadronic phase is created. Then the nucleons can recombine into new hadrons and the produced hadrons can be detected after the hadron gas phase freeze-out. However, in cases where the initial energy density and/or temperature is exceptionally high, allowing for the possible formation of QGP, the space-time evolution of relativistic nucleus-nucleus collisions will resemble the scenario depicted on the right side of Fig. 1.6. In this cartoon, "A" and "B" refer to two opposite directions along the beam axis (z, longitudinal direction). The horizontal axis is "z: space, t: time". A hyperbola (line) represents particles with the same proper time. The evolution begins with the collision of two incoming nuclei, first hard and soft scatterings of partons generate a large energy density. Subsequently, the system undergoes a process of approximate thermalization, leading to the formation of the quark-gluon plasma. As the system progresses, it gradually cools down through hydrodynamic expansion. When the temperature reaches the confinement transition value, partons undergo hadronization and engage in re-scatterings within a hadron gas until they freelystream to infinite. Each phase of this evolution will be elaborated upon in the following discussion based on the chronological sequence of events.

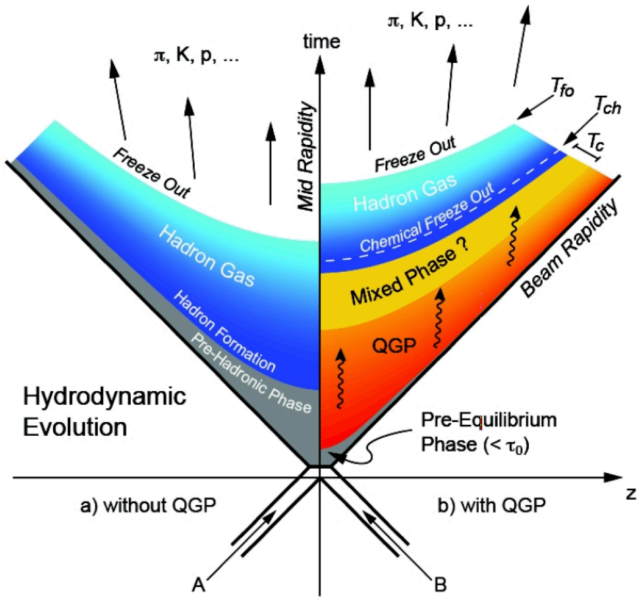

Figure 1.6: Space time evolution of the particle production in a hadronic interaction. Figure from Ref. [5].

Until interaction ($\tau < 0$): Before the collision, the two nuclei are accelerated in opposite directions to nearly the speed of light. Due to Lorentz-contraction, in the laboratory frame they look like thin disks contracted along the longitudinal direction by a factor of $\sim$ 100 compared to the radial extent in the transverse plane [61].

Pre-equilibrium stage ($0 < \tau < \tau_0$ (1 fm/c)): The collision of the two incoming nuclei takes place at $z = 0$ and $t = 0$. Right after the collision, multiple interactions among the partons occur during the pre-equilibrium phase. Partons re-scatter leading to the thermalisation of the system. During the early pre-equilibrium phase, hard particles, such as jets, dileptons pairs, heavy quarks, direct photons, etc. are produced via hard processes with large momentum ($Q \gtrsim 10$ GeV) transfer. The semi-hard processes corresponding to momentum transfer of $Q \sim 1$ GeV, start to develop at a time $\tau \sim 0.2$ fm/c, where the bulk of the partonic constituents are liberated by the collisions. If the produced partons do not interact with each other or the interactions are negligible, they evolve independently and separate rapidly without reaching an equilibrium state. This is the case in low multiplicity pp events at LHC. Data from Pb–Pb collisions and high multiplicity pp events exhibit collective phenomena which indicate that the partons liberated in the collisions interact strongly. Due to these interactions, partonic matter approaches towards thermal equilibrium on relatively short thermalisation time of the order of 1 fm/c.

QGP formation and hydrodynamic expansion ($1 < \tau < 10$ fm/c): The fireball reaches the critical energy density and/or temperature in a local equilibrium. Lattice QCD calculations indicate that QGP is formed beyond a critical energy density of 1 GeV/fm^3 or beyond the critical temperature. The elastic and inelastic interactions between quarks and gluons in QGP lead to the thermalization phase. Due to the inelastic interactions, the flavor composition of the partons of the system changes. Because of the high internal pressure and temperature, the system begins to expand rapidly [62].

Mixed state ($10 < \tau < 20$ fm/c): The QGP keeps expanding and cooling down until hadronisation of quarks and gluons occurs as the temperature drops below the critical temperature. A mixed phase is expected to form comprising of quarks and gluons together with the hadrons. A $chemical\ freeze-out$ occurs when no more inelastic scatterings take place and the number of particles is fixed.

Hadron gas phase ($\tau \geq 10$ fm/c) and Freeze-out ($1 < \tau < 20$ fm/c) : Once all the quarks and gluons are again confined, the system can be described by an expanding hadronic gas. There could be two possible mechanisms of hadronization, namely fragmentation and coalescence. Hadronization from fragmentation dominates at high energy which happens when a high-p_{T} parton fragments into lower p_{T} hadrons. Coalescence occurs when low momenta partons combine to form higher p_{T} hadrons.

After hadronization, hadrons continue to interact with each other via elastic and inelastic interactions until they reach freeze-out. When the inelastic collisions ceases the system reaches $chemical\ freeze-out$ and the corresponding temperature is called as chemical freeze-out temperature ($T_{\rm ch}$). This is the phase where the stable particle ratios gets frozen. But, still the elastic collision takes place at this stage. When the mean free path gets high enough, the elastic collisions among the hadrons cease and the $kinetic/thermal\ freeze-out$ is reached and the corresponding temperature is called as kinetic freeze-out temperature ($T_{\rm fo}$) [63]. This is the phase where the transverse momentum spectral shape of a particle gets frozen. After the freeze-out, all the particles fly towards the detectors and only decays of unstable hadrons take place.

1.5.2 Experimental variables

Before describing specific high-energy heavy-ion measurements, it will be useful to define common experimental variables: kinematic variables, including the spatial and momentum coordinates, and centrality, which is the observable used to define the impact parameter.

First, let's define the kinematic variables. In a heavy-ion collision many outgoing particles are produced. For detectors such as ALICE, the spatial coordinates of the particles are described using cylindrical coordinates, θ denotes the polar angle with respect to the beam axis, and ϕ denotes the azimuthal angle. The radius r is generally irrelevant to describe the particle's kinematics, since particles propagate along the radial direction.

The three-momentum of a final-state particle in a collision is decomposed into its transverse and longitudinal components relative to the beam-line: $\mathbf{p} = \mathbf{p}_{\rm T} + \mathbf{p}_{\rm L}$. The transverse momentum, $p_{\rm T} \equiv |\mathbf{p}_{\rm T}|$, serves as a proxy for the momentum transfer Q. The longitudinal momentum by the initial longitudinal momentum carried by the parton inside a colliding nucleon. While $p_{\rm T}$ is approximately conserved in a collision, $p_{\rm L}$ is not, since two colliding partons will carry a different momentum fraction x of their parent nucleons. Instead of using the longitudinal momentum, particles are typically described by rapidity, $y = \frac{1}{2}\ln\frac{E+cP_{\rm L}}{E-cP_{\rm L}}$. The rapidity adds for boost β along the longitudinal direction: $y' = y + \beta$, which has the advantage that the shape of a distribution differential in y does not depend on the reference frame. Often, however, the rapidity is approximated in the massless limit by the pseudo-rapidity, $\eta = \frac{1}{2}\ln\frac{|\mathbf{p}|+P_{\rm L}}{|\mathbf{p}|-P_{\rm L}}$. Note that pseudo-rapidity diverges along the beam axis, while the rapidity does not, since it is cut off by the particle mass. The pseudo-rapidity has the advantage, however, that it can be written purely in terms of the polar angle: $\eta = -\ln\left[\tan\frac{\theta}{2}\right]$. Intuitively, then, we can think of η as depending on the relative amount of $p_{\rm T}$ compared to $p_{\rm L}$. It is useful also to note that the distance $R = \sqrt{(\phi_1-\phi_2)^2+(\eta_1-\eta_2)^2}$ is invariant under Lorentz transformations along the beam line. We will typically describe the complete

particle three-momentum **p** by the coordinates p_{T}, η and φ.

Aside from the kinematics of the outgoing particles, we need to describe the geometrical overlap of two colliding nuclei. When two nuclei collide, only a few nucleons participate in the collision. The number of participating nucleons, referred to as N_{part}, is defined as the number of nucleons from one nucleus that undergo one (or more) binary collision(s) with nucleons of the other nucleus. The total number of binary collisions is referred to as N_{coll}. The number of nucleons that do not participate in the collision (or "spectate") is referred to as N_{spec}. Therefore, by definition, $N_{\mathrm{part}} = 2A - N_{\mathrm{spec}}$, where A is the atomic mass of the colliding nucleus ($A = 208$ for Pb–Pb collisions). The number of participating nucleons is determined in part by the impact parameter b of the collision, which is defined as the distance between the centers of the two colliding nuclei in the transverse plane. Hence N_{part} scales with the overlap between the two nuclei. The geometry of a heavy-ion event both before and after the collision is schematized in Fig. 1.7.

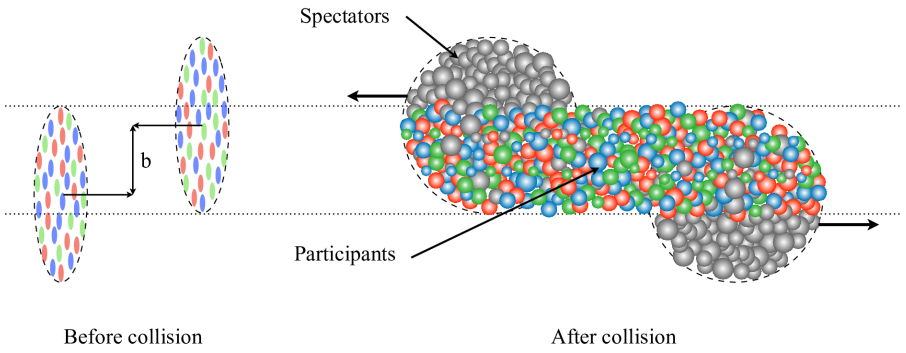

Figure 1.7: A schematic view of a heavy-ion collision. The impact parameter b is shown as well as the spectator nucleons and the participant nucleons. Figure from Ref. [6].

As effects due to the QGP medium may vary with the impact parameter, it is common to perform analyses on collections of events with a similar collision geometry, determined by the so-called "centrality". Due to the experimentally inaccessible nature of b, analogs are used instead, for example the average charged-particle multiplicity ($\langle N_{\mathrm{ch}} \rangle$) that increases monotonically with b. In ALICE, the centrality is determined by the information delivered by the V0 detector and scaling with the charged-particle multiplicity. The measured multiplicity distribution, shown for ALICE data in Fig. 1.8, is then fitted with the Glauber model [64] coupled to a particle production model to determine the corresponding N_{spec} and N_{part}. Smaller percentile values of centrality (for example 0–2.5% or yet more central collisions) refer to

collisions with large overlap and therefore small values of b and large percentile values of centrality (for example 70–80% or peripheral collisions) refer to collisions with small overlap. Another experimental observable that can be related to the number of spectators is the energy carried by particles close to the beam direction and deposited in the ALICE Zero-Degree Calorimeters.

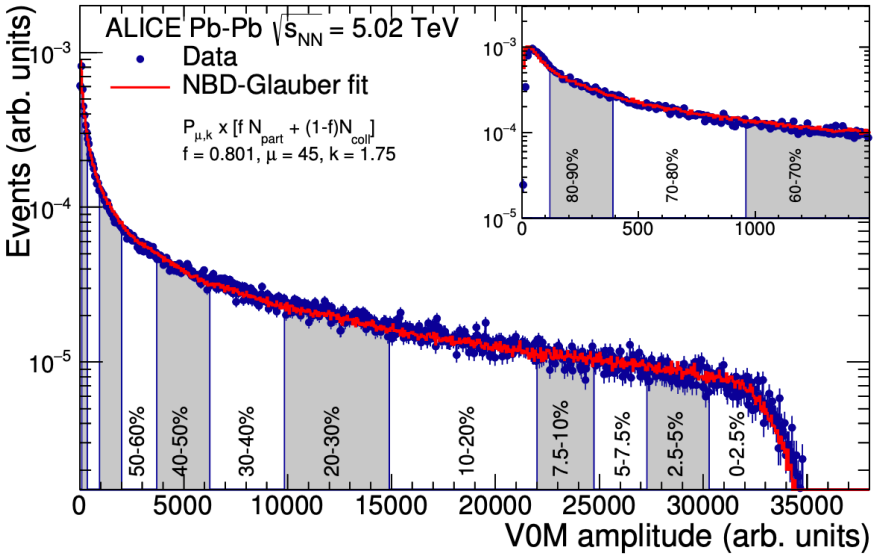

Figure 1.8: Number of events as a function of charged particle multiplicity in V0 detector for Pb–Pb collisions at $\sqrt{s_{NN}}$ = 5.02 TeV. The distribution is fitted with the NBD-Glauber fit shown as a line. The inset shows a zoom of the most peripheral region. Figure from Ref. [7].

As the phenomena studied in heavy-ion collisions have been observed in increasingly smaller systems (at ALICE, pp or p–Pb collisions) [7, 65], this approach to determining centrality has been applied to studies of these smaller systems as well. While the term "centrality" or "percentile" may still be used, this is perhaps better understood as event activity, since the correlation between multiplicity and impact parameter is weaker in these systems. More details about the categorization of multiplicity in pp collisions are given in Section 4.2.

1.6 Signatures of the quark-gluon plasma

Due to very short lifetime of the QGP (a few fm/c), direct observation of the QGP isn't feasible. Following its formation, it expands, cools down and hadronizes into final state hadrons. It is not possible to observe each stage separately in the experiment. Instead, we can measure the time integrated final state quantities like charged particle multiplicities, photon or lepton multiplicities, particle and jet transverse momentum spectra, energy, anisotropic flow etc. In experiments studying the QGP properties and its dynamics, probes are grouped in three categories: soft probes, electroweak probes, and hard probes. Their

classification largely depends on the specific processes at their origin. More details will be provided in the upcoming discussion.

1.6.1 Soft probes

The soft probes pertain to the hadronization products of the QGP medium, often associated with collective QGP properties, like radial flow. One exception includes measurements of the enhancement of (multi-)strange hadrons [66], which are expected to be created throughout the evolution of the QGP.

Since the QGP medium is expanding during its evolution, massive particles that interact with the QGP will be collectively affected by the expansion, generating what is referred to as flow. We can study the expansion of the medium through both **radial and anisotropic flow**, which are sensitive to the bulk and shear viscosity of the QGP, respectively. Radial flow occurs due to an extremely strong pressure at the centre of the QGP compared to the outskirts, and this leads to a common velocity field outwards. Anisotropic flow is a natural consequence of a hydrodynamical expansion developing from a non-uniform geometry of the overlap region between the two colliding nuclei, at first order an elliptical almond-shaped geometry symmetric with respect to the reaction plane, as illustrated in Fig. 1.9. Measuring the p_{T} spectra of identified particles is a suitable probe of radial flow, where higher mass

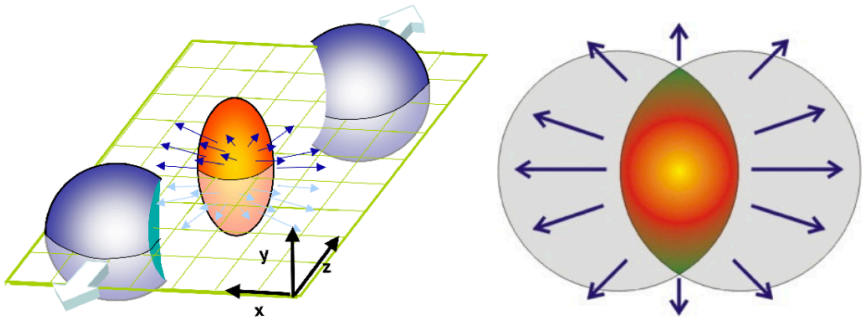

Figure 1.9: A schematic illustration of the almond shaped impact region in the reaction plane, after a non-central collision, as it evolves into anisotropic expansion in momentum space. Figure from Ref. [8].

particles are expected to exhibit a higher p_{T} boost. In order to investigate anisotropic flow, we construct the (Lorentz-invariant) azimuthal distribution of particles relative to the reaction plane. This distribution is expanded in a Fourier decomposition in φ as follows

$$E\frac{\mathrm{d}^3N}{\mathrm{d}p^3} = \frac{1}{2\pi}\frac{\mathrm{d}^2N}{p_{\mathrm{T}}\mathrm{d}p_{\mathrm{T}}\mathrm{d}y}\left\{1+2\sum_{n=1}^{\infty}v_n\left(p_{\mathrm{T}}\right)\cos\left[n\left(\varphi-\Psi_n\right)\right]\right\}, \tag{1.7}$$

The v_n terms, which can be determined experimentally, are referred to as the coefficients for different flow harmonics. They depend on the particle species, p_{T} and y. The term n corresponds to the order of

harmonic (anisotropic flow), and Ψ_n is the corresponding symmetry plane angle, which is the angular direction of anisotropic flow for the order n of interest. φ represents the angular component of the transverse momentum vector. $\varphi - \Psi_n$ denotes the azimuthal angle relative to the n^{th} order reaction plane. The harmonics represent shapes of different anisotropic flow, each sensitive to fluctuations in different ways. The elliptic flow is characterized by the 2nd harmonic, v_2, and shapes up to the fifth harmonic are illustrated in Fig. 1.10.

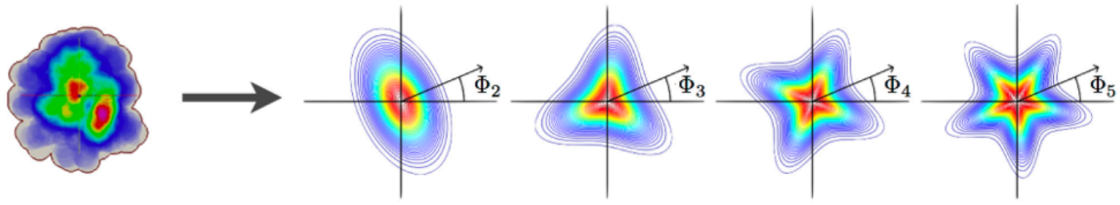

Figure 1.10: Visual representation of the Fourier decomposition of the flow harmonics, Here Ψ_n reflects the n^{th} order harmonic. Figure from Ref. [9].

For the vast majority of produced hadrons, non-zero v_n coefficients arise mainly from the QGPs hydrodynamic response (with a relatively small contribution from the hadronic state). Regarding the coupling of the created electromagnetic fields with quarks, the Chiral Magnetic Effect (CME) [67] introduces charge-dependent sine terms in Eq. 1.7 for the produced hadrons with corresponding coefficients. These are small relative to the v_n coefficients, but can also be explored experimentally. Any motion due to an electric field in the QGP will lead to charge-dependent v_1 coefficients.

We also have a little brief introduction relative to **(multi)-strangeness enhancement** in the exploration of QGP soft probes. In the standard model, the s quark is the third lightest quark, as illustrated in Fig. 1.1, and it belongs to the second generation with a mass of 96 MeV and no valence strange quarks is are present in the initial colliding nucleons. Therefore, most of the strangeness are created during the collision. The s quarks can be found in many kinds of hadrons, such as K^0_S $(d\bar{s}+\bar{d}s)$, Λ (uds), Ξ^- (dss) and Ω^- (sss) etc. A larger production of hadrons with strange-quark content in nucleus–nucleus collisions with respect to pp collisions is predicted to be a signature of the hadronic matter deconfinement, and it is denominated strangeness enhancement [68]. In fact, the absence of valence strange quarks in the colliding nuclei implies that they must be produced in the collision or during the QGP phase. Below the critical temperature for the phase transition, the production of ss pairs is suppressed, since the strange-quark effective mass implies a production threshold of about 1 GeV. In the QGP, the effective mass of strange quarks reduces by a factor up to 10 due to the chiral-symmetry restoration [69]. Therefore, ss

pairs are expected to be abundantly produced via gluon-fusion processes in the QGP, where the gluon density is large, resulting in an increase of the strangeness production in heavy-ion collisions.

In an alternative approach based on the statistical hadronisation model, the strangeness enhancement can be explained as a suppression of the strangeness production in small collision systems, referred to as canonical suppression [70]. The gran-canonical description, where quantum numbers are conserved on average over relatively large volumes, cannot be applied in pp and p–A collisions due to the small number of produced particles. Instead, the canonical formulation must be adopted, which requires an exact quantum-number conservation. Therefore, the phase space available for particle production is reduced, and the strange-hadron production is suppressed. In this context, the strangeness enhancement in heavy-ion collisions is interpreted as the lifting of the canonical suppression typical of small systems.

An enhanced production of strange hadrons was observed in heavy-ion collisions at SPS [71], RHIC [72], and LHC [66] energies. Recently, it was observed for the first time also in high-multiplicity pp collisions by the ALICE Collaboration [73]. In Fig. 1.11, the p_{T}-integrated yields of strange and multi-strange hadrons divided by that of charged pions as a function of the charged-particle multiplicity at mid-rapidity are reported for different collision systems and centre-of-mass energies per nucleon pair. The measured strange-hadron production is larger in Pb–Pb collisions with respect to low-multiplicity pp collisions, and it increases smoothly with increasing charged-particle multiplicity. The observed enhancement is more pronounced for hadrons with a higher strange-quark content. The production yields are compatible in collisions characterised by similar final state multiplicities, showing no significant dependence on the centre-of-mass energy or the collision system. This points to an origin of the strangeness production in hadronic collisions driven by the properties of the final state.

1.6.2 Electroweak probes

The electroweak probes, also referred to as non-interacting probes, relate to particles weakly interacting with the QGP, such as photons, leptons, or Z/W bosons. These particles have a mean-free-path larger than the QGP size. If these particles arise from hard processes in the initial stages, measurements of nuclear modification factor R_{AA} at high-p_{T} are expected to be unity, and any deviations from this reveal the influences of non-QGP processes that affect this measurement. Here we will focus on the measurements of real photons and virtual photons measured via lepton pairs (called dileptons), which can be measured by the ALICE experiment.

Photons produced via the decay of other particles are called decay photons, and all other photons are referred to as direct photons. At low transverse momenta, the direct photon spectrum is expected to

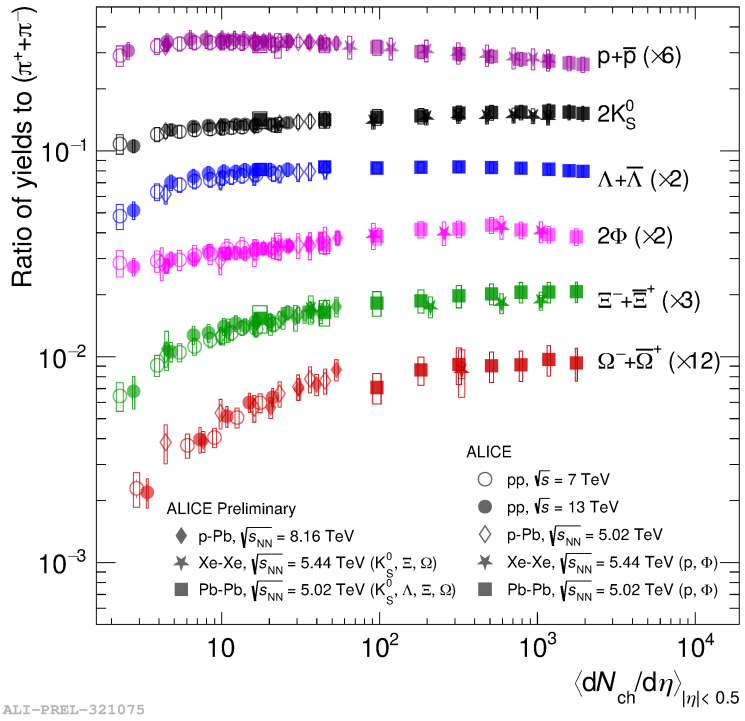

Figure 1.11: Ratios of the p_T-integrated yield of hadrons with strange-quark content and charged pions as a function of the charged-particle multiplicity at mid-rapidity, measured by the ALICE Collaboration in various collision systems and at different energies. Figure from the ALICE figure repository.

arise mainly from the softer processes in the QGP involving charged quarks and dominated by photons radiated during QGP evolution, or so-called "thermal photons". Experimental measurements of thermal photons provide powerful constraints on the temperature and the space-time evolution of the QGP as well as useful input for the QCD equation of state [74]. Dileptons originating from various sources can be separated via the mass of the dilepton pair, where at low invariant mass the dominant contribution is from thermal radiation from the hot hadron gas. At larger masses there are contributions both from semi-leptonic decays of open heavy-flavor hadrons and thermal radiation from the QGP. Current ALICE measurements of dileptons are not yet sensitive to signals of thermally produced dileptons, but such measurements may be possible in Run 3 and Run 4 of the LHC [75].

1.6.3 Hard probes

The hard probes result from high momentum transfer parton scatterings and are calculable in pQCD, including measurements of heavy flavor (charmonium and bottomonium) particles, hard charged hadrons, jets and so on. As these partons are produced in the earliest times of the collision before QGP formation they experience its full evolution and serve as a colored probe of the colored medium. The partons are expected to lose energy via interactions with the QGP and this energy loss can be useful in the determi-

nation of the various intrinsic and dynamic QGP properties. The most relevant QGP property related to the study of hard probes is the transport coefficient, $\hat{q} = d\left\langle k_{\perp}^{2}\right\rangle / dL$, which quantifies the momentum transfer between a hard parton and the soft QGP medium per unit length.

Different partons may interact differently with the QGP and therefore it is useful to isolate and study the interactions of different types of partons, for example heavy quarks with the QGP. Heavy quarks are expected to interact differently with the QGP than light quarks and measurements of heavy quarks can be used to constrain intrinsic properties of the QGP and various dynamical properties of the QGP. Heavy-flavor measurements can be broken up into open heavy-flavor measurements and hidden heavy-flavor measurements. Open heavy-flavor measurements refer to the direct measurement of a heavy-flavor meson (mesons containing c and b quarks, such as D and B mesons, respectively), serving as a proxy for a hard-scattered heavy quark (c and b). Hidden heavy-flavor, or quarkonia states, refer to bound $q\bar{q}$ states (so $c\bar{c}$ and $b\bar{b}$ states). Common examples include the charmonium states of J/ψ and $\psi\ (2s)$, and the bottomonium states of $\Upsilon\ (1s)$, $\Upsilon\ (2s)$, and $\Upsilon\ (3s)$. An additional hard probe of the QGP is the measurement of hard charged hadrons. These roughly correspond to the hadronization products originating from the hard-scattered partons, and therefore retain the signature of parton energy loss effects in the QGP. Another proxy for the dynamics of the hard-scattered parton is via jets, which will be discussed at length below and the remainder of this thesis.

The hard probes signature of the QGP can be explored by extracting the nuclear modification factor R_{AA}. This observable is constructed to be sensitive to changes in the dynamics of hard scattered partons in heavy-ion collisions with respect to expectations from elementary pp collisions. Within a y or η interval, R_{AA} as a function of transverse momentum is defined as follows:

$$R_{\mathrm{AA}} = \frac{\mathrm{d}N_{\mathrm{AA}}/\mathrm{d}p_{\mathrm{T}}}{\langle N_{\mathrm{coll}}\rangle\,\mathrm{d}N_{\mathrm{pp}}/\mathrm{d}p_{\mathrm{T}}} = \frac{\mathrm{d}N_{\mathrm{AA}}/\mathrm{d}p_{\mathrm{T}}}{\langle T_{\mathrm{AA}}\rangle\,\mathrm{d}\sigma_{\mathrm{pp}}/\mathrm{d}p_{\mathrm{T}}}, \tag{1.8}$$

The average nuclear overlap function $\langle T_{\mathrm{AA}}\rangle = \frac{\langle N_{\mathrm{coll}}\rangle}{\sigma_{\mathrm{inel}}^{\mathrm{NN}}}$ is calculated as the ratio of the average number of binary collisions (N_{coll}) between two nucleons, calculated by a Glauber model, and the inelastic nucleon-nucleon cross section [64], as discussed in the previous Section 1.5.2. For hard processes, the yield (N_{AA}) in heavy-ion collisions is expected to scale with the average nuclear overlap function ($\langle T_{\mathrm{AA}}\rangle$) when compared to the production cross section (σ_{pp}) in pp collisions, assuming the absence of any QGP or initial state nuclear effects. If $R_{\mathrm{AA}}(p_{\mathrm{T}}) = 1$, the production from heavy-ion collisions can be considered a superposition of nucleon–nucleon collisions, assuming the QGP is not formed in pp collisions. Any deviation from unity reveals how these processes are modified in heavy-ion collisions. In particular, R_{AA} is expected to be below unity at high-p_{T} for inclusive hadrons originating from partons

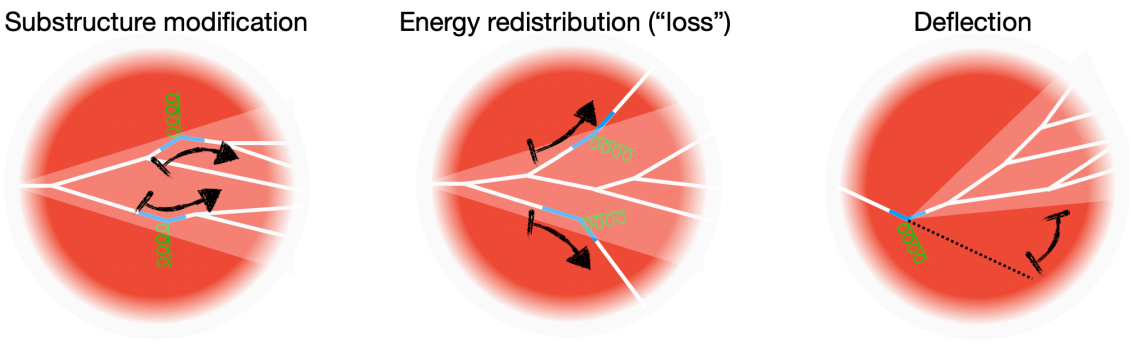

Figure 1.12: Three manifestations of jet quenching in experimental measurements.

that have experienced an energy loss. Jets is a better observable to identify hard-scattered partons. The internal structure of a jet is governed by quantum interference effects, resulting in the phenomenon of angle-ordering, whereby the highest p_{T} hadrons in the shower are, on average, most closely aligned with the nominal jet axis. A key parameter in jet measurements is the jet radius or jet resolution parameter R, which effectively represents the size of the aperture through which the jet shower is viewed. The measured jet yields can be used to determine R_{AA}, while the jet radius dependence of the R_{AA} or jet substructure measurements provides information about the medium modifications of the quark and gluon radiation patterns. Heavy-ion jets can be compared to jets in pp collisions, where no such modifications are expected.

A specific class of hard probes, heavy quarks, provides insights into various QGP features through differential measurements of R_{AA} and v_n. A key distinction is that the associated hadrons are linked to early-stage probes across their entire p_{T} range. D mesons, carrying the majority of produced charm quarks, can be differentially investigated as a function of p_{T} through measurements of v_n and R_{AA}. Low-p_{T} measurements of v_n are sensitive to the extent to which heavy quarks participate in the collective expansion of the QGP and approach thermalisation. High-p_{T} measurements of R_{AA} offer insights into the energy loss processes of heavy quarks, which may be smaller than those for light quarks or gluons, due to the dead cone effect [76].

The focus of this section is to introduce another hard probe, jets, to understand the production and propagation of high-momentum jets in the QGP. A scattered parton with p_{T} greater than a few GeV/c propagates and evolves independently of other products of the same high-Q^2 interaction, starting at a time earlier than 1 fm/c. The QGP has an extended size, with a lifetime in the order of 10 fm/c, so that the jet shower propagates through the expanding and cooling QGP. During this process, the jet shower itself evolves, and its color-charged constituents interact with the color-charged constituents of

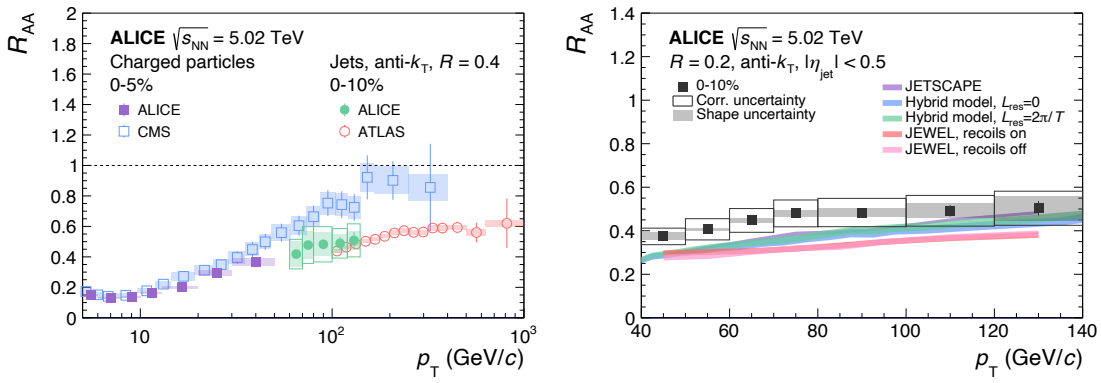

Figure 1.13: Left: Measurement of R_{AA} for charged hadrons (ALICE [10] and CMS [11]) and jets (ALICE [12] and ATLAS [13]) in central Pb–Pb collisions. Right: ALICE measurements of R_{AA} for charged jets [12] in central Pb–Pb collisions compared to different model calculations.

the QGP, resulting in the modification of the shower. Such modifications, called "jet quenching," are observable experimentally and calculable theoretically. Comparisons of jet quenching between data and calculations provide unique, probes of QGP structure and dynamics. Experimentally, jet quenching manifests in several ways, as shown in Fig. 1.12: Medium-induced modification of the distribution of jet constituents is observed through the radial energy profile, jet substructure, and fragmentation functions; Medium-induced energy transport to large angles to the hard parton or jet direction, commonly called "energy loss," is observed through inclusive yield suppression; Jet centroid deflection due to soft multiple scattering or scattering from quasi-particles in the QGP is observed as medium-induced acoplanarity in coincidence measurements. This multifaceted approach to quantifying jet quenching is a valuable opportunity as it must provide a consistent picture of jet quenching, thereby significantly constraining our understanding of its underlying processes. Next, a detailed summary of what has been learned from jet measurements is summarized.

Energy loss of jets and hadrons

High-p_T hadrons and reconstructed jets explore different aspects of jet quenching. Hadrons are sensitive principally to energy loss in the hardest branch of the jet shower, while jets, which subtend an area approximately πR^2 for jet resolution parameter R, are sensitive more broadly to modification of the shower. A comprehensive understanding of jet quenching requires measurements of both high-p_T hadrons and reconstructed jets, with the latter spanning significant range in jet p_T and R. In this section inclusive jet measurements are discussed and compared to the inclusive hadron measurements.

Left plot in Fig. 1.13 illustrates R_{AA} in central Pb–Pb collisions at $\sqrt{s_{NN}}$ = 5.02 TeV for inclusive jets with R = 0.4, together with charged hadrons. Jet R_{AA} show more pronounced suppression than hadrons

at the same p_T. At higher p_T, the ALICE [12] and ATLAS [13] jet data measurements are consistent, revealing a gradual increase in R_{AA} with rising p_T. In general, a reconstructed jet will catch a fraction of medium-induced radiation, and the inclusive p_T-spectrum of jets is significantly harder than that of hadrons. Both factors suggest that R_{AA} for inclusive jets will be larger than that for inclusive hadrons. It is important to note that, although the opposite is observed in the p_T region where the measurements of hadrons and jets overlap, a direct comparison is not meaningful since hadrons and jets at any given p_T originate from different parton energies. For a proper interpretation of this observation, the inclusive hadron population must be mapped to that of jets, considering the bias imposed by selecting high-p_T hadrons.

The right panel in Fig. 1.13 shows comparisons of the measured R_{AA} for reconstructed $R = 0.2$ jets with JETSCAPE [77], JEWEL [31, 78, 79], and the hybrid model [80, 81] (more detailed description of the model see Section 2.4). Jets with $R = 0.2$ are used for this comparison due to their higher precision and larger p_T range. The JETSCAPE calculations broadly describe the jet measurements over the entire measured p_T interval. However, JEWEL tends to overestimate the suppression for jet R_{AA}, regardless of the inclusion of medium recoil, although the inclusion of recoil tends to align the model more closely with the data. While the hybrid model captures the general trends of the jet R_{AA}, it does exhibit some degree of tension.

As discussed above, jet yield suppression measurements are only indirectly related to jet energy loss, as yield suppression depends on both the population-averaged energy loss and the shape of the spectrum. However, these effects can be disentangled for jet yield suppression measurements because reconstructed jets encompass all correlated hadronic energy within the jet cone. Jet yield suppression must, therefore, arise from energy transport out of the jet cone, i.e., jet energy loss. Several recent papers have carried out such a phenomenological extraction of energy loss by converting yield suppression to the equivalent p_T-shift of the spectrum [15, 82–84].

Jet substructure modification

Modifications to the internal structure of jets can be studied with jet-substructure observable – defined by first clustering a jet, and then constructing an observable as a function of the properties of the constituents of that jet [85–89]. Jet substructure observable can be constructed to be sensitive to specific regions of jet radiation phase space in a way that is theoretically calculable from first principles [90–93], and can target limited regions of phase space to explore specific jet quenching mechanisms that cannot be resolved using jet p_T measurements alone [94–101]. Questions addressed include the strength of the jet-medium coupling, the rate of medium-induced emissions, and constraints on medium properties such as

coherence scales and the nature of the QGP degrees of freedom.

The jet-substructure observable is used to investigate modifications of the internal structure of jets. These observable are created by first clustering a jet and then forming an observable based on the properties of its constituents. These observable are designed to be sensitive to specific regions of the jet radiation phase space, allowing for theoretical calculations from first principles. By targeting limited phase space regions, specific jet quenching mechanisms can be explored and that cannot be fully understood through jet p_{T} measurements alone. The questions addressed in these studies include understanding the strength of the jet-medium coupling, the rate of medium-induced emissions, and constraints on medium properties such as coherence scales and the nature of the QGP degrees of freedom [75].

Jet substructure measurements can be classified into two distinct types: measurements of jet structure and measurements of jet substructure. Jet structure variables probe the distribution of radiation within a jet at the hadron level, while jet substructure variables focus on the hard substructure of the jet at the parton level. Examples of jet structure variables include jet "fragmentation functions", as defined in Equation 1.9 below

$$D(z) \equiv \frac{1}{N_{\mathrm{jet}}} \frac{\mathrm{d}n_{\mathrm{ch}}}{\mathrm{d}z}, \tag{1.9}$$

where $z = \frac{p_{\mathrm{T,i}}}{p_{\mathrm{T,jet}}} \cos(\Delta R)$ is the fraction of jet p_{T} carried by a jet constituent (in some cases, the $\cos(\Delta R)$ term is omitted in this definition). The fragmentation functions of jets has been measured many times: for inclusive jets, photon-tagged jets, and D^0 mesons within jets. [102–104], showing a significant modification in heavy-ion collisions of this observable. The radial fragmentation function measures a similar quantity differentially in angle by looking at the number density in transverse rings outward from the jet axis [105]. The jet shape (also referred to as the jet profile) measures the radial distribution of momentum carried by the constituents of the jet. The jet shape has been measured for inclusive jets [106, 107], photon-tagged jets [108], and to measure the radial distribution of D0 mesons within jets [109].

Jet substructure observable probe partonic splittings via subjets within the jet (or 'prongs'). A grooming procedure is typically applied to reduce sensitivity to the non-perturbative effects and focus on the hard substructure of the jet (perturbative part). In this approach, jet grooming algorithms such as Soft Drop (SD) [91, 110, 111] are applied to remove soft, wide-angle radiation and identify a single hard "splitting". To achieve this, we first identify a jet using the anti-k_{T} algorithm and then re-cluster the jet constituents according to the Cambridge-Aachen algorithm to produce an angularly ordered tree, similar to a parton shower. We then unwind the last clustering step and check the SD condition $z > z_{\mathrm{cut}}(\frac{\Delta R}{R})^{\beta}$, where z_{cut}

and β are tunable parameters of the SD algorithm. Here, z_{cut} serves as a soft threshold, and β serves as the angular exponent, typically taken as $z_{\text{cut}} = 0.1$, $\beta = 0$. If the condition is met, we consider the two subjets as a hard splitting of the jet and characterize them by the shared momentum fraction,

$$z_{\text{g}} \equiv \frac{p_{\text{T,sub-leading}}}{p_{\text{T,leading}} + p_{\text{T,sub-leading}}}, \tag{1.10}$$

where $z_{\text{g}} \to 0.5$ denotes a symmetric splitting, and $z_{\text{g}} \to 0$ denotes an asymmetric splitting. The angle θ is defined as the angular distance between the two branches of the identified splitting,

$$\theta_{\text{g}} \equiv \frac{R_{\text{g}}}{R} \equiv \frac{\sqrt{\Delta y^2 + \Delta\varphi^2}}{R}, \tag{1.11}$$

in this equation, y is the rapidity, φ is the azimuthal angle, and R is the jet resolution parameter. The groomed splitting can be characterised by two kinematic observable: the groomed momentum splitting fraction (or the splitting function), z_{g}, and the groomed jet radius, θ_{g}, with z and θ for the groomed splitting as defined in Eq. 1.10 and 1.11.

The initial heavy-ion jet substructure measurements conducted by CMS [88] and ALICE [85] pointed to a suppression of symmetric splittings relative to asymmetric splittings in Pb–Pb collisions when compared to pp collisions. However, further analysis uncovered additional background contributions from mistagged splittings originating from the underlying event [112]. Recently, ALICE addressed these mistagging effects by implementing more robust grooming conditions and smaller R, conducting measurements in more peripheral collisions. In Fig. 1.14, the left panel illustrates the measurement of z_{g}, revealing no significant modification in the z_{g} distribution for Pb–Pb collisions compared to pp collisions. This observation aligns, within uncertainties, with various jet quenching models, also depicted.

The analysis techniques employed also allow for measurements of the angular distribution θ_{g} as depicted in the right panel of Fig. 1.14. It reveals a notable narrowing of the θ_{g} (R_{g}) distribution in central Pb–Pb collisions compared to pp collisions, providing direct evidence of the modification of the angular scale of jets within the quark-gluon plasma.

Medium-induced acoplanarity

Jet medium-induced modification is studied via intrajet shapes and substructure, which are sensitive to the redistribution of jet momentum and constituents toward wider angles. This subsection explores these effects through the analysis of semi-inclusive azimuthal angular distributions of jets recoiling from

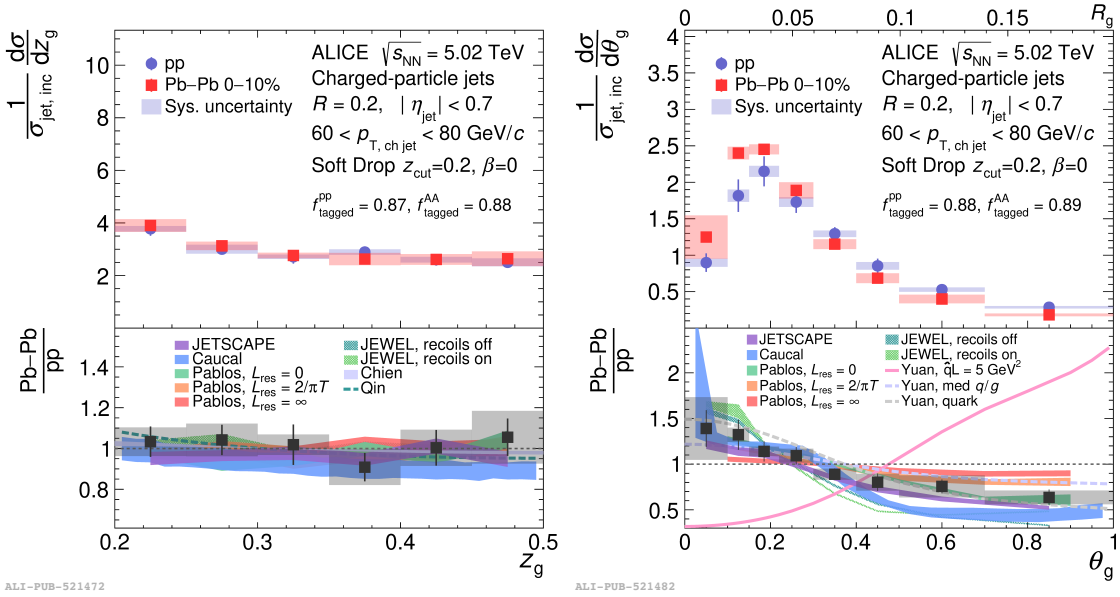

Figure 1.14: Jet z_g (left) and θ_g (right) in 0–10% centrality for R = 0.2 charged-particle jets [14]. The ratio of the distributions in Pb–Pb and pp collisions is shown in the bottom panels and is compared to various jet quenching calculations.

a hadron trigger [15, 83]. In vacuum, the width of the azimuthal distribution of recoil jets primarily results from soft radiation (Sudakov radiation [113]), while for in-medium jets, modification of the vacuum angular distribution arises from (inelastic) gluon emission and elastic scattering off the medium constituents. Measurements distinguishing vacuum and medium-induced azimuthal decorrelation effects directly probe the transport coefficient $\hat{q}$. Since Sudakov radiation dominates at high jet p_T compared to medium effects [113], studying azimuthal decorrelation at low $p_{T,jet}$ is desirable, though challenging due to a large uncorrelated background in low-$p_{T,jet}$ measurements in heavy-ion collisions, requiring new experimental approaches.

The expected difference in the parametric dependence of jet energy loss and momentum broadening on the medium path length L [114, 115] motivates the simultaneous measurement of observable sensitive to both energy loss and momentum broadening, discriminating between weakly- and strongly-coupled scenarios.

Measurement of the rate of jet scattering to large angles with respect to the trigger axis may also provide evidence of weakly-coupled degrees of freedom within the strongly-coupled QGP ("quasi-particles"), similar to the Rutherford scattering experiment revealing the atomic nucleus [116, 117]. The deflection of an energetic quark projectile in the QGP is expected to be Gaussian if the QGP is strongly coupled at all scales. However, QCD is asymptotically free and thus weakly-coupled quark and gluon quasi-particle degrees of freedom are expected to emerge when the QGP is probed at sufficiently short distances. The

scattering off point-like quasi-particles will lead to a power-law tail in the momentum transfer ($1/k_{\mathrm{T}}^4$), known as Moliere scattering [116, 117]. An excess of large-angle deflections observed in Pb–Pb relative to pp collisions would directly observe such quasi-particles in the QGP. The large-angle scattering signal is expected to be small, however, requiring high experimental sensitivity to observe it.

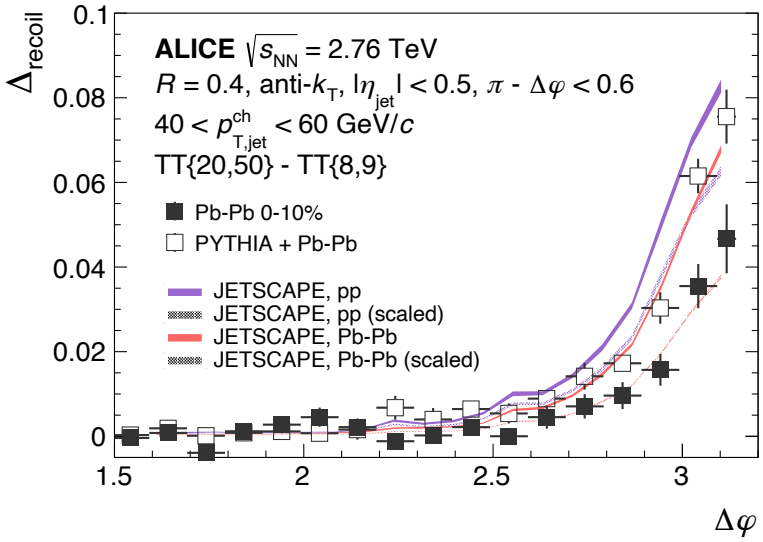

Figure 1.15: ALICE measurement of h+jet acoplanarity in 0-10% Pb–Pb collisions at $\sqrt{s_{\mathrm{NN}}}$ = 2.76 TeV [15] compared to an embedded PYTHIA+Pb–Pb reference and JETSCAPE calculations, in pp and Pb–Pb collisions for charged-particle recoil jets with R = 0.4 and $40 < p_{\mathrm{T,jet}} < 60$ GeV/c. Figure from Ref. [16].

Figure 1.15 shows the first ALICE measurement of the azimuthal decorrelation in 0–10% Pb–Pb collisions at $\sqrt{s_{\mathrm{NN}}}$ = 2.76 TeV [15]. The horizontal axis represents the azimuthal angle $\Delta\varphi$ between a high-p_{T} charged hadron and the recoiling jets. The vertical axis corresponds to the Δ_{recoil} observable (Eq. 5.2) measured differentially in $\Delta\varphi$. The widths of the distributions in Pb–Pb data and in the vacuum reference, which in this case is a PYTHIA calculation for pp collisions embedded into Pb–Pb data, are statistically compatible. The absolute yield of the Pb–Pb distribution is seen to be smaller than that of the pp reference, indicating that the recoiling jet yield is suppressed in Pb–Pb collisions.

For the selected kinematic cuts and jet resolution R, the strong energy loss is therefore not accompanied by a medium-induced acoplanarity within the statistical and systematic limits of our measurement. The change of recoil jet yield at large angles with respect to the PYTHIA reference was also studied, and within the uncertainties of the ALICE Run1 experiment, no signs of large-angle scattering were observed. In this thesis, we utilize the larger data statistics from ALICE Run2 to further explore this phenomenon of large-angle scattering.

The figure also shows the result of JETSCAPE calculations which have been smeared to account for

instrumental effects and background fluctuations for comparison, since the data have not been unfolded for such effects. JETSCAPE overpredicts the magnitude of the $\Delta\varphi$ distribution, and slightly underpredicts the level of suppression in Pb–Pb collisions compared to the PYTHIA reference. In order to factor out the effect of an overall yield suppression and compare shapes directly as a function of $\Delta\varphi$, which could reveal quasi-particle effects, the JETSCAPE distributions are shown scaled to the same integrals of the corresponding pp and Pb–Pb distributions in data. The scaled JETSCAPE distributions reproduce the data well, likewise exhibiting no evidence of in-medium acoplanarity broadening or quasi-particle scattering.

1.7 QGP-like behaviours in small systems

In Section 1.6 we present the probes of the QGP in heavy-ion collisions as well as the results of experimental measurements. These signatures were believed to be unique features of heavy-ion collisions, and robust probes for investigating the properties of the QGP. However, several results from high-multiplicity pp and p–Pb collisions in recent years have revealed that these signatures are also present in smaller collision systems [118–125]. This raised the question if the QGP could be formed as well in small systems and if so what is the real mechanism leading to the QGP formation? This also creates a difficult challenge for current theoretical frameworks, as smaller collision systems produce a very small volume. Consequently, these small volumes will have too short lifetimes to allow the system to fully equilibrate. This has generated a lot of confusion, as previously non-controversial interpretations of past measurements have to be re-examined in this new context, leading to several potential outcomes: Either the lifetime in small volumes is long enough to allow equilibration and to create droplets of QGP, or the medium does not need to be fully equilibrated to form the QGP. This would imply that previous measurements are signs of a QGP forming, for small and large systems alike. QCD-inspired models being able to describe "QGP features" in smaller collision systems opens up the possibility that no QGP is formed in heavy-ion collisions. Instead, these features could be described by different phenomenological adaptations of QCD. While the signatures are qualitatively similar, the collective effects (**a double ridge extended in pseudorapidity, strangeness enhancement**, anisotropic flow, **increasing baryon-to-meson ratios at intermediate** p_{T}**,** nuclear modification) in small and large systems could still originate from different phenomena.

These fundamental issues and confusions have received great attention, and their investigation can be considered among the main novel aspects. At the same time, some of the typical dense QCD medium effects, such as jet-quenching or heavy flavor R_{AA} modification, have not yet been observed in small collision systems [126–128]. Thus, we aim to investigate the jet quenching effect with the current level

of accuracy in high-multiplicity pp collisions. In this subsection, we will briefly describe and discuss the main results obtained by the current experiment to this exciting endeavour.

Long-range ridge: A measurement of the two-particle angular correlation in pp collisions with different multiplicity intervals has been performed by the CMS collaboration [17]. Fig. 1.16 presents the two-particle correlation functions ($\Delta\eta - \Delta\varphi$) measured by the CMS collaboration in pp collisions at $\sqrt{s} = 13$ TeV. The left panel reports the two-particle correlation for low-multiplicity events, which reflects what would be expected from a hard dijet; a leading jet with strong correlation at $\Delta\varphi \approx \Delta\eta \approx 0$, followed by a ridge from the subleading jet at $\Delta\varphi \approx \pi$ along the entire $\Delta\eta$ range. Remarkably, the same measurement at high multiplicity presents a significant ridge along the nearside jet, at $\Delta\varphi \approx 0$, along the entire $\Delta\eta$ range. The strength of this correlation is suggested to increase linearly with multiplicity and indicates that longitudinal collective behavior is also present in smaller collision systems.

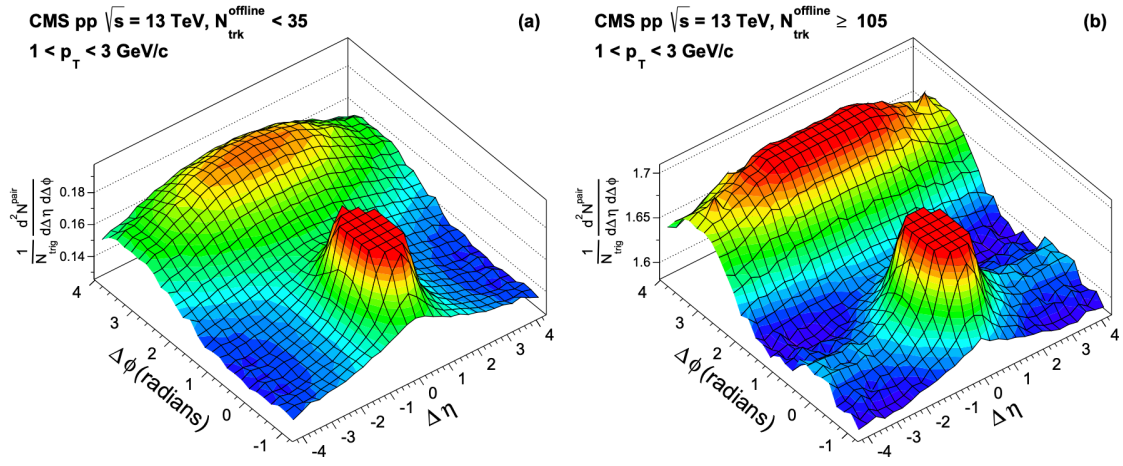

Figure 1.16: Two-particle correlation distributions as function of $\Delta\eta$ and $\Delta\varphi$ in pp collisions at $\sqrt{s} = 13$ TeV, for low (high) multiplicity events in the left (right) panel. Figure from Ref. [17].

Strangeness enhancement: As demonstrated by the strangeness enhancement observed in Pb–Pb collisions in Fig. 1.11, this effect is also observed in high-multiplicity pp and p–Pb collisions. In the figure, the hadron-to-π ratios are listed, for several hadrons containing strange quarks, as a function of midrapidity multiplicity. It can be seen that the smaller collision systems follow the same, universal curve as the Pb–Pb curves. Both pp and p–Pb exhibit strangeness enhancement, seeing large relative increases at higher multiplicities. Furthermore, similar to the observation in Pb–Pb, the enhancement grows stronger with increased strangeness content.

Baryon-to-meson ratio: In high-multiplicity pp and p–Pb collisions, a notable feature is the enhancement of the baryon-to-meson yield ratios, p/π and Λ/K^0_S, at intermediate transverse momentum p_{T}

(2–6 GeV/c) [73, 126, 129–131], which is qualitatively similar to that observed in Pb–Pb collisions. Fig. 1.17 illustrates the Λ/K^0_S yield ratios as a function of p_{T} in pp collisions at $\sqrt{s}$ = 7 TeV (left), p–Pb (middle), and Pb–Pb collisions at $\sqrt{s}$ = 5.02 TeV (right) for the lowest and highest multiplicity classes. These ratios manifest a distinctive depletion at $p_{\mathrm{T}} \sim 0.7$ GeV/c and an enhancement at intermediate p_{T} ($\sim$ 3 GeV/c) in high-multiplicity events compared to low-multiplicity events, similar to observations in pp, p–Pb, and Pb–Pb collisions. Such behavior might indicate a common mechanism of baryon-to-meson enhancement at work in different collision systems that depends solely on final-state multiplicity density. Moreover, this finding adds to the evidence that small systems also exhibit collective behaviour, which may have similar physical origins in pp, p–Pb, and Pb–Pb collisions [65].

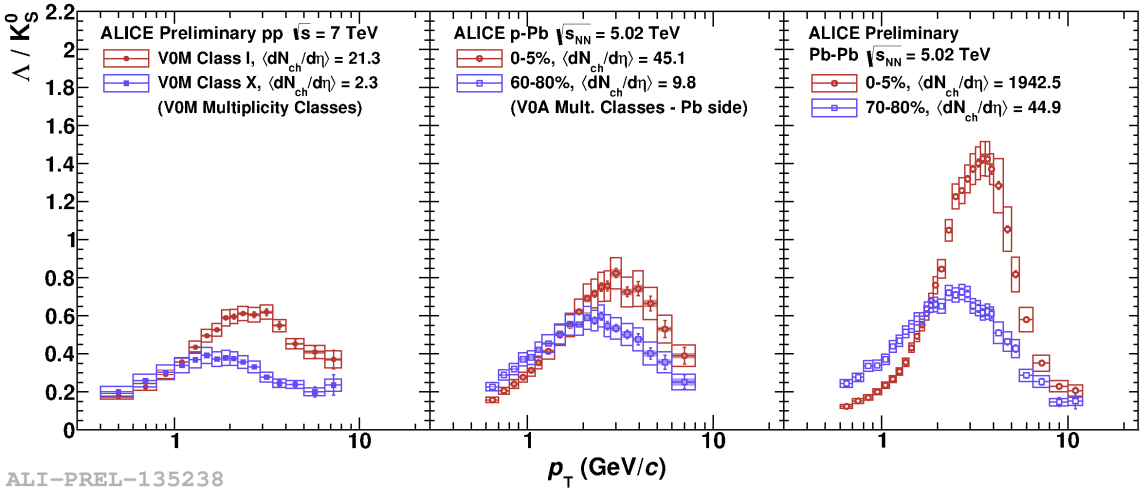

Figure 1.17: p_{T}-differential Λ/K^0_S ratios. From the left to the right subpanel in figures, the results from pp, p–Pb and Pb–Pb collisions are shown. Two event multiplicity classes are shown: red (blue) markers represent the results from the highest (lowest) multiplicity events in the respective colliding systems. Figure from the ALICE figure repository.

The observation of these phenomena in high-multiplicity proton-proton collisions resembling collective effects from heavy-ion collisions has been met with great interest from theorists. There are two main directions how to interpret the observations: One idea is that indeed at high enough multiplicities in proton-proton collisions, a medium is formed, for which a hydrodynamic description is adequate. The same concepts as for nuclear collision then can be applied, one has “one fluid to rule them all” [132]. The other approach is to explain the observations without the formation of a deconfined medium. In order to do this, one has to give up the interpretation of one proton-proton collision as the independent superposition of several partonic interactions. For example, the flow-like patterns in the azimuthal particle correlations can be ascribed to QCD interference between the produced partons [133], saturation effects in the initial state parton density functions in the framework of CGC [134], or the rearrangement of the initial color strings of the produced partons, known as “color reconnection” [135]. The

observed strangeness enhancement with multiplicity can be explained under the assumption of interacting strings fusing into ropes ("rope hadronization" [136]). Further extensions of the rope model ("rope shoving", see [137]) are also able to explain the azimuthal particle correlations. It can thus be said that the emergence of effects reminiscent of collective phenomena in small systems at high-multiplicity is theoretically not well understood yet, but of great importance for the correct interpretation of effects in heavy-ion collisions, which are traditionally seen as clear indications for the creation of a medium.

This thesis is divided into seven chapters. Chapter 1 gives an background introduction to the theoretical basis of high energy collisions relevant to the content of this thesis. Chapter 2 provides information on the components of the ALICE detector utilized for subsequent analyses, along with a brief overview of the ALICE offline framework and a description of the Monte Carlo simulations employed in this thesis. Chapter 3 covers the introduction to general techniques of track and jet reconstruction, as well as specialized correction techniques. Chapter 4 discusses the measurement of the multiplicity dependence of charged-particle jet production for different jet resolution parameters in pp collision at $\sqrt{s}$ = 13 TeV. Chapter 5 discusses the measurement of semi-inclusive hadron-jet correlations in pp collisions at $\sqrt{s}$ = 5.02 TeV. Chapter 6 briefly presents the progress of heavy-flavor jet correlation using machine learning technique. Finally, Chapter 7 includes a discussion of these results and an outlook for future measurements.

2 ALICE: A Large Ion Collider Experiment

In this chapter, we provide a brief overview of the Large Hadron Collider (LHC) particle accelerator, outlining its main characteristics and associated experiments. In particular the ALICE experiment is the experiment dedicated to the heavy-ion program for the investigation of the QGP. The data used for the analyses presented in this thesis were collected by the ALICE detectors. A detailed description of the various ALICE subsystems will be presented, in particular those relevant to our analyses, including VZER0 (V0), Inner Tracking System (ITS), Time Projection Chamber (TPC), and Time of Flight (TOF). Additionally, a brief introduction to the ALICE offline framework is provided to grasp the operational mode of AliPhysics. Given the significance of Monte Carlo (MC) simulations utilizing various models (PYTHIA, POWHEG, JETSCAPE, JEWEL, and Hybrid Model calculations), we also present a concise introduction to the fundamental principles of the framework.

2.1 The Large Hadron Collider

The Large Hadron Collider (LHC) [54, 138] is the world's largest and most powerful particle accelerator system. It consists of a set of particle accelerators injecting into a synchrotron ring. It is operated and has been constructed by the European Organization of Nuclear Research (CERN), located near Geneva on the border between Switzerland and France. The LHC is located about 100 m underground, and spans a circumference of 27-kilometres, with 1232 superconducting dipole magnets, which can accelerate protons and ions in two separate beam-lines and create collisions of pp, p–Pb, and Pb–Pb nuclei. The peak center-of-mass energies reached during Run2 period were respectively 13, 8.16 and 5.02 TeV.

Particles are accelerated in several steps to reach the peak collision energy. This is achieved through a complex system of several accelerators [18, 139], illustrated in Fig. 2.1. After being stripped from electrons, the protons and ions are accelerated up to 2 GeV by the Proton Synchrotron Booster (PSB). Their energy is then ramped up to 26 and 450 GeV respectively by the Proton Synchrotron (PS) and Super Proton Synchrotron (SPS). The protons and ions are then finally injected into the LHC ring, where they are accelerated to their final peak energies ready for collisions.

The LHC physics program is currently driven by four major experiments. A Toroidal LHC Apparatus (ATLAS) [140] and the Compact Muon Solenoid (CMS) [141], are two general-purpose pp experiments, which are primarily focused on the study of rare physics processes searching for dark matter and other physics beyond the Standard Model. Two other experiments are specialized, the Large Hadron Collider-beauty (LHCb) [142] experiment is designed to study flavor physics, in particular $b\bar{b}$ physics, while A

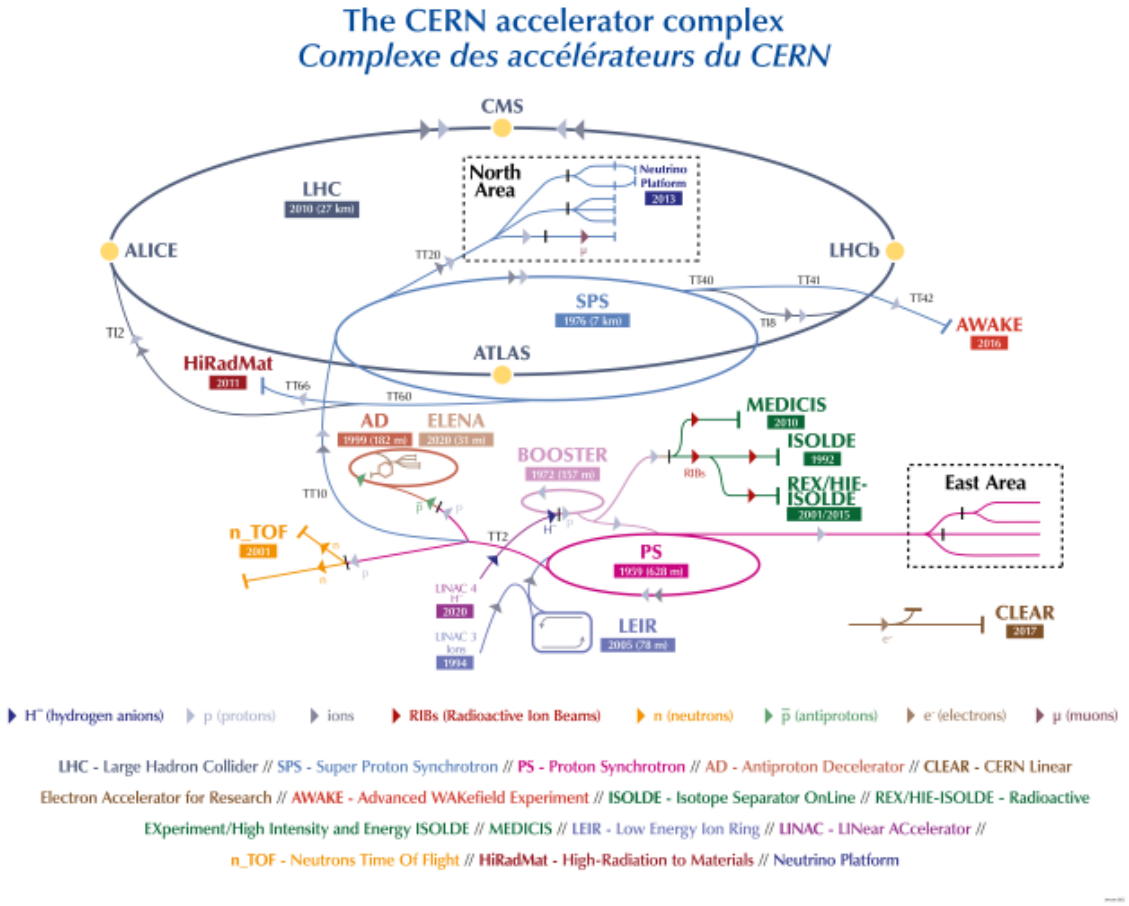

Figure 2.1: Schematic of the LHC accelerator and its injection system. The four main LHC experiments are also shown. Figure from Ref. [18].

Large Ion Collider Experiment (ALICE) [54] is the only experiment optimized for heavy-ion collisions in the LHC physics program. The LHC yearly operation is mainly dedicated to proton–proton collisions, and a short period is allocated to heavy-ion data taking, with so far either p–Pb, Pb–Pb, Xe–Xe collisions or Oxygen–Oxygen.

Whereas the pp experiments are designed to operate at maximum collision rate (luminosity), luminosities for heavy-ion collisions being relatively low, the challenge of ALICE was primarily to design a detector that can cope with the extremely large low-p_{T} charged particle densities produced in central heavy-ion collisions. When used in pp collisions data taking mode, ALICE has not the sensitivity for rare probes as the dedicated pp experiments have, but ALICE is unique in low-p_{T} measurements, and in particle identification (PID) capabilities extending thus the physics reach of the pp experiments. The studies presented in this thesis benefit strongly from both of these two factors.

The LHC delivered the first pp collisions in 2009. During the first data taking period (Run 1, 2009-2013) protons were accelerated up to $\sqrt{s}$ = 8 TeV , Pb–Pb collisions were delivered at $\sqrt{s_{\rm NN}}$ = 2.76 TeV , and p–Pb collisions at $\sqrt{s_{\rm NN}}$ = 5.02 TeV. After the first Long Shutdown (LS1), the LHC began the second data taking period (Run 2, 2015–2018), during which it collided protons up to $\sqrt{s}$ = 13 TeV , p–Pb collisions up to $\sqrt{s_{\rm NN}}$ = 8.16 TeV and Pb–Pb collisions at $\sqrt{s_{\rm NN}}$ = 5.02 TeV. During Run 2, the LHC also provided Xe–Xe collisions at $\sqrt{s_{\rm NN}}$ = 5.44 TeV. During the third data taking period (Run 3), which officially started in July 2022 after the second Long Shutdown (LS2), pp collisions are delivered at $\sqrt{s}$ = 13.6 TeV and lead ions at $\sqrt{s_{\rm NN}}$ = 5.5 TeV. After Run 3, during the third Long Shutdown, the LHC will be upgraded to High Luminosity LHC, which will deliver proton collisions at a peak luminosity 5 to 7 times larger than the present nominal value of 10^{34} cm^{3}s^{-1}. Afterwards, in 2029, the Run 4 data taking period is expected to start.

2.2 The ALICE experiment and detectors

A Large Ion Collider Experiment (ALICE) [54] is one of the four main experiments at the LHC. ALICE is an experiment that is primarily intended to study nucleus–nucleus collision, which is reflected in the overall design of the detector. ALICE is capable of capturing the full dynamics, at midrapidity, of Pb–Pb nuclei colliding at relativistic energies. Unlike a pp collision, with charged particle densities at midrapidity of $\langle {\rm d}N_{\rm ch}/{\rm d}\eta \rangle \approx 7$ at $\sqrt{s}$ = 13 TeV [143], a Pb–Pb collision at $\sqrt{s_{\rm NN}}$ = 5.02 TeV produces $\langle {\rm d}N_{\rm ch}/{\rm d}\eta \rangle \approx 1950$ for the top-5% most central collisions [144]. Superb spatial resolution is required to reconstruct each individual particle trajectory. However, this precision comes at a cost of a slow recording rate; during LHC Run 2, ALICE was only able to operate at a rate of 0.2 kHz for Pb–Pb collisions, and 350 kHz for pp collisions, out of the 8 kHz and 40 MHz collisions rate provided by the LHC for Pb–Pb and pp collisions, respectively.

The ALICE detector, located 56 m underground, has a total weight of approximately 10000 tons, and its overall dimensions are 16 × 16 × 26 m^3. The configuration of the ALICE detector during Run 2 is illustrated in Fig. 2.2. Based on their pseudorapidity coverage, the apparatus is primarily composed of two main components: a central barrel and the forward detectors.

The central barrel comprises essential systems for track reconstruction, collision-vertex reconstruction, and particle identification. Enclosed within the large L3 solenoid magnet (depicted as the red structure in Fig. 2.2), weighing 7800 tons, and featuring a nominal magnetic flux density of 0.5 T, the central barrel spans a pseudorapidity range of $0.9 < \eta < 0.9$ and the full azimuth. It includes the following detection subsystems: Inner Tracking System (ITS), Time Projection Chamber (TPC), Transition Radi-

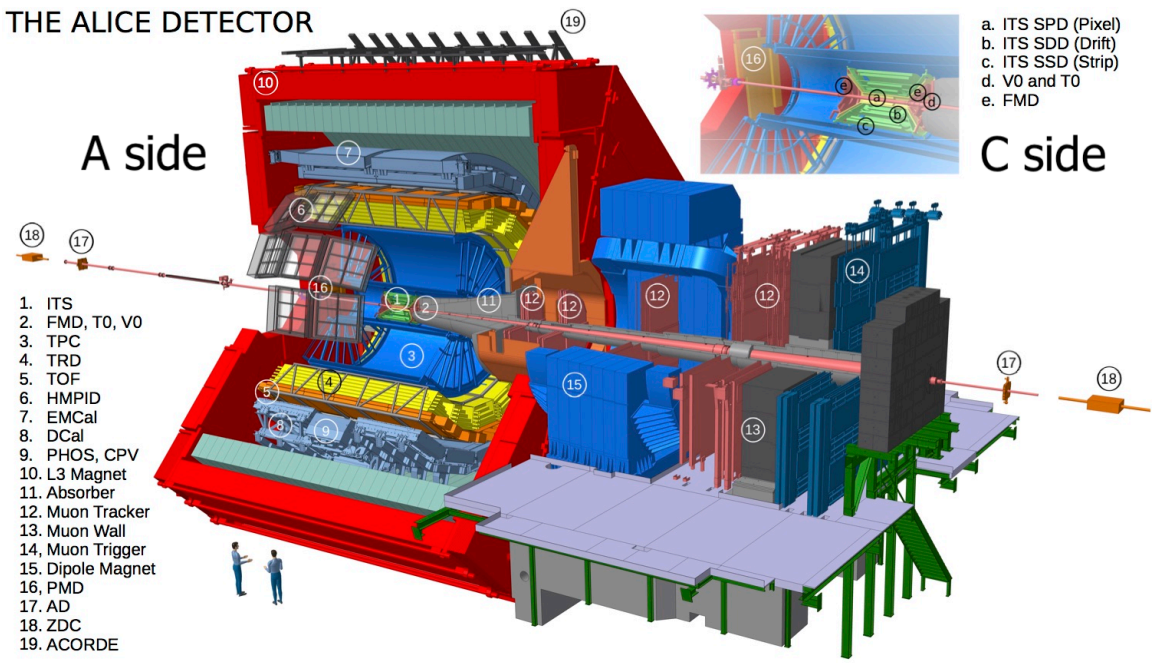

Figure 2.2: The ALICE detector, with all components labeled. The right-hand side is the "C"-side, and the left-hand side if the "A"-side. Figure from Ref. [19].

ation Detector (TRD), Time of Flight (TOF) detector, High-Momentum Particle Identification Detector (HMPID), Photon Spectrometer (PHOS), Electromagnetic Calorimeter (EMCal), the Dijet Calorimeter (DCAL). EMCal and DCal are primarily designed and employed to measure jet physics and reconstruct particles decaying to electrons and photons. The ALICE Cosmic Ray Detector (ACORDE) positioned on top of the solenoid L3 magnet is used to trigger on muons originating from cosmic rays, which can be used for alignment purposes and cosmic-ray measurements.

The forward detectors refer to the detectors located outside the central barrel. The forward detectors are locate on opposite "sides", with respect to the central barrel; The "C"-side, which points toward the CMS experiment (right-direction w.r.t Fig. 2.2), and the "A"-side, facing the ATLAS experiment (left-direction w.r.t Fig. 2.2). The forward muon spectrometer is dedicated to muons detection. It consists of various absorbers, a dipole magnet, ten planes of cathode pad chambers, and four planes of resistive plate chambers. The muon spectrometer covers the pseudorapidity range of $4 < \eta < 2.5$ and the entire azimuth. The other forward detectors, such as Zero Degree Calorimeter (ZDC), Photon Multiplicity Detector (PMD), Forward Multiplicity Detector (FMD), TZERO (T0), V0A and V0C, are located at forward and backward pseudorapidity, i.e. at small polar angles, are used for global events characterisation and for triggering purposes.

V0 detectors

The V0 detector (also referred to as VZERO) [145] consists of two arrays of scintillation counters, called V0A and V0C, placed at forward rapidity. The V0A, with a radius of 41.2 cm, is located at 340 cm from the interaction point and covers the pseudorapidity range of $2.8 < |\eta| < 5.1$, whereas the V0C, with a radius of 32.0 cm, is placed on the opposite side at 90 cm from the interaction point and covers the pseudorapidity range of $3.7 < |\eta| < 1.7$. The V0 detector contributes to the minimum bias (MB) trigger, to identify and select inelastic pp, p–Pb and Pb–Pb collisions. It is also used to determine the centrality of p–Pb and Pb–Pb collisions via the measurement of the multiplicity of produced charged particles, and to classify pp collisions in multiplicity classes. It also participates to the determination of the luminosity in pp collisions.

The measured response correlates to the total amount of charged particles produced in the V0 pseudo-rapidity interval. The charged particle multiplicity is then estimated through percentiles of the V0M distribution, which is the mean between the raw V0A and V0C signals. The self-normalized V0M distribution for pp collisions at $\sqrt{s} = 13$ TeV is presented in Fig. 2.3. A comparison to the equivalent V0M distribution for Pb–Pb collisions, presented previously in Fig. 1.8, highlights that the overall multiplicity distribution is much broader in Pb–Pb collisions. In pp collisions, even though the V0A covers a broader rapidity interval, the signal delivered by V0C is usually dominant for the multiplicity estimation, since it is located closer to the interaction point (and thereby faces a larger charged particle density).

The multiplicity measured in the V0 detectors can thus be correlated with multiplicity and other physics observables measured with the central barrel detectors in a distinct pseudorapidity regions. Examples are the jet measurements and multiplicity estimation presented in this thesis. The benefit of this approach is that one avoids possible auto-correlations, which could otherwise bias observables toward unphysical results. If the particle extraction and multiplicity estimation occur in the same pseudorapidity region, one risks biasing the event selection toward local fluctuations that produce an abundance of charged particles. In subsequent sections of this thesis we will show more details about multiplicity measurement and compare the jet physical measurements from the two pseudorapidity regions.

Inner Tracking System

The Inner tracking system (ITS) [146] is the first detector located radially outward from the interaction point. The central motivations of the ITS are to identify the primary vertex of the collision, to extend the lever arm of the tracking system, to provide $\mathrm{d}E/\mathrm{d}x$ measurements at low p_{T}, and to measure secondary vertices from long-lived unstable particles such as heavy-flavor hadrons (D mesons and b-hadrons). For the purpose of this thesis, the relevant elements are the determination (identification) of the primary

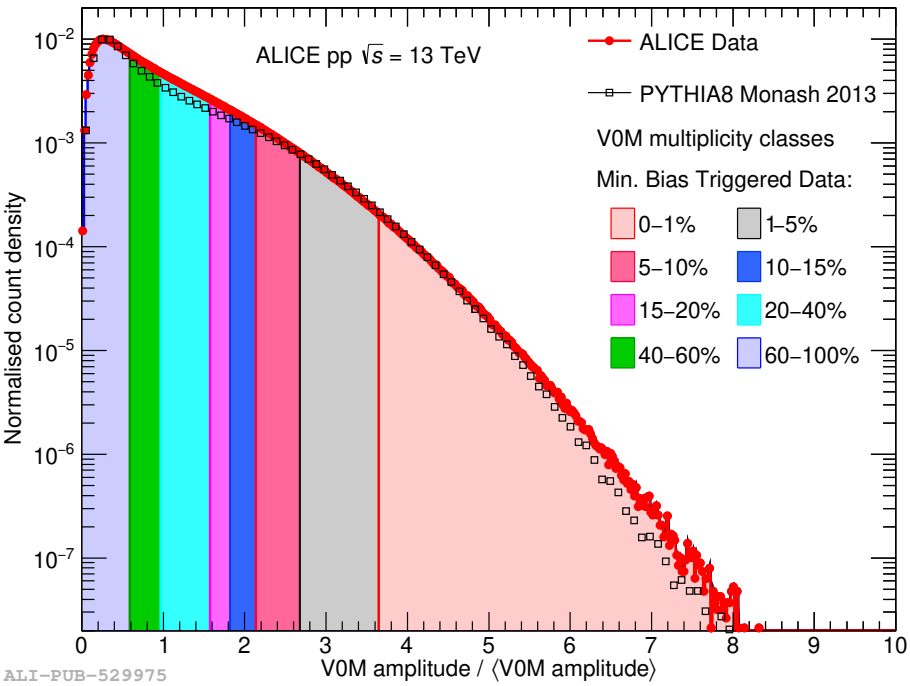

Figure 2.3: Scaled V0M distribution which is used to determine the forward multiplicity classes in pp collisions at $\sqrt{s}$ = 13 TeV. The colour shaded areas represent V0M multiplicity classes obtained from real data. The PYTHIA8 distribution is shown with the open black markers. Figure from Ref. [20].

vertex, separation of this vertex from the secondary decay vertex and the extension of the tracking system lever arm.

The ITS is a cylindrical device consisting of six layers of three different silicon detectors directly surrounding the beryllium beam pipe. They have have been designed for their fast response and good spatial resolution. They cover a wide pseudorapidity range ($|\eta| < 0.9$). The Silicon Pixel Detector (SPD) is closest to the beam pipe, followed by the Silicon Drift Detector (SDD) and the Silicon Strip Detector (SSD) ranging up to a radius of 43 cm. The innermost and most crucial layers, the SPD, extends to $|\eta| < 2$ and has its inner layer is located 3.9 cm from beam axis. In order to cope with a high track density (tens of tracks per cm^2), the sensors have a fine segmentation $50\,\mu m \times 425\,\mu m$ and provide $\approx$ 10M readout channels. This results in a primary vertex resolution of $\approx 12\,\mu$m. The two outer silicon detectors are involved in the particle identification via $\mathrm{d}E/\mathrm{d}x$ energy loss measurements. The SPD can be used for event triggering. The ITS is directly or indirectly involved in nearly all physics analyses.

Time Projection Chamber

The Time Projection Chamber (TPC) [21, 147] is the largest tracking device of the ALICE detector, providing, based on their curvature and energy deposition, excellent ability to identify charged particles

down to $p_{\mathrm{T}} \approx 150$ MeV/c. The schematic layout of TPC is shown in Fig. 2.4. TPC covers the pseudo-rapidity range $|\eta| < 0.9$ and full azimuthal angle. TPC is cylindrical in shape with an inner radius of 80 cm and an outer radius of 250 cm. It occupies an active volume of 88 m^3 covering a length of 500 cm along the beam axis. When a charged particle traverses the TPC, it ionizes the TPC gas (usually 90% noble gas and 10% quencher gas) along its track. The charged particle loses an amount of energy per unit track length ($\mathrm{d}E/\mathrm{d}x$) different for each particle type. The free ionisation electrons drift towards the endplates of the cylinder under the influence of the electric field and the gaz ions drift towards the high voltage cathode placed at the centre of the TPC. The magnetic field is oriented parallel to the electric field such that the drifting electrons are not influenced by it. At the end of drift path of the electrons, they are amplified by an avalanche process around the anode wires. For the readout of the signal Multi-Wire Proportional Chambers (MWPCs) at the end plates are used. There are two endplates and each endplate has 36 readout chambers arranged in 18 sectors. Each sector contains an Outer Readout Chamber (OROC) and an Inner Readout Chamber (IROC).

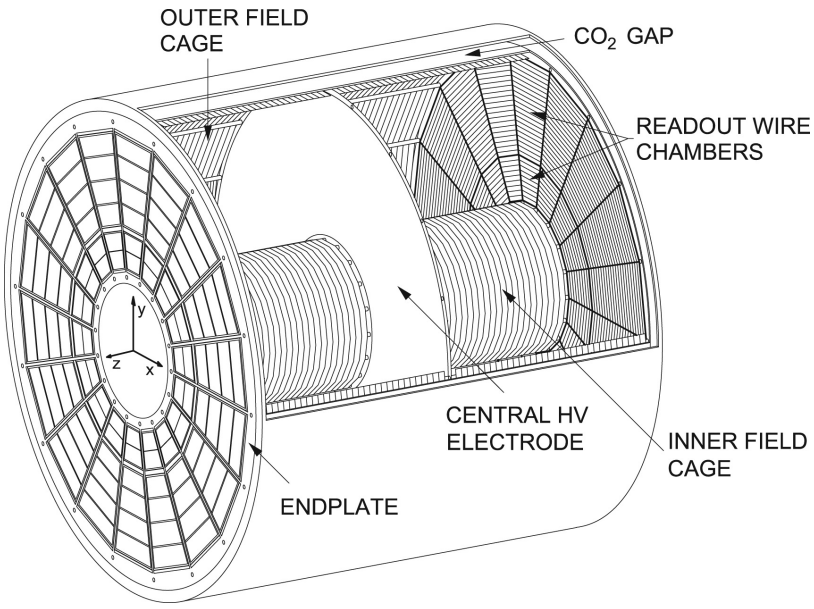

Figure 2.4: 3D view of the TPC field cage. The high voltage electrode is located at the center of the drift volume. Figure from Ref. [21].

The ALICE TPC can detect up to 159 space points along a track's trajectory. The x-y coordinates of the track (perpendicular to the beamline) are determined by the drift electrons induced signal on the 2D readout pad structure. The z-coordinate of the track (along the beamline) is then determined by the drift time of the electrons. Tracks are reconstructed using an iterative "inward-outward-inward" Kalman Filter based approach [148]. The track reconstruction process begins with a clusterization procedure performed separately in each detector to form "clusters" with a characteristic position, signal amplitude,

signal time, and error. So-called tracklets in the SPD are then formed by connecting clusters in the two layers of the SPD. The single space point where a maximum number of tracklets converge in the SPD is then used as a preliminary interaction vertex. Cluster information is then combined to form a track in a procedure with three iterations. The first iteration starts at the TPC and works inwards, matching TPC tracks to those in the ITS in order to construct a vertex. Then in the second iteration tracks are propagated from this vertex outwards through the ITS, TPC and to outer detectors such as the TRD and TOF. The third iteration moves from the outward TRD and TOF and moves inward, further constraining the primary vertex. Typically, the tracking efficiency is 80–90%; below $p_{\mathrm{T}} \approx 0.5$ GeV/c, the tracking efficiency drops due to energy loss from the detector material.

In addition to track reconstruction, TPC is crucial for particle identification. The particle identification in the TPC is performed by the simultaneous measurement of the charge, momentum and specific energy loss $\mathrm{d}E/\mathrm{d}x$ of each particle that traverses the chamber, using a truncated mean of the distribution of cluster energies of the track. This allows for the separation of pions from electrons up to several GeV/c, as well as the identification of pions from kaons and protons up to several GeV/c, as shown in Fig. 2.5 (left). The black lines show the mean energy loss predicted by the Bethe-Bloch formula for different particle species. This method of particle identification is very limited in the range of applications in the case of particle-by-particle identification. For particles with a momentum greater than 1 GeV/c, one can observe the intersection of the lines for the pion and kaon, making a PID decision in that region ambiguous. Therefore, yields of different particle species are extracted on a statistical basis with a template fit method. This approach can be applied to particles with transverse momenta up to 20 GeV/c. The TOF can enhance the PID capability of the TPC.

Time-of-Flight detector

The ALICE Time of Flight (TOF) detector [149] is an array of multigap resistive plate chambers (MRPCs) which covers the pseudorapidity range of $|\eta| < 0.9$ and has full azimuthal acceptance. It is positioned within a cylindrical shell with internal radius of 370 cm and external radius of 399 cm, and it is segmented into 18 azimuthal (18ϕ) sectors, called supermodules, each of which is segmented into five modules along the z direction ($5z$). Its main purpose is to provide particle identification of massive particles, by measuring the time-of-flight relative to the momentum of each reconstructed track.

An MRPC consists of a stack of resistive plates (in the case of ALICE, two rows of 5 glass plates surrounded, by anode and cathode plates). The resistive glass plates are spaced with nylon fishing lines to create gas-filled gaps, filled with a mixture of SF_6 and $C_2F_4H_2$. A 6.5 kV potential is applied symmetrically w.r.t. the middle plate in each MRPC stack. The potential is only applied between the

outer-to-middle stack, while the in-between stacks are left electrically floating. When a particle traverses the MRPC stack, an electron avalanche is produced in each gas gap. The resistive plates themselves are transparent to the electromagnetic signal generated by the electron avalanches, thereby allowing one to retrieve the full signal deposited on the external electrodes, by integrating the signal produced in each gas gap. The narrow gaps allow for more precise time measurements, as the time jitter scales with the propagation distance (from plate to plate) through the gas. This allows for a very precise measurement of the arrival time of each particle, with a time resolution of less than 50 ps [150].

In preparation for Run 3, the TOF underwent an important upgrade which mainly involved its readout electronics, with the purpose to accomplish the continuous readout of data.

The TOF identifies the particle species measuring their time of flight from the interaction point to the detector chambers. The start time for the TOF measurement is the time of the primary-collision event, which is estimated by using the signal from the T0 detector or the particle arrival times at the TOF detector. In the latter case, a combinatorial minimisation algorithm accounting for all the possible mass hypotheses is used. If both methods are available, the start time is the average of the T0 and TOF information weighted by their respective resolution.

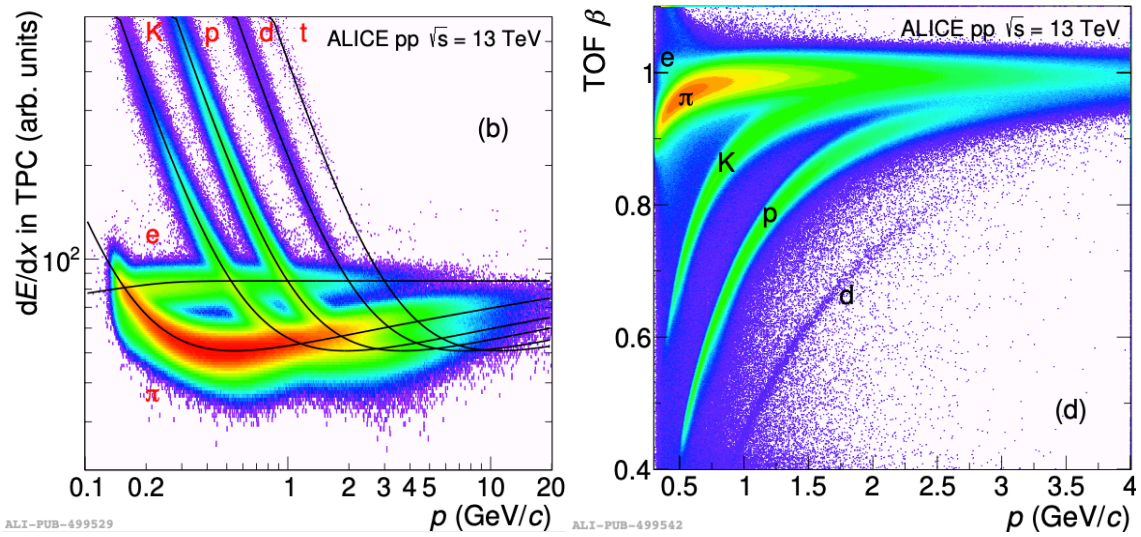

Figure 2.5: The dE/dx as a function of momentum p is used to identify charged particles measured by the TPC (left) and TOF (right). Figure from Ref. [22].

The distribution of particle velocities β measured by the TOF as a function of momentum is displayed on the right of Fig. 2.5 for pp collisions at $\sqrt{s}$ = 13 TeV. The background is caused by tracks which are incorrectly matched to TOF hits. The electron, pion, kaon, proton, and deuteron bands are clearly separated. The TOF detector provides a good pion-kaon separation for $p_{\mathrm{T}} < 3$ GeV/c and a satisfactory

kaon-proton discrimination up to $p_{\mathrm{T}} \simeq 5$ GeV/c. At $p_{\mathrm{T}} < 1$ GeV/c, the fraction of tracks matched to the TOF detector is small. Therefore, in the analyses, low-p_{T} tracks without the TOF particle-identification information are usually identified using only the TPC.

2.3 The ALICE offline framework

In this thesis, we utilize the ALICE Run 2 offline framework [151, 152], which includes AliRoot and AliPhysics, built upon ROOT [153], a sophisticated scientific software toolkit developed at CERN for data analysis. ROOT, an object-oriented framework written in C++, is tailored for handling extensive data processing. It provides functionalities for I/O handling, visualization, and statistical analysis, also integrated with other languages such as Python and R. AliRoot contributes a set of software classes and macros designed for detector alignment, calibration, data reconstruction, and visualization. These tools are instrumental in processing data collected during experiments and steering Monte Carlo (MC) simulations. To facilitate comprehensive simulations, AliRoot interfaces with event-generator codes, including PYTHIA 6 [154], PYTHIA 8 [33] for pp collisions, and HIJING [155] for heavy-ion collisions. The software incorporates various transport codes such as GEANT3 [156], GEANT4 [157], and FLUKA [158] to simulate particle interactions with detectors and support structures. AliRoot includes detailed descriptions of detector geometry, material budget, and response, implemented in independent modules dedicated to different detectors. The physics analyses of reconstructed data, whether from experiments or simulations, are encapsulated in the AliPhysics repository. This code, built on top of ROOT and AliRoot, consists of multiple tasks with a predefined structure, continually updated by data-analysis groups.

The ALICE experiment has collected over 160 PB of raw data, requiring substantial computing and storage resources. The Worldwide LHC Computing Grid (WLCG) [159, 160] provides these resources, serving as the largest global computing grid with 170 centers across 42 countries. The Grid operates in three Tiers, with Tier-0 centers like CERN and Wigner Research Centre initiating raw data reconstruction. Thirteen Tier-1 centers store a second data replica and engage in reconstruction and reprocessing. Smaller Tier-2 centers handle MC simulations and user data analyses. Access to data across the Grid is facilitated by ALICE Environment (AliEn) [161, 162] middleware, offering a dedicated interface for data access and executing tasks like reconstruction, simulation, and analysis, with real-time monitoring.

Physical data for reconstructing collisions from both real data and Monte Carlo simulations is stored in Event Summary Data (ESD) files. ESD files primarily serve detector calibration, alignment, and performance studies. The pertinent information for physics analyses is stored in a more condensed

format known as Analysis Object Data (AOD), typically processed by analysis tasks. AOD files are approximately six times smaller than ESD files, with an average size of about 400 kB/event for pp collisions and 2.2 MB/event for Pb–Pb collisions.

2.4 Monte Carlo simulations

Monte Carlo (MC) based random sampling simulation techniques are essential tools for today's high energy physics. The primary applications include the generation of collision events according to a theoretical model and a full simulation of the detector performance for particle detection and reconstruction. This simulation is crucial for correcting the measured distributions for instrumental effects. In this thesis, the default simulations used to correct for instrumental effects are carried out with the PYTHIA8 MC generator (Monash 2013 tune) [33, 34] in pp collisions. The detector response is simulated using GEANT 3.21 [156]. In Pb–Pb collisions, additional corrections for the residual background fluctuations are carried out by embedding PYTHIA8 pp events into Pb–Pb data events.

2.4.1 Event Generators in pp

In high-energy collisions, partons inside the colliding nucleons can scatter off one another with a high momentum transfer (Q^2) in a process referred to as a hard scattering. A majority of hard scatterings in the vacuum are $2 \rightarrow 2$, resulting in high-p_{T} partons traveling 180 degrees apart in the transverse plane with approximately equal p_{T}. The computation of the production cross-section of jets in QCD is discussed in Section 1.3. The out-going partons then fragment via a parton shower and hadronize into a spray of particles called a jet as shown in Fig. 1.3. MC models that simulate jets in vacuum typically include simulation of four different effects; **the parton shower, underlying event, hadronization, and hadronic decays**. In this section, the ways that available MC model each of these effects and the underlying physics mechanisms at play will be discussed.

Parton Shower

Analogous to the emission of photons from an accelerated electric charge, accelerated color charges can also emit gluons. However, these gluons themselves carry a color charge and can themselves emit further gluons. In addition, they can also produce quark-antiquark pairs. The combination of these two processes is referred to as the parton shower. This manifests itself as higher-order corrections to the original hard process described in Section 1.3. Due to the difficulty of the explicit calculation, the dominant contributions at each order, mostly soft gluon emission and collinear splittings, are instead approximated.

The parton shower process description above is for a Q^2- or virtuality-ordered shower, where the hardest

interactions occur first. However, there can be other types of showers that may be employed in MC. One such shower is a coherent shower, which produces an angular-ordered shower with less soft gluon emission as compared to a virtuality-ordered shower. This manifests itself in a different number and energy distribution of hadrons after hadronization. Another approach is a dipole shower where gluon emission is generated by the dipole radiation pattern of the parton pair. In this picture, each quark/anti-quark is uniquely connected to a color partner and gluons are connected to multiple color partners. Each pair of color partners forms a dipole that splits into two upon the emission of a gluon.

Underlying event

The term Underlying event (UE) in the context of jet measurements refers to anything that does not originate from the hard scattering of interest. One source of the UE is the fragmentation of non-colliding partons. Another source of UE is collisions between partons in the incoming hadrons that do not directly participate in the hard scattering. The extent of these multi-parton interactions (MPIs) and therefore the impact of the UE depends on the impact parameter structure of the hadron-hadron collision. The overlap of the partonic structures of the proton is directly related to the number of MPI, and therefore is important to model accurately. Both in- and out-of-bunch pileup can also contribute to the UE and may also be taken into account in simulations. Pileup refers to a phenomenon where a single event recorded in the detector contains information from multiple collisions. It can either occur for two collisions in the same bunch crossing (called in-bunch pileup) or two collisions in different bunch crossings (called out-of-bunch pileup).

Hadronization Models

As mentioned in Section 1.3, the transition from partons to hadrons is non-perturbative in nature and therefore difficult to calculate. To evolve parton-level predictions to the hadron-level and compare to experimental measurements, correction factors that estimate the size of non-perturbative effects are typically applied. These correction factors are determined by taking the ratio of predictions from event generators including and not-including non-perturbative effects such as hadronization and multi-parton interactions.

All partons in the final state, whether originating from the hard scattering of interest or the UE, must hadronize. There are two common models for hadronization; the cluster hadronization model [163, 164] and the string hadronization model [165]. **The cluster hadronization model** is based on the property of QCD where at evolution scales much less than the hard process scale, the partons in a shower are clustered into colorless groups. These groupings will only depend on q and Λ_{QCD}, and will be independent of the hard subprocesses. These clusters can be identified at the hadronization scale as proto-hadrons

that decay into the observed final-state hadrons. An illustration of the cluster hadronization model can be found in the left panel of Fig. 2.6 [23].

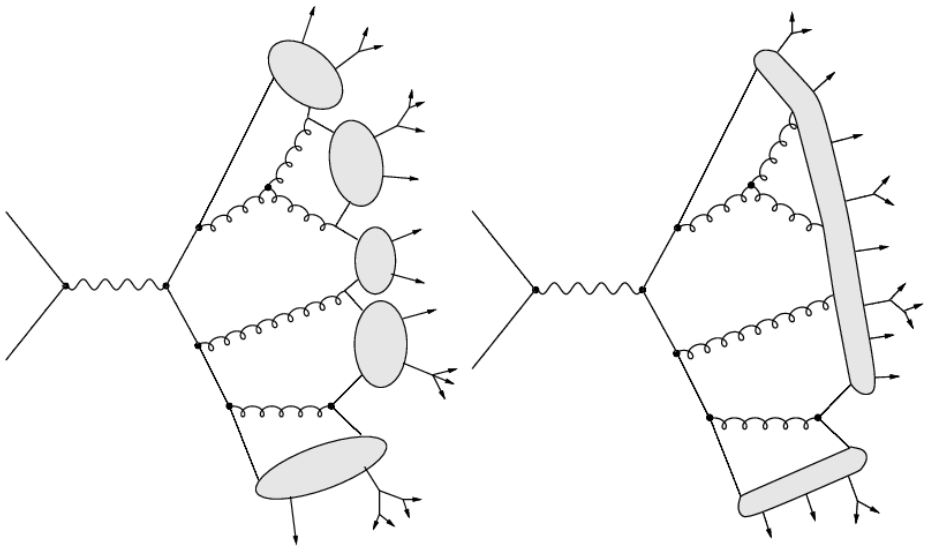

Figure 2.6: Illustrations of two different hadronization models. Cluster (left) and string (right) hadronization models. Figure from Ref. [23].

The string model is based on the observation from Lattice QCD that at large distances the potential energy of color sources increases linearly with their separation, creating a string (or tube). For example, when quarks and anti-quarks are separated a narrow flux tube (also called a string) forms between them with a constant strong force along the tube. As the distance between the two quarks becomes larger and larger, it becomes energetically favorable for an additional $q\bar{q}$ pair to arise from the vacuum as opposed to the flux tube getting larger. This process will then repeat itself until all available energy has been converted into $q\bar{q}$ pairs, which can be identified with mesons. Baryons are formed in a similar manner, but with a quark-diquark pair. Another illustration of the string hadronization model can be found in the right panel of Fig. 2.6.

Hadronic Decays

Following the hadronization step, the decay of any unstable hadrons must also be modeled. The decay products of excited hadronic states make up a large fraction of the observed final state, thus all excited states and all of the potential decay modes must be modeled with great accuracy. This process can be difficult as some properties of these hadronic decays are not yet established experimentally.

Example event generators

In PYTHIA [33, 154], event generation starts with a primary process that defines the nature of each

event. At LHC energies, this is in most cases a LO pQCD partonic scattering. At small p_{T} values, color screening effects need to be taken into account. Therefore a p_{T} cut-off called $p_{\mathrm{T},0}$ is introduced, which damps the QCD cross section for $p_{\mathrm{T}} \ll p_{\mathrm{T},0}$. This cut-off is one of the main tunable parameters. Subsequent partonic processes calculable in pQCD are initial- and final-state radiation interleaved with MPI, in addition to the structure of beam remnants. After these steps, a realistic partonic structure including jets and UE activity is obtained. The partonic configuration then is linked to hadronization using string fragmentation as described by the Lund string model, followed by the decays of unstable particles. In collisions with MPI, individual long strings connected to the remnants are replaced by shorter additional strings connecting partons from different MPIs. This mechanism, called color reconnection, has been introduced to reproduce the increase of average transverse momentum with multiplicity observed in data. For comparison with measured observables, MC simulated samples with the Monash-2013 set of tuned parameters (tune) [34] for the underlying event (UE) and NNPDF2.3 LO PDF set [166] are used in this thesis.

Furthermore, in order to reduce the large theoretical uncertainties affecting the computations at LO in perturbative QCD, like the residual dependence of the unphysical factorisation and renormalisation scales, jet production at Next-to-Leading Order accuracy was obtained within the POWHEG framework [35–38, 167]. The POWHEG framework is used for NLO pQCD calculations of $2 \rightarrow 2$ and $2 \rightarrow 3$ parton scattering. The outgoing partons from POWHEG are passed to PYTHIA8 on a event-by-event basis where the subsequent parton shower is performed. Double-counting of partonic configurations is inhibited by a matching scheme based on shower emission vetoing. Contrary to fixed-order NLO calculations at parton level, the POWHEG MC approach has the advantage that the same selection criteria and jet finding algorithm can be used on the final state particle level as in the analysis of the real data. It is worth noticing that only charged particles can be selected. For the comparison with the measured differential jet cross sections, the CT14nlo PDF [167] set is used in POWHEG. The dominant source of uncertainty in the parton-level calculation is from the choice of renormalization, μ_R, and factorization scale, μ_F. The default value is chosen to be $\mu_R = \mu_F = p_{\mathrm{T}}$ of the underlying Born configuration, hereby a $2 \rightarrow 2$ QCD scattering [168]. Independent variations by a factor of two around the central value are evaluated as the corresponding systematic uncertainty. The PYTHIA8 A14 tune configuration [169] is used to perform parton shower, hadronization and underlying event simulations.

In addition, JETSCAPE [30] is a versatile Monte-Carlo software package designed for simulating high-energy nuclear collisions. It is a modular and extendable event generator, incorporating state-of-the-art physics components to model every aspect of the collision process. The JETSCAPE configuration in

pp mode, known as PP19 tune [170], utilizes PYTHIA 8 for generating hard processes and fragmenting QCD strings. The final state parton showers are handled by MATTER [171] with $\hat{q} = 0$, supplemented by two string formation procedures developed specifically for JETSCAPE 1.0: Colored and Colorless Hadronization. In order to be useful in future studies of A–A collisions, JETSCAPE with MATTER parton showers, in conjunction with JETSCAPE hadronization, must provide an overall acceptable description of pp data sets.

2.4.2 Event Generators in heavy-ion collisions

In heavy-ion collisions, the high p_{T} partons will interact with the colored medium resulting in jet energy loss and substructure modification, a phenomenon collectively referred to as jet quenching. The formation of partons via the hard-scattering occurs early in the collision before QGP formation, meaning that the partons (or jets) experience the full evolution of the medium.

In order to model jet-quenching effects, two main categories of effects can be included. The first is the impact of the QGP on the jet, which can be formulated via weakly- or strongly-coupled mechanisms. The weakly-coupled limit consists of radiative and collisional energy loss mechanisms as described earlier and shown in Fig. 2.7. Various pQCD formalism implement these mechanisms either as multiple soft scatterings such as in the Baier-Dokshitzer-Mueller-Peigne-Schiff-Zakharov (BDMPS-Z) [172, 173], Arnold-Moore-Yaffe (AMY) [174], and Amesto-Salgado-Wiedemann (ASW) [175] formalisms, or as few hard scatterings as in the Higher Twist (HT) [176] and Gyulassy-Levai-Vitev (GLV) [177] formalism. The formalism used will determine the extent of the quenching, and each will result in slightly different predictions for energy loss. The strong coupling limit utilizes AdS/CFT where the main mechanism for energy loss is a drag force. Different models use different combinations of the above implementations.

The influence of the jet on the medium can also impact jet quenching as the response of the medium can result in additional particles being added to the jet cone. The medium response can also be implemented in a weakly- or strongly-coupled way. In the case of the weakly-coupled limit, the medium response is implemented using a kinetic-theory-based approach where medium partons pick up energy scattered from the jet and recoil [178]. Correspondingly after the recoil there remains a hole in place of the parton. This process is illustrated in the left panel of Fig. 2.8. In the strongly-coupled limit, the medium response is implemented via hydrodynamic theory where the evolution is a bulk medium with a diffusive wake. In addition, there can also be a negative wake formed behind a hard parton, which is analogous to holes in the weakly-coupled case. An illustration of the hydrodynamic medium response via a wake can be found in the right panel of Fig. 2.8.

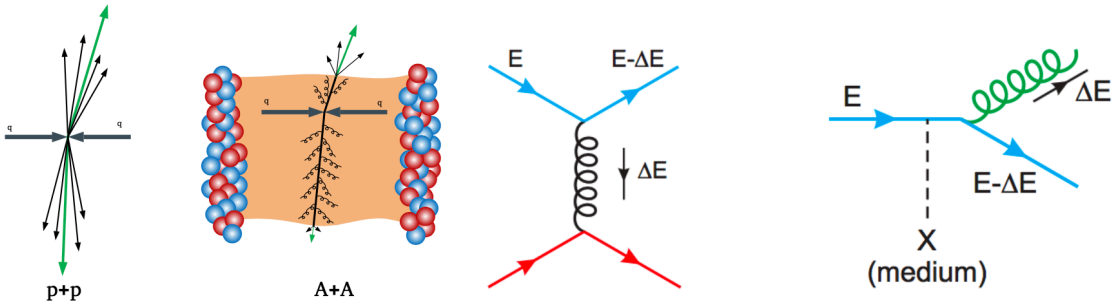

Figure 2.7: Left: Back-to-back jets in pp collisions and heavy-ion(AA) collisions. Jets in pp exist in vacuum whereas jets in AA traverse the QGP medium and lose energy. Right: Feynman diagrams for the energy loss ΔE of a quark with energy E due to collisional (left diagram) and radiative (right diagram) processes, originally appearing in Ref. [24].

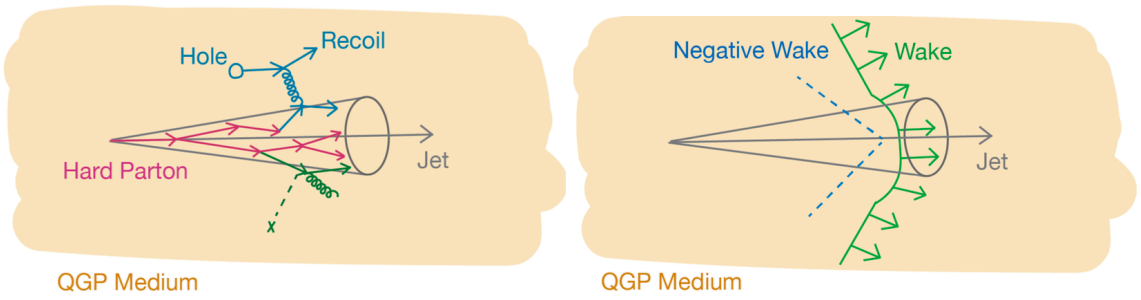

Figure 2.8: The weakly-coupled medium response via recoils (left) and a strongly-coupled medium response via a hydrodynamic wake (right).

These different modeling choices can result in many different models, each of which with varying predictions for jet-quenching effects. Below, some of the available jet quenching models will be described and categorized in this scheme. These models are based on PYTHIA8 (except JEWEL which is based on PYTHIA6 [154]) to generate hard processes, but differ in their treatment of jet–medium interactions and response of the QGP medium to the traversing jet.

JETSCAPE with Pb–Pb tune [30, 179] is an MC generator of multistage calculation for full simulation of heavy-ion collisions, which can include a medium-modified shower as well as the medium response in both the weakly- and strongly-coupled approaches. The partonic evolution in the QGP is modelled using MATTER at high virtuality [180, 181] and LBT at low virtuality [182, 183]. For pp simulations, the entire parton vacuum evolution is carried out in the matter generator by switching off the medium effect.

Another common model between proton–proton and heavy-ion collision events, JEWEL [31, 32, 79], is

an MC generator that includes both collisional and radiative parton energy loss mechanisms in a pQCD approach. It consists of a weakly-coupled MC implementation of BDMPS-based medium-induced gluon radiation in a medium modeled with a Bjorken expansion. Additionally, JEWEL includes the option of whether or not to implement the medium response via recoils. The JEWEL prediction "recoils on, 4MomSub", which includes medium recoil particles in the jet finding and subtracts the recoil partons' 4-momentum from $p_{\mathrm{T,jet}}$ [101], substantially differs from the JEWEL prediction "recoil off", which neglects medium recoil particles.

Hybrid Model [184] is an MC generator which incorporates both weakly- and strongly-coupled elements of jet quenching by describing the pQCD jet dynamics using DGLAP evolution, and the soft jet-medium interaction using a holographic description based on the AdS/CFT correspondence. Model predictions optionally include the effects of Molière elastic scattering [117] and wake effects.

The acoplanarity distributions are also compared to an analytical calculation pQCD@LO, LO pQCD calculation with Sudakov resummation [113] based on the framework in Refs. [185, 186]. Azimuthal broadening due to gluon radiation in vacuum is treated separately from medium-induced broadening, with the latter controlled by the in-medium jet transport coefficient $\hat{q}$.

3 Basic analysis techniques

The analysis of jets is inherently complex, involving various steps such as definition, reconstruction, application of cuts, and correction techniques. These factors contribute to the ambiguity surrounding the concept of a jet. At the end, one has to be content with the fact that oneself somehow *defines* what a jet is. However, the main constraint is to ensure that the resulting jet exhibits as many properties as possible consistent with the conceptual physical objects arising from hard parton scatterings, while also ensuring comparability with other measurements.

This section provides a comprehensive overview of the fundamental techniques and algorithms utilized in our data analysis. Following a discussion on the basics of track reconstruction and jet reconstruction, we delve into the methodology of background subtraction. Subsequently, we describe the fundamental unfolding correction technique as applied to jet measurements.

3.1 Track reconstruction with ALICE

The ALICE detectors provide excellent charged particle tracking capabilities, especially for low transverse momenta. Tracks are the basic objects of interest for this thesis since they are used to reconstruct the charged-particle jets. Track reconstruction or tracking in general refers to the momentum measurement of charged particles traversing a detector. In contrast to the energy measurement in a calorimeter, the measurement is non-destructive, though the particles of course loose energy in the detector. A complex multi-step procedure is applied to reconstruct the tracks. Here, only the main steps are described. A detailed technical overview can be found in Volume II of the ALICE Physics Performance Report [187]. Three basic parts of the track reconstruction can be distinguished. **Space point reconstruction**: The raw detector-output is used to reconstruct space points that are created by traversing particles. **Primary vertex reconstruction**: The primary vertex, where the collisions took place, can be used as an additional constraint for the tracking procedure. **Track finding**: The space points and the vertex are used to reconstruct the actual tracks in the detector. Note that the space points are also often referred to as clusters. The reconstruction of the space points is a subdetector-specific procedure. The space point reconstruction includes the determination of the corresponding spatial position and uncertainty. Space points are finally used for the track fitting procedure. To find the primary vertex of a collision, the two innermost layers of the ITS, corresponding to the layers of the Silicon Pixel Detector, are used. As the beams are collimated at the interaction point, the vertex diamond, where the collisions take place, is Gaussian-shaped in the z-direction (beam direction) and in the xy-plane. While the beams are strongly

collimated in the xy-plane ($\sigma_{xy} \approx 10$ μm), it is much broader in z ($\sigma_z \approx 5$ cm). The resolution of the vertex position strongly depends on the available particle multiplicity and, thus, on the collision system. For Pb–Pb collisions, it is of the order of 10 μm. For pp collisions, where the average multiplicity is much lower, it is of the order of 100 μm [54].

The algorithm to determine the vertex position is performed separately for the z-direction and the xy-plane. For the z-coordinate of the vertex, the procedure works as follows. A first estimate of the vertex position is given by calculating the centroid of the reconstructed spatial z-coordinates in the SPD. This centroid is monotonously correlated to the true vertex position if this position is within $z_{\text{true}} < 12$ cm. The correlation is known and, therefore, the vertex position is calculable. Using this first vertex estimate, the final vertex position is given by correlations of hits in the first and second layer of the SPD. Eventually, the correlations form a Gaussian distribution of the position estimate. The centroid of a Gaussian fit is taken as primary vertex position.

ALICE' track finding procedure is based on a Kalman filter [188]. It allows a computationally relatively fast simultaneous track fitting. The first step consists in finding seed space points at outer radii of the TPC, in which the occupancy is lower than in the middle of the detector. Proceeding to smaller TPC radii, space points are associated to the track candidates. At the inner radius of the TPC, the ITS tracking system prolongs the TPC tracks through the ITS using the vertex position. Reconstructed ITS clusters lying on that track are assigned to it. Additionally, the ITS tracker searches for ITS-standalone tracks that do not correspond to a TPC-found track, e.g. due to inefficiencies in the TPC or because of too low transverse momentum. The tracking is run a second time, now from the vertex to the outer radius of the TPC. In this step, the tracks are also extrapolated to other central barrel detectors like the TRD, TOF, etc. Ultimately, another refit procedure is performed from the outer side of the detector to the vertex.

This procedure is utilized for the reconstruction of all tracks examined in this thesis. Internally, the tracks are represented as a set of five parameters for the curvatures and angles of the track. Additional constraints on the event and track quality are applied by imposing cuts, as follows.

Event and track cuts in this thesis

For the offline analysis, a standard event selection is applied to the entire Run 2 dataset to reject events with incomplete detector information or those lacking a precisely defined primary vertex. Selected events require: a primary vertex constructed from at least two tracklets, which are tracks formed by hits in the SPD with constraints on their resolution; a primary vertex formed by tracks from the full tracking system $|z_{\text{vtx}}^{\text{track}}| < 10$ cm relative to the nominal center of ALICE to ensure full geometrical acceptance in

the ITS for $|\eta| < 0.9$; and consistency in the location of the two vertices, $|z_{\rm vtx}^{\rm track} - z_{\rm vtx}^{\rm SPD}| < 0.5$ cm. Event pileup, defined as the average number of simultaneous interactions per bunch crossing, is suppressed by rejecting events where multiple vertices are reconstructed from TPC and ITS tracks. After applying these cuts, we obtained the vertex and multiplicity distributions shown in Fig. 3.1 where data are compared to a Monte Carlo simulation.

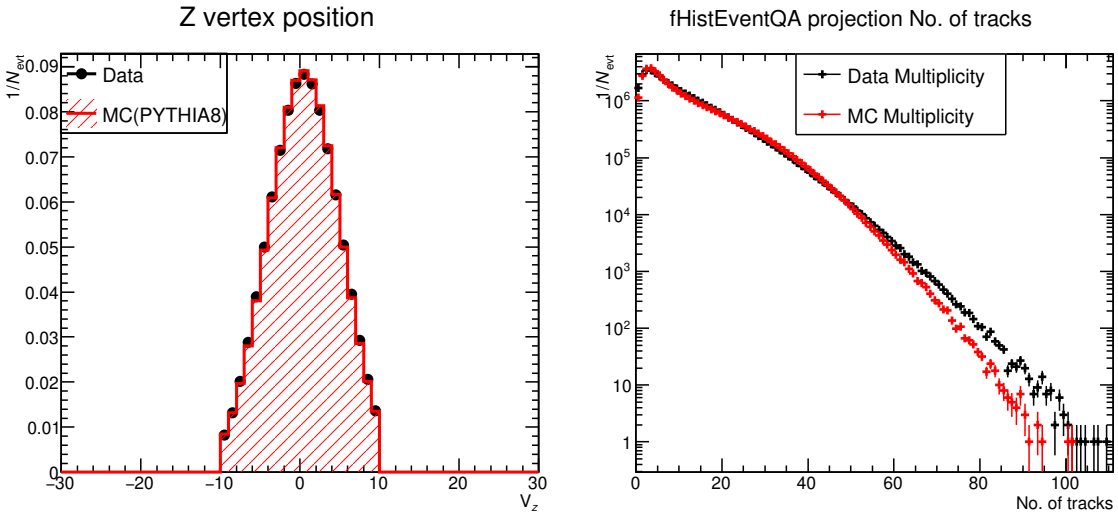

Figure 3.1: The event vertex distribution (left) and multiplicity distribution (right) between data and MC samples in pp collisions at $\sqrt{s} = 13$ TeV.

Charged-particle tracking is performed using hits in the ITS and TPC, both covering $|\eta| < 0.9$ over the full azimuth. The SPD had spatially non-uniform and time-varying coverage during the data recording period. To ensure uniform and stable tracking efficiency in the analysis, "hybrid" tracks are therefore employed for the analysis of the pp data. Hybrid tracks consist of two exclusive sets of tracks: "global tracks", which are tracks with at least one SPD hit and good track-fit residuals in the ITS, but without a primary vertex constraint; and "complementary" tracks, which do not have any SPD hits, are constrained by the primary vertex, and have good track-fit residuals in the ITS. Fig. 3.2 displays three types of charged-track η and φ distributions independently in pp collisions at $\sqrt{s} = 13$ TeV. From the distributions, we conclude that with hybrid tracks we can recover an approximately uniform track distribution in both the η and φ directions. Both sets of tracks are required to have at least 70 active pad rows and at least 80% of the geometrically findable space-points in the TPC, as shown in Table 3.1 (which also lists the other cuts). Tracks accepted for the analysis have $|\eta| < 0.9$ over the full azimuth, and transverse momentum of $p_{\rm T} > 0.15$ GeV/c.

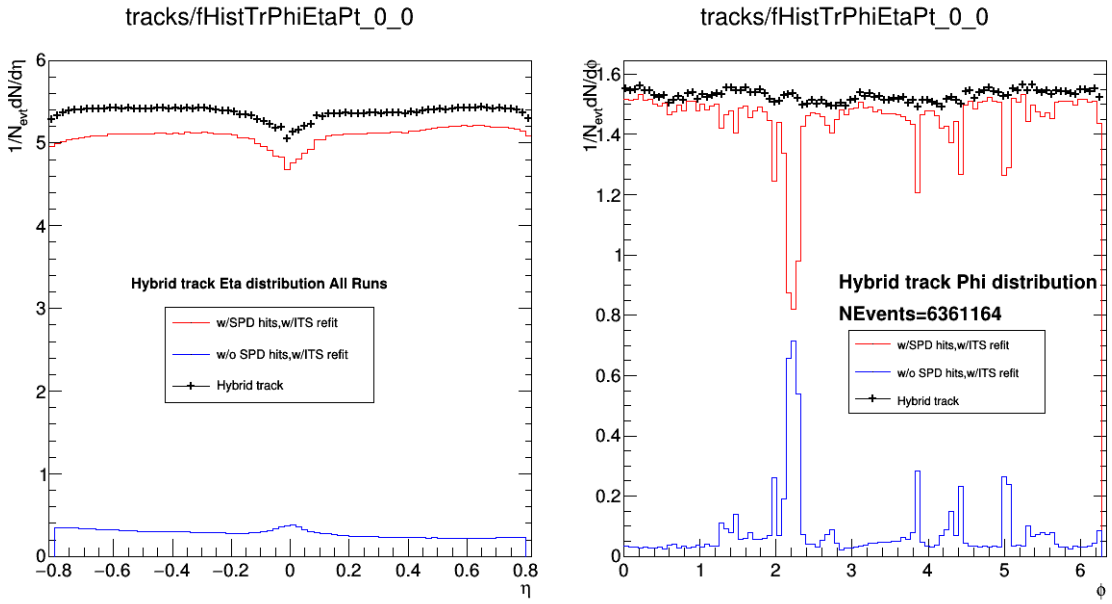

Figure 3.2: η and φ distributions of charged tracks in pp collisions at $\sqrt{s}$ = 13 TeV:(a) with Hybrid track cut (black), (b) with SPD hits and ITS refit(red), and (c) without SPD hits and ITS refit (blue).

Figure 3.3 shows respectively the azimuthal, pseudo-rapidity, and transverse momentum distributions of the two-component hybrid tracks. Both φ and p_{T} of hybrid tracks have been monitored for all runs used in this analysis and no run dependence was observed. A flat φ distribution is seen by combining global tracks and complementary tracks. Fig. 3.4 shows the azimuthal, pseudo-rapidity, and transverse momentum distributions of the hybird tracks in different multiplicity percentiles.

The tracking efficiency is estimated from a full detector simulation. For pp collisions, the tracking efficiency is 60% for $p_{\mathrm{T}} = 0.15$ GeV/c, increasing to 80% for $p_{\mathrm{T}} > 0.4$ GeV/c [26]. The momentum resolution in pp collisions is better than 3% for hybrid tracks for $p_{\mathrm{T}} < 1$ GeV/c, increasing linearly to 10% at $p_{\mathrm{T}} = 100$ GeV/c [189].

3.2 Jet definition and reconstruction

Jet definition: If the momentum transfer in the parton scattering is large enough, jets can be formed in the collision. From the perspective of the observer, jets are sprays of particles in the detector that fly roughly into the same direction. In lepton collisions at very high momentum transfer, of the order of GeV/c, jets can be easily identified from the tracks reconstructed in the detector. For hadron collisions and especially for heavy-ion collisions, this turns out to be much more difficult because of the presence of a large fluctuating background.

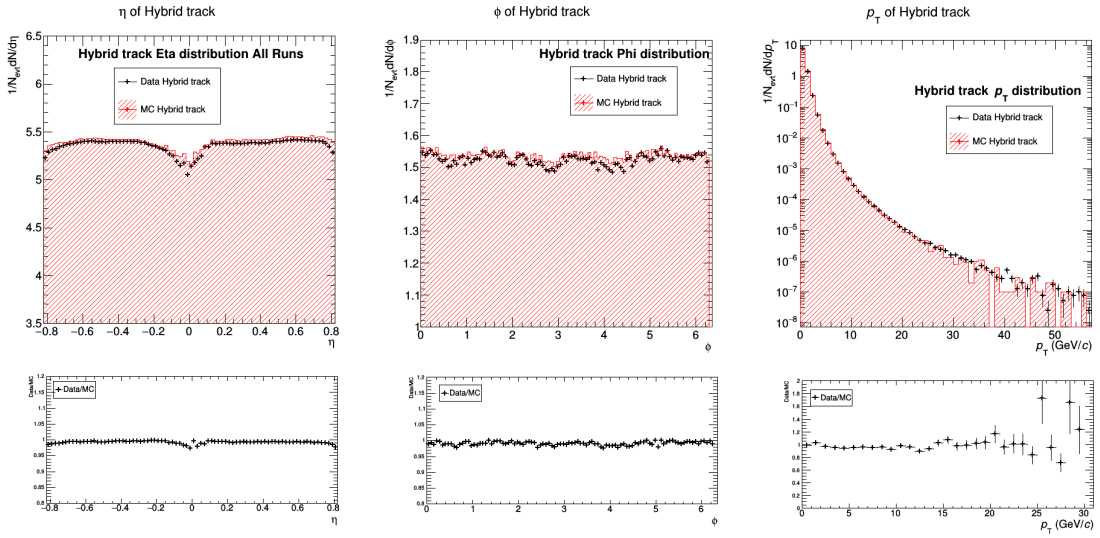

Figure 3.3: Hybrid track $\eta - \varphi - p_{\mathrm{T}}$ distributions between data and MC samples in pp collisions at $\sqrt{s}$ = 13 TeV.

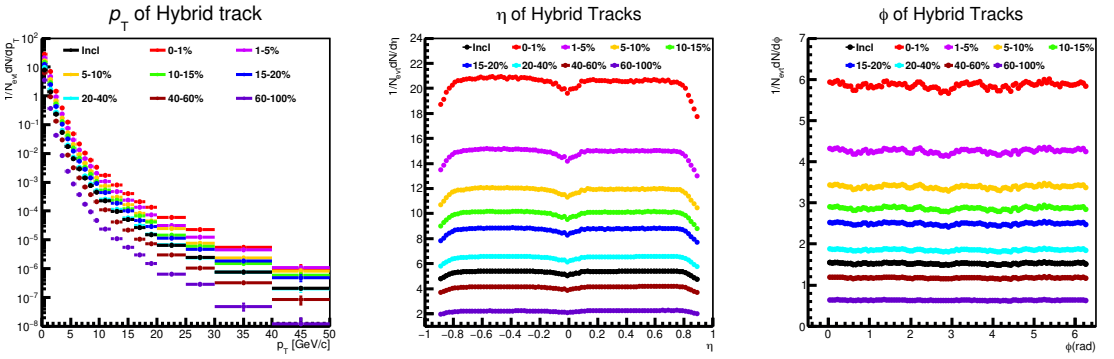

Figure 3.4: Hybrid track $p_{\mathrm{T}} - \eta - \phi$ distribution for different multiplicity intervals in pp collisions at $\sqrt{s}$ = 13 TeV.

Table 3.1: List of the hybrid track cuts from the AliRootAliESDtrackCuts class implementation.

AliESDtrackCuts method	value
Hybrid tracks (Global tracks and Complementary tracks)	
SetMinNCrossedRowsTPC	70
SetMaxChi2PerClusterTPC	4
SetAcceptKinkDaughters	kFALSE
SetRequireTPCRefit	kTRUE
SetRequireITSRefit	kTRUE
SetClusterRequirementITS kSPD,	Off
SetMaxDCAToVertexZ	2
SetDCAToVertex2D	kFALSE
SetRequireSigmaToVertex	kFALSE
SetMaxChi2PerClusterITS	36
SetMaxDCAToVertexXY	2.4
SetMaxDCAToVertexZ	3.2
SetDCAToVertex2D	kTRUE
SetMaxChi2TPCConstrainedGlobal	36
SetMaxFractionSharedTPCClusters	0.4
SetMinRatioCrossedRowsOverFindableClustersTPC	0.8
Global tracks only	
SetClusterRequirementITS	kSPD, Any

In theory, jets are produced in elastic scattering of partons. The initial scattering can take place between any constituent of the colliding hadrons. At lower Q^2, i.e. low transferred four-momentum, collisions of valence quarks contribute dominantly to this initial scattering. At higher Q^2, interactions of sea quarks and gluons becomes more and more probable. While all individual particles of a jet are created in a non-perturbative process (i.e. by hadronization), the four-momentum of the reconstructed jets is close to that of the incident partons. This means the jets production are mainly determined by perturbative processes with high momentum transfer and, thus, the cross sections can be directly compared to pQCD calculations.

As evidenced by the above description and Section 2.4, jets are theoretically complex objects representative of the original parton kinematics and sensitive to various physical scales from the hard-scattering scale set by the amplitude (or matrix elements) for the process to the hadronization scale. Jets are useful for three main avenues of study, which are listed below.

1. Studying processes of a specific origin: Jets are useful objects to tag processes of a specific type or origin. Some examples include decays of the Higgs Boson, beyond the Standard Model processes, dynamics of quarks or gluons, and decays of heavy quarks.
2. Tests of fundamental QCD: The production of the high p_{T} parton that forms the jet is calculable in pQCD. As jets in vacuum serve as a proxy for these partons, jets are ideal probes of pQCD. Additionally,

jets can be used to probe non-perturbative QCD via measurements that isolate the non-perturbative process of hadronization.

3. Probing the QGP in heavy-ion collisions: Jets in vacuum additionally serve as a reference for jets in heavy-ion collisions, where any difference between the two systems serves as a marker of in-medium effects. This is described earlier in Section 1.6.

A jet algorithm is in principle a set of definitions of how to group particles in the detector and how to assign their momenta to the jets' momenta. The rules how to cluster particles together are given by a distance measure, the jet momentum definition by the so-called recombination scheme.

Good jet algorithms must be somehow universal [190]: They should be experiment- and detector-independent and should be applicable to all experimental or theoretical levels.

Infrared and Collinear (IRC) safety (see Fig. 3.5) is an important property of many jet algorithms. While an infrared-safe algorithm should not yield different results if a very soft particle is added to the event, collinear safety of an algorithm means the insensitivity to the splitting of one jet into two collinear ones. The main reason why an IRC-safe algorithm is favored is simple: Due to their partly non-perturbative nature, the effect of those collinear splittings and soft particle emissions is not calculable and not predictable for a given event. IRC-safe algorithms are not affected by those differences. Many jet algorithms exist and they are typically divided into two classes: Cone algorithms and sequential recombination algorithms. While cone algorithms rely on the assumption that the QCD branching and the hadronization do not change the parton properties in the considered cones, sequential algorithms subsequently cluster all particles into jets according to a given distance measure.

In this thesis, only sequential recombination algorithms are used: the k_{T} and anti-k_{T} algorithms [191]. The implementation in the FastJet package [192] is used. Those jet algorithms are briefly described in the following.

The anti-k_{T} and k_{T} algorithms: Together with the Cambridge/Aachen jet finding algorithm [193], the anti-k_{T} [194] and k_{T} [195] algorithms belong to a general class of sequential recombination algorithms [191]. Those algorithms are based on the following iterative procedure: (1.) Calculate distances according to a given measure between the objects (particles, in later iterations pseudo-jets) by

$$d_{ij} = \min(k_{\mathrm{T,i}}^{2p}, k_{\mathrm{T,j}}^{2p}) \frac{\Delta R_{ij}^2}{R^2} \tag{3.1}$$

where $\Delta R_{ij}^2 = (\eta_i - \eta_j)^2 + (\varphi_i - \varphi_j)^2$ a measure for the geometric distance of the objects, p is the sequential

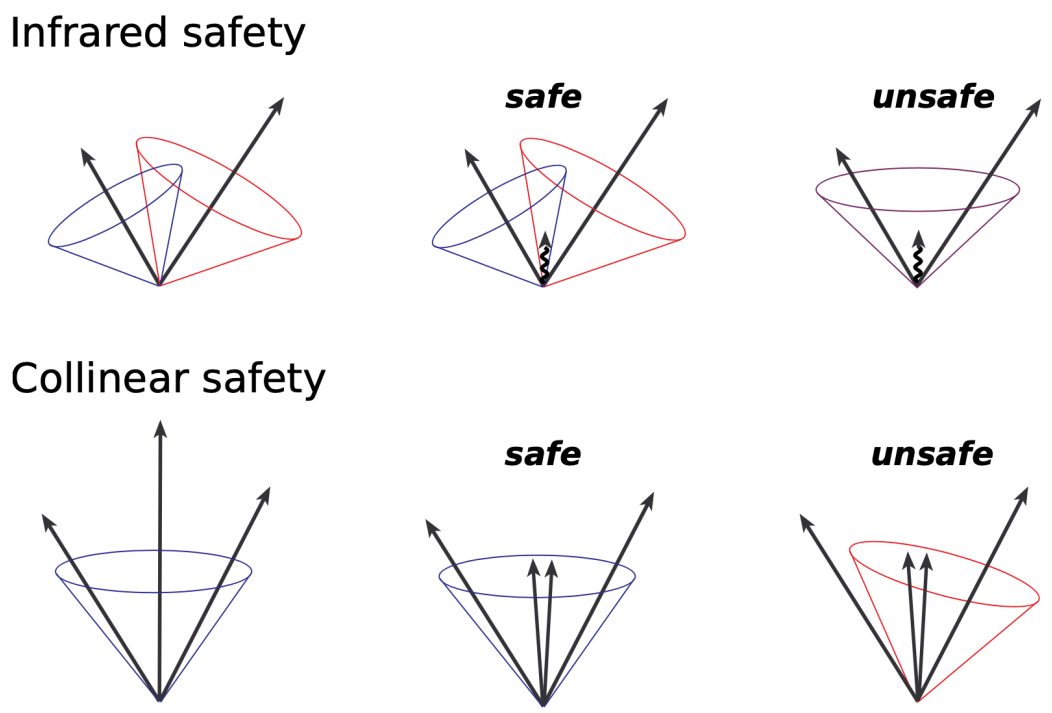

Figure 3.5: Illustration of infrared and collinear safety. The lines are particles in a spatial representation and the cones indicate how the jet algorithm clusters the jet. Figure adapted from Ref. [24].

recombination algorithm-specific parameter, $k_{\mathrm{T,i}}$ is the transverse momentum of the ith particle, and R is the resolution parameter that roughly corresponds to the radius of the jet cone in natural angular units. For comparison, the distance between each particle and the beam is calculated as

$$d_{iB} = k_{\mathrm{T,i}}^{2p} \tag{3.2}$$

When considering a given pair of particles, the distances specified by Equations 3.1 and 3.2 will be compared. (2.) When Equation 3.1 is the smallest of the two, these particles will then be grouped into a pseudo-jet. When Equation 3.2 is smaller, the ith pseudo-jet is removed and named a jet. (3.) This procedure is then repeated until all particles in the event are clustered into jets, or until an alternate stopping condition specified by the user is reached. In order to combine particles into pseudo-jets, there are two different recombination schemes that can be used. The first is the E-scheme recombination in which the four-vectors of individual particles are combined in order to form a (pseudo) jet four-vector. The second is the p_{T}-scheme recombination that imposes an additional scaling that makes the jet's energy equivalent to its three-momentum.

The sequential recombination algorithm that is most commonly used for the reconstruction of signal

jets at the LHC is the anti-k_T algorithm, which corresponds to $p = -1$ in the above procedure. As a consequence of the choice of $p = -1$, the anti-k_T algorithm clusters high p_T particles first, a feature that creates "soft-resilient" jets that are relatively insensitive to the presence of an underlying event (UE) or pileup. For this reason the anti-k_T algorithm is favorable in noisy environments such as the LHC. The k_T algorithm [195] corresponds to $p = 1$ in the above procedure. The k_T algorithm favors the clustering of lower p_T particles. As a result of this feature, the k_T algorithm tends to create "soft adaptable" jets that are more influenced by the presence of an UE or pileup. The k_T algorithm is useful for studies of the UE due to its tendency to naturally organize a uniform soft background into clusters of variable area. The third and final type of sequential recombination algorithm is the Cambridge/Aachen (C/A) algorithm [193], which corresponds to $p = 0$ in the above procedure. As a consequence, the C/A algorithm does not take p_T into account and is purely geometric. Though this tends to produce jets with irregular shapes, the C/A algorithm is useful to enforce angular ordering that mimics the QCD branching sequence where each emission is expected to be at a smaller angle than the previous emission. A comparison of the jets formed by the k_T, C/A, and anti-k_T algorithms is shown in Fig. 3.6.

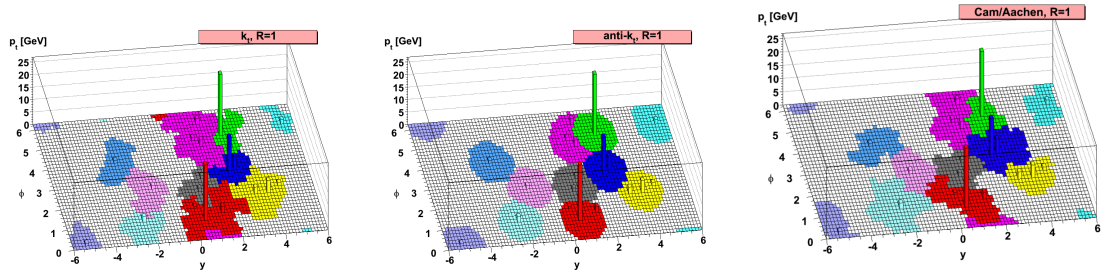

Figure 3.6: Illustration of an event clustered with the k_T (left), anti-k_T (middle)and C/A (left) sequential recombination algorithms. The colored areas represent the areas that are associated to the jets. Figure from Ref. [17].

The charged-particle jets are composed of only charged constituents. Charged-particle jets are commonly measured, particularly for measurements of jet substructure, in ALICE in order to take advantage of its precise tracking. Though charged jets have the clear disadvantage that they are missing neutral information, the probability distributions for charged particles compared to all particles are found to be very similar.

Jet area calculation: To subtract the correct amount of background energy on a jet-by-jet basis, knowledge of the jet area is necessary. The calculation is performed with the active area approach, implemented in FastJet (cf. [196]). It works as follows. For each jet, the area A is determined by distributing so-called ghost particles to the detector acceptance. Ghost particles have vanishing momenta and, therefore, do not influence jets that include these particles in the jet finding procedure. On the other hand,

the amount of ghost particles in a jet is a direct measure for the jet area. The area resolution is driven by the size that is assigned to the ghost particles and thereby by their density. A smaller size corresponds to more ghost particles but also requires more computational power. For the presented pp analyses, the area of one ghost particle corresponds to an area of 0.01 (0.005 in Pb–Pb collisions) in the (η, φ)-plane.

Jet recombination scheme: The jet recombination scheme defines how the jet momentum is calculated with respect to its constituents. Several schemes are commonly used: the E-scheme, p_{T}-scheme, and boost-invariant p_{T}-scheme. The E-scheme is conceptually the simplest approach: It adds up the four-momenta of the particles. When combining two particles or pseudo-jets in the p_{T} or boost-invariant p_{T}-scheme, the direction of the jet axis is formed using the p_{T}-weighted directions of the single objects. The transverse momentum is simply added up:

$$p_{\mathrm{T}} = p_{\mathrm{T},1} + p_{\mathrm{T},2}, \quad \eta = \frac{p_{\mathrm{T},1}\eta_1 + p_{\mathrm{T},2}\eta_2}{p_{\mathrm{T},1} + p_{\mathrm{T},2}}, \quad \varphi = \frac{p_{\mathrm{T},1}\varphi_1 + p_{\mathrm{T},2}\varphi_2}{p_{\mathrm{T},1} + p_{\mathrm{T},2}} \tag{3.3}$$

In contrast to the boost-invariant p_{T}-scheme, the p_{T}-scheme includes a preprocessing stage, in which the energy is rescaled assuming massless particles. This does not change the particles momenta but the jets (pseudo)rapidity is affected by the rescaling. On the other hand, a test calculation shows that the effect of the energy rescaling is negligible for jets in measured data even if low-p_{T} jets are considered. The jet energy difference for p_{T}- and boost-invariant p_{T}-scheme is given by:

$$\Delta E = E_{\mathrm{BIpt}} - E_{\mathrm{pt}} = \sqrt{p^2 + m^2} - |p|. \tag{3.4}$$

Note that technically, the track mass m is fixed to the pion mass 0.1396 GeV/c, because the mass is only known with a certain probability. As an example, the ΔE for different recombination schemes using jets with a momentum of 10 GeV/c consisting of 5 particles is given by $\Delta E = 0.024$ GeV, corresponding to 0.24% energy difference. Note that this example already shows the largest possible effect for measured jets. For jets with larger momenta, the effect is even smaller. In this thesis, the p_{T}-scheme is used.

Jet reconstruction in this thesis

Several types of jets are used in this thesis, which are distinguished by labelling their assigned p_{T} as follows [15]:

1. For real data, $p_{\mathrm{T,ch\ jet}}^{\mathrm{raw}}$ refers to the raw output of the jet-reconstruction algorithm; $p_{\mathrm{T,ch\ jet}}^{\mathrm{corr}}$ denotes $p_{\mathrm{T,ch\ jet}}^{\mathrm{raw}}$ after event-wise subtraction for the uncorrelated background energy (Equation 3.7); and $p_{\mathrm{T,ch\ jet}}$ denotes p_{T} for fully corrected jet distributions.
2. For simulations, $p_{\mathrm{T,ch\ jet}}^{\mathrm{part}}$ refers to jets reconstructed from generated charged particles (particle level), and $p_{\mathrm{T,ch\ jet}}^{\mathrm{det}}$ refers to jets built from reconstructed charged tracks from the simulated data (detector level);

3. Generic reference to a jet without specification of its level of correction or simulation is denoted $p_{\mathrm{T,jet}}$.

In the second analysis, which involves hadron-jet correlation measurements, the measured distributions are two-dimensional functions of $p_{\mathrm{T,ch\ jet}}$ and $\Delta\varphi$. The same labeling convention is applied to $\Delta\varphi$ distributions. However, for simplicity, the jet type label (reco, part, or det) of the $\Delta\varphi$ distributions is suppressed and can be deduced from the context. In the third analysis, focusing on heavy-flavour jet production, the measured yield as a function of ΔR uses similar labels.

In conclusion, jet reconstruction in this thesis is carried out twice on each event. The first jet reconstruction pass utilizes the anti-k_{T} algorithm from the FastJet package with E-scheme recombination for different jet resolution parameters. Charged-particle jets utilize charged tracks with with $p_{\mathrm{T,track}} > 0.15$ GeV/c and $|\eta_{\mathrm{track}}| < 0.9$ as constituents. Jets are required to be contained within $|\eta_{\mathrm{jet}}| < 0.9 - R$ to ensure they remain in the fiducial acceptance of the TPC [197], R is jet resolution parameter. For different analyses we choose different jet resolution parameters. A jet area cut is applied to suppress contamination by non-physical jets [198]. The second reconstruction pass utilizes the k_{T} algorithm with the E-scheme recombination scheme in the FastJet package. The resulting jets are used to determine ρ (see Section 3.3), the event-by-event estimate of the background energy density [199]. For the ρ calculation, a jet radius of $R = 0.2$ is used in the analysis of jet versus multiplicity in pp collisions regardless of the radius of the desired signal jet because of their lower sensitivy to fluctuations, though this is shown to have a small effect.

The fundamental event, track, and jet quality assurance (QA) plots are shown next, primarily focusing on the analysis of jet production in pp collisions at $\sqrt{s} = 13$ TeV as an illustrative example. This includes examining Figures 3.1 and 3.3 for event multiplicity and track QA, respectively. Additionally, we present inclusive charged-particle jet p_{T}-η-ϕ distributions reconstructed using the anti-k_{T} algorithm for different radii (e.g., radii 0.2, 0.4, 0.6) and compare data with MC simulation in Fig. 3.7. Fig. 3.8 shows the inclusive jet area distributions as a function of jet p_{T} before applying an area cut.

3.3 Background subtraction

In pp collisions, reconstructed high-p_{T} jets are most likely produced in hard parton–parton interactions. Next to these hard interactions with high momentum transfer Q^2, there are also softer contributions including everything that does not originate from a hard collision. The contributions are mainly from semihard parton interactions at transverse momenta of the order of a few GeV/c that cannot be resolved as jets. These objects are sometimes called minijets. Given a measured event, it is not clear which

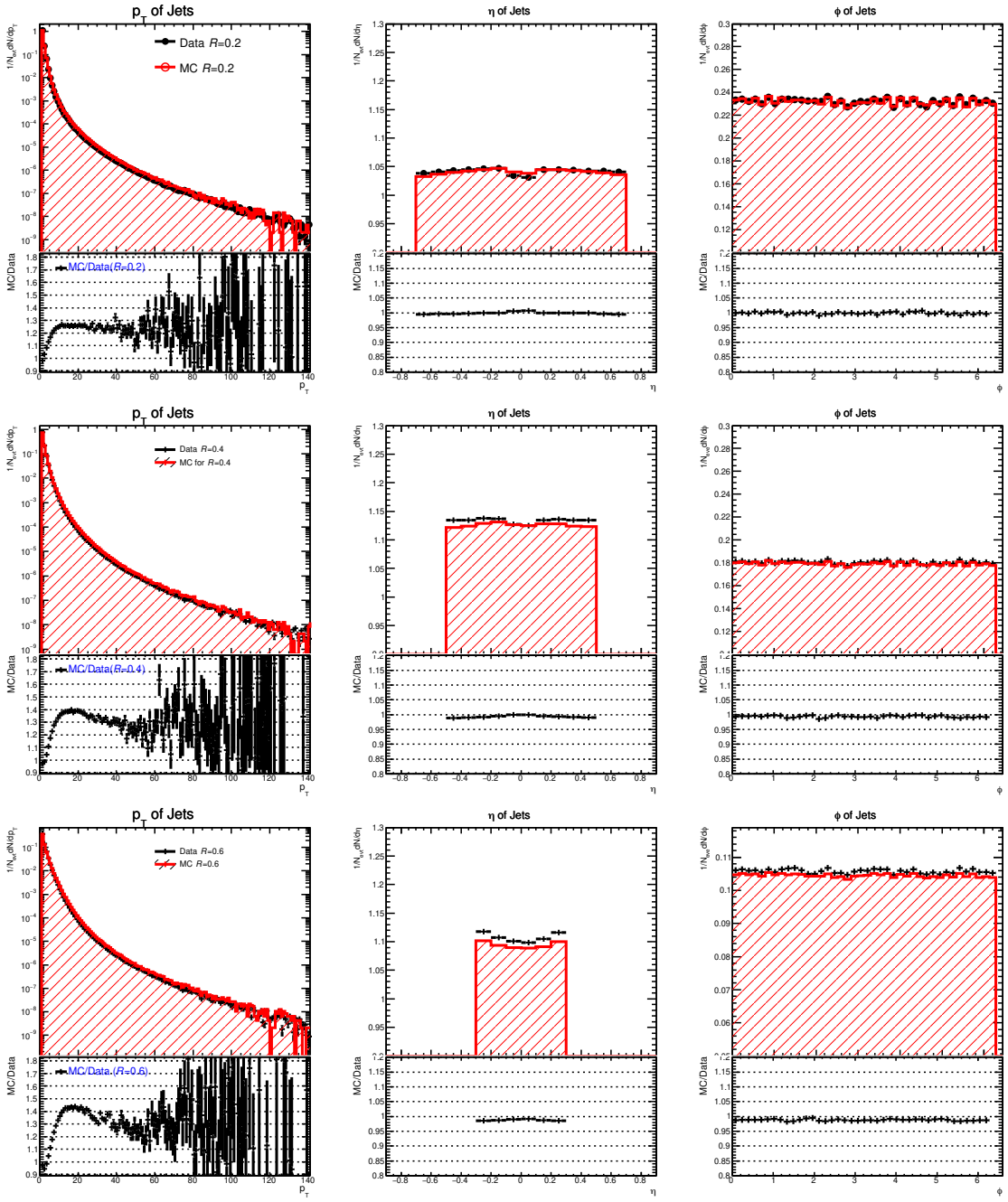

Figure 3.7: Inclusive charged-particle jet p_{T}-η-ϕ distributions between data and MC for different jet radii $R = 0.2, 0.4, 0.6$ without UE subtraction in pp collisions at $\sqrt{s} = 13$ TeV.

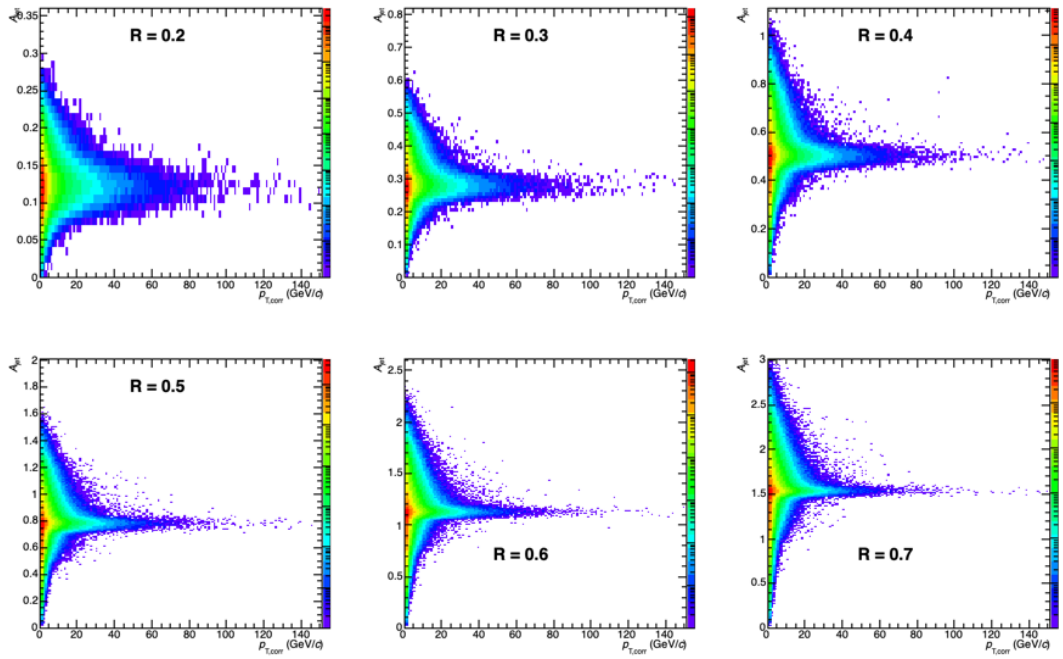

Figure 3.8: Inclusive charged-particle jet area distributions for different jet radii $R = 0.2$ to $R = 0.7$ in pp collisions at $\sqrt{s} = 13$ TeV, before area cut.

particle tracks or energies originate from a hard collision and which do not. Even for simulated Monte-Carlo events, for which the initial hard scattering is known, it is not clearly recognizable what to define as background and what as signal. Like for jets, the background is also defined by the algorithm. However, in contrast to the jet definition, particles are not divided in background and non-background particles. Background is defined as a property of the whole event. However, in Pb–Pb collisions, the background has a huge impact on the reconstructed jet momentum. In ALICE, it is estimated using a statistically robust median of all jet transverse momenta per area within one event for clusters/jets reconstructed with the k_{T} algorithm. The approach is well proven to work in Pb–Pb (cf. [199, 200]), but it is not necessarily working for the much more diluted pp collision system. And indeed, the method cannot simply be used for pp but has to be adapted as described below. In the Pb–Pb, the background density is calculated by

$$\rho = \mathrm{median}\left\{\frac{p_{\mathrm{T,ch\ jet}}^{\mathrm{raw},i}}{A_{\mathrm{jet}}^{i}}\right\}, \tag{3.5}$$

where $p_{\mathrm{T,ch\ jet}}^{\mathrm{raw},i}$ and A_{jet}^{i} are the raw (uncorrected) k_{T} jet p_{T} and area of the i^{th} jet in the event, respectively. Jet area is calculated using ghosts with area 0.005 [196]. The full k_{T}jet sample also contains signal from hard interactions. The utilization of the median method ensures stability in the presence of outliers, specifically those originating from the hard signal. Another approach to mitigate the impact of the signal

is k_{T} jet exclusion, where the two leading jets, defined as those with the highest transverse momentum (p_{T}), are excluded from the jet sample.

For pp collisions a modified definition appropriate for sparse events [201] is utilized. The basic idea is to account for empty areas not by including ghost jets but by introducing a factor correcting for the emptiness of the event.

$$\rho = C \times \text{median}\left\{\frac{p_{\mathrm{T,ch\ jet}}^{\mathrm{raw},i}}{A_{\mathrm{jet}}^{i}}\right\};\quad C = \frac{\sum_i A_{\mathrm{jet}}^{i}}{A_{\mathrm{total}}}, \tag{3.6}$$

in which i enumerates reconstructed k_{T} jet candidates, C is the charged particle occupancy factor. It represents the fraction of the area populated by charged particles. Roughly speaking, the factor specifies how full or empty the event is. $A_{\mathrm{total}} = 1.8 \times 2\pi$ corresponds to the total detector acceptance. The two hardest jets in the event are also excluded from the median calculation in Equation 3.6 - like it was done in the Pb–Pb approach in Eq. 3.5. Fig. 3.9 shows the correlation of ρ as function of charged track multiplicity, the ρ is increased with multiplicity. Fig. 3.9 displays the correlation of ρ as a function of charged track multiplicity, with ρ increasing with multiplicity. Fig. 3.10 depicts the averaged ρ as a function of leading jet p_{T} for both data and MC. These distributions reveal a sharp rise in underlying event activity in the transverse region with increasing leading jet p_{T}, followed by a plateau above 10 GeV/c, suggesting a weaker correlation with the hard process. The data is also compared to recent tunes of the PYTHIA8 Monte Carlo event generator, indicating that the simulation reproduces the measured transverse momentum density.

After obtaining the reconstructed anti-k_{T} jets and estimating background density ρ, the raw jet p_{T} is then corrected on an event-by-event basis using the estimated background density ρ, as described in [199]. This correction is illustrated in the following equation,

$$p_{\mathrm{T,ch\ jet}}^{\mathrm{corr},i} = p_{\mathrm{T,ch\ jet}}^{\mathrm{raw},i} - \rho A_{\mathrm{jet}}^{i}, \tag{3.7}$$

where ρ for the event is calculated using either Equation 3.5 or 3.6 (pp collisions). This adjustment accounts largely for event-wise variation in the overall level of background, which can be significant for high multiplicity pp collisions due to the broad distribution of charged-particle multiplicity within the 0 – 1% class, as discussed in Section 4.3. Fig. 3.11 shows the measured inclusive jet yield $p_{\mathrm{T,ch\ jet}}^{\mathrm{raw}}$ (left panel) and $p_{\mathrm{T,ch\ jet}}^{\mathrm{corr}}$ (right panel) distributions without and with UE subtraction in pp collisions at

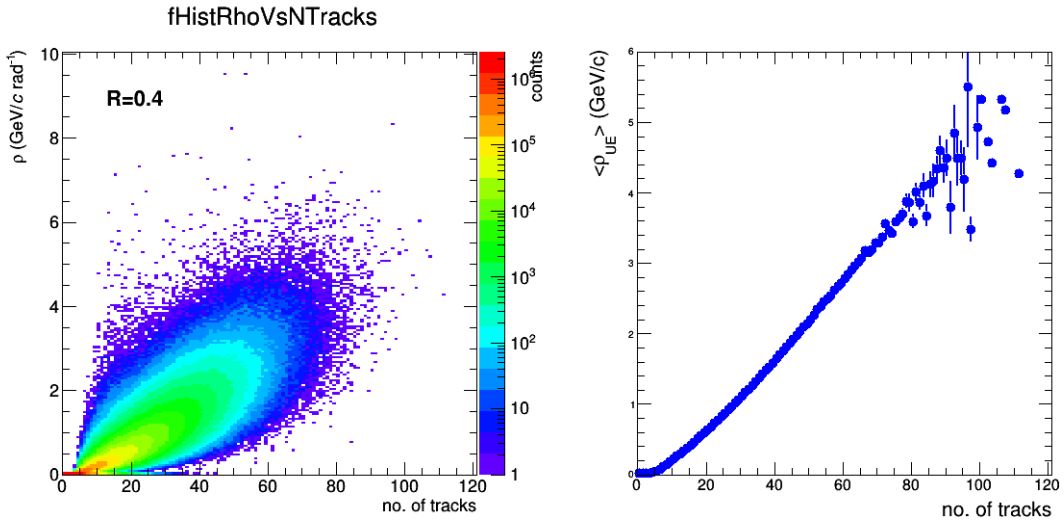

Figure 3.9: Background density ρ_{UE} as a function of multiplicity 2-dimensional distribution in pp collisions at $\sqrt{s}$ = 13 TeV (left), and distribution of average ρ_{UE} with multiplicity obtained by projection from the left 2d histogram.

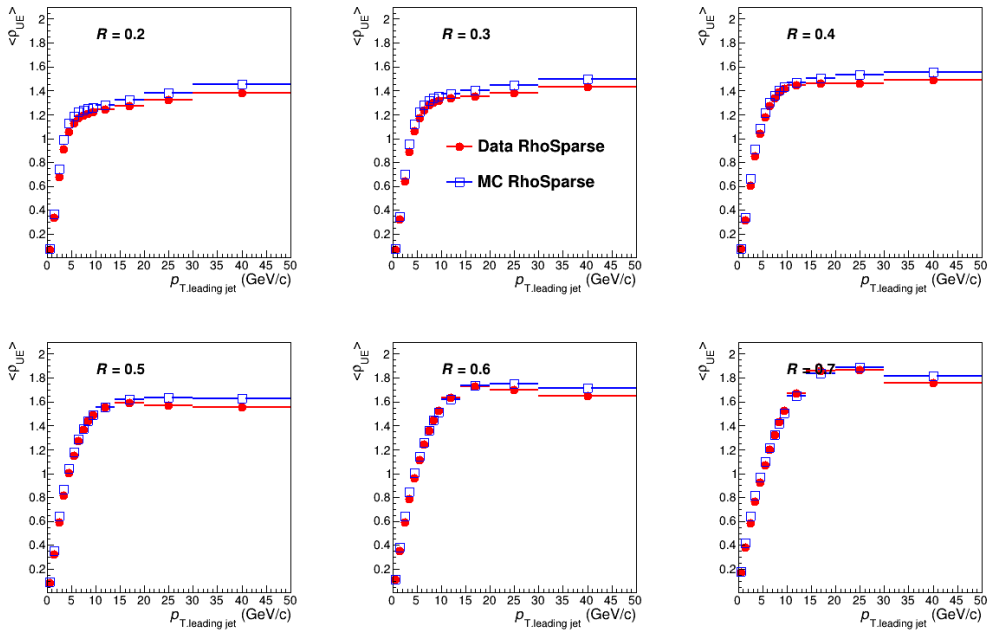

Figure 3.10: Average ρ_{UE} as a function of leading jet transverse momentum distributions between data and MC for R = 0.2 to R = 0.7 in pp collisions at $\sqrt{s}$ = 13 TeV.

$\sqrt{s}$ = 13 TeV for jet resolution parameters ranging from R = 0.2 to R = 0.7 and pseudo-rapidity ranges $|\eta_{\rm jet}| < 0.9 - R$. Fig. 3.12 shows the uncorrected charged-particle jet yields in different V0M multiplicity percentile intervals for resolution parameters R varied from 0.2 to 0.7 in pp collisions at $\sqrt{s}$ = 13 TeV. These spectra in these two figures will be applied to the unfolding correction and systematic calculation to obtain the final physics results.

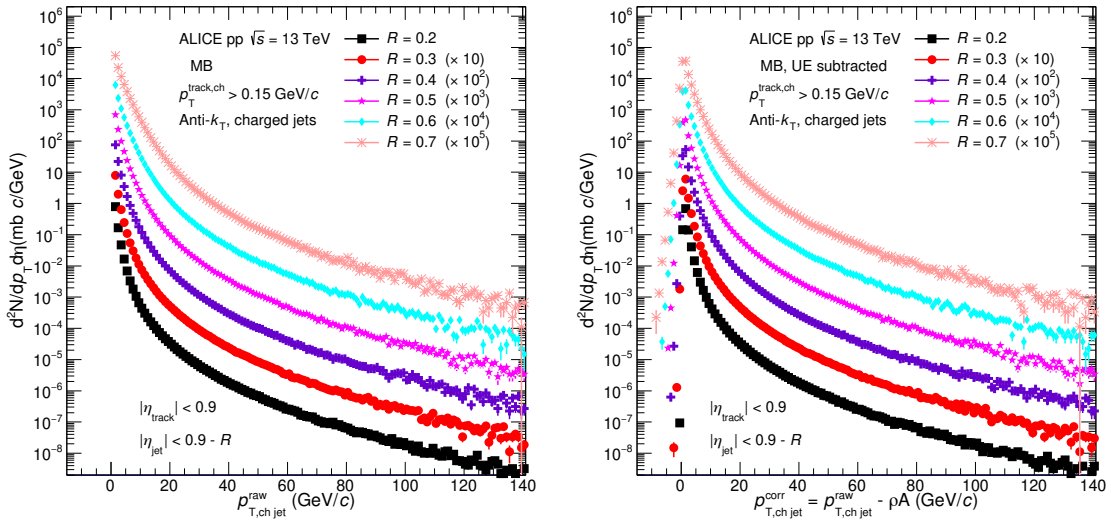

Figure 3.11: Inclusive raw jet $p_{\rm T}$ distributions without (left) and with UE substraction (right) for different radii in pp collisions at $\sqrt{s}$ = 13 TeV.

3.4 Unfolding technique

In High Energy Physics (HEP) and various fields, researchers frequently analyze distributions of quantities like particle energies or other characteristics of observed events. Due to the fact that the experimental apparatus (the "detector") inevitably have a limited resolution and acceptance, the measured (or "reconstructed") information of the quantity of interest typically deviates from its "true information". This leads to a distortion or smearing in the observed distribution. The statistical process to estimate the "true distribution" from the one measured is commonly known as unfolding (see Refs. [25, 202–204]). The RooUnfold package provides a common framework to evaluate and use concurrently different unfolding algorithms. We refer to the "true distribution" as the particle level jet distribution. This "true information" is then used to make comparisons between jets measured in experiment and jets calculated in theory. Theoretical calculations are typically performed at the parton level, where non-perturbative corrections for effects like hadronization and the UE must be applied to compare at the particle-level with jet measured in experiment.

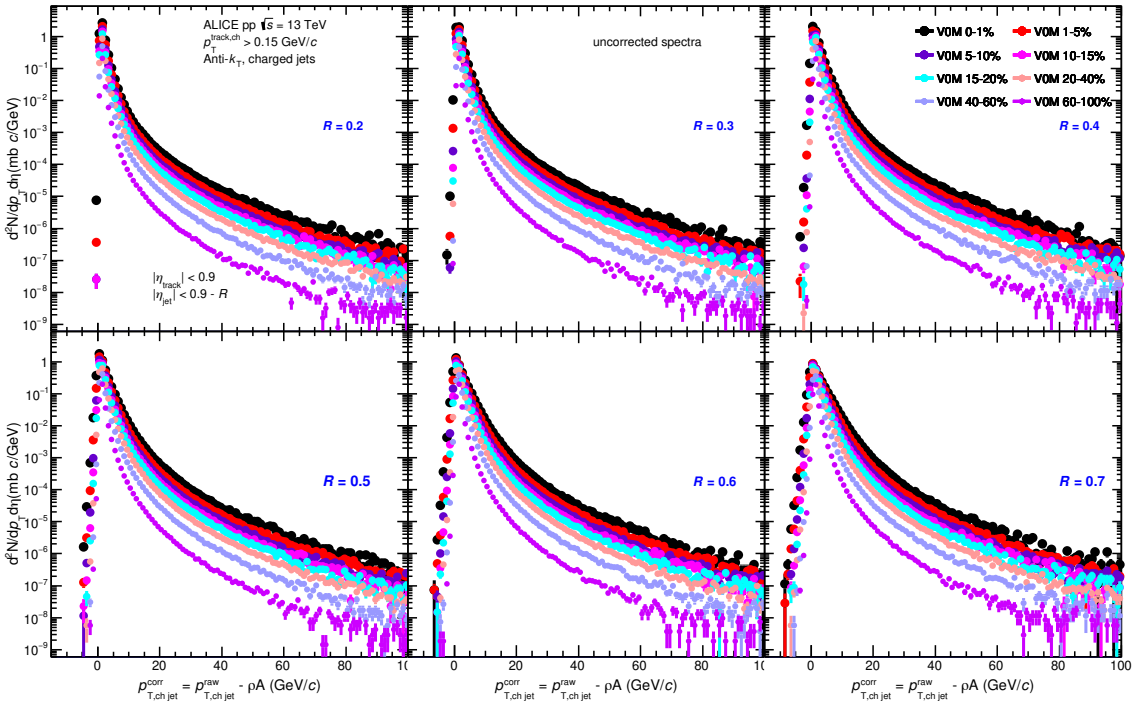

Figure 3.12: Multiplicity dependent raw jet p_T distributions for different radii in pp collisions at $\sqrt{s}$ = 13 TeV after UE subtraction.

Unfolding is used after the background subtraction to remove residual fluctuations, uncorrelated effects of the underlying event, and detector effects. The detector effects include tracking inefficiency, track p_T resolution, missing long-lived neutral particles, gaps in acceptance, etc. The better the correction for the background is, the more mathematically stable the unfolding procedure will be. Though unfolding is an effective tool, there are a few ambiguities in the procedure.

Figure 3.13 summarizes how the RooUnfold classes in ROOT are used. A mapping is created by a MC simulation linking true jets to reconstructed jets. This mapping is represented in a matrix form and is commonly referred to as the response matrix, which is mathematically defined in Equation 3.8.

$$\hat{A} p_{T,MC}^{part} = p_{T,MC}^{det} \tag{3.8}$$

Here, mathematically the response matrix ($\hat{A}$) represents the probability as given in Equation 3.9.

$$\hat{A}_{ij} = \text{Prob (observed in bin i | true in bin j)} \tag{3.9}$$

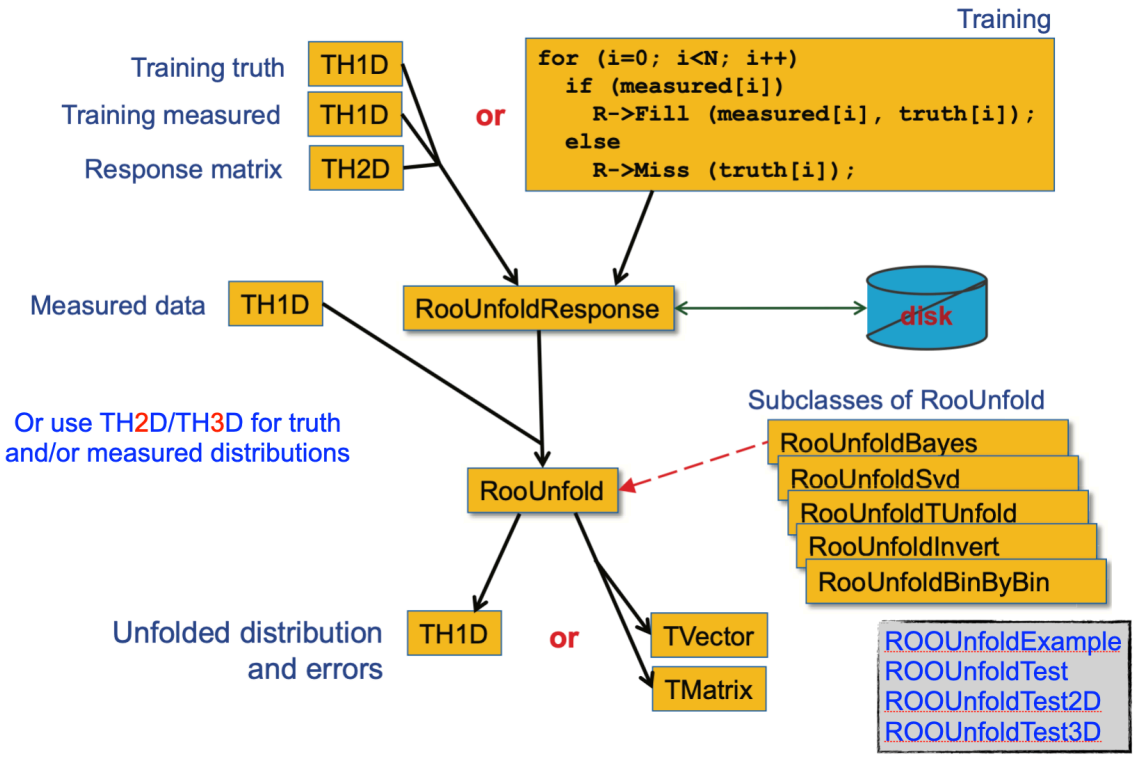

Figure 3.13: The RooUnfold classes. The training truth, training measured, measured data, and unfolded distributions can also be given as TH2D or TH3D histograms. Figure adapted from Ref. [25].

To obtain the true jet from the reconstructed jet the inverse of the response matrix is calculated, as shown in Equation 3.10.

$$p_{\mathrm{T,data}}^{\mathrm{part}} = \hat{A}^{-1} p_{\mathrm{T,data}}^{\mathrm{det}} \tag{3.10}$$

If the response matrix has strong non-diagonal components, then the matrix inversion, and therefore the unfolding, becomes difficult. This is one reason why it is necessary to subtract the background prior to unfolding. Taking the inverse also often results in an instability with respect to statistical fluctuations. Within statistical uncertainties the smeared data can be explained by the actual physical solution, but also by a large family of unphysical solutions. In a physical solution, a degree of smoothness can be expected, which is imposed in the unfolding procedure through a process called regularization. There are many different unfolding methods, each of which handles regularization differently. The two most common methods are the Bayesian unfolding [205] and the Single Value Decomposition (SVD) unfolding [203]. The works presented in this thesis utilizes both.

RooUnfoldSvd provides an interface to the TSVDUnfold class implemented in ROOT, which employs the single value decomposition method to decompose a given matrix $\hat{A}$ with dimensions $n \times m$ into three

matrices, as described in Equation 3.11. Here, U is an $n \times m$ matrix with n orthogonal columns, S is an $m \times m$ diagonal matrix where the diagonal elements are singular values that are ≥ 0, and V is an $m \times m$ matrix with m orthogonal columns.

$$\hat{A} = USV^T \tag{3.11}$$

$$UU^T = U^TU = I, \quad VV^T = V^TV = I, \tag{3.12}$$

$$S_{ij} = 0 \ \text{ for } \ \mathrm{i} \neq \mathrm{j}, \quad \mathrm{S_{ii}} \equiv \mathrm{s_i} \geq 0 \tag{3.13}$$

The quantities s_i are called singular values of the matrix $\hat{A}$, and columns of U and V are called the left and right singular vectors.

The singular values contain very valuable information about the properties of the matrix. If, for example, $\hat{A}$ is itself orthogonal, all its singular values are equal to 1. On the contrary, a degenerate matrix will have at least one zero among its singular values. In fact, the rank of a matrix is the number of its non-zero singular values. If the matrix and/or the r.h.s. of a linear system is known with some level of uncertainty, and some singular values of the matrix are significantly smaller than others, the system may be difficult to solve even if formally the matrix has full rank. In many aspects such matrices behave like degenerate ones, and SVD suggests a method of treating such problems, which is common for small and exactly zero singular values.

The SVD method is easily adaptable for unfolding problems as it is easy to compute the inverse by taking the inverse of the different decomposed matrices. This process is easier to perform on the decomposed matrices, exploiting for example the fact that the inverse of an orthogonal matrix is its transpose. This is written mathematically in Equation 3.14.

$$\hat{A}^{-1} = VS^{-1}U^T \tag{3.14}$$

Regularization is imposed in this procedure by a regularization parameter, k, which prevents high-frequency singular values in the inverse by replacing each singular value, s_i with $s_i^2 \rightarrow s_i^2/(s_i^2 + s_k^2)$. When the value of k is too small the result can be dominated by information from the prior and when the value of k is too large the result can be dominated by statistical fluctuations.

All unfolding methods should yield consistent results within their associated uncertainties, which is described in Section 4.5. Each method must also pass the various checks of the unfolding procedure in order to ensure that the result is not dependent on the parameters associated with that method, or the simulation utilized for the unfolding procedure.

The RooUnfoldBayes algorithm uses Bayes Theorem by D'Agostini to estimate the true distribution given the prior, the response matrix and the measured distribution. Repeated application of Bayes theorem is used to invert the response matrix. Regularization is achieved by stopping iterations before reaching the 'true' (but wildly fluctuating) inverse, where the true distribution for one iteration will be taken as the "prior" for the next iteration. This should not bias result once we have iterated, but could reach an optimum after fewer iterations. In principle, this has to be tuned according to the sample statistics and binning. In practice, the results are fairly insensitive to the precise setting used and four iterations are usually sufficient.

This implementation takes account of errors on the data sample but not, by default, uncertainties in the response matrix due to finite MC statistics. That calculation can be very slow, and usually the training sample is much larger than the data sample.

4 Multiplicity dependence of jet production in pp collisions at $\sqrt{s} = 13$ TeV

During the last decade, the study of colliding small systems has gained increased interest in its own right as a field of research. In particular, effects qualitatively similar as those observed in heavy-ion collisions and attributed to the formation of the QGP have also been observed in high multiplicity pp and p–Pb collisions where the formation of a QGP was not expected [119, 122]. These include, for example, long-range angular correlations [122] and the elliptic flow of heavy-flavour hadrons [119], the enhancement of the baryon-to-meson yield ratios at intermediate transverse momentum p_{T} (2–6 GeV/c) [130]. Another of such observations is the strange to non-strange hadron ratio which increases continuously from low-multiplicity pp to high-multiplicity p–Pb collisions to eventually reach the values observed in Pb–Pb collisions [73]. These findings suggest the possible existence of an underlying mechanism that would determine the dynamics and chemical composition of particles common to small and large collision systems. This possibility triggered the search for jet quenching effects in high-multiplicity events created in small collision systems. We have therefore studied the multiplicity dependence of the charged-jets production in pp collisions at $\sqrt{s} = 13$ TeV by ALICE.

Building upon the introduction to event selection, track reconstruction, jet reconstruction, and jet background subtraction in Chapter 3, this section delves into the experimental setup and data samples used for the analysis. It introduces the categorization of event multiplicity, explores the introduction of background fluctuations, provides insights into unfolding corrections, performs systematic uncertainty calculations, and presents the final physical results.

4.1 Experimental setup and data samples

The measurement was based on the data from pp collisions at a centre-of-mass energy of $\sqrt{s} = 13$ TeV collected between 2016 and 2018. During this period, minimum bias (MB) events were selected online using the high purity V0-based MB trigger (AliVEvent::kINT7) [206], defined by a charged-particle signal coincidence in the V0A and V0C arrays. The visible cross section satisfying this MB trigger was determined in a van der Meer scan [207, 208]. The integrated luminosity of the used sample, measured with V0, is 8.12 ± 0.16 nb^{-1} for 2016, 10.67 ± 0.29 nb^{-1} for 2017, and 13.14 ± 0.27 nb^{-1} for 2018. The luminosity uncertainty was evaluated to be 1.6 % by taking into account the correlations during the combination of the samples [209]. The final selected dataset consists of approximately 2.5×10^9 and 2.2×10^9 events before and after the trigger and offline selection. The datasets are listed in Table 4.1.

Additionally, we examined inclusive jet $p_{\mathrm{T}}, \eta, \varphi$ distributions for different periods relative to a baseline of LHC16k, as illustrated in Fig. 4.1. The top row represents the ratios of data samples from the year 16 to LHC16k, the middle row displays the ratios of data samples from the year 17 to LHC16k, and the bottom row showcases the ratios of data samples from the year 18 to LHC16k. These ratios are consistent across different periods, allowing us to aggregate them during the uncorrected stage to obtain the total statistic.

Table 4.1: Analyzed data samples and corresponding event numbers with after event selection.

period	events	period	events	period	events
LHC16e	8.03e7	LHC17c	3.9e6	LHC18d	5.32e7
LHC16g	3.47e7	LHC17e	0.99e7	LHC18e	3.65e7
LHC16h	8.65e7	LHC17f	0.94e7	LHC18f	7.25e7
LHC16j	4.12e7	LHC17g	1.56e7	LHC18g	1.20e7
LHC16k	1.83e8	LHC17h	7.54e7	LHC18h	0.34e7
LHC16l	3.1e7	LHC17i	7.97e7	LHC18i	2.93e7
LHC16o	4.65e7	LHC17j	1.75e7	LHC18j	72836
LHC16p	2.088e7	LHC17k	1.67e8	LHC18k	1.2e7
		LHC17l	9.94e7	LHC18l	9.0e7
		LHC17m	1.12e8	LHC18m	2.01e8
		LHC17o	1.4e8	LHC18n	0.22e7
		LHC17r	3.04e7	LHC18o	3.39e7
				LHC18p	8.57e7
total	2.22e9				

The analysis also uses PYTHIA MB and jet-jet (JJ) $p_{\mathrm{T,hard}}$ MC data (Pythia8, Monash 2013 tune) with a full GEANT3 ALICE detector simulation. The $p_{\mathrm{T,hard}}$-binned MC production is designed to ensure a high statistic while allowing jet yield to reach high transverse momenta p_{T}. The corresponding MB MC samples contain about 4.7×10^8 after event selection. The jet-jet MC production consists of 20 $p_{\mathrm{T,hard}}$ bins, each populated with approximately 6.7×10^7 events, with bin edges: [5, 7, 9, 12, 16, 21, 28, 36, 45, 57, 70, 85, 99, 115, 132, 150, 169, 190, 212, 235, 1000] GeV/c. In the next paragraph contains a simply description of how these $p_{\mathrm{T,hard}}$ bins are combined together, as shown in Fig. 4.2, the $p_{\mathrm{T,hard}}$ distribution before and after normalisation in pp collisions at $\sqrt{s} = 13$ TeV. The MCs are anchored run-by-run to data-taking runs, based on the DPG homepage, the good runlist in this analysis is defined as the largest existing subset of the good measured runs above. From QA Figures 3.1, 3.3, 3.7 and 3.10 of Chapter 3, illustrating event selection, track reconstruction, and jet reconstruction, data and MC simulation are consistent. The MC simulation results can be used to correct experimental measurements. In this analysis the PYTHIA MB MC sample is used to evaluate the lower p_{T} jet yield, while the jet-jet $p_{\mathrm{T,hard}}$ MC production is

utilized to measure the higher p_{T} jet yield. As a result, we obtain two sets of corrected physics results from two different MC simulation corrections. Finally, we combine these two sets of results to obtain the final physics outcome.

Combining $p_{\mathrm{T,hard}}$ bins: In order to construct a minimum bias equivalent sample from a set of $p_{\mathrm{T,hard}}$ bins, we must properly scale each $p_{\mathrm{T,hard}}$ bin according to the cross-section of that $p_{\mathrm{T,hard}}$, the average number of trials to produce an accepted event in our detector acceptance, and the relative number of events in each $p_{\mathrm{T,hard}}$ bin. For a generic counting histogram $h(x)$, we combine the $p_{\mathrm{T,hard}}$ bins k as:

$$h(x) = \sum_k c_k h_k(x), \quad c_k = \frac{1}{N_{\mathrm{event}}^{p_{\mathrm{T,hard}}}} \times \frac{\sigma_{p_{\mathrm{T,hard}}} \text{ per event}}{N_{\mathrm{trials}} \text{ per event}} \tag{4.1}$$

The relative weights can be verified to be correct by plotting the re-weighted $p_{\mathrm{T,hard}}$ distribution in Fig. 4.2. There is a generic pathology in constructing a weighted sum of finitely sampled statistical distributions: it tends to be highly sensitive to statistical fluctuations in distributions with large weights. In our case, the problem is that the low $p_{\mathrm{T,hard}}$ bins may fluctuate to have a count when the expected value is smaller than one count. If left unaddressed, significant spikes may occur in the merged distributions. To mitigate this issue, we discard events with $p_{\mathrm{T,chjet}} > 4 \times p_{\mathrm{T,hard}}$.

4.2 Multiplicity selection

In order to study the multiplicity dependence of inclusive charged-particle jet production, the MB sample was divided into event classes based on the "V0M amplitude" that is proportional to the total number of charged particles passing through the V0A and V0C detectors. The distribution of the self-normalised V0M amplitude from data and the PYTHIA8 event generator is shown in Fig. 2.3. The distribution is normalised to its average value, ⟨V0M amplitude⟩, to reduce the sensitivity of the multiplicity percentile determination on the amplitude. PYTHIA8 MC does not reproduce the measured multiplicity distribution, as was already reported in Ref. [29]. To reduce the potential model-dependent bias, corrections of the multiplicity dependent jet yields were done, using, instead of pure MC samples, a data-driven method as discussed in Sec. 4.5.

The event classes used in the analysis and the corresponding midrapidity charged-particle densities ($\langle \mathrm{d}N_{\mathrm{ch}}/\mathrm{d}\eta \rangle_{|\eta|<1}$) for experimental data are summarised in Table 4.2. The multiplicity classes were defined in terms of percentile intervals of experimental V0M amplitude /⟨V0M amplitude⟩ as shown in Fig. 2.3. These classes are delineated as follows: 0–1%, 1–5%, 5–10%, 10–15%, 15–20%, 20–40%,

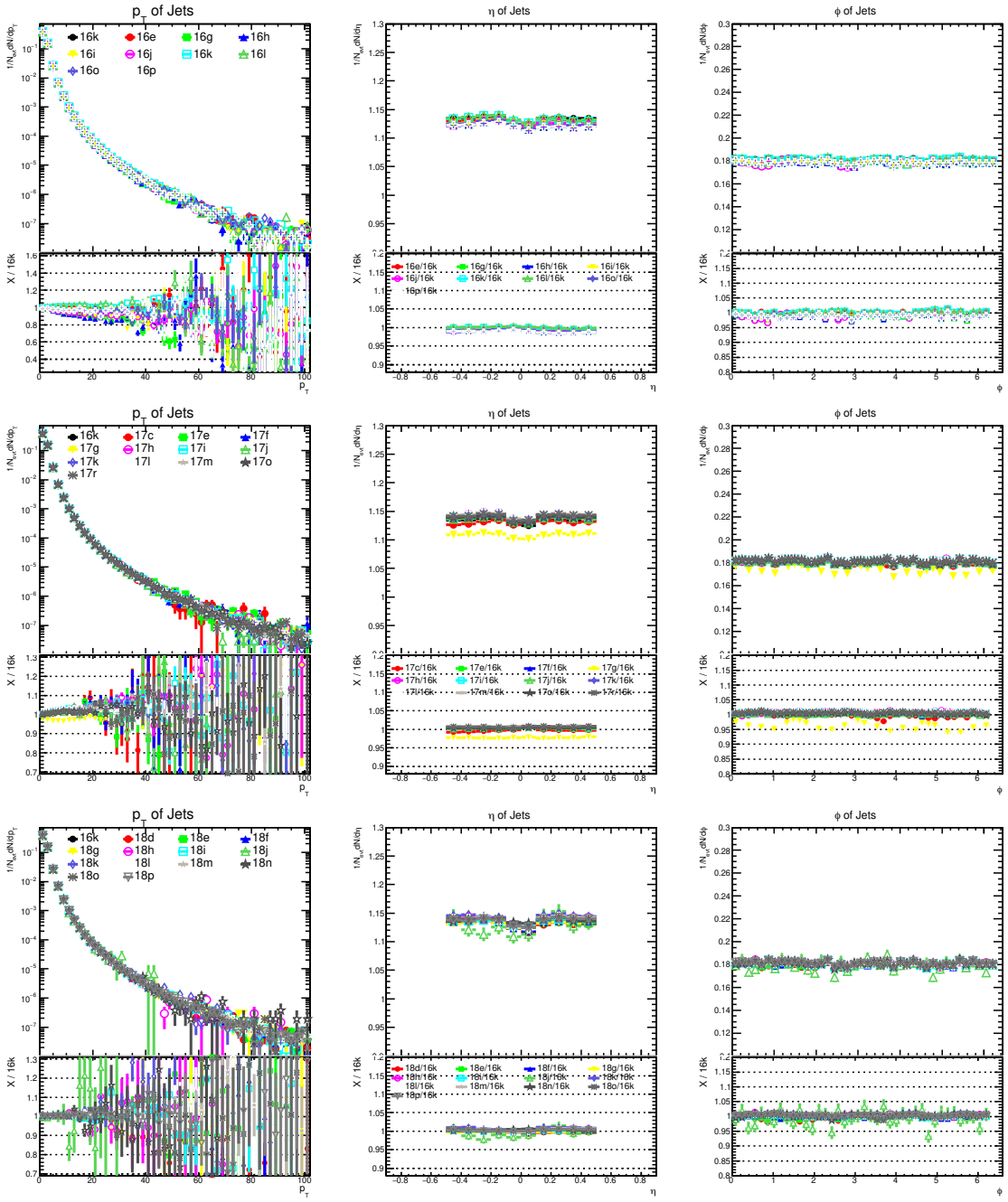

Figure 4.1: Inclusive charged-particle jet $p_{\mathrm{T}}, \eta, \varphi$ distributions are collected different data periods and the ratios relative to a baseline of 16k in pp collisions at $\sqrt{s}$ = 13 TeV.

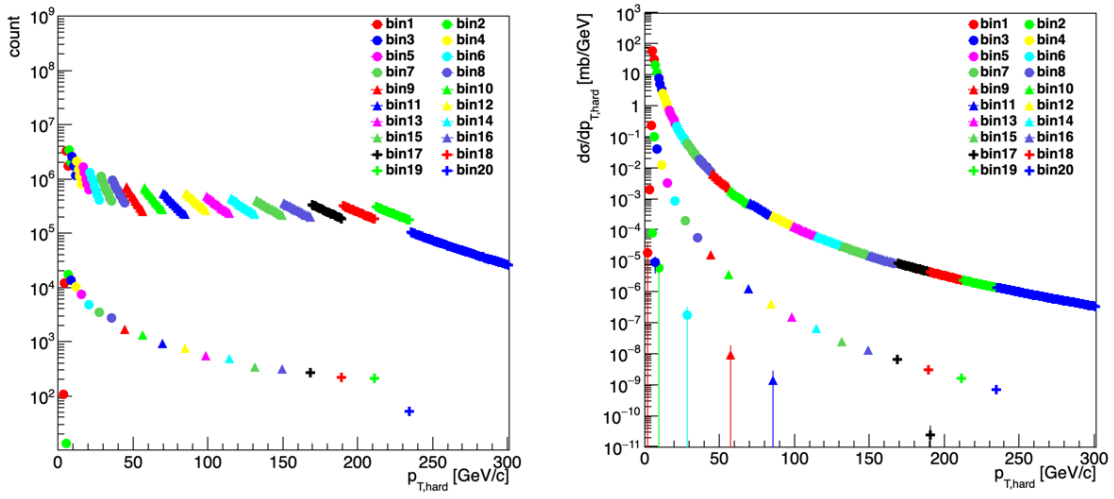

Figure 4.2: The $p_{\mathrm{T,hard}}$ distributions before (left) and after (right)normalisation from PYTHIA jet-jet $p_{\mathrm{T,hard}}$ MC productions in pp collisions at $\sqrt{s}$ = 13 TeV.

Table 4.2: Average charged-particle pseudorapidity densities at midrapidity $\langle \mathrm{d}N_{\mathrm{ch}}/\mathrm{d}\eta \rangle$ from data for inclusive events and different V0M multiplicity classes [29].

Class	V0M percentile	V0M amplitude /⟨V0M amplitude⟩	$\langle \mathrm{d}N_{\mathrm{ch}}/\mathrm{d}\eta \rangle_{\lvert\eta\rvert<1}$
MB	0–100%		6.93 ± 0.09
I	0–1%	≥ 3.66	26.01 ± 0.34
II	1–5%	2.68–3.66	19.99 ± 0.24
III	5–10%	2.15–2.68	16.18 ± 0.20
IV	10–15%	1.84–2.15	13.78 ± 0.18
V	15–20%	1.59–1.84	12.01 ± 0.16
VI	20–40%	0.97–1.59	9.18 ± 0.10
VII	40–60%	0.59–0.97	5.78 ± 0.06
VIII	60–100%	0–0.59	2.94 ± 0.03

40–60%, 60–100% of the MB trigger event sample. The average charged-particle multiplicity densities in MB pp collisions and for events of a given multiplicity class were obtained by integrating the corresponding fully corrected p_{T} spectra given in Ref. [29]. With this reference we can comapre the charged-particle density from data and PYTHIA8 MC, noting that PYTHIA8 MC does not describe the ALICE measurement obtained with the forward rapidity multiplicity estimator. When comparing the data to MC predictions, the multiplicity percentile was calculated from data and MC using their respective self-normalised distribution accordingly in order to minimise the difference observed in the V0M amplitude distribution. The 0–1% range corresponds to the highest multiplicity class (I), while the 60–100% interval corresponds to the lowest multiplicity class (VIII). Jet production differential yields and their ratios, together with ratios of integrated jet production yields are measured for different multiplicity classes.

4.3 Background fluctuations

Measurements of the multiplicity-dependence of the charged-particle jet yield rely on the ability to measure over a broad range in R and p_{T}. In order to perform this measurement, the background must be accounted for and removed, as outlined in Section 3.2.

On an event-by-event basis, the background density is computed using particles within the full acceptance. Each jet undergoes correction based on its area, assuming a uniform background distribution—an assumption necessitated by the impossibility of accurately determining real background of a jet. Despite this assumption, the background is not uniformly distributed; it fluctuates within the acceptance, primarily due to the statistical nature of these fluctuations. Uncorrelated random fluctuations in particle production result in a Poissonian distribution of particle count. Another source of background stems from the jets themselves, as multiple nucleon-nucleon interactions in an event may lead to the overlapping of two jets within the acceptance. The statistical fluctuations can cause both negative and positive values of δp_{T}. Fluctuations caused by overlapping jets or, in general, hard scattering processes, only affect the positive part of the distribution. The mean fluctuations can be taken into account on a statistical basis in an unfolding procedure. In order to study this fluctuations of the background, we have used the Random Cone (RC) method and perpendicular track embedding method [198]. In the RC method, cones of radius R positioned at random (η, φ) coordinates within the detector acceptance (fiducial region) were generated in each event. The sum of the charged-particle p_{T} in a given cone was then compared to the expected average background obtained from ρ_{ch} as follows:

$$\delta p_{\mathrm{T}}^{\mathrm{RC}} = \sum^{\mathrm{RC}} p_{\mathrm{T,track}} - \rho_{\mathrm{ch}} \pi R^2, \tag{4.2}$$

where the sum runs over tracks p_{T} inside the random cone, and πR^2 is the area of the random cone. The width of $\delta p_{\mathrm{T}}^{\mathrm{RC}}$ is a measure of the momentum smearing due to local background fluctuations [210]. To minimise the influence of signal jets on the $\delta p_{\mathrm{T}}^{\mathrm{RC}}$ distribution, a minimum distance from the random cone to the two highest momentum jets (leading jets) in the event was required.

In the alternative track embedding method, a probe track was embedded into an event [211]. The azimuthal angle of the probe track was required to be perpendicular to the jet ($\varphi_{\mathrm{track}}^{\mathrm{emb}} = \varphi_{\mathrm{ch\,jet}} + \pi/2$) while retaining its η value ($\eta_{\mathrm{track}}^{\mathrm{emb}} = \eta_{\mathrm{ch\,jet}}$). The transverse momentum of the probe track ($p_{\mathrm{T}}^{\mathrm{emb}}$) was uniformly chosen between 0 and 100 GeV/c. After embedding the probe track into the event, the jet finding algorithm was relaunched with the same background subtraction method as described above. The embedded $\delta p_{\mathrm{T}}^{\mathrm{emb}}$ was evaluated in a similar way to Equation 4.2 after removing the momentum of the embedded probe track:

$$\delta p_{\mathrm{T}}^{\mathrm{emb}} = p_{\mathrm{T,ch\,jet}}^{\mathrm{raw,emb}} - \rho_{\mathrm{ch}} A_{\mathrm{ch\,jet}}^{\mathrm{emb}} - p_{\mathrm{T}}^{\mathrm{emb}}, \tag{4.3}$$

where $p_{\mathrm{T,ch\,jet}}^{\mathrm{raw,emb}}$ and $A_{\mathrm{ch\,jet}}^{\mathrm{emb}}$ are the transverse momentum and area of the reconstructed jet with the embedded probe track.

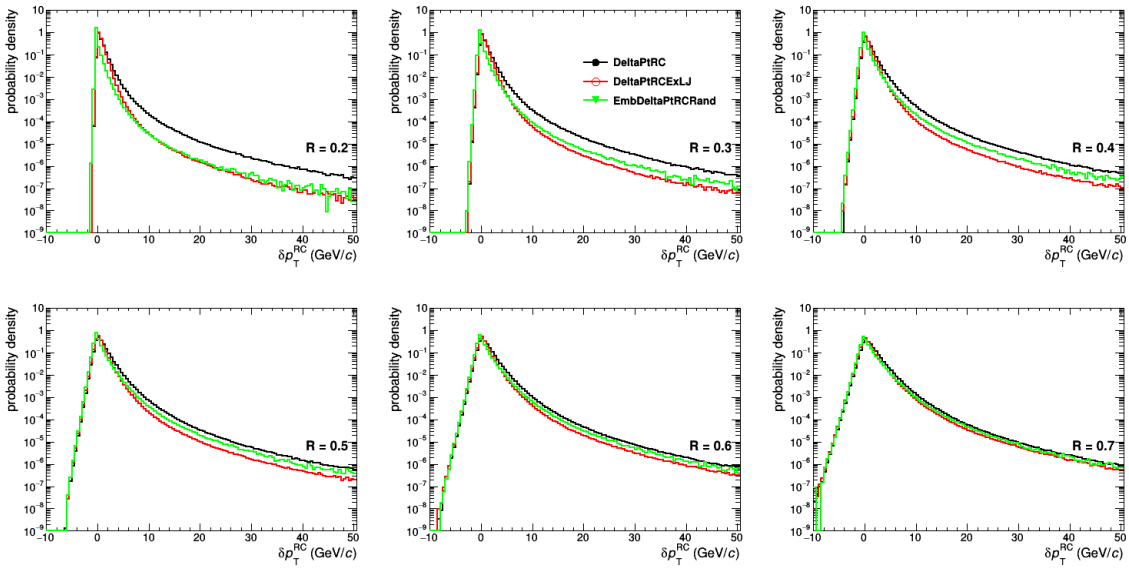

Figure 4.3: The inclusive jet δp_{T} distributions smearing due to local background fluctuations using different methods with R = 0.2 to 0.7. Each panel contains δp_{T} spectra obtained with random cone and track embedding methods.

The background fluctuations, determined by both the random cone and track embedding methods, are illustrated in Figures 4.3, 4.4, 4.5, and 4.6. Figure 4.3 displays the inclusive jet δp_{T} distributions for various jet resolution parameters ranging from R = 0.2 to 0.7, while Figures 4.4, 4.5, and 4.6 depict the multiplicity dependence of δp_{T} distributions with jet resolution parameters of R = 0.2, 0.4, and 0.7,

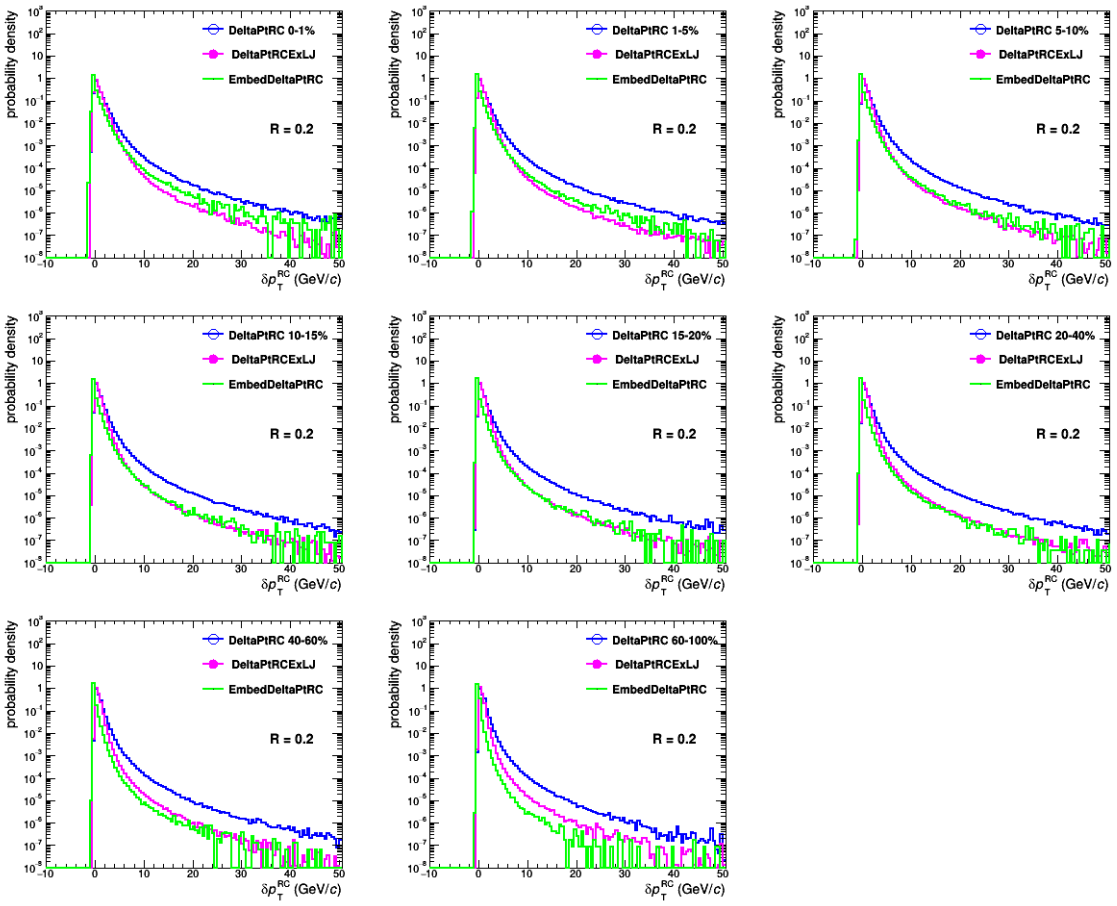

Figure 4.4: The δp_{T} distributions for different multiplicity percentiles using different methods with $R = 0.2$. Each panel contains δp_{T} spectra obtained with random cone and track embedding methods.

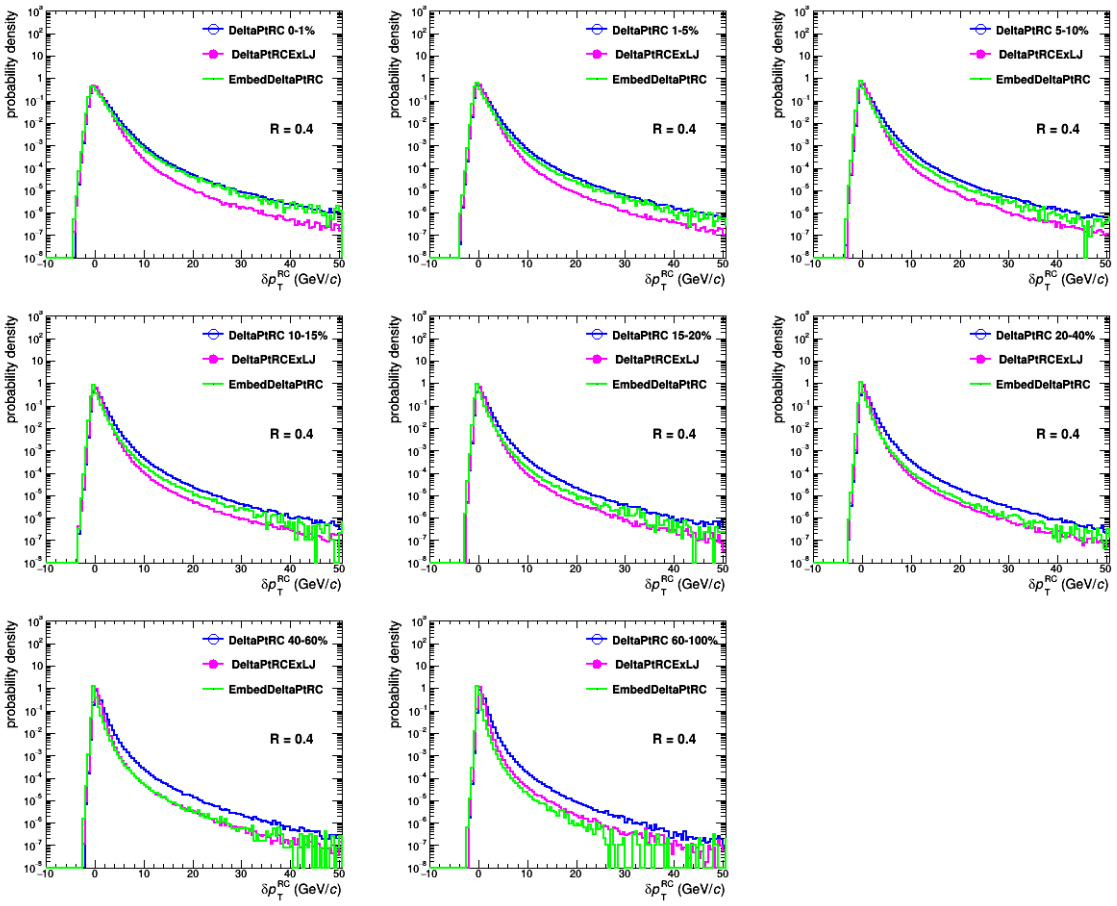

Figure 4.5: The δp_{T} distributions for different multiplicity percentiles using different methods with $R = 0.4$. Each panel contains δp_{T} spectra obtained with random cone and track embedding methods.

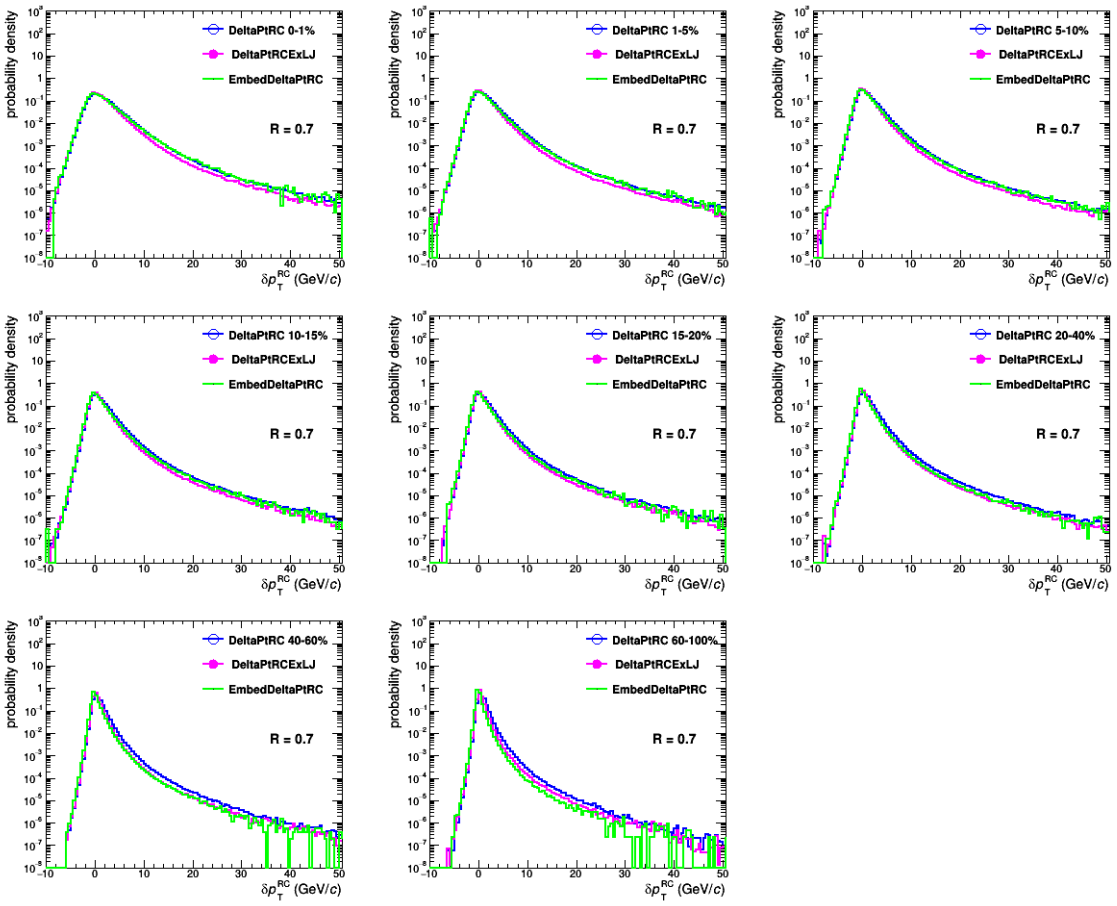

Figure 4.6: The δp_{T} distributions for different multiplicity percentiles using different methods with $R = 0.7$. Each panel contains δp_{T} spectra obtained with random cone and track embedding methods.

respectively. The black and red lines represent the results obtained using the RC method with different RC definitions: the black distribution corresponds to RC construction with the full $\eta-\varphi$ space within the detector acceptance, while the red distribution corresponds to RC construction excluding the two leading jet areas with a required distance $\Delta R > 1.0$ between the jet axis and RC center. The green lines represent the results obtained using the embedded track method. Both approaches provide similar distributions with a prominent peak at 0 GeV/c and a steep fall on both sides of the peak. The left-hand side of the peak in the δp_{T} distribution represents on the one hand downward fluctuations of the background in the probing cone and, on the other hand, can also be interpreted by an overestimated background. Roughly speaking, the background can be influenced by the signal jets.

A clearer and more intuitive comparison of the dependence of δp_{T} on the jet resolution parameter, computational method, and multiplicity percentile, is shown in Fig. 4.7. The first panel of Fig. 4.7 displays the $\delta p_{\mathrm{T}}^{\mathrm{RC}}$ distribution, obtained for various cone radii $R = 0.2, 0.4, 0.7$ in events where two leading jets are excluded. This panel distinctly illustrates stronger background fluctuations with increasing jet radius, due as expected to the larger number of particles within the jet cone. The middle panel of Fig. 4.7 compares the distribution of δp_{T} using the RC method and the track embedding approach for $R = 0.4$. While the distributions obtained from the two methods exhibit very similar negative tails, the right-hand tail of the distribution, caused by real jets, is notably less pronounced when a minimum distance to the two leading jets is required. Consequently, the δp_{T} distribution from the RC method without the requirement of two leading jets was used as the default in this analysis to build up the background fluctuation response, while the track embedding method was used for the assessment of the systematic uncertainty on the background fluctuation estimate. The right panel of Fig. 4.7 juxtaposes the δp_{T} distribution in different multiplicity intervals using the RC method and ensuring that the cone does not overlap with the two leading jets. This panel suggests that the magnitude of local background fluctuations increases, as anticipated, when a multiplicity bias is required.

4.4 Unfolding correction

To be able to compare the jet results to those obtained by other experiments or those from theory predictions, they should be as close as possible to the true spectrum free of detector or environment biases. Our this thesis, the measured background-corrected jet spectra differ from the true spectra mainly in two aspects. First, they are detector-specific and will be affected by a variety of instrumental effects. Due to the finite single-track momentum resolution and reconstruction efficiency, jets are reconstructed with different transverse momenta than in a perfect detector. Second, although the mean background is subtracted, jets can be subject to background fluctuations. Both effects cannot be corrected on an

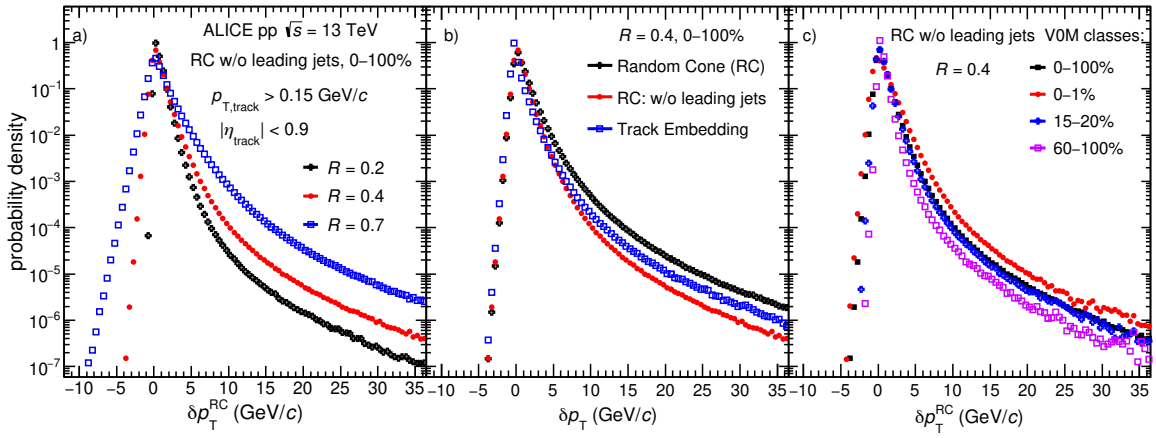

Figure 4.7: Left: Comparison of the δp_T distribution obtained for different random cone radii ($R = 0.2, 0.4, 0.7$). Middle: Comparison of the δp_T distribution with the RC method (including and excluding two leading jets) and the track embedding approach for $R = 0.4$. Right: Comparison of measured δp_T distribution using RC method without leading jets for $R = 0.4$ in different multiplicity classes.

event-by-event basis and must be corrected statistically for the whole event sample. To that purpose, we generate a response matrix that simultaneously describes both bias, and then use a statistical unfolding procedure [198] to correct the measured $p^{\text{det}}_{\text{T,ch jet}}$ ($p^{\text{raw/corr}}_{\text{T,ch jet}}$) to the true jet $p^{\text{part}}_{\text{T,ch jet}}$ ($p^{\text{true}}_{\text{T,ch jet}}$). The Unfolding technique is described in detail in Section 3.4.

Jet detector performance

First, the particle-level true jets were constructed from the PYTHIA8 (Monash 2013) event generator, which is described in Section 2.4.1, by selecting only those stable charged particles defined as particles with a mean proper lifetime larger than 1 cm/c, and excluding the decay products of these particles [212]. Next, jets were reconstructed at detector level from tracks coming from MC particles propagated through the GEANT3 model of the ALICE setup. A comprehensive evaluation of jet reconstruction performance is critical for any jet measurement and evaluates how well that jet measurement can be done. Typically, this jet performance evaluation relies on two key quantities: Jet Energy Scale (JES) and Jet Energy Resolution (JER), which are formally defined by Equations 4.4 and 4.5, respectively. These quantities are not used for correction of the data.

$$\text{JES} = \frac{(p^{\text{det}}_{\text{T,ch jet}} - p^{\text{part}}_{\text{T,ch jet}})}{p^{\text{part}}_{\text{T,ch jet}}} \tag{4.4}$$

That responds to the detector effects which smear the $p_{T,\text{jet}}$ distribution are characterized in pp simulations with the relative difference between the detector level $p^{\text{det}}_{\text{T,ch jet}}$ and particle level $p^{\text{part}}_{\text{T,ch jet}}$.

$$\mathrm{JER} = \frac{\sigma(p_{\mathrm{T,ch\ jet}}^{\mathrm{det}})}{p_{\mathrm{T,ch\ jet}}^{\mathrm{part}}} \tag{4.5}$$

That is, for a fixed $p_{\mathrm{T,ch\ jet}}^{\mathrm{part}}$, the width of the distribution $p_{\mathrm{T,ch\ jet}}^{\mathrm{det}}$ that is measured.

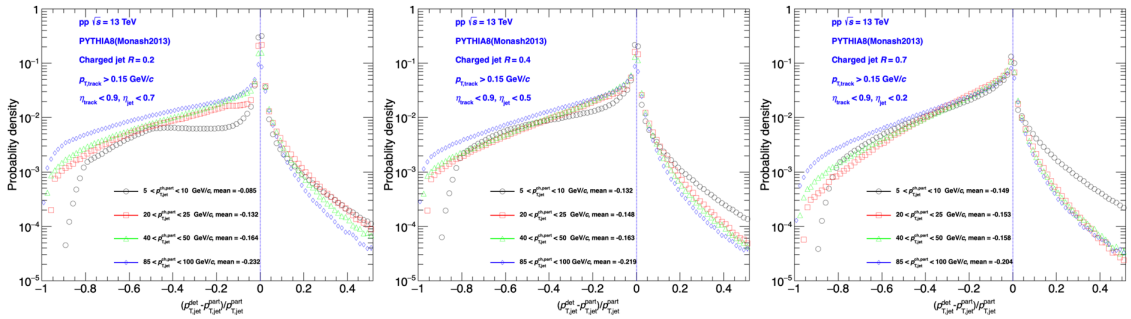

Figure 4.8: Inclusive jet energy scale residual distributions for $R = 0.2, 0.4, 0.7$ jets with various $p_{\mathrm{T,ch\ jet}}^{\mathrm{part}}$ intervals in pp collisions at $\sqrt{s} = 13$ TeV.

The jet reconstruction performance is shown below for charged-particle jets: Fig. 4.8 shows the jet energy scale residual distributions in pp collisions at $\sqrt{s} = 13$ TeV for $R = 0.2, 0.4, 0.7$ jets with various $p_{\mathrm{T,ch\ jet}}^{\mathrm{part}}$ intervals [5, 10], [20, 25], [40, 50], and [85, 100] GeV/c. In this figure are also given the width and median shift of this JES shift distribution in selected $p_{\mathrm{T,ch\ jet}}^{\mathrm{part}}$ intervals. Since a value of $p_{\mathrm{T,ch\ jet}}^{\mathrm{det}}$ larger than $p_{\mathrm{T,ch\ jet}}^{\mathrm{part}}$ can only arise from $p_{\mathrm{T,jet}}$ resolution effects, and the distribution is not symmetric about zero, the $p_{\mathrm{T,jet}}$ resolution is determined by fitting a Gaussian function to the distribution for $(p_{\mathrm{T,ch\ jet}}^{\mathrm{det}} - p_{\mathrm{T,ch\ jet}}^{\mathrm{part}})/p_{\mathrm{T,ch\ jet}}^{\mathrm{part}} > 0$ while fixing the mean of the fit to zero, since resolution effects are symmetric. The median relative $p_{\mathrm{T,ch\ jet}}^{\mathrm{part}}$ shift, which is non-zero due to detector inefficiencies, is also reported. These values are representative of the instrumental effects in pp collisions.

Fig. 4.9 shows the jet energy resolution for $R = 0.2$ to 0.7 jets. Here we observe that JER exhibits minimal dependency on the jet radius. At low p_{T}, there are significant disparities arising from background fluctuations (which leads to a broader JER), while at high p_{T} JER is dominated by detector effects. At jet $p_{\mathrm{T}} > 10$ GeV/c, there is a slight increase in JER distribution with p_{T}, but the difference in the mean value of the distribution remains small. The corresponding jet energy resolution were estimated to be about 20% for jet p_{T} larger than 10 GeV/c with jet resolution parameter $R = 0.2$.

Response matrix details

A simple unfolding procedure, solely based on the response matrix as defined in Equation 3.8, is employed. This response matrix can be understood as a mapping between true (particle-level) and measured

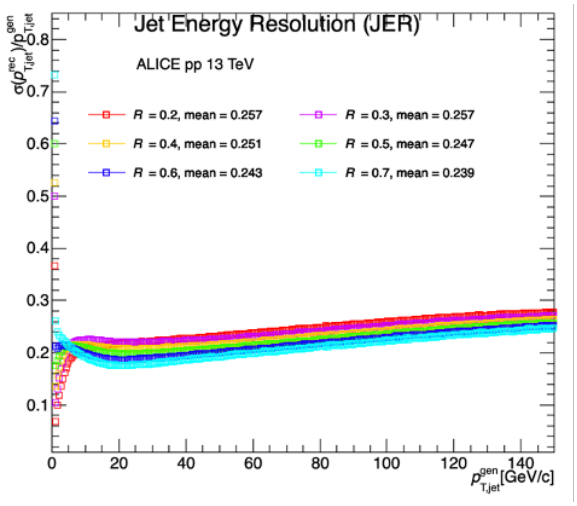

Figure 4.9: Jet energy resolution distribution for $R = 0.2 - 0.7$ in pp collisions at $\sqrt{s} = 13$ TeV.

(detector-level) jet p_{T}. Specifically, each true jet p_{T} is associated with a probability distribution of measured jet transverse momenta, while conversely, each measured jet p_{T} is linked to a distribution of true jet p_{T}, indicating the likelihood that a measured jet is derived from a certain true jet.

The response matrix directly connects two physical quantities: the measured and true jet transverse momenta. As already stated above, the response matrix used in the unfolding procedure includes detector effects and also the smearing caused by background fluctuations. In the matrix representation, a perfect detector and no background fluctuations would produce a 1-matrix with vanishing off-diagonal elements. While the unfolding of detector response and background fluctuation matrices can principally be carried out separately, it is more convenient to combine both matrices in one response matrix through matrix multiplication so that the unfolding is only performed once. **The combined response matrix** is given by $\mathrm{RM}_{\mathrm{full}} = \mathrm{RM}_{\mathrm{bkg}} \times \mathrm{RM}_{\mathrm{det}}$. where $\mathrm{RM}_{\mathrm{bkg}}$ represents **the background fluctuation response matrix** and $\mathrm{RM}_{\mathrm{det}}$ **the detector response**. Note that the order of the matrices in the multiplication is not arbitrary. Roughly speaking, the fluctuations matrix $\mathrm{RM}_{\mathrm{bkg}}$ has to be applied on jets which have already been smeared by the detector response matrix.

the detector response matrix: The main component of the response matrix is due to detector smearing. the detector response matrix for unfolding is constructed using pp events simulated using the PYTHIA8 event generator and the GEANT3 transport code. Particle-level information are available from PYTHIA, GEANT3 generates detector-level information using a detailed model of the ALICE detector. Particle-level jets are jets as they would be seen by a perfect detector, detector-level jets include all detector effects. Detector-level jets are geometrically matched to particle-level jets based on their relative sepa-

ration in rapidity and azimuth, $\Delta R = \sqrt{\Delta\eta^2 + \Delta\varphi^2}$, and requiring ΔR to be less than 0.1 for $R = 0.2$ jets, 0.15 for $R = 0.3$ jets, 0.25 for $R = 0.4$ jets, 0.3 for $R = 0.5$ jets, 0.35 for $R = 0.5$ jets, and 0.4 for $R = 0.7$. The x-axis is measured and the y-axis is true jet momentum. The response matrix is generated in a fine binning, with 1 GeV/c bin widths on both axes. This is then re-binned into a more coarse binning to be used in the actual unfolding. Fig. 4.10 presents the inclusive jet re-binned detector response matrices. We utilized this detector response matrix to unfold measured data without subtracting the underlying event.

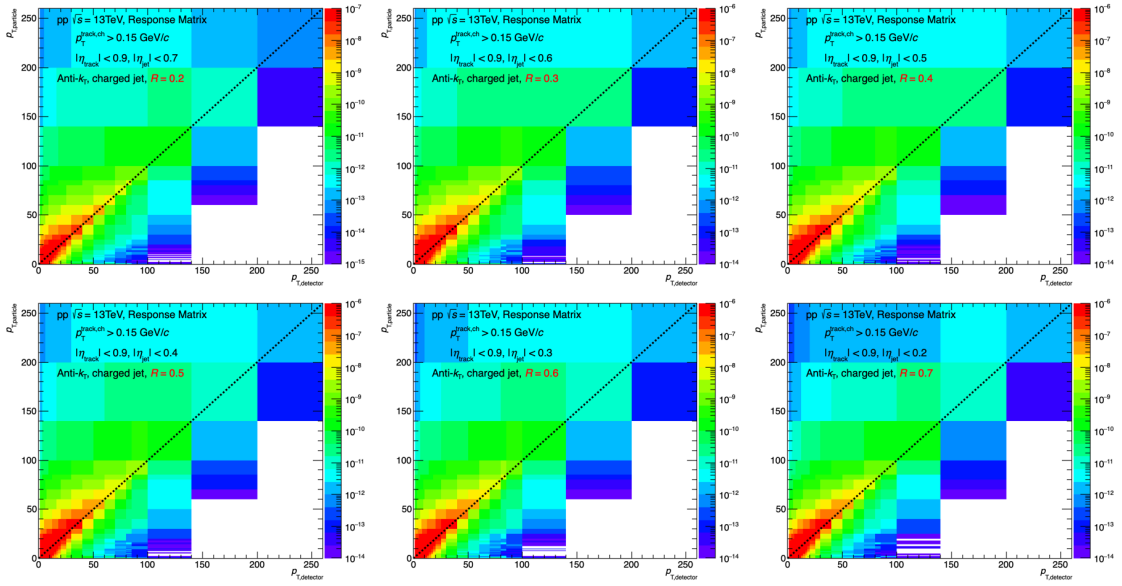

Figure 4.10: The inclusive jet re-binned detector response matrix for different radii in pp collisions at $\sqrt{s} = 13$ TeV. The X axis is the detector level jet $p^{\text{det}}_{\text{T,ch jet}}$, Y axis is particle level jet $p^{\text{part}}_{\text{T,ch jet}}$.

We must also calculate the efficiency for successfully reconstructing accepted jets, referred to as the jet reconstruction efficiency. This is defined as the ratio of the number of accepted detector-level jets geometrically matched to a particle-level jet (N_{matched}) and the total number of particle-level jets within a given $p^{\text{part}}_{\text{T,ch jet}}$ interval, as expressed in Equation 4.6. This measurement accounts for the efficiency of matching jets as well.

$$\varepsilon(p^{\text{part}}_{\text{T,ch jet}}) = \frac{N_{\text{matched}}(p^{\text{part}}_{\text{T,ch jet}} \text{ to } p^{\text{det}}_{\text{T,ch jet}})}{N_{\text{true}}(p^{\text{part}}_{\text{T,ch jet}})} \tag{4.6}$$

Given a truth-level jet with $p^{\text{part}}_{\text{T,ch jet}}$, the probability that we will reconstruct it as an accepted jet at any $p^{\text{det}}_{\text{T,ch jet}}$. Note that this quantity will be used to correct the unfolded spectrum for the fact that we fail to measure a certain fraction of jets. Fig. 4.11 shows the inclusive jet reconstruction efficiency for jet resolution parameters from $R = 0.2$ to 0.7. The corresponding jet reconstruction efficiency for all R is greater than 90% for jet $p_{\text{T}} \geq 10$ GeV/c, and close to unity at $p_{\text{T}} = 140$ GeV/c.

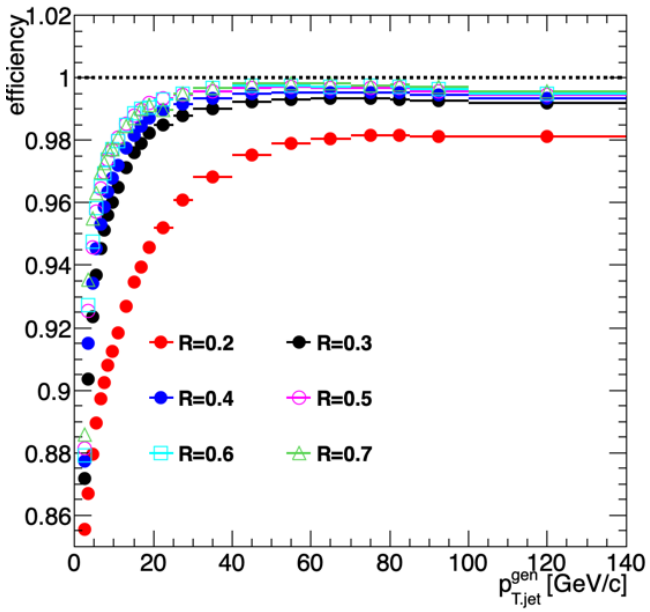

Figure 4.11: Jet reconstruction efficiency distribution for $R = 0.2 - 0.7$ in pp collisions at $\sqrt{s} = 13$ TeV.

The background fluctuation response matrix: The second contribution to the response matrix is the smearing matrix, which corresponds to the distribution of background fluctuations δp_{T} from data, as shown in Figures.4.3, 4.4, 4.5, and 4.6 in Section 4.3. This smearing matrix is created drawing on the δp_{T} distribution calculated for the whole event sample assuming that the background fluctuations are independent of jet transverse momentum.

Technically, the matrix is constructed by inserting the one-dimensional δp_{T} distribution to all slices in particle-level jet transverse momentum. The distribution is shifted by the $p_{\mathrm{T,ch\ jet}}^{\mathrm{part}}$ according to the each individual slice. This guarantees the correct behavior of the smearing matrix: if the δp_{T} distribution were a δ function, the matrix would simplify to the unit matrix.

Fig. 4.12 depicts the fine-binned background fluctuation matrix for $R = 0.7$ from inclusive (left), $(0 - 1)\%$ (middle) and $(60 - 100)\%$ (right) multiplicity events. To enable multiplication of the two matrices, multiplicity dependent background fluctuation matrix depicted in Fig. 4.12 and inclusive jet detector response matrix depicted in 4.10, a rebinning and reweighing process for both background and detector response matrices is necessary. This process ensures normalization of the y-axis ($p_{\mathrm{T,ch\ jet}}^{\mathrm{part}}$axis) to one, as illustrated in the first two columns of Fig. 4.13. The response matrix is normalized so as to preserve the number of jets upon unfolding. That is, each truth-level jet should map with probability 1 to a

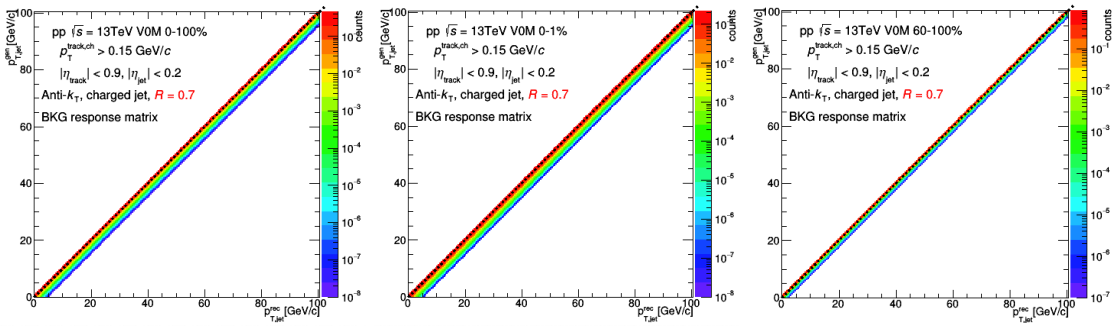

Figure 4.12: The fine-binned background fluctuation response matrix for inclusive (left), $(0-1)\%$ (middle) and $(60-100)\%$ (right) multiplicity events with $R = 0.7$.

detector-level jet.

The final combined response matrix is then obtained by multiplying these two matrices, as shown in the third column of Fig. 4.13. The combined response matrix, which corrects for both background fluctuations and detector effects, has ultimately been used in the unfolding procedure.

Perform unfolding

The binning of the matrices have to be set according to the desired binning of the final unfolded spectrum and according to the binning of the measured spectrum, which is adapted to the spectrum fluctuations. Both binning are given by the following sets:

Measured pp: $[0, 1, 2, 3, 4, 5, 6, 7, 8, 9, 10, 12, 14, 16, 18, 20, 25, 30, 40, 50, 60, 70, 85, 100, 140, 200]$ GeV/c;

Unfolded: $[0, 1, 2, 3, 4, 5, 6, 7, 8, 9, 10, 12, 14, 16, 18, 20, 25, 30, 40, 50, 60, 70, 85, 100, 140, 200, 250]$ GeV/c;

Both SVD and Bayes unfolding methods require a reference spectrum, known as a prior, which should be close enough to the truth spectrum. To obtain such a prior, we utilize PYTHIA8 and EPOS generator [5] to generate the MC truth spectrum as a prior for our analysis, with the prior from PYTHIA being the default choice.

In this analysis, the default unfolding method was based on the SVD approach as implemented in the RooUnfold package. The regularisation parameter k, which suppresses high-frequency variations in the unfolded result, was selected by examining the d-vector distribution [203]. In addition to the SVD unfolding, Bayesian unfolding was also used for systematic uncertainty evaluation. Consistent results were obtained between both unfolding methods. To validate the unfolding process and identify potential biases, closure tests that compare the unfolded distributions to the particle-level true distributions were performed (unfolded closure). The consistency of the unfolding procedure was also checked by folding

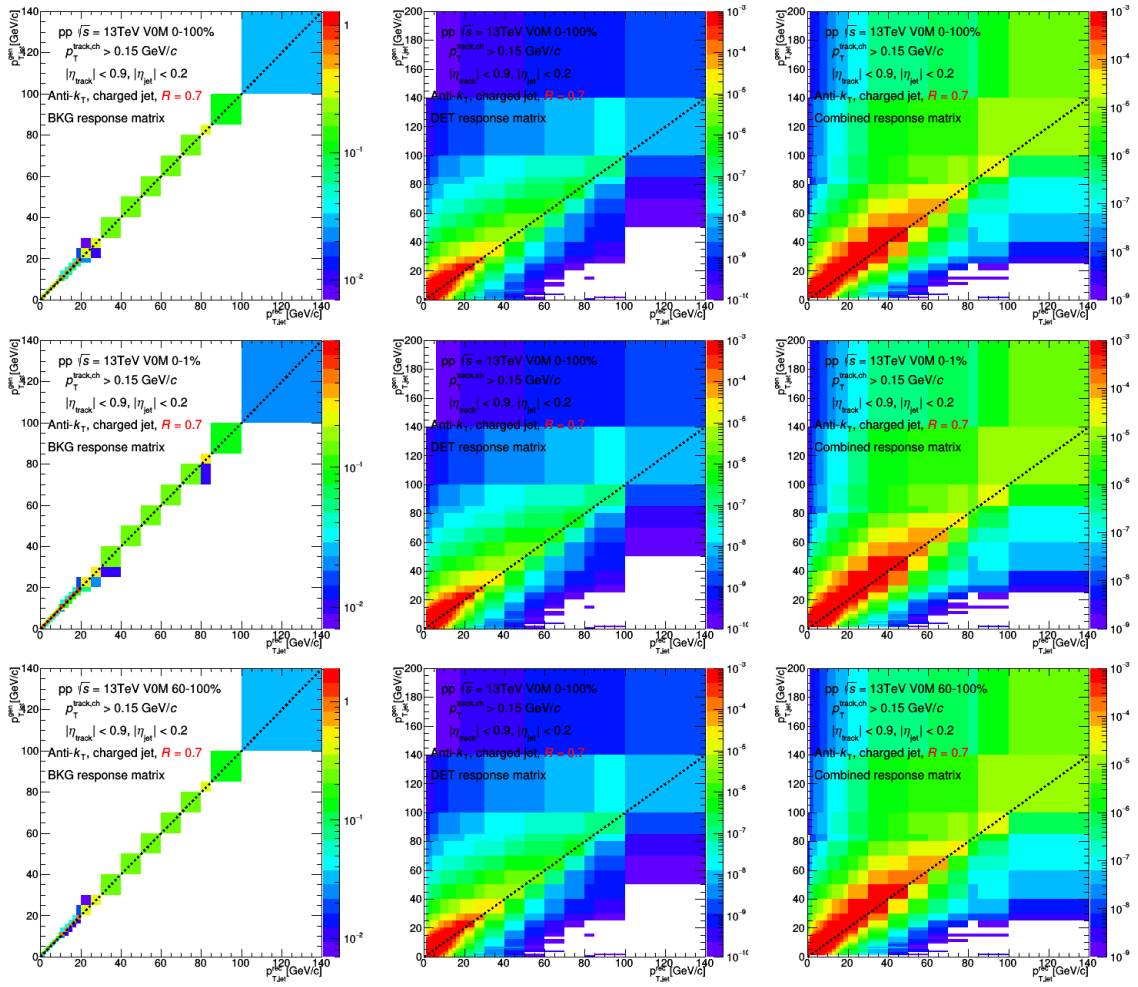

Figure 4.13: The background fluctuation response matrix (left column), detector response (middle column) and combined response matrices (right column) for inclusive (top row), (0−1)% (middle row) and (60−100)% (bottom row) multiplicity events after rebinning and reweighting with $R = 0.7$.

the solution to detector level and comparing it to the measured raw spectrum (refolded closure). In both cases, no significant difference was found.

The SVD unfolding algorithm also performs statistical error propagation. Note that the statistical uncertainties may therefore be partially correlated. We use the default error propagation in RooUnfold, which computes the statistical errors according to the square root of the diagonal elements of the covariance matrix.

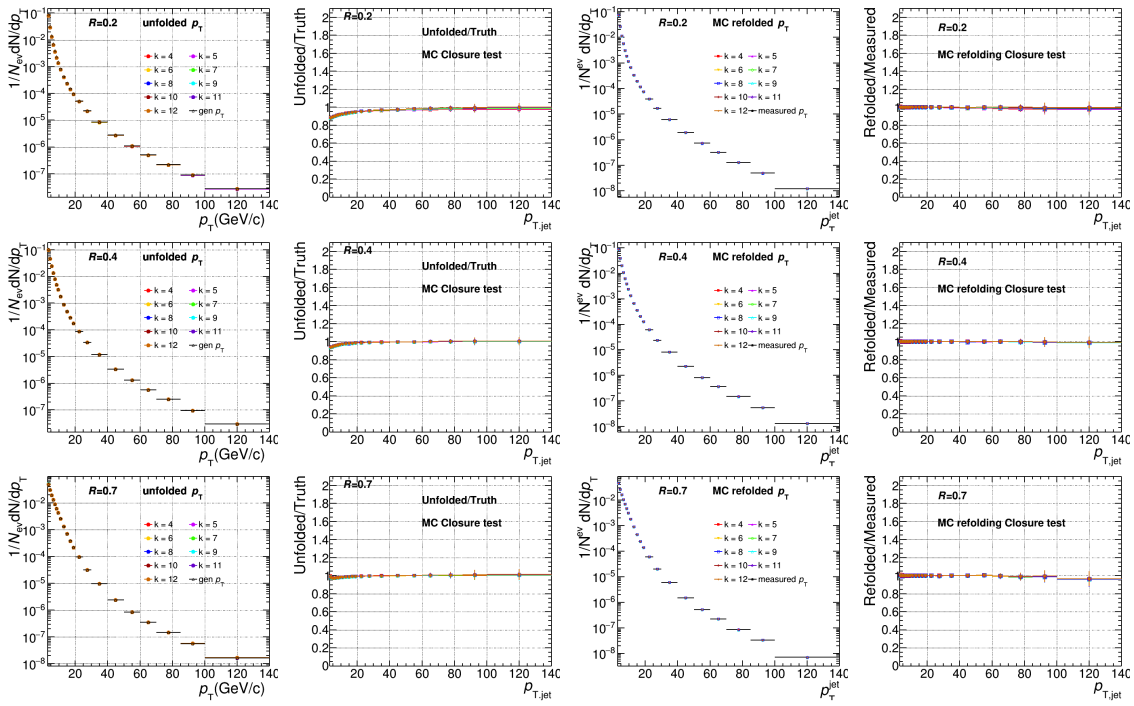

Figure 4.14: First column: MC unfolded distributions for each regularization parameter (k) of the SVD unfolding procedure for the split MC test. Second column: Ratio of the unfolded to true distribution for inclusive charged jets with $R = 0.2, 0.4, 0.7$. Third column: MC refolded distribution as a function of the k of the SVD unfolding procedure. Fourth column: Ratio of the refolded to raw distribution for inclusive charged jets with $R = 0.2, 0.4, 0.7$.

The basic MC closure test was first performed to check the validity of the unfolding procedure using SVD method. This test works by unfolding the same distribution that is used to fill the response. This means that the detector-level spectra, the response matrix and the prior (particle-level spectra) required for unfolding procedure are derived from the MC productions. However, to avoid the self-association of detector-level spectra and response matrix in unfolding procedure, the MC production is split into two parts with comparable statistics. One part is used to generate the response matrix, while the other part generates the detector-level and particle-level spectra for subsequent unfolding. The detector-level spectra is then unfolded and checked for consistency with the true distribution. The unfolded results from the split MC closure test for each regularization parameter (k = 4 to 12) of the SVD unfolding procedure

for $R = 0.2$ (top), 0.4 (middle), 0.7 (bottom) inclusive charged jets, which indicate good closure, are presented in the left panel of Fig. 4.14. The first column displays the unfolded results from $k = 4$ to 12, and the true distribution. The second column represents the ratio of the unfolded to the true distribution. The refolded to raw ratio test ensures that the unfolding procedure has cyclic closure. Cyclic closure implies that the reverse of the unfolding procedure, known as refolding, can be applied to the unfolded distribution, returning the originally measured distribution used as input, as written in Equation 3.8. The ratio of the MC refolded to raw distribution for inclusive charged jets with $R = 0.2, 0.4, 0.7$ in pp collisions, also demonstrating good closure, can be seen in the right panel of Fig. 4.14 (the last two columns).

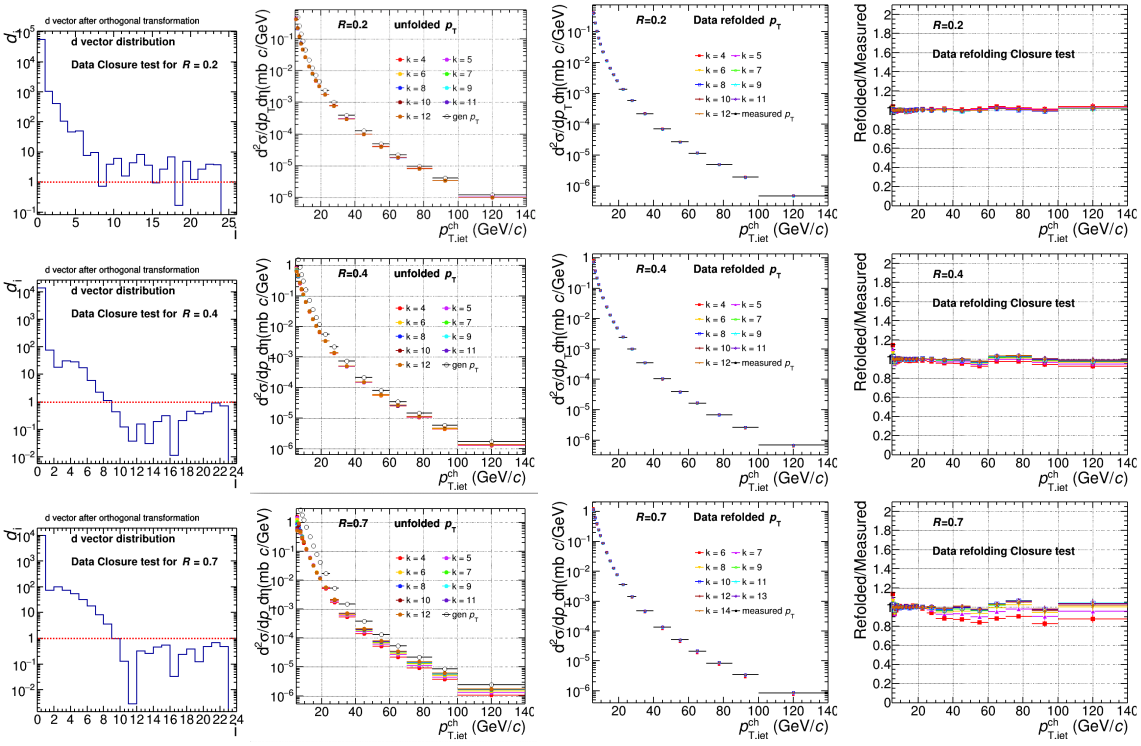

Figure 4.15: First column: D-vector distribution for $R = 0.2, 0.4, 0.78$ inclusive jets from data unfolding. Second column: Unfolded inclusive jet p_{T} distributions as a function of k of the SVD unfolding procedure. Third column: Data refolded distribution as a function of the k. Fourth column: Ratio of the refolded to raw distribution for inclusive charged jets with $R = 0.2, 0.4, 0.7$.

After verifying the validity and feasibility of the unfolding corrections obtained by MC self-closure test and refolded test, we then corrected the experimental measurements using SVD unfolding. As an illustration of the unfolding procedure we plot here the unfolding plots for $R = 0.2, 0.4, 0.7$. Fig. 4.15 is the inclusive jet results and Fig. 4.16 is the multiplicity-dependent jet results. The first column of Fig. 4.15 shows the d-vector distribution as a function of k for different jet radii $R = 0.2, 0.4, 0.7$, which

suggests that $k = 8$ is a reasonable solution. The second column displays the data unfolded result as a function of k. The last two columns of Fig. 4.15 and Fig. 4.16 test the feasibility of the SVD unfolding in the measured data through the results of refolded closure test for inclusive and different multiplicity event jets.

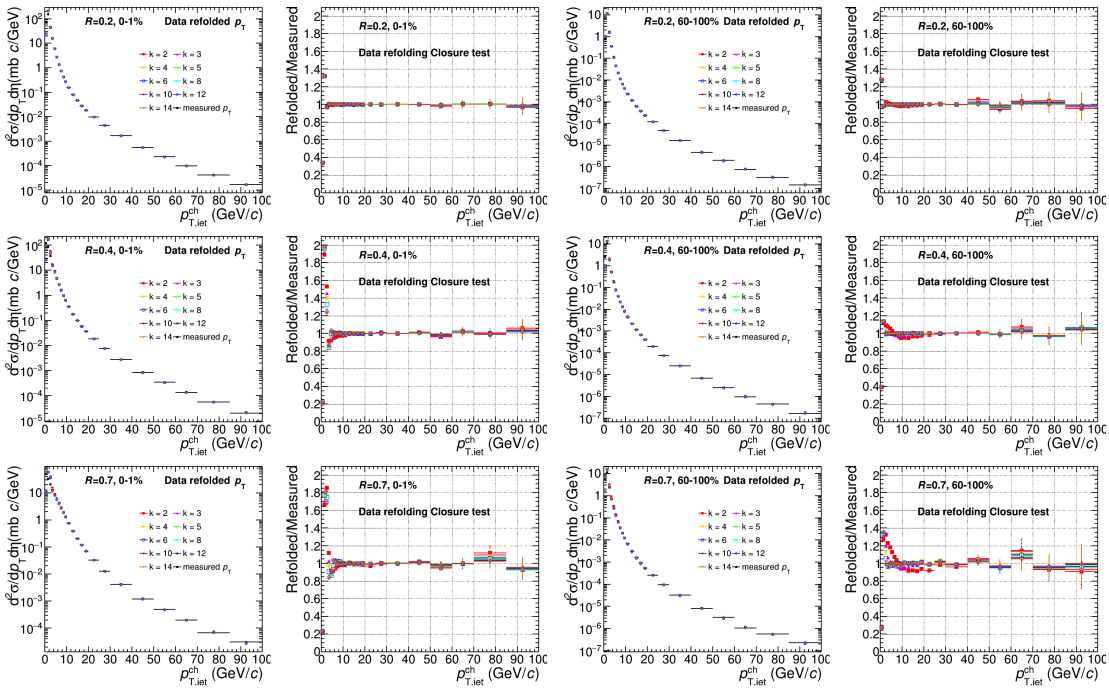

Figure 4.16: Data refolded distribution as a function of the k and ratio of the refolded to raw distribution in different multiplicity events (0–1%, 60–100%) for jet radii $R = 0.2, 0.4, 0.7$.

Figure 4.17 displays the ratio of the unfolded results corrected by the response matrix generated from the jet-jet $p_{\mathrm{T,hard}}$ Monte Carlo simulation to that from the Minimum Bias MC simulation. It can be observed that the two results are nearly same at transverse momenta around 20 GeV/c. Therefore, we opted to utilize the response matrix extracted from the MB MC data for the low p_{T} region ($p_{\mathrm{T,jet}} < 20$ GeV/c) to avoid anomalies in the final results. Conversely, the response matrix from $p_{\mathrm{T,hard}}$ production is employed for the higher p_{T} region ($p_{\mathrm{T,jet}} > 20$ GeV/c) to ensure sufficient statistics in the high p_{T} region.

4.5 Systematic uncertainties

This section aims to provide a detailed analysis of the calculation of systematic uncertainties of the measured jet observable in the analysis. The measurement of jet spectra depends on various parameters. Some of the parameters are chosen for good reasons or they define the considered observable, e.g. the jet resolution parameter or the jet algorithm. Others are more or less arbitrary or at least less verified

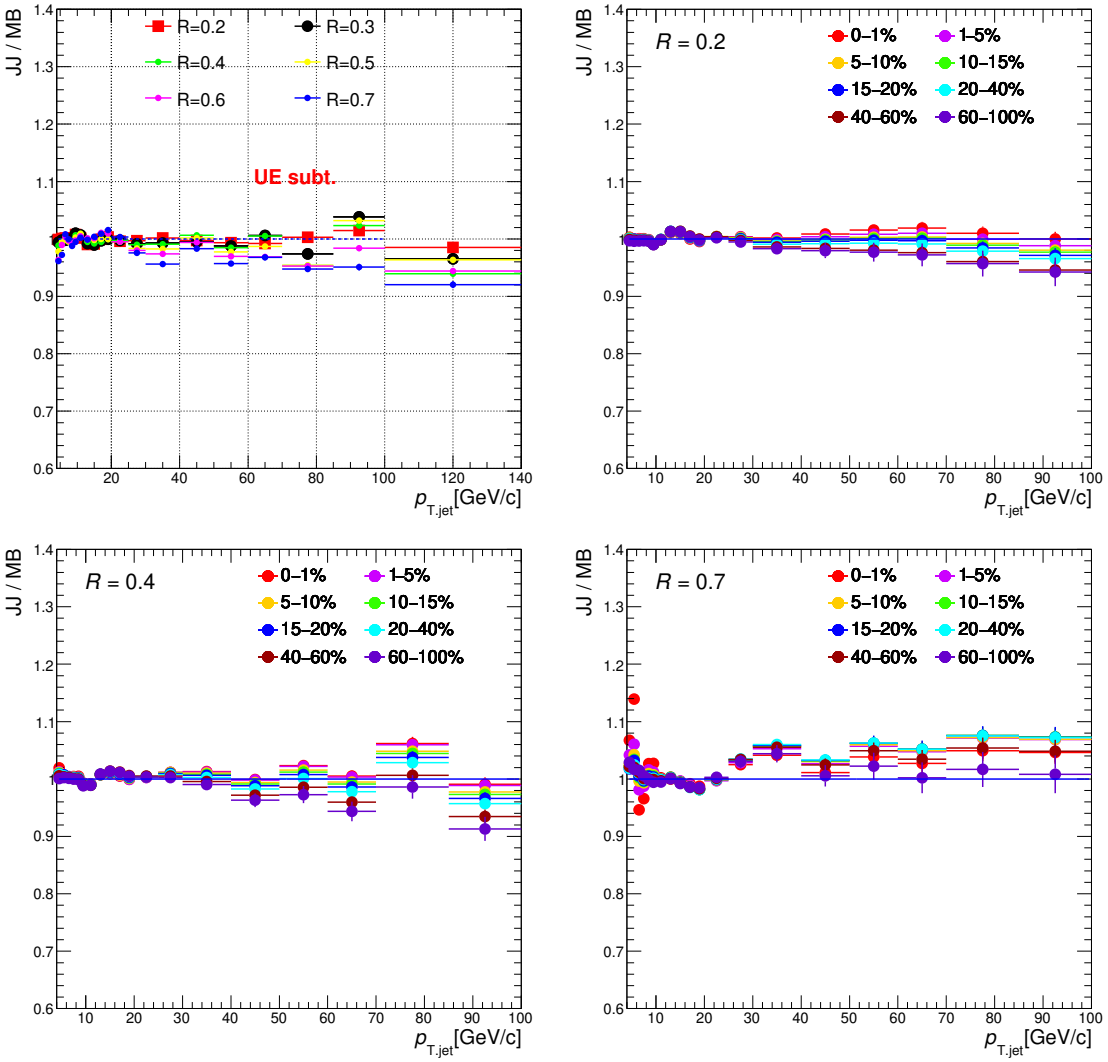

Figure 4.17: Ratio of data corrected spectra from different response matrix between MB and jet-jet $p_{T,hard}$ MC production. First panel: Inclusive jet rations from jet-jet $p_{T,hard}$ response matrix to MB matrix; Other panels: Ratios in different multiplicity percentiles for $R = 0.2, 0.4, 0.7$.

to be the best and unique choice like the background correction method. Systematic uncertainties are calculated to account for different possible configurations and parameter settings.

We used a simple approach to calculate these uncertainties on a bin-by-bin basis. The procedure works as follows: first we will choose the tunable parameters. A given parameter configuration is then defined to provide the baseline result. This particular choice is the one considered to be the optimal and least biased choice. Next, for every tunable parameter, a reasonable variation is defined. The parameter can be a number, e.g. the tracking efficiency, or a method like the unfolding algorithm. For some parameters, more than one variation is taken into account. The measured distribution is recalculated for every varied tunable parameter, one at a time. Finally, those measurements are compared to the baseline result and the deviations are taken as the uncertainty $\Delta^{i}_{\mathrm{sys}}(x)$, where i specifies the changed parameter and x the bin. In case that more than one parameter was tested, the higher uncertainty or a mean value is selected, depending on the analysis parameter.

A drawback of this bin-by-bin calculation is that potentially also statistical fluctuations contribute to the systematic uncertainties. To get a smooth estimate, for some parameters the uncertainty performs a smooth fit. Also, for some parameters, one mean value is taken as uncertainty. Examples are the uncertainties of the unfolding corrections that come from several correlated sources. Therefore, the uncertainty of the unfolding category is calculated by varying each source and calculating the RMS of all variations.

Then, all systematic uncertainty categories were treated separately and their respective contributions we added in quadrature, as written in Equation 4.7:

$$\Delta^{\mathrm{tot}}_{\mathrm{sys}}(x) = \sqrt{\sum_{i} \Delta^{i}_{\mathrm{sys}}(x)^2} \tag{4.7}$$

Note that this equation implicitly assumes uncorrelated uncertainties. This assumption is based on the fact that the degree of correlation of the single uncertainties is unknown.

In this analysis, the main tunable parameters we consider are the following:

- Tracking efficiency
- Tracking resolution
- Underlying event fluctuation (δp_{T})
- Unfolding
    - Unfolding closure test

- Choice of regularization parameter
- Choice different prior by changing event generator
- Choice different p_{T} binning (truncation)
- Choice different unfolding methods

- Contamination from secondary charged particles
- Cross section normalization (inclusive analysis only)
- Multiplicity estimation (multiplicity analysis only)

4.5.1 Systematic uncertainty: Tracking efficiency and resolution

The measured jet spectra are corrected for tracking efficiency and momentum resolution during the unfolding. To propagate the uncertainty on the single track efficiency to the jet spectrum measurement, we can use a full production simulation to estimate this systematic uncertainty.Using fast simulation to estimate the systematic uncertainty on tracking momentum resolution, while using full production to estimate the systematic uncertainty on tracking efficiency.

The tracking-efficiency uncertainty on the measured jet spectra is estimated by modifying the response matrix used in the unfolding procedure via random rejection of a given fraction of tracks prior to jet finding, with the fraction corresponding to the uncertainty of the single-track efficiency. The single-track efficiency and its corresponding uncertainty is the combination of two contributions. The first contribution originates from the track selection criteria in the TPC. The second contribution originates from the matching of TPC tracks to the ITS hits. The single-track efficiency uncertainty is approximately 3% in pp collisions, its value is approximately 6% for tracks with $p_{\mathrm{T}} = 1$ GeV/c, decreasing to approximately 3% for tracks with $p_{\mathrm{T}} = 15$ GeV/c and above. The difference between the spectra corrected with the default response matrix and with the modified response matrix obtained with the tracking efficiency reduction is taken as a systematic uncertainty. The relative uncertainty on tracking efficiency increases slowly with increasing jet p_{T} and it has a weak multiplicity dependence. The systematic uncertainty from the tracking uncertainty for different jet radius is shown in Fig. 4.18 and Fig. 4.19. For the inclusive jet resolution parameter 0.2 (0.7) the uncertainty is 2.6% (3.9%) at $p_{\mathrm{T}} = 6$ GeV/c and increases gradually to 6.9% (10.6%) at $p_{\mathrm{T}} = 100$ GeV/c.

The fast simulation allows us to systematically vary detector resolution within the systematic uncertainties, in order to propagate the uncertainties on the simulated detector resolution through the unfolding to the corrected jet spectra. The relative systematic uncertainty on track momentum resolution is estimated from the study of the invariant mass distributions of Λ and $\mathrm{K}^0_{\mathrm{s}}$ as a function of p_{T} and amounts to 20%. We unfold the data with the nominal and varied response matrices and use the resulting differences in

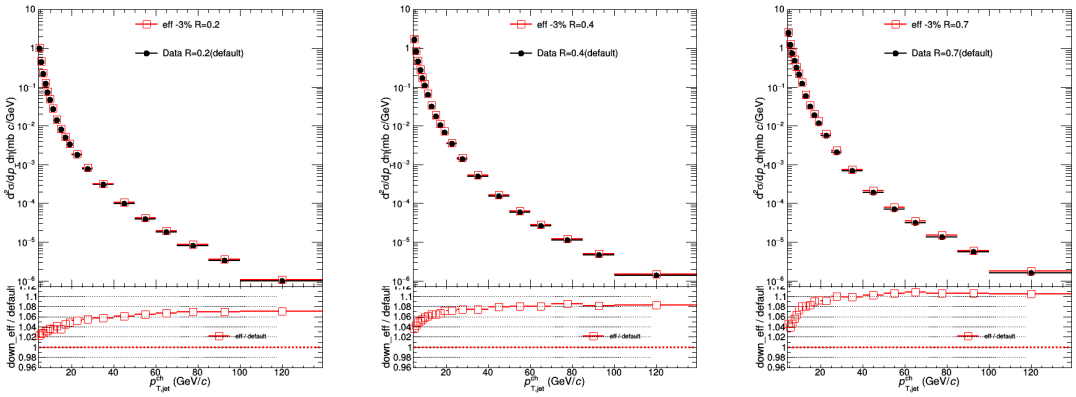

Figure 4.18: Systematic uncertainty from track efficiency on inclusive jet p_T for different jet cone $R = 0.2$ (left), $R = 0.4$ (middle) and $R = 0.7$ (right).

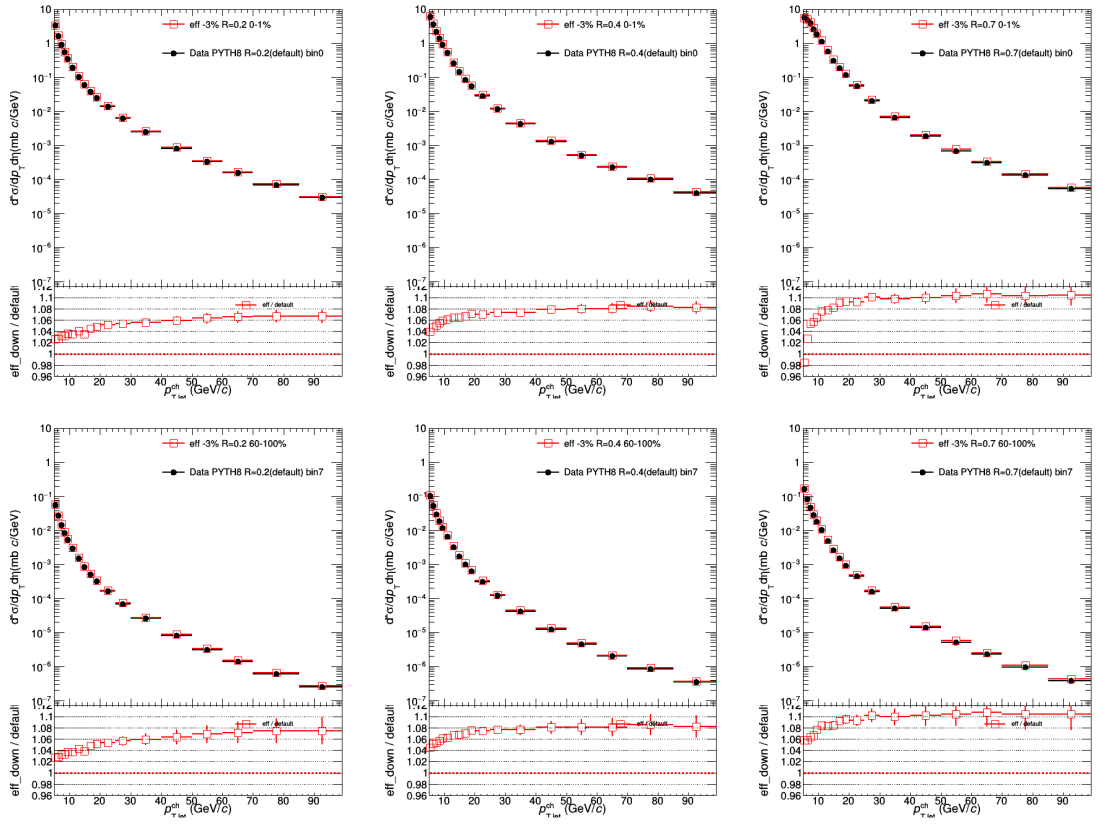

Figure 4.19: Systematic uncertainty from track efficiency on jet p_T in different multiplicity classes for jet cone $R = 0.2$ (left), $R = 0.4$ (middle) and $R = 0.7$ (right), top row is 0–1%, bottom row is 60–100%.

the unfolded spectra to assign systematic uncertainties. Since the statistics is limited, we fitted the difference ratio and extended the p_{T} to the high ranges. The systematic uncertainty from p_{T} resolution is of the order of 2%, show in Fig. 4.20 and Fig. 4.21.

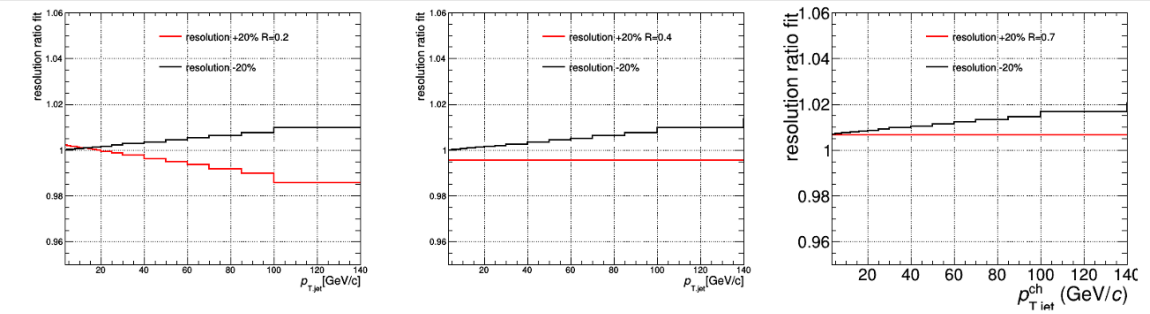

Figure 4.20: Systematic uncertainty from track momentum resolution on inclusive jet p_{T} for different jet radii R = 0.2, 0.4, 0.7.

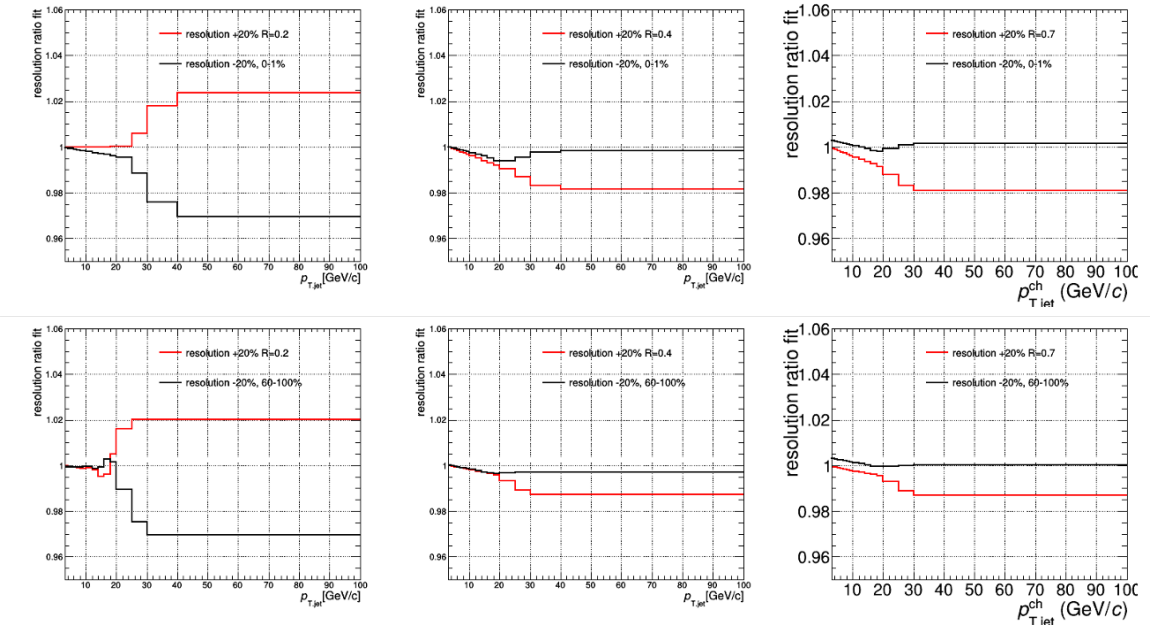

Figure 4.21: Systematic uncertainty from track momentum resolution on jet p_{T} in different multiplicity classes for jet cone R = 0.2 (left), R = 0.4 (middle) and R = 0.7 (right), top row is 0–1%, bottom row is 60–100%.

4.5.2 Systematic uncertainty: Unfolding

There are several sources contributed to unfolding uncertainty, the choice different unfolding methods, the unfolding closure, the different regularization parameters, the bin truncations and the prior spectrum from different MC models. The unfolding closure test is discussed in Section 4.4, and the systematic

uncertainty is directly taken from the refolded closure ratios in Figures 4.15 and 4.16. The other sources for unfolding uncertainty is discussed below in details.

Choice of unfolding methods

As a cross-check and validation of the unfolded results, we compare our results for SVD unfolding with the results obtained with the Bayes method as implemented in RooUnfold. The ratio of spectra unfolded with the Bayes method for different choices of the regularization parameter to the default (SVD) is shown in Fig. 4.22 and Fig. 4.23. Fig. 4.22 is the inclusive jet p_{T} systematic uncertainty, Fig. 4.23 is multiplicity dependent jet systematic uncertainties (0–1% and 60–100%). Within uncertainties, the solutions from both unfolding methods are in excellent agreement. To smoothen statistical fluctuations in the determination of the systematic error, we fit bin-by-bin the absolute deviation from 3 to 50 GeV/c with a constant fit, to obtain the systematic uncertainty with full p_{T} range.

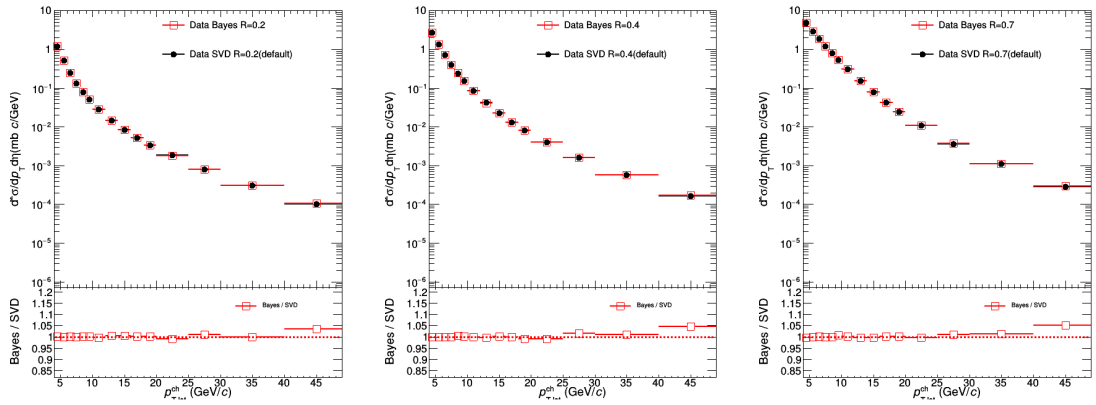

Figure 4.22: Systematic uncertainty from unfolding methods on inclusive jet p_{T} for different jet cone $R = 0.2$ (left), $R = 0.4$ (middle) and $R = 0.7$ (right).

Choice of regularization parameter

SVD unfolding is regularized by the choice of an integer valued parameter which separates statistically significant and insignificant Singular Values of the orthogonalized response matrix. The choice is made via inspection of the 'd-vector', but this approach is not unambiguous. To estimate the related systematic uncertainties, we vary the regularization parameter by ±2 . The resulting variations are shown in Fig 4.24 and Fig 4.25, Fig 4.24 is the inclusive jet p_{T} systematic uncertainty, Fig 4.25 is multiplicity dependent jet systematic uncertainties (0–1% and 60–100%), We observe differences of the order of 1–2%.

Choice of event generator

In this section we discuss the uncertainties related to the choice of the MC event generator used to change the initial guess prior. We used the prior from EPOSLHC generator (LHC17d20b2 MC sample)

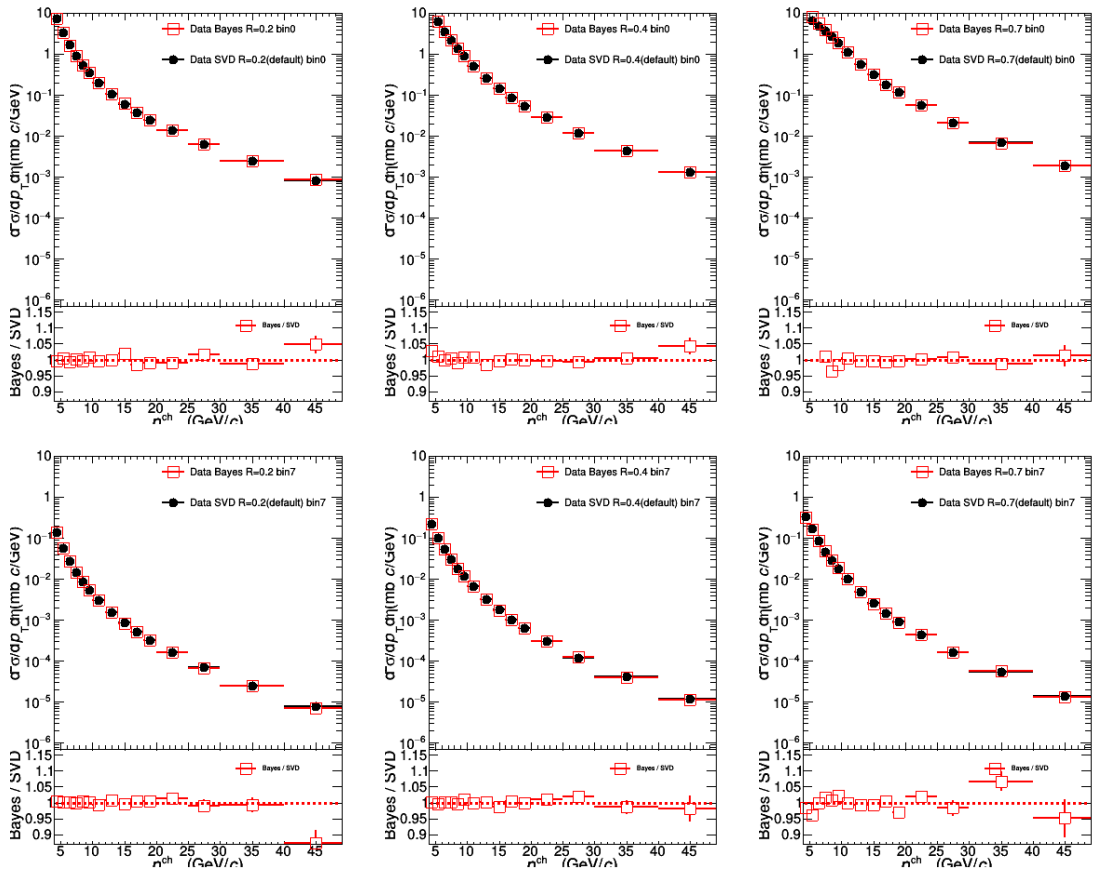

Figure 4.23: Systematic uncertainty from unfolding method on jet p_{T} in different multiplicity classes for jet cone $R = 0.2$ (left), $R = 0.4$ (middle) and $R = 0.7$ (right), top row is 0–1%, bottom row is 60–100%.

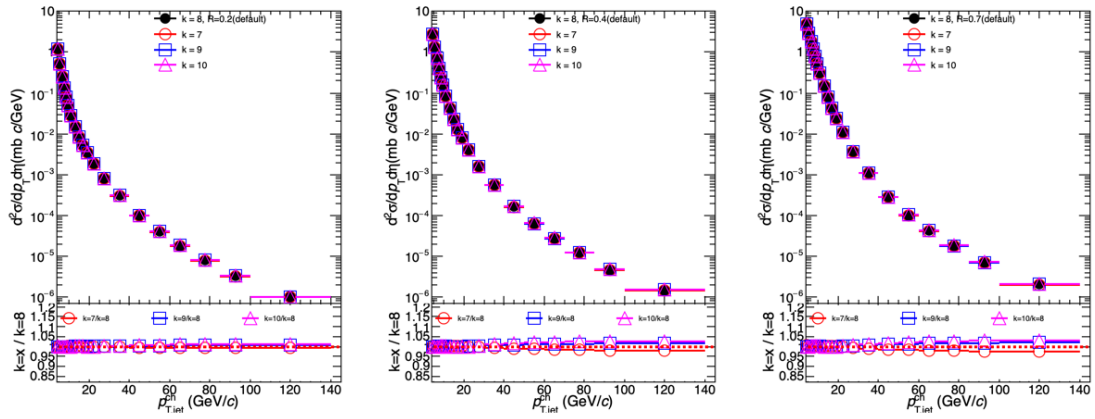

Figure 4.24: Systematic uncertainty from unfolding regularization parameter on inclusive jet p_{T} for different jet cone $R = 0.2$ (left), $R = 0.4$ (middle) and $R = 0.7$ (right).

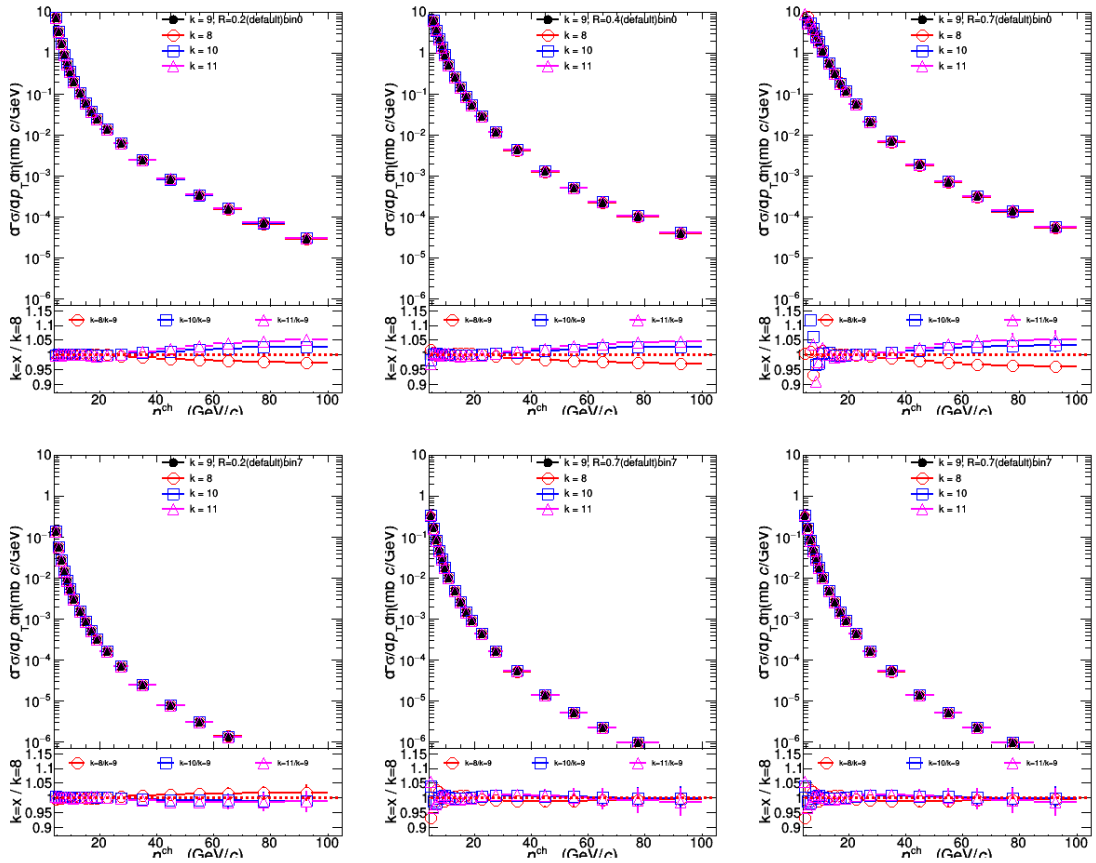

Figure 4.25: Systematic uncertainty from unfolding regularization parameter on jet p_{T} in different multiplicity classes for jet cone $R = 0.2$ (left), $R = 0.4$ (middle) and $R = 0.7$ (right), top row is 0–1%, bottom row is 60–100%.

to simulate the data and got the unfolded results. Compare the unfolded spectra using the prior from default generator (PYTHIA8) with those obtained from EPOS generator with LHC tune, using the ratio to estimate the uncertainty. The resulting uncertainties are of the order of 3%, as shown in Fig. 4.26 and Fig. 4.27.

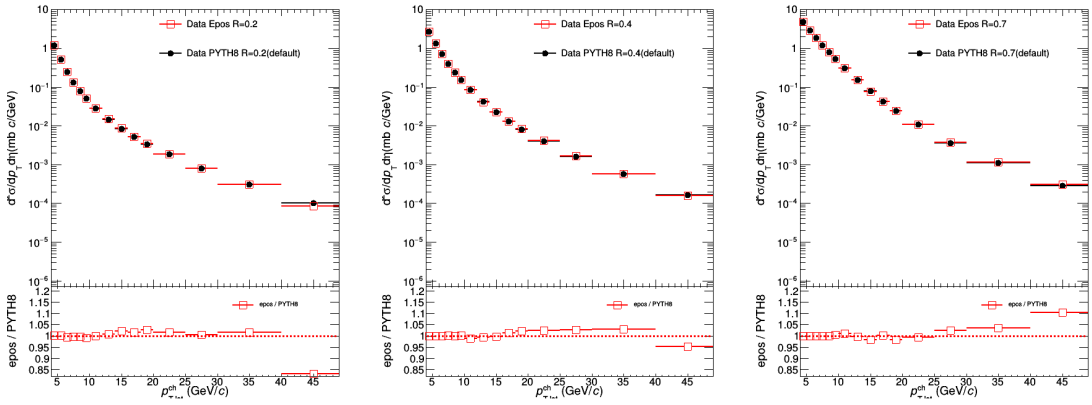

Figure 4.26: Systematic uncertainty from unfolding prior on inclusive jet p_{T} for different jet cone $R = 0.2$ (left), $R = 0.4$ (middle) and $R = 0.7$ (right).

Choice different p_{T} binning

The unfolded p_{T} range is set to be wider than measured p_{T} range to cover the feed-in and feed-out of the measured p_{T} range. The reference analysis uses the following binning of the input raw jet p_{T} spectra $\{0, 1, 2, 3, 4, 5, 6, 7, 8, 9, 10, 12, 14, 16, 18, 20, 25, 30, 40, 50, 60, 70, 85, 100, 140, 200\}$ GeV/c.
We changes the default the p_{T} range of the unfolded jet spectrum varied to lower and higher value for the upper limit and lower limit as shown in Fig. 4.28 and Fig. 4.29 for inclusive jet production and multiplicity dependent jet yield for different jet radii. This variation has very small impact to unfolded spectrum.

The total systematic uncertainty of the unfolding is evaluated from the contributions due to the choice of the unfolding MC closure test, unfolding prior, different p_{T} binning, the variation of the regularization parameter, and the event generator dependence. Finally, the systematic uncertainty due to unfolding is obtained for each bin in jet p_{T} using the Root Mean Square (RMS) method by $\delta^{\mathrm{tot}}_{\mathrm{sys}}(x) = \sqrt{\sum_{i=1}^{N} \delta^{i}_{\mathrm{sys}}(x)^2/N}$, $N = 5$.

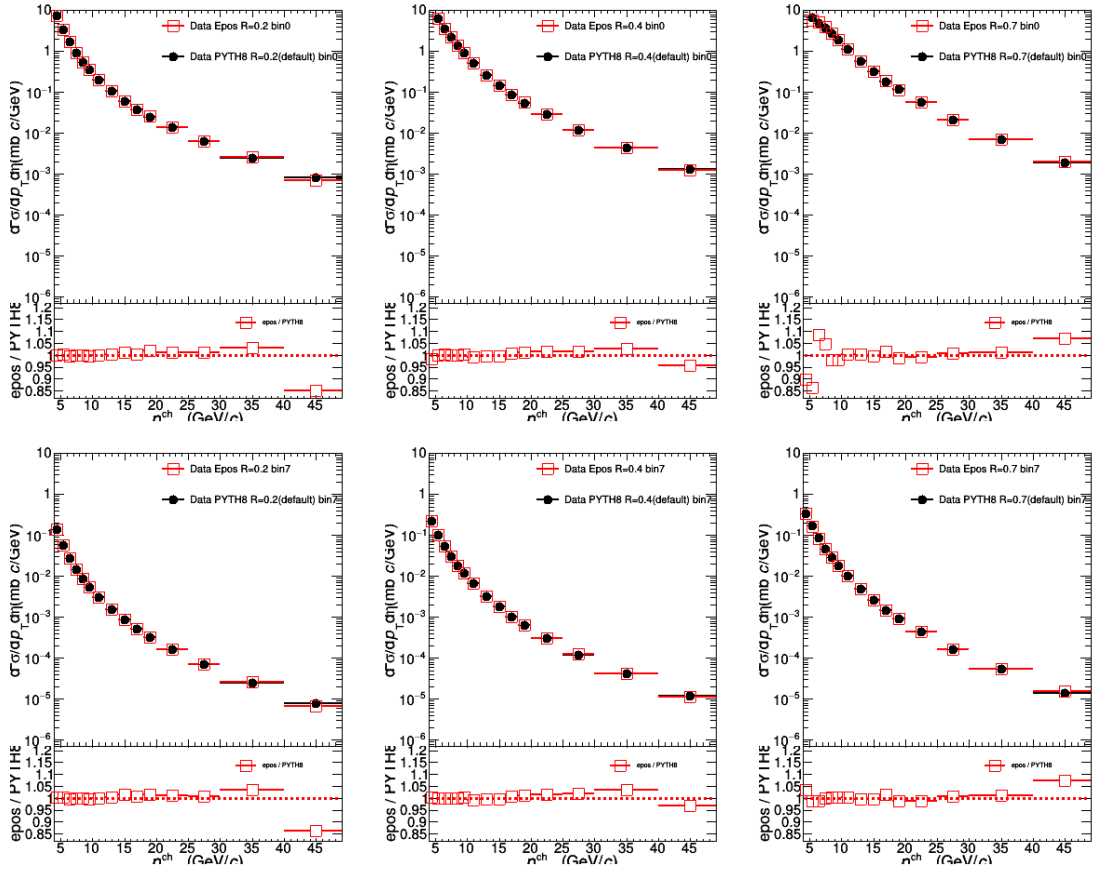

Figure 4.27: Systematic uncertainty from unfolding prior on jet p_T in different multiplicity classes for jet cone R = 0.2 (left), R = 0.4 (middle) and R = 0.7 (right), top row is 0–1%, bottom row is 60–100%.

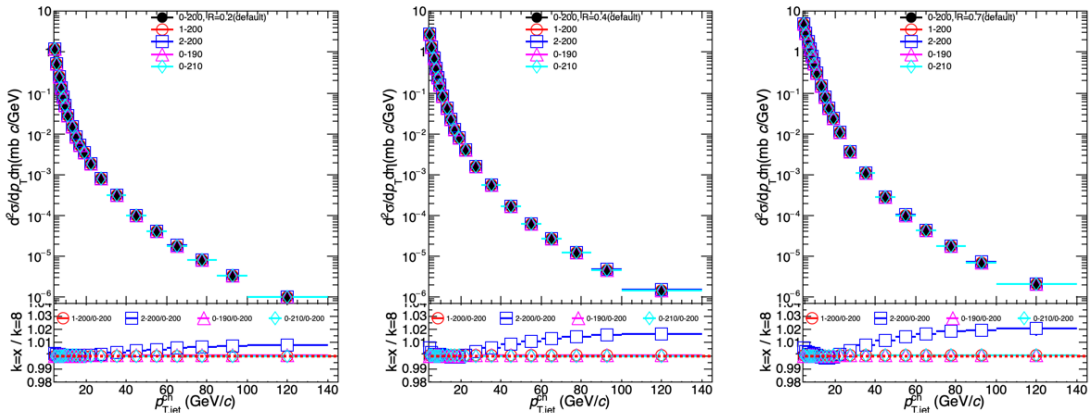

Figure 4.28: Systematic uncertainty from unfolding p_T binning on inclusive jetp_T for different jet cone R = 0.2 (left), R = 0.4 (middle) and R = 0.7 (right).

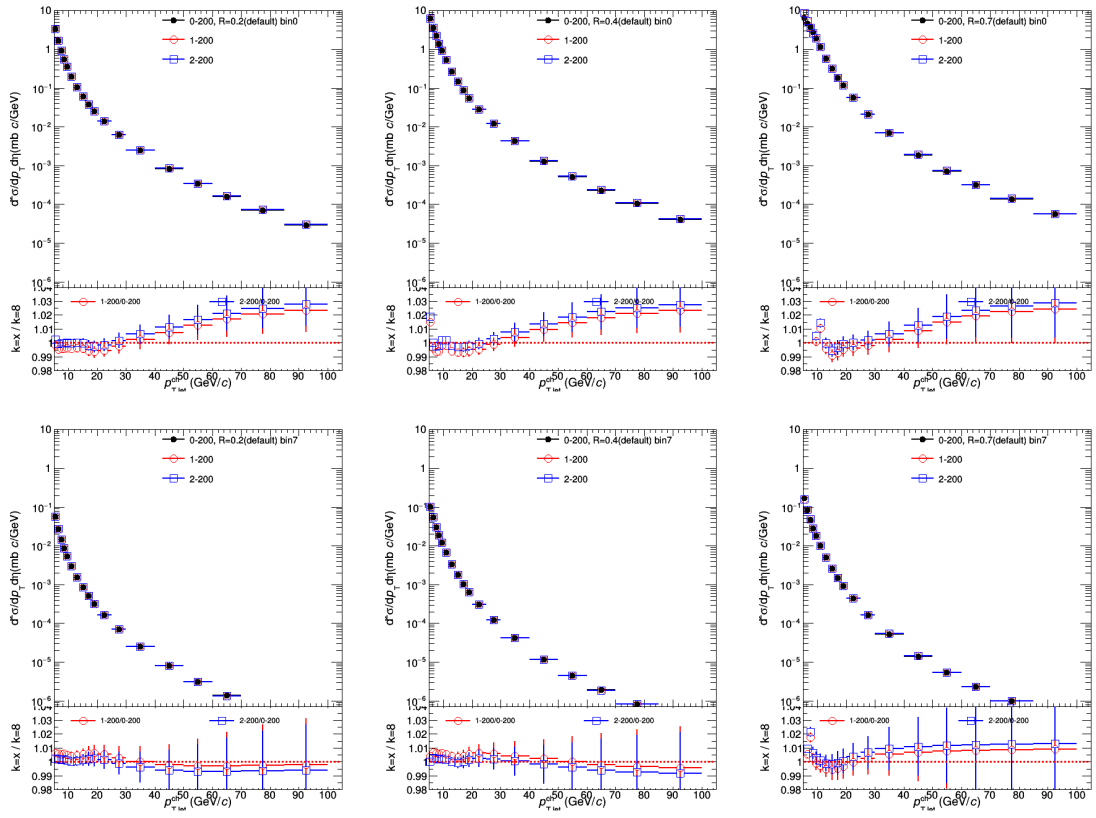

Figure 4.29: Systematic uncertainty from unfolding p_{T} binning on jet p_{T} in different multiplicity classes for jet cone $R = 0.2$ (left), $R = 0.4$ (middle) and $R = 0.7$ (right), top row is 0–1%, bottom row is 60–100%.

4.5.3 Systematic uncertainty: contamination from secondary charged particles

Secondary charged particles are mostly produced by weak decays of strange particles (K^0_s, Λ, etc.), photon conversions, hadronic interactions in the detector material, and decays of charged pions. Conversion and hadronic interaction products are not part of the jet fragmentation. Neutral strange particles stem from fragmentation, but are not relevant for our analysis of charged particle fragmentation. Their decay products are considered a contamination to our measurement.

We estimate the uncertainty on the secondaries contribution to correspond to a jet transverse momentum scale uncertainty of 0.5%, using the same value as in the run1 pp charged jet analysis [27]. To propagate this uncertainty to the measured cross section, we use a fit with two modified Tsallis functions:

$$f(x) = (p_2 + p_3 * x)(1 + \frac{x}{p_0 * p_1})^{(-p_1)} + (p_6 + p_7 * x)(1 + \frac{x}{p_4 * p_5})^{(-p_5)}$$

The result of this fit and the ratio of the data to the fit are shown in Fig. 4.30 to Fig. 4.33 for different jet radii (the open black marker is the ratio of the data to the fit). For various choices of R, the fit function gives a generally consistent description of the spectra at low p_{T}. To evaluate the impact of the scale uncertainty on the jet cross section, we use the two-Tsallis fit, shift the argument of the fit function by 0.5% and use the observed variation of the spectrum as systematic error. The original and shifted fit functions are also shown in Fig. 4.30 to Fig. 4.33. The resulting systematic uncertainty is about 3%, with a slight rise as function of jet p_{T}, you can the red and magenta lines in ratio panel of Fig. 4.30 to Fig. 4.33.

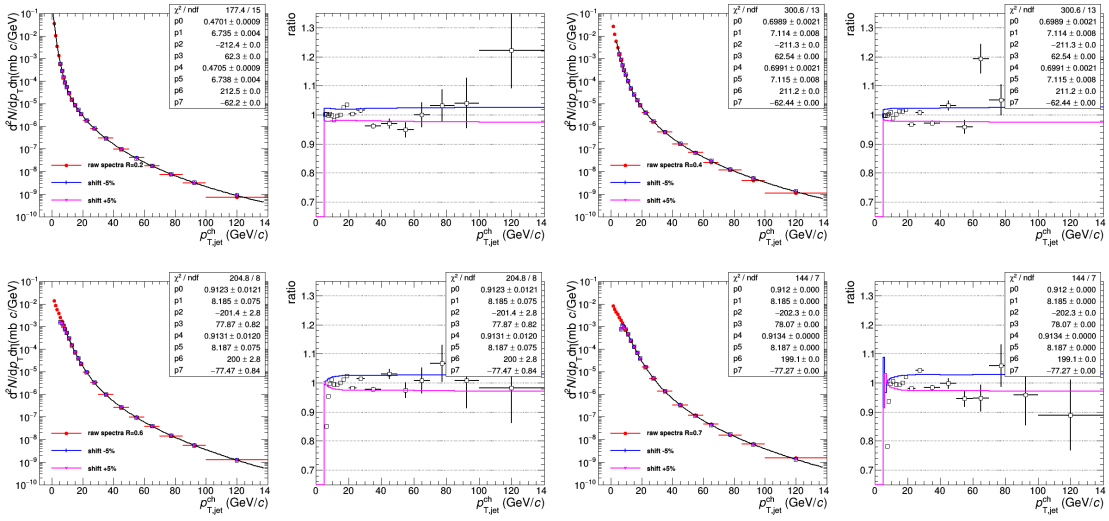

Figure 4.30: Raw inclusive jet spectra fitted with a sum of two Tsallis functions for different jet radii $R = 0.2 - 0.7$.

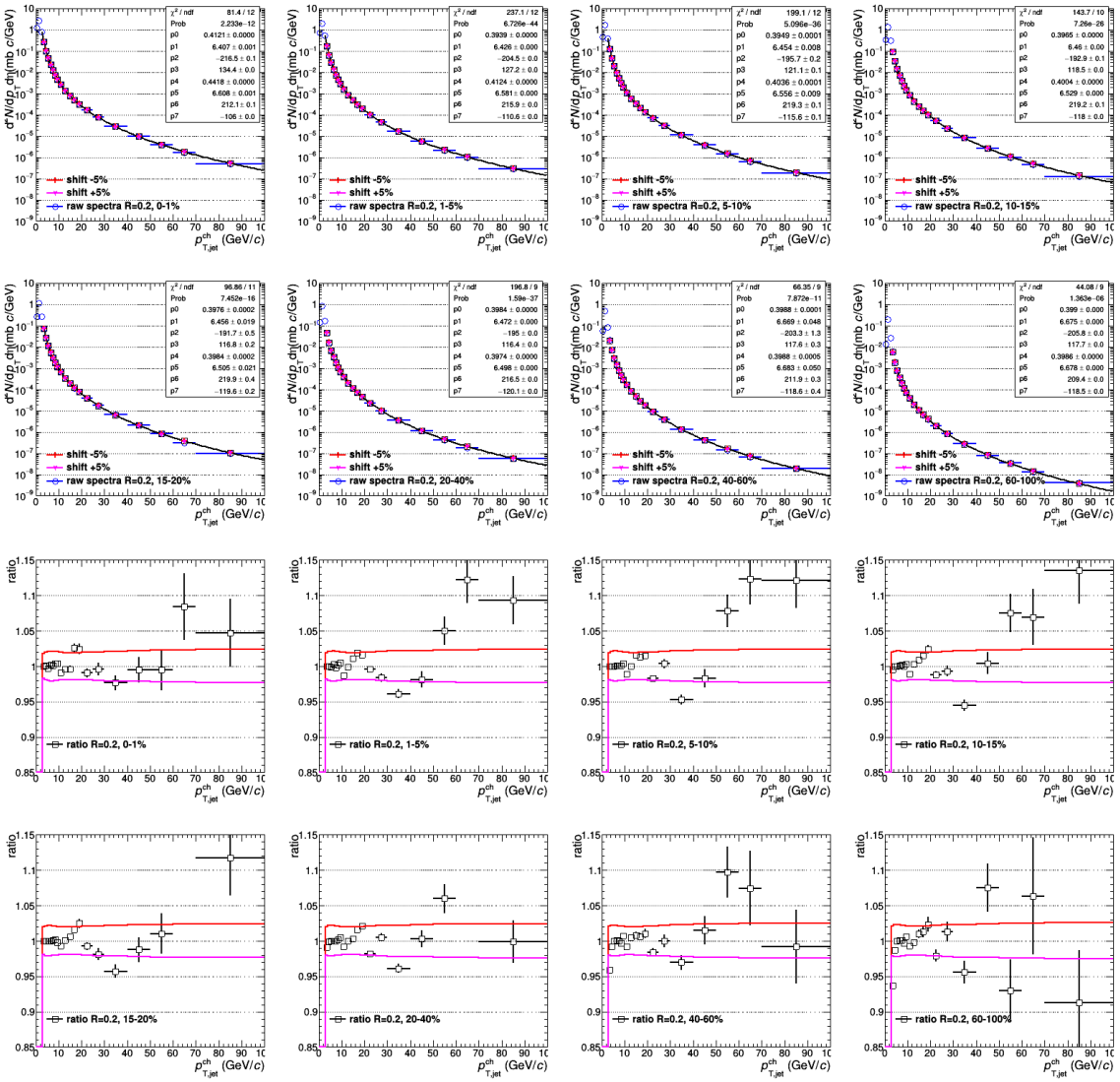

Figure 4.31: Raw jet spectra fitted with a sum of two Tsallis functions for $R = 0.2$ in different multiplicity classes.

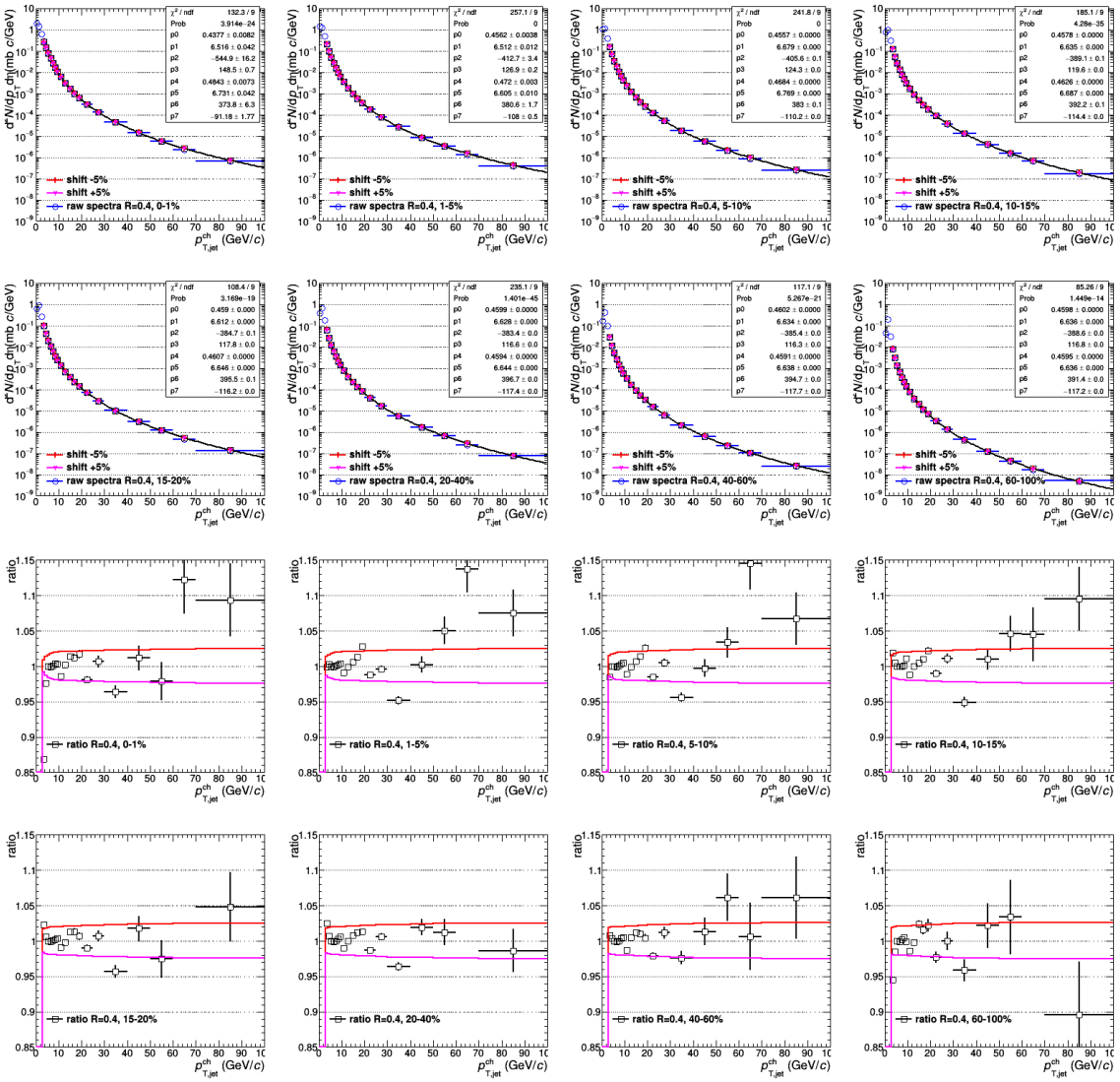

Figure 4.32: Raw jet spectra fitted with a sum of two Tsallis functions for $R = 0.4$ in different multiplicity classes.

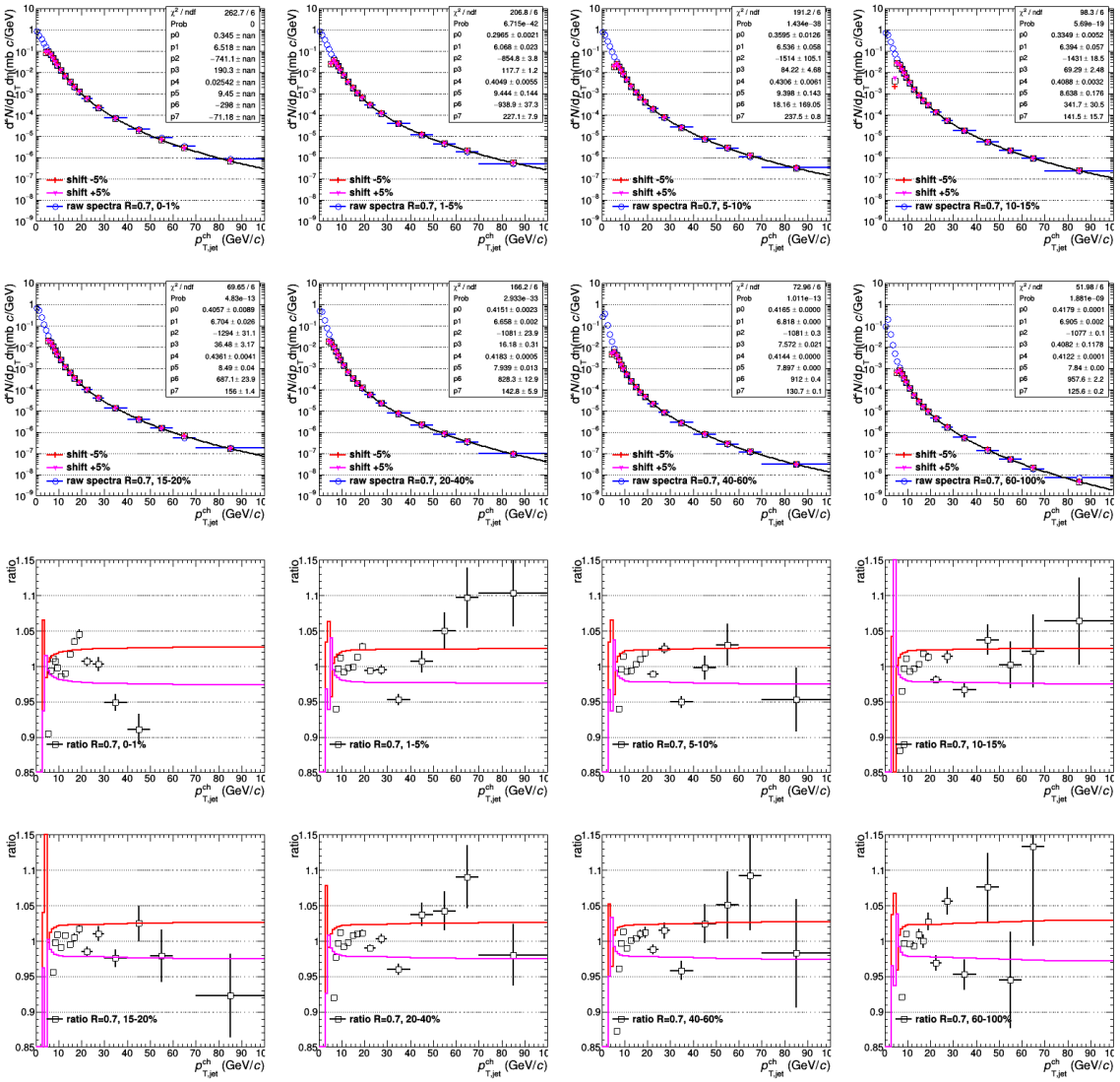

Figure 4.33: Raw jet spectra fitted with a sum of two Tsallis functions for $R = 0.7$ in different multiplicity classes.

4.5.4 Systematic uncertainty: underlying event subtraction

The systematic uncertainty due to background fluctuation estimation is quantified by comparing background responses constructed from δp_{T} distributions using the RC method without two leading jets and the track embedding method as shown in Fig. 4.3 to Fig. 4.6 of Section 4.3. The default background response is obtained by the RC method by excluding two leading jets. The difference on the corrected jet spectrum obtained from the default method and the track embedding method is assigned as background fluctuation uncertainty, as shown in Fig. 4.34 and Fig. 4.35. Fig. 4.34 is inclusive jet results and Fig. 4.35 is multiplicity dependent distributions, which are highest at low p_{T}.

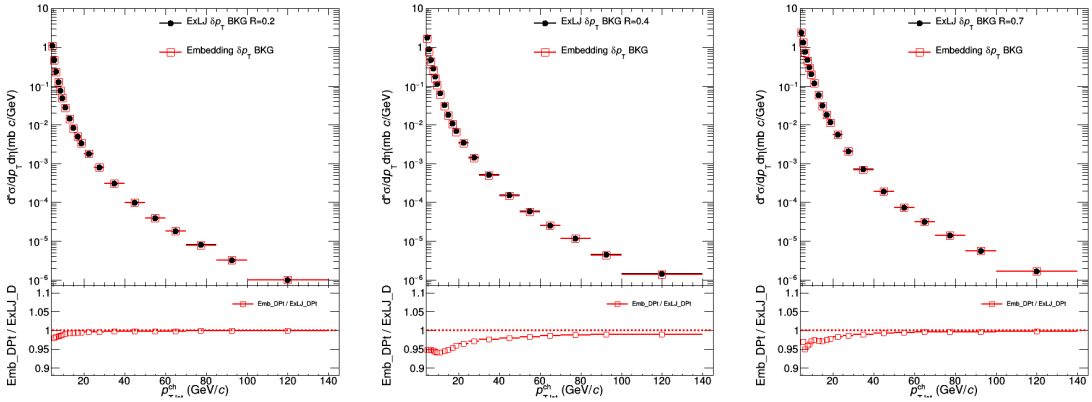

Figure 4.34: Systematic uncertainty from background fluctuation on inclusive jet p_{T} for different jet cone $R = 0.2$ (left), $R = 0.4$ (middle) and $R = 0.7$ (right).

4.5.5 Systematic uncertainty: multiplicity estimation

Because the PYTHIA MC event generator fails to reproduce the measured multiplicity distribution as shown in Fig. 2.3, which is mainly attributed to a limited description of the UE, the multiplicity percentile is determined from the V0M amplitude in data as listed in Table 4.2. During unfolding, the background fluctuation response matrix is directly estimated from data as shown in Fig. 4.3 to Fig. 4.6 for inclusive and each event multiplicity class. Regarding the detector response, it is calculated from MB events (0–100%) generated by PYTHIA MC. To account for the multiplicity estimation uncertainty, a response matrix obtained from pure MC simulation is used, where the multiplicity intervals and the background fluctuations, as shown in Fig. 4.36, are both determined by PYTHIA. The combined response matrix as shown in the right side of Fig. 4.37 for different jet radii $R = 0.2, 0.4, 0.7$ with $(0-1)\%$ and $(60-100)\%$ multiplicity event classes [$R = 0.2$, $(0-1)\%$, $R = 0.4$, $(0-1)\%$, $R = 0.7$, $(0-1)\%$ and $R = 0.7$, $(60-100)\%$]. The corrected spectrum using this pure MC response matrix in different multiplicity intervals is then compared to the one obtained from data-based background response matrix, as shown in Fig. 4.13. The assigned uncertainty is 5.7% for low p_{T} jets in the highest multiplicity class,

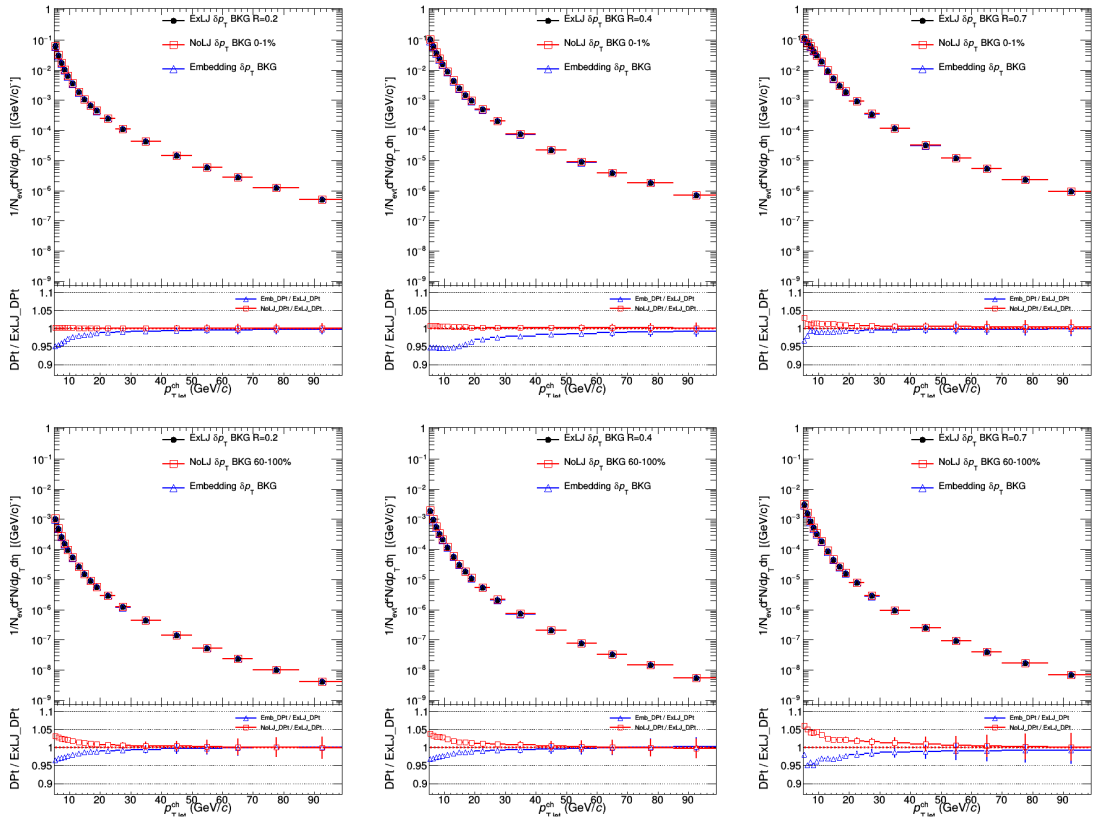

Figure 4.35: Systematic uncertainty from background fluctuation on jet p_{T} in different multiplicity classes for jet cone $R = 0.2$ (left), $R = 0.4$ (middle) and $R = 0.7$ (right), top row is 0–1%, bottom row is 60–100%.

and decreases in the lower multiplicity percentile. The uncertainty is independent of the jet R since the multiplicity estimation is at the event level. We choose multiplicity dependence MC response matrix (pure MC response matrix) to perform data unfolding as systematic uncertainty, as shown in Fig. 4.38.

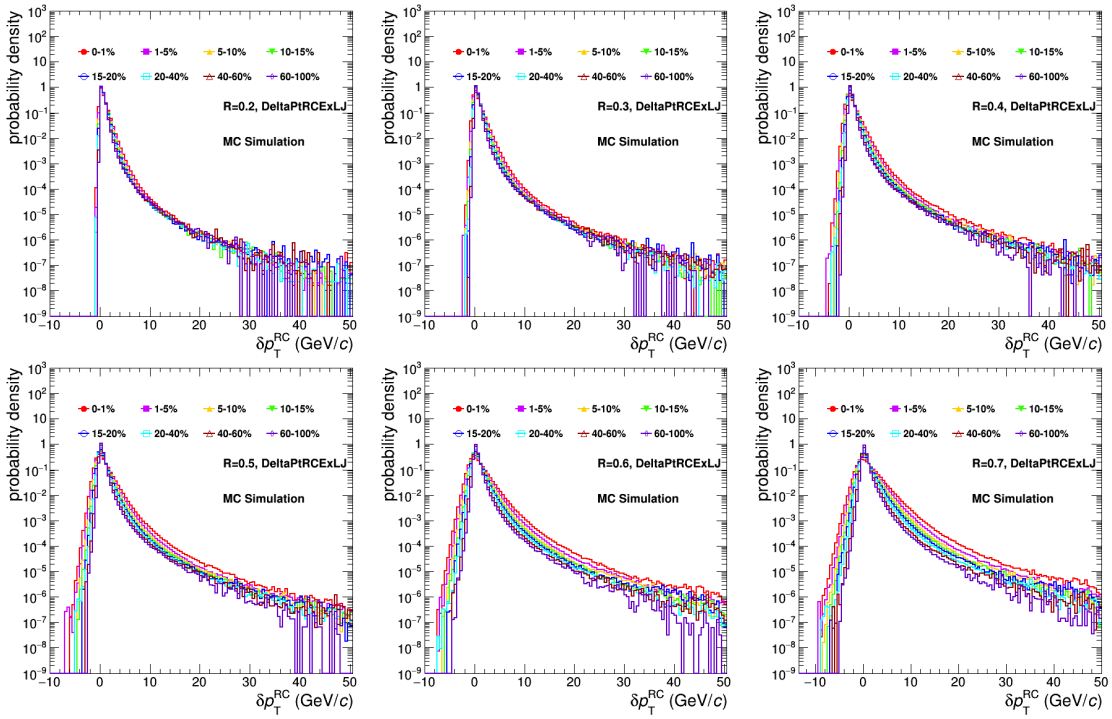

Figure 4.36: Two leading jets removed δp_T distributions using RC method in different multiplicity classes from MC simulation with $R = 0.2 - 0.7$.

4.5.6 Cross section normalization

In the inclusive jet analysis, we normalize the measured jet spectra per event and multiply with the measured visible inelastic cross section, as shown in equation 4.8:

$$\frac{\mathrm{d}^2\sigma^{\text{ch jet}}}{\mathrm{d}p_T\mathrm{d}\eta}(p_T^{\text{ch jet}}) = \frac{1}{\mathcal{L}_{\text{int}}}\frac{\Delta N_{\text{jets}}}{\Delta p_T \Delta\eta}(p_T^{\text{ch jet}}) = \frac{\epsilon_{\text{vertex eff}}\cdot\sigma_{\text{V0}}}{N_{\text{ev}}}\frac{\Delta N_{\text{jets}}}{\Delta p_T\Delta\eta}(p_T^{\text{ch jet}}) \tag{4.8}$$

For the normalization, we use the number of Minimum Bias events selected by the trigger after physics selection, vertex quality cuts and z-Vertex cut, as shown in Fig. 4.39. The number of events is divided by the efficiency of the vertex requirement, since all events with a jet in the TPC acceptance also should have a vertex, and correspondingly events rejected by this cut have no jet. The efficiency is evaluated before the z-Vertex cut, assuming negligible z-Vertex dependence. So the $\epsilon_{\text{vertex eff}} = \frac{N_{\text{events}}^{\text{w/vertex}}}{N_{\text{events}}^{\text{all}}} \approx \frac{2.28}{2.46} \approx 0.93$.

$$\sigma_{\text{tot}} = \frac{\sigma_{V0,16}\cdot N_{\text{evt},16} + \sigma_{V0,17}\cdot N_{\text{evt},17} + \sigma_{V0,18}\cdot N_{\text{evt},18}}{N_{\text{evt},16} + N_{\text{evt},17} + N_{\text{evt},18}} \approx 58.02 \pm 0.03\ (mb) \tag{4.9}$$

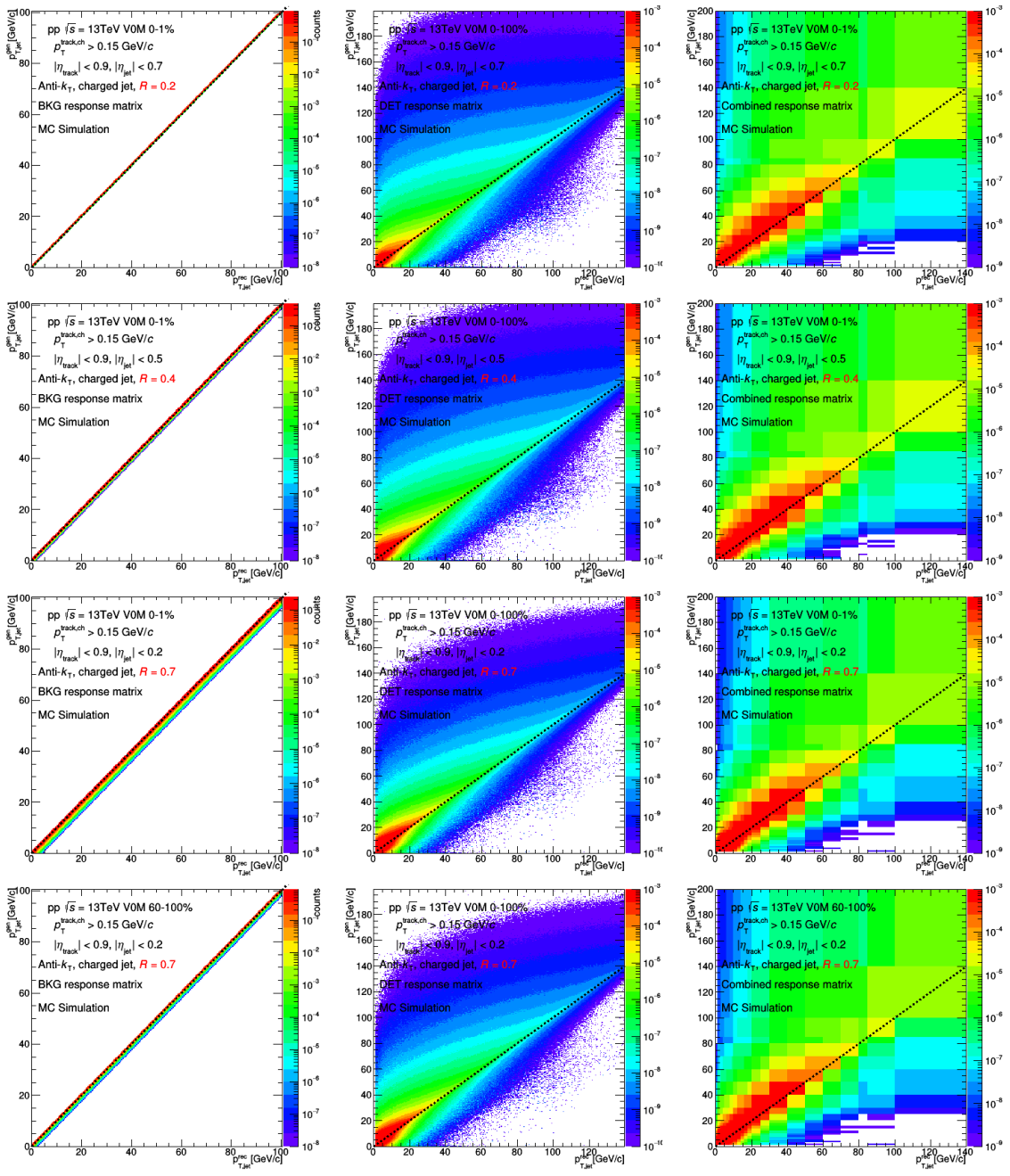

Figure 4.37: The multiplicity background, detector response (both from the MC simulation) and combined response matrices, in $(0-1)$% and $(60-100)$% multiplicity events for jet radii R = 0.2, 0.4, 0.7.

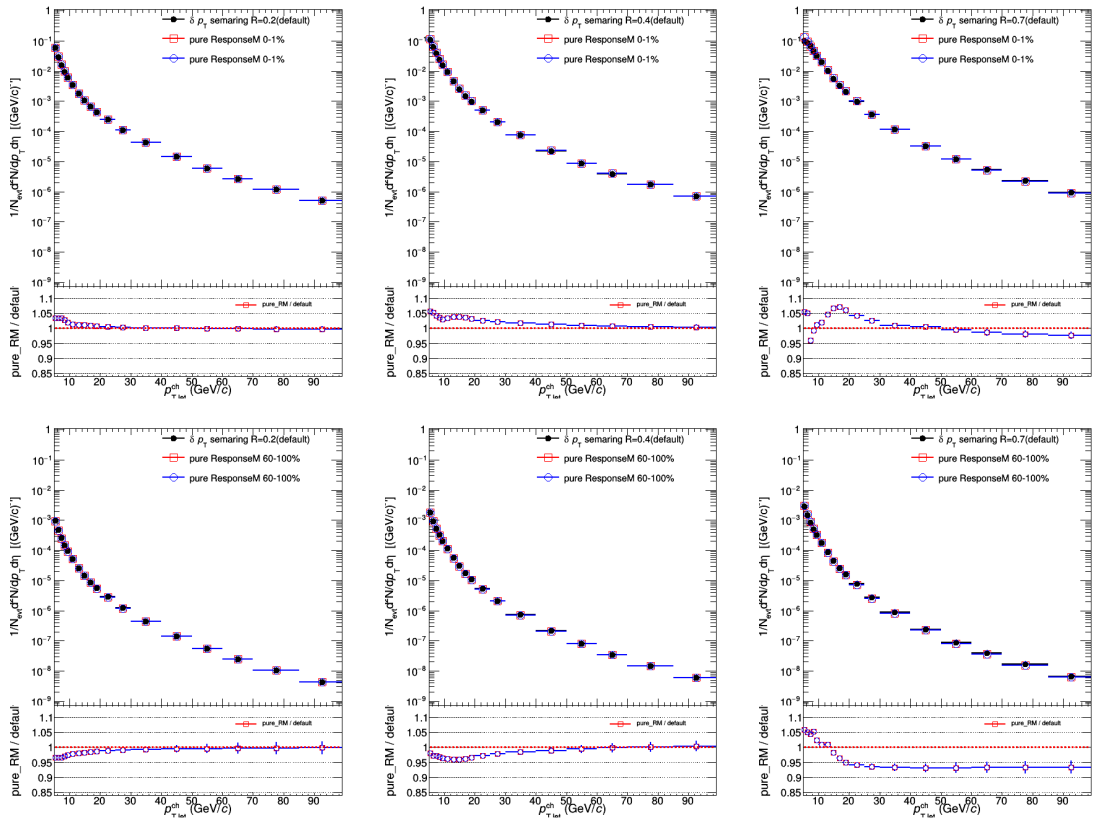

Figure 4.38: Systematic uncertainty from the different response matrix on jet p_{T} in different multiplicity classes for jet cone $R = 0.2$ (left), $R = 0.4$ (middle) and $R = 0.7$ (right), top row is 0–1%, bottom row is 60–100%.

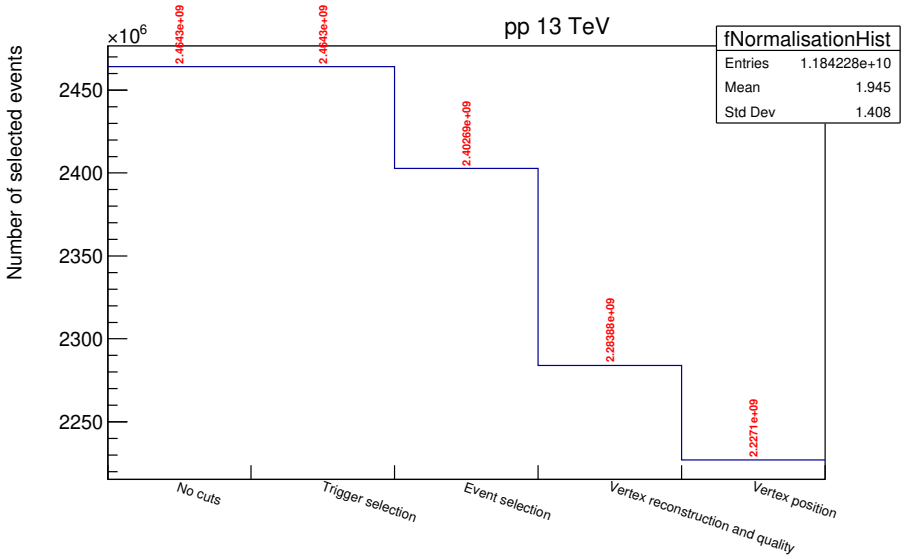

Figure 4.39: The all Minimum Bias event numbers selected by the trigger after physics selection, vertex quality cuts and z-Vertex cut.

Table 4.3: p_{T}-integrated production cross sections in pp collisions at $\sqrt{s}$ = 13 TeV.

year	2016	2017	2018
σ_{V0} (mb)	58.44 ± 0.03	58.10 ± 0.04	57.52 ± 0.03

The inelastic pp cross section for $\sqrt{s}$ = 13 TeV, as measured in VdM scans [209], is displayed in Table 4.3. We calculated the mean cross section from three years to be approximately 58.02 ± 0.03 mb (syst.), as described in Equation 4.9, corresponding to a normalization systematic uncertainty of 1.6% [209].

Finally, all systematic uncertainty categories are treated separately and their respective contributions are added in quadrature. The total systematic uncertainty for inclusive jet production is depicted in Fig. 4.40, the systematic uncertainties for multiplicity-dependent jet production are shown in Fig. 4.41. The systematic uncertainties are presented from the top-left to the bottom-right, covering multiplicity classes ranging from 0–1% to 60–100%.

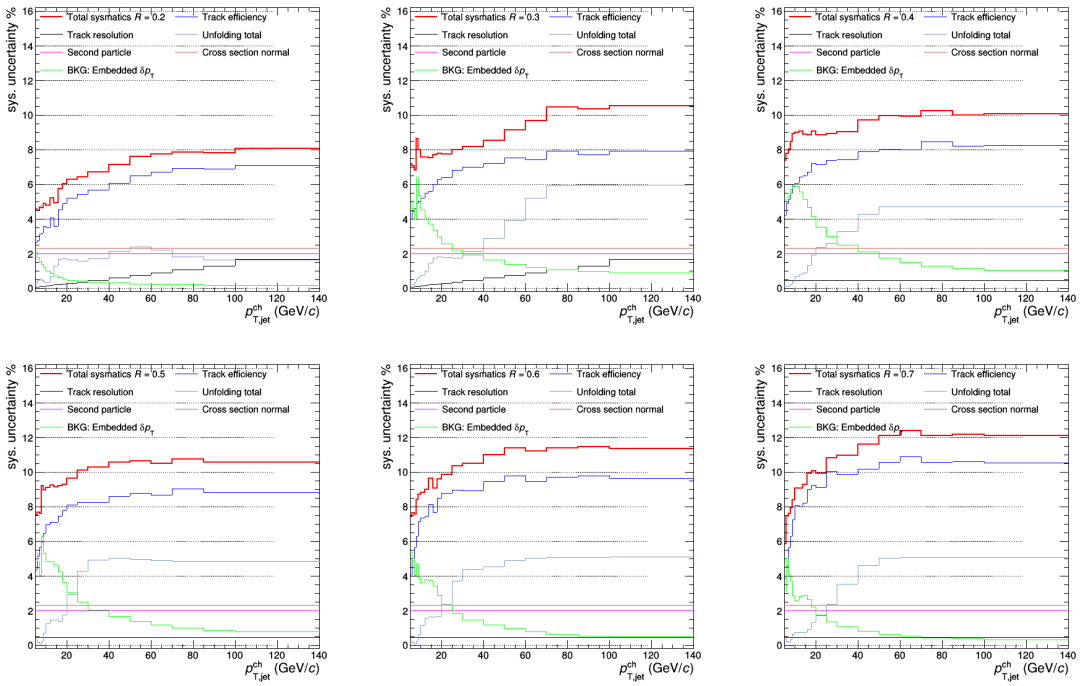

Figure 4.40: The total systematic uncertainty for inclusive jet production for R = 0.2 – 0.7.

When calculating the systematic uncertainties on the ratio of jet spectra, a given uncertainty source variation affects simultaneously both the numerator and denominator. This results in a significant reduction of the correlated uncertainties between the numerator and the denominator. The correlated uncertainties from the same source cancel out partially, while the shape uncertainties are added in quadrature.

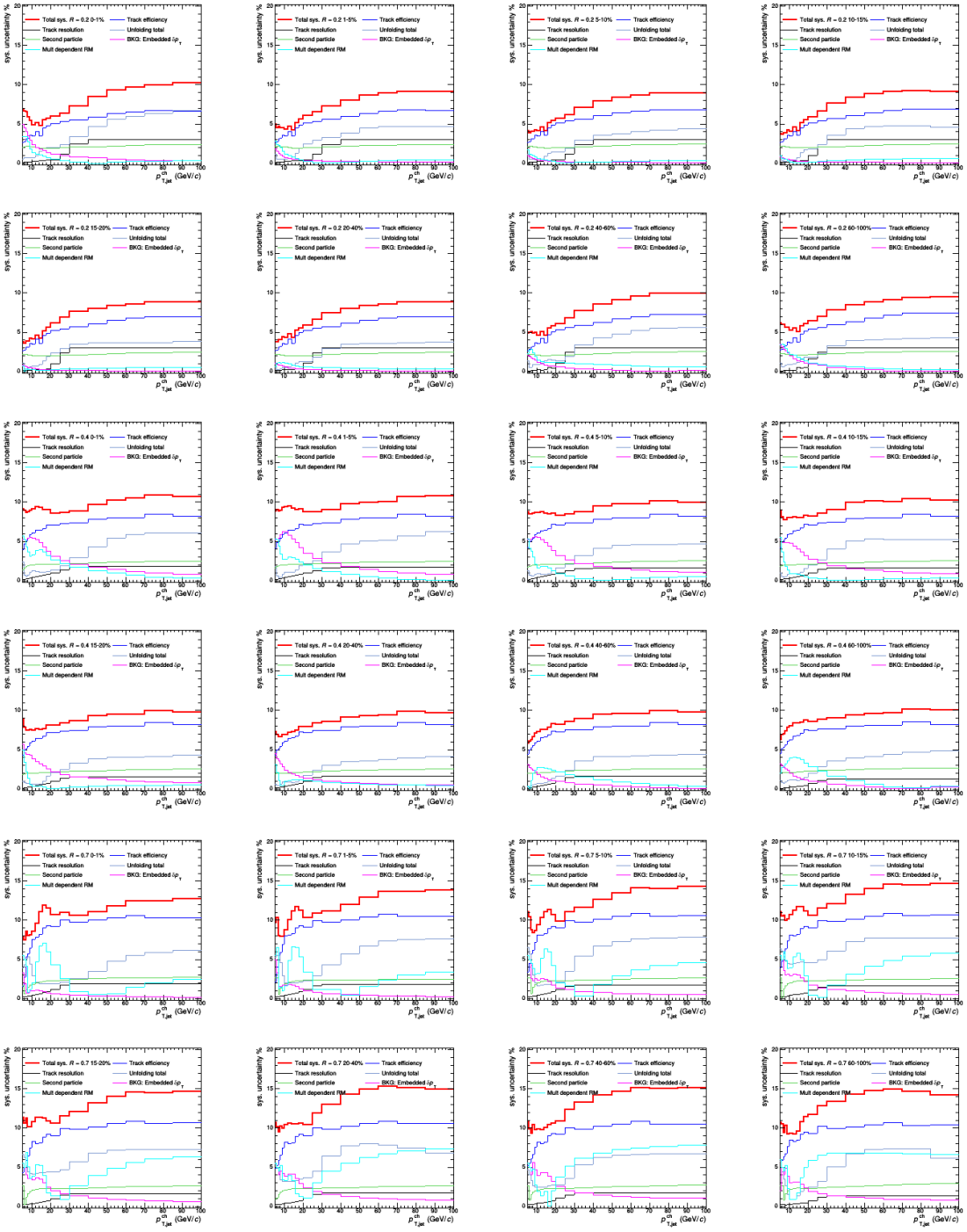

Figure 4.41: Total systematic uncertainty for multiplicity-dependent jet production for R = 0.2, 0.4 and 0.7.

Correlated uncertainties are correlated change in magnitude of the spectrum. The contributions to such type of uncertainty are the uncertainty on tracking efficiency and momentum resolution, uncertainty on multiplicity determination, background fluctuations, uncertainty from the normalisation and secondary particles. Shape uncertainties are alter the shape of the final spectrum. The uncertainties from the unfolding procedure fall into this category. The total uncertainties on the ratios are determined then by adding the correlated and shape uncertainties from the different sources.

The statistical uncertainties on the jet production ratio are also obtained by taking into account the correlation between the uncertainties on the numerator and denominator. To avoid these statistical correlations, the total event sample is divided into two parts for the calculation of the numerator and denominator, respectively. The derived statistical uncertainty on the ratio remains smaller than the systematic uncertainty.

4.6 Results and discussion: Multiplicity-dependent jet production

4.6.1 Inclusive jet cross section measurements

The fully-corrected inclusive charged-particle jet cross sections after underlying event subtraction in pp collisions at $\sqrt{s}$ = 13 TeV are shown in Fig. 4.42 as a function of jet p_{T} for jet resolution parameters ranging from R = 0.2 to R = 0.7 and pseudorapidity ranges $|\eta_{\mathrm{jet}}| < 0.9 - R$. The choice of R changes the relative strength of perturbative and non-perturbative (hadronisation and UE) effects on the jet transverse momentum distribution [213]. To be consistent with the multiplicity dependent results, all figures presented hereafter are obtained with UE subtraction, while the same measurements without UE subtraction are listed in Appendix A.1.

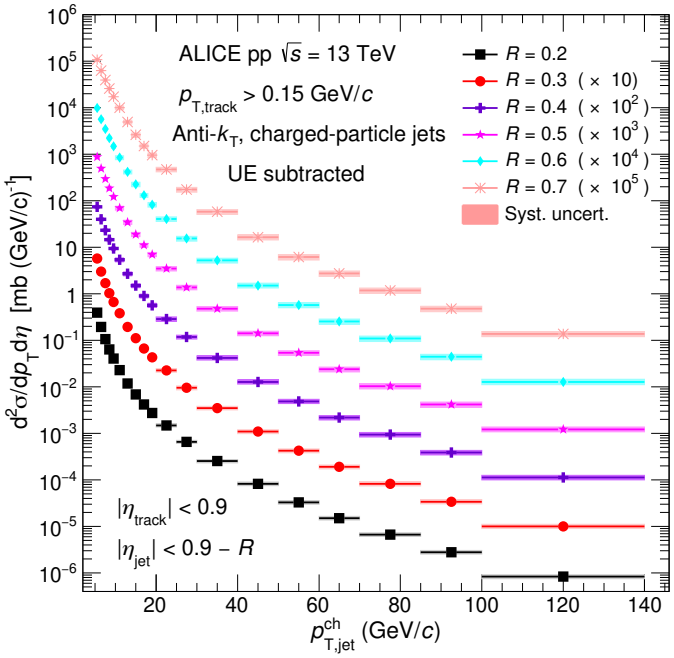

Figure 4.42: Inclusive charged-particle jet cross sections in pp collisions at $\sqrt{s}$ = 13 TeV using the anti-k_{T} algorithm for different jet resolution parameters R from 0.2 to 0.7, with UE subtraction. Statistical uncertainties are displayed as vertical error bars. The total systematic uncertainties are shown as solid boxes around the data points.

Figure 4.43 compares the inclusive charged-particle jet cross sections with predictions from the PYTHIA8 and POWHEG MC event generators after UE subtraction, with the same selections and background subtraction procedure applied. The ratios of the MC simulations to ALICE data are shown in the bottom panels of Fig. 4.43. The POWHEG MC provides a better description of the data within uncertainties for $p^{\mathrm{ch}}_{\mathrm{T,jet}} \gtrsim 20$ GeV/c. Nevertheless, large deviations occur for jet transverse momenta below 20 GeV/c where POWHEG overestimates the data. Such deviation increases with the jet R. A similar enhancement of POWHEG with respect to the data is also observed at 7 TeV [214], where the implementation

of MPI in PYTHIA shows a significant effect on the low p_{T} jet yield when coupled with POWHEG.

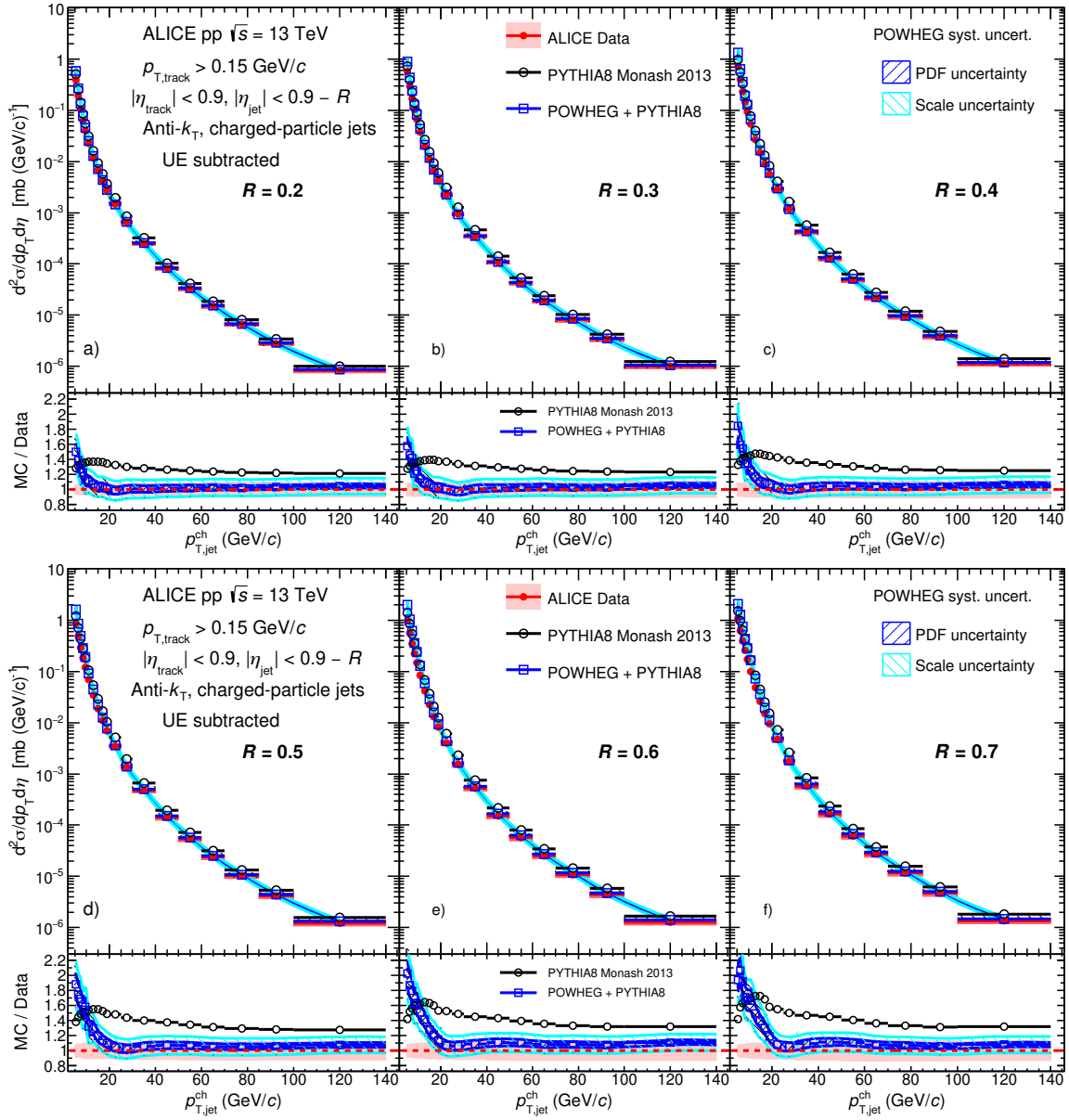

Figure 4.43: Inclusive charged-particle jet cross sections in pp collisions at $\sqrt{s}$ = 13 TeV with UE subtraction. Data for different jet resolution parameters R varied from 0.2 to 0.7 are compared to LO and NLO MC predictions. The statistical uncertainties are displayed as vertical error bars. The systematic uncertainties on the data are indicated by shaded boxes in the top panels and shaded bands drawn around unity in the bottom panels. The red lines in the ratio correspond to unity.

Figure 4.44 shows the inclusive jet cross section ratios for jets reconstructed with a resolution parameter of $R = 0.2$ to other resolution parameters $R = 0.3$ to 0.7. The observable defined by the ratio of inclusive jet cross sections relates directly to the relative difference between jet p_{T} distributions when

using different resolution parameters and therefore provides insights into the angular dependence of jet fragmentation.

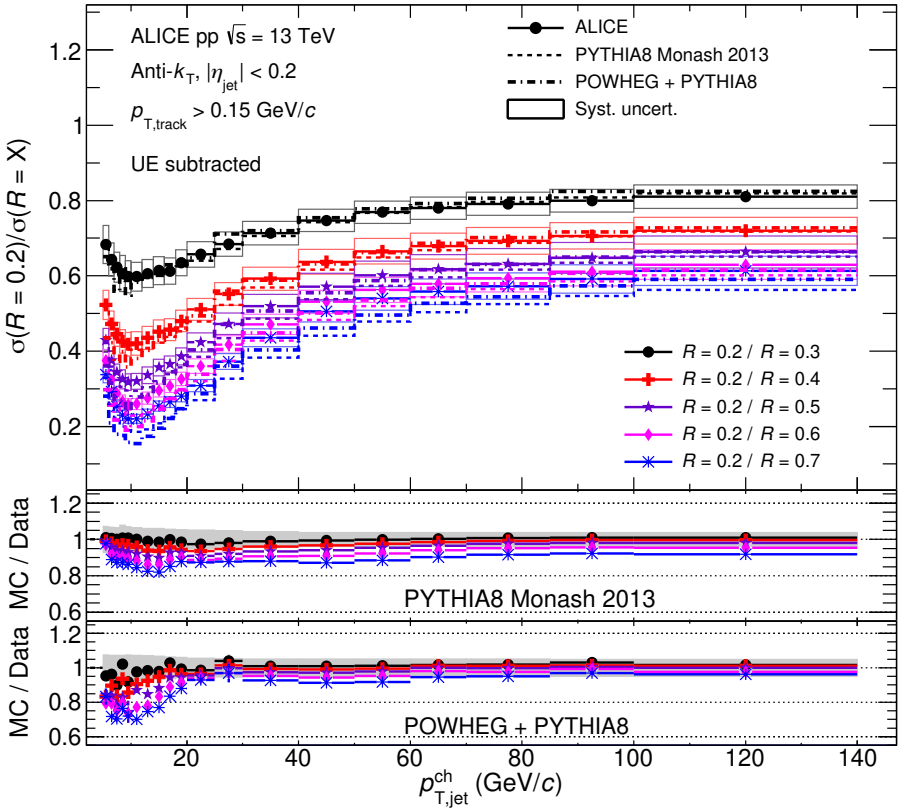

Figure 4.44: Ratio of charged-particle jet cross section for resolution parameter $R = 0.2$ to other radii $R = X$, with X ranging from 0.3 to 0.7, after UE subtraction. Data are compared with LO (PYTHIA) and NLO (POWHEG+PYTHIA8) predictions as shown in the bottom panels. The systematic uncertainties of the cross section ratios from data are indicated by solid boxes around data points in the upper panel and shaded bands around unity in the mid and lower panels. No uncertainties are shown for theoretical predictions for better visibility.

This observable is also less sensitive to experimental systematic uncertainties since the correlated uncertainty on the numerator and denominator spectra are largely cancelled in the ratio. Consequently, the comparisons between data and model predictions provide better precision than those for inclusive spectra. In order to compare the ratios within the same jet pseudorapidity range, the ratios were studied for jet $|\eta_{\rm jet}| < 0.2$, which coincides with the fiducial jet acceptance for the largest resolution parameter studied ($R = 0.7$). Statistical correlations between the numerator and denominator of the jet cross section ratios were removed by using exclusive subsets events for their respective assessments. The measured ratios were compared with PYTHIA and POWHEG calculations in Fig. 4.44. Both predictions give a reasonable description of the data for high-$p_{\rm T}$ jets within 10%, although they fail to describe the low-$p_{\rm T}$ region, especially for large resolution parameters, where non-perturbative and UE contributions become

large. Even though PYTHIA8 overestimates the jet yields (see Fig. 4.43), the jet production ratio can still be well described by PYTHIA8 MC.

Figure 4.45 shows the ratio of the charged-particle jet cross section with different R values for a) $R = 0.2/R = 0.4$ and b) $R = 0.2/R = 0.6$ in pp collisions at $\sqrt{s} = 5.02$ [26], 7 [27], 13 TeV, and p–Pb collisions at $\sqrt{s_{\mathrm{NN}}} = 5.02$ TeV [28]. These results, which are in good agreement within uncertainties, show a similar increase of the jet cross section ratio as a function of jet p_{T}, as expected from the stronger collimation of high-p_{T} jets. No significant energy nor collision species dependence is observed within uncertainties.

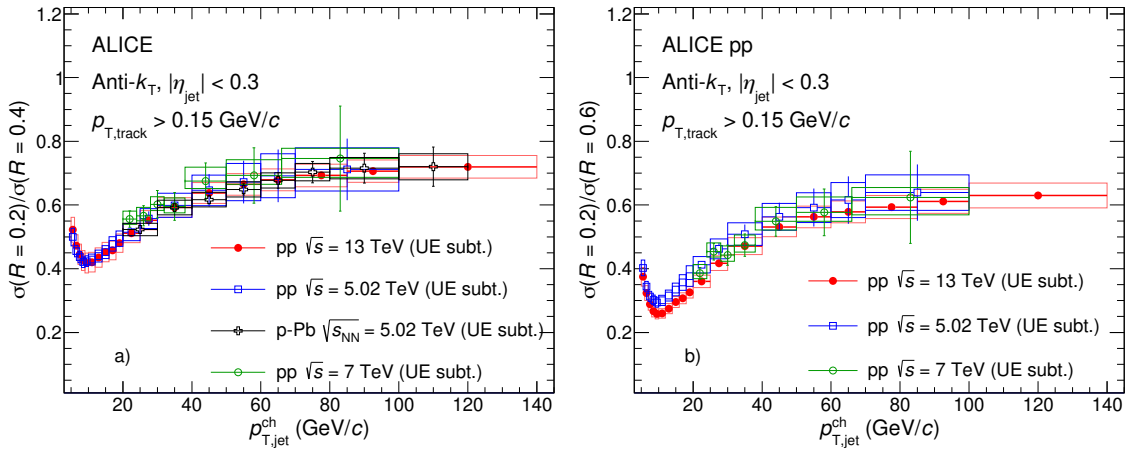

Figure 4.45: Comparison of charged-particle jet cross section ratio with UE subtraction in pp collisions at $\sqrt{s} = 5.02$ [26], 7 [27], and 13 TeV and in p–Pb collisions at $\sqrt{s_{\mathrm{NN}}} = 5.02$ TeV [28]. Results are a) $\sigma(R = 0.2)/\sigma(R = 0.4)$, and b) $\sigma(R = 0.2)/\sigma(R = 0.6)$.

4.6.2 Multiplicity dependence of jet production

The jet production yields measured in different V0M multiplicity intervals as a function of jet p_{T} for different resolution parameters R varied from 0.2 to 0.7 in pp collisions at $\sqrt{s} = 13$ TeV are shown in Fig. 4.46. There exists a multiplicity dependence of jet yields, with higher (lower) jet yields observed at higher (lower) multiplicity classes. To better investigate this multiplicity dependence, the ratios of jet spectra from multiplicity classes and with MB events (Fig. 4.42) are presented in Fig. 4.47. The charged-particle jet yield ratio in the highest event multiplicity class (0–1%) is about 10 times higher than in the MB case, independent of the jet resolution parameter R, while in the lowest event class (60–100%), it amounts to only about 10% of the MB yield. Furthermore, such ratio has a weak p_{T} dependence, except for the very low p_{T} region. This indicates that jet production changes with event activity, but the slope of the spectrum stays similar to the one measured in MB events.

Figure 4.48 shows the ratios of the $R = 0.2$ jet spectrum to other radii for different multiplicity classes.

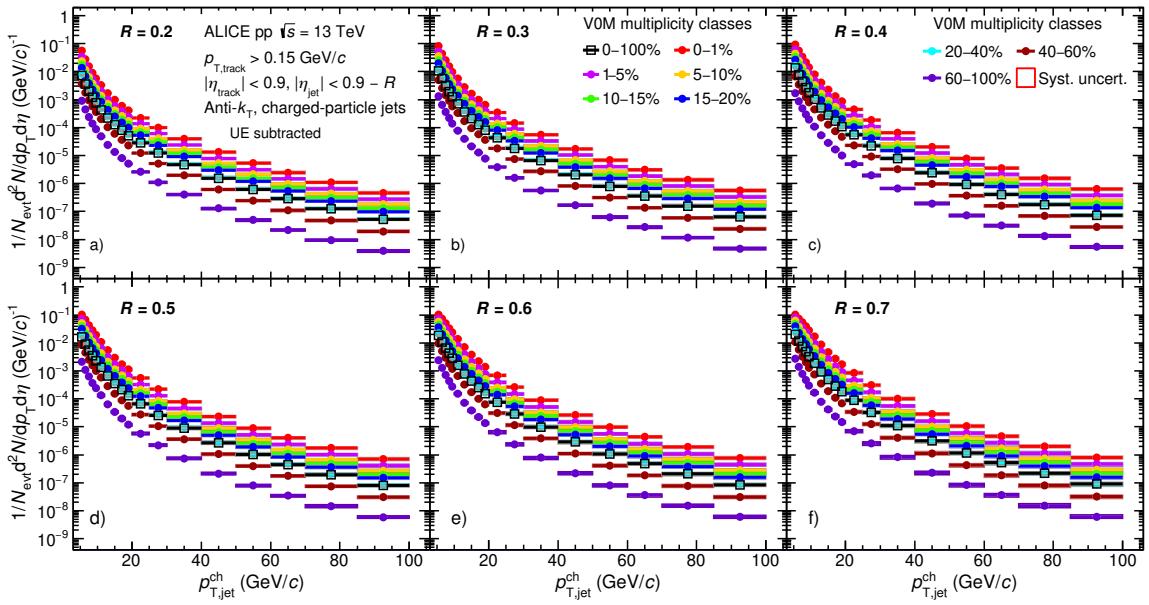

Figure 4.46: Charged-particle jet yields in different V0M multiplicity percentile intervals for resolution parameters R varied from 0.2 to 0.7 in pp collisions at $\sqrt{s}$ = 13 TeV. Statistical and total systematic uncertainties are shown as vertical error bars and boxes around the data points, respectively.

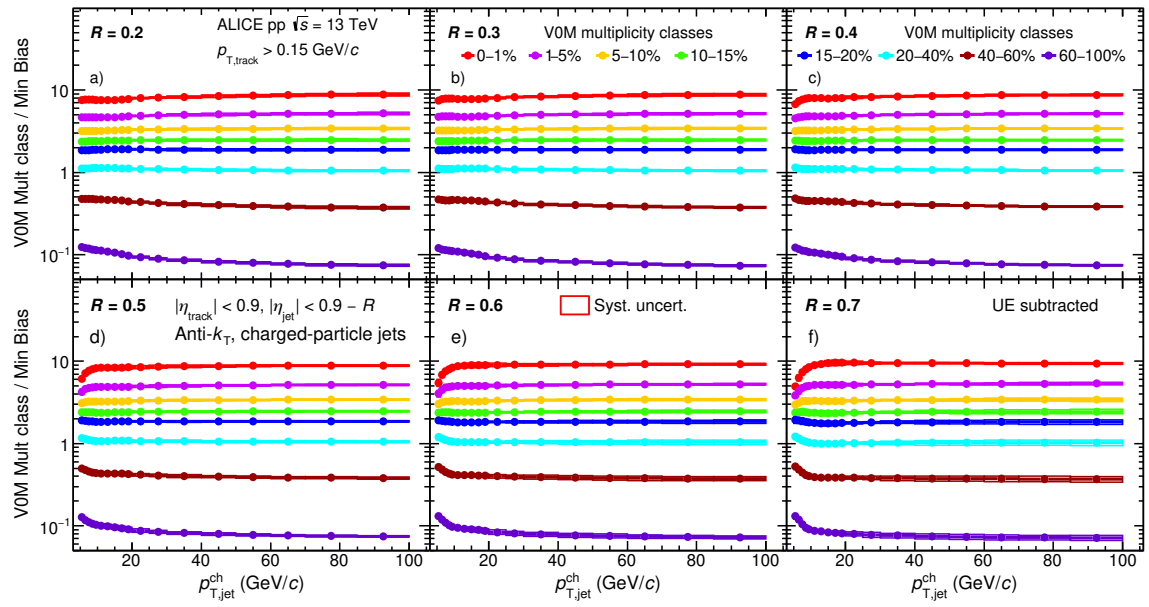

Figure 4.47: Ratio of charged-particle jet yield measured in different multiplicity classes with respect to that in MB events as a function of p_{T} for different resolution parameters R from 0.2 to 0.7. Statistical and total systematic uncertainties are shown as vertical error bars and boxes around the data points, respectively.

To better understand the multiplicity dependence of the jet spectra ratios, Fig. 4.49 compares these ratios observed in three selected multiplicity intervals (0–1%, 10–15% and 60–100%) to the ones measured in MB events for $R = 0.2/(X = 0.3, 0.4, 0.5, 0.6, 0.7)$, top panels represent $R = 0.2/0.3$, $R = 0.2/0.5$ and $R = 0.2/0.7$, while the bottom panels represent $R = 0.2/0.4$, $R = 0.2/0.6$. The ratios are consistent with the ones obtained in the MB case (Fig. 4.44) for small jet radii. At larger jet radii, a hint of ordering of the jet production ratios with event multiplicity is observed. It is more pronounced for large radii ($R = 0.2/0.7$) and low p_{T}. However, with the current systematic uncertainty on data, it is difficult to draw final conclusions on such dependence. Similar behaviour is observed in MC simulations as shown in Fig. 4.50. The MC predictions tend to underestimate the data and this discrepancy increases with jet radius. However, within the current experimental systematic uncertainties, there is no clear indication of multiplicity dependence for jet yield ratios.

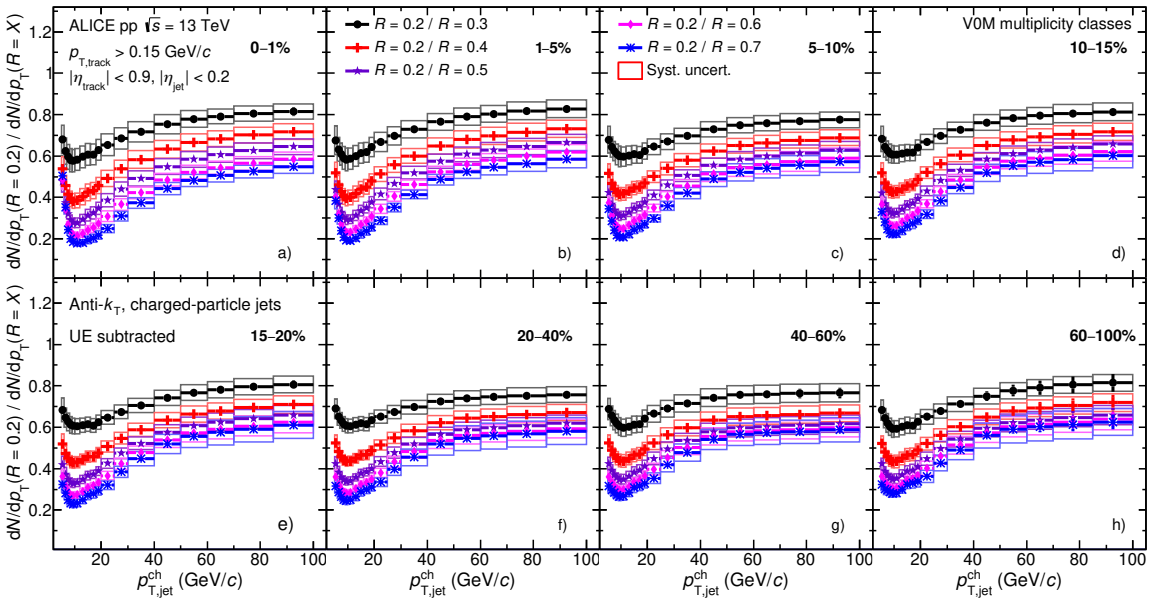

Figure 4.48: Ratios of charged-particle jet spectra with $R = 0.2$ to that with other jet resolution parameters R from 0.3 to 0.7, shown in different V0M multiplicity classes. Statistical and systematic uncertainties are shown as vertical error bars and boxes around the data points, respectively.

The p_{T}-integrated ($5 \leq p_{\mathrm{T}} < 100$ GeV/c) jet yields and the average transverse momentum of charged-particle jets as a function of the self-normalised charged-particle multiplicity, $\langle \mathrm{d}N_{\mathrm{ch}}/\mathrm{d}\eta \rangle_{|\eta|<1}$, are shown in Fig. 4.51 for different resolution parameters R from 0.2 to 0.7. Both jet yields and the average jet p_{T} increase with multiplicity, the increase is more evident at larger R. Jets with $R = 0.2$ exhibit very weak dependence of their $\langle p_{\mathrm{T}} \rangle$ on multiplicity, indicating that jets reconstructed with small radii are dominated by the leading particle inside in the jet.

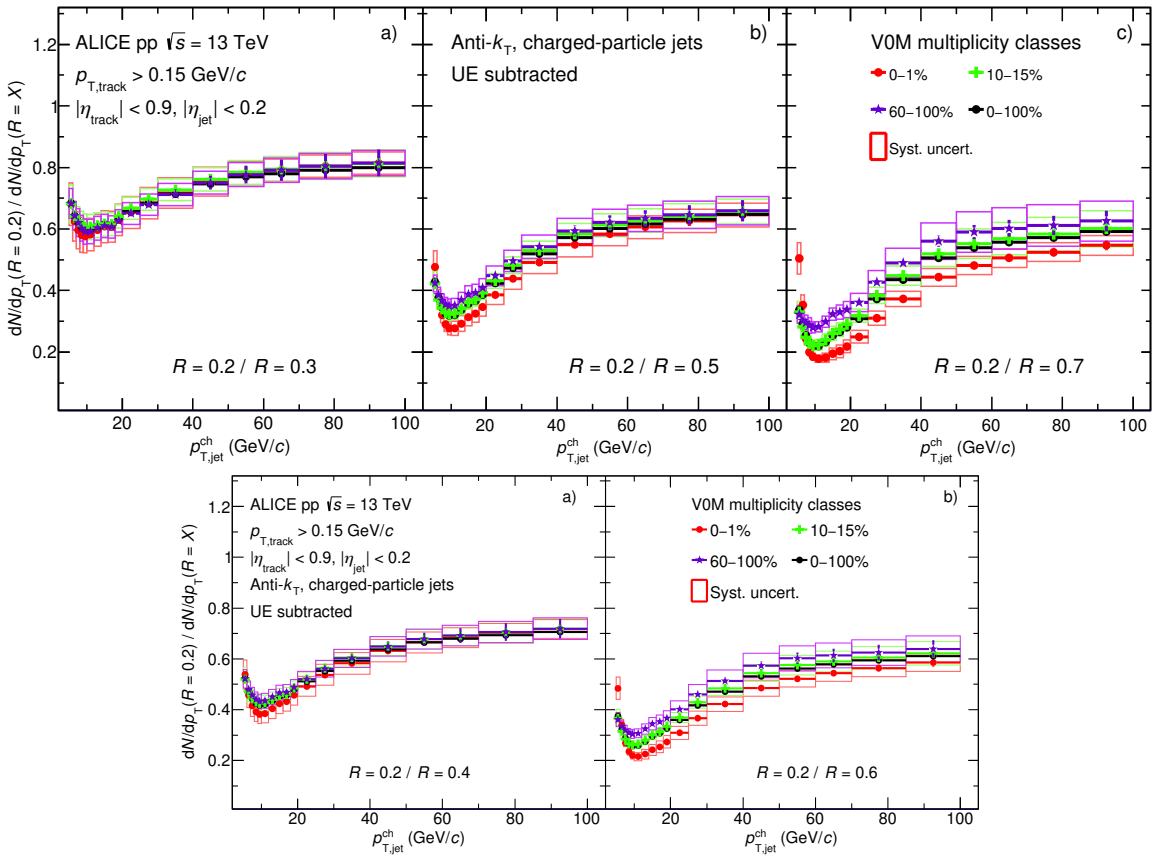

Figure 4.49: Comparison of jet spectra ratios of $R = 0.2$ to other radii $R = 0.3 - 0.7$ in MB events and in three multiplicity intervals (0–1%, 10–15% and 60–100%). Statistical and systematic uncertainties are shown as vertical error bars and boxes around the data points, respectively.

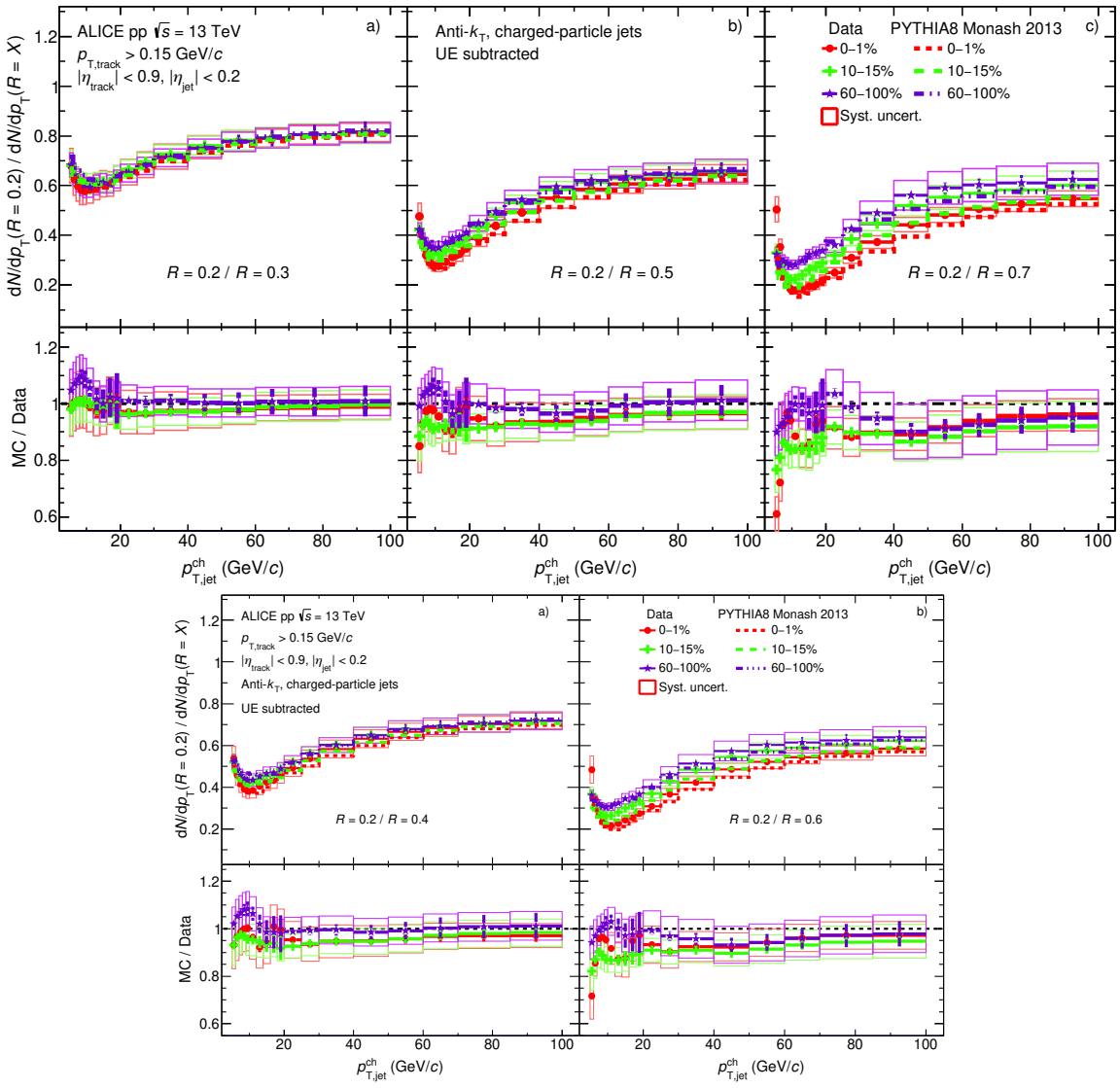

Figure 4.50: Comparison of jet spectra ratios of $R = 0.2$ to $R = 0.3 - 0.7$ in three multiplicity intervals (0–1%, 10–15% and 60–100%) and compared with PYTHIA8 simulations. Statistical and systematic uncertainties are shown as vertical error bars and boxes around the data points, respectively.

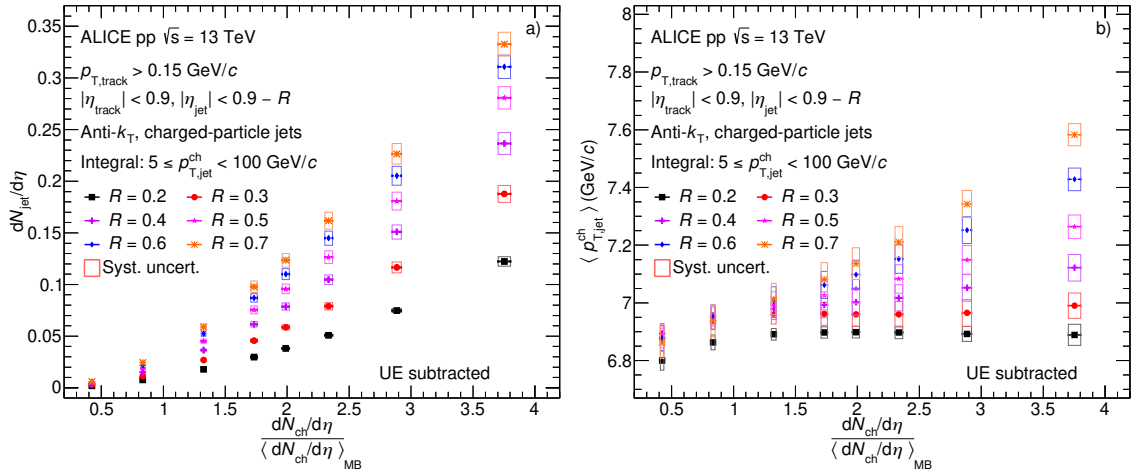

Figure 4.51: Integrated jet yields (left) and $\langle p_T \rangle$ (right) of jets with $5 \le p_{T,jet}^{ch} < 100$ GeV/c as a function of self-normalised charged-particle multiplicity for different resolution parameters R varied from 0.2 to 0.7, with the charged-particle multiplicities provided in Ref. [29]. Statistical and systematic uncertainties are shown as vertical error bars and boxes around the data points, respectively.

Fig. 4.52 presents the integral jet yield ratios in different multiplicity percentiles with respect to MB events as a function of self-normalised charged-particle multiplicity. The ratios are shown for four selected jet p_T bins ($5 \le p_{T,jet}^{ch} < 7$ GeV/c, $9 \le p_{T,jet}^{ch} < 12$ GeV/c, $30 \le p_{T,jet}^{ch} < 50$ GeV/c, and $70 \le p_{T,jet}^{ch} < 100$ GeV/c), and for resolution parameters $R = 0.2 - 0.7$. The jet yield ratios increase with multiplicity for all resolution parameters and p_T intervals. No significant dependence of the jet yields with the jet resolution parameter R is seen.

To explore the p_T dependence of the normalised jet production as a function of self-normalised charged-particle multiplicity, Fig. 4.53 shows the self-normalised jet yields as a function of the self-normalised multiplicity in four selected jet p_T intervals for resolution parameter $R = 0.2 - 0.7$, top panels depict $R = 0.2, 0.4, 0.6$, bottom panels depict $R = 0.3, 0.5, 0.7$. The PYTHIA8 predictions are also compared against data.

A same analysis we also study using mid-rapidity SPD multiplicity estimator as a cross-check, obtaining that jet yield as a function multiplicity with the event selection based on SPD tracklets at midrapidity in pp collisions at $\sqrt{s} = 13$ TeV, as presented in Chapter A.2 of the Appendix. Fig. A.13 shows the jet yield and yield ratios (multiplcity classes over MB) as a function of the normalized charged-particle pseudorapidity density at midrapidity, $\langle dN_{ch}/d\eta \rangle_{|\eta|<1}$, with the event selection based on V0 amplitude at forward rapidity (full markers) and on SPD tracklets at midrapidity (open markers). The results for the two event selection methods are in rough agreement within uncertainty.

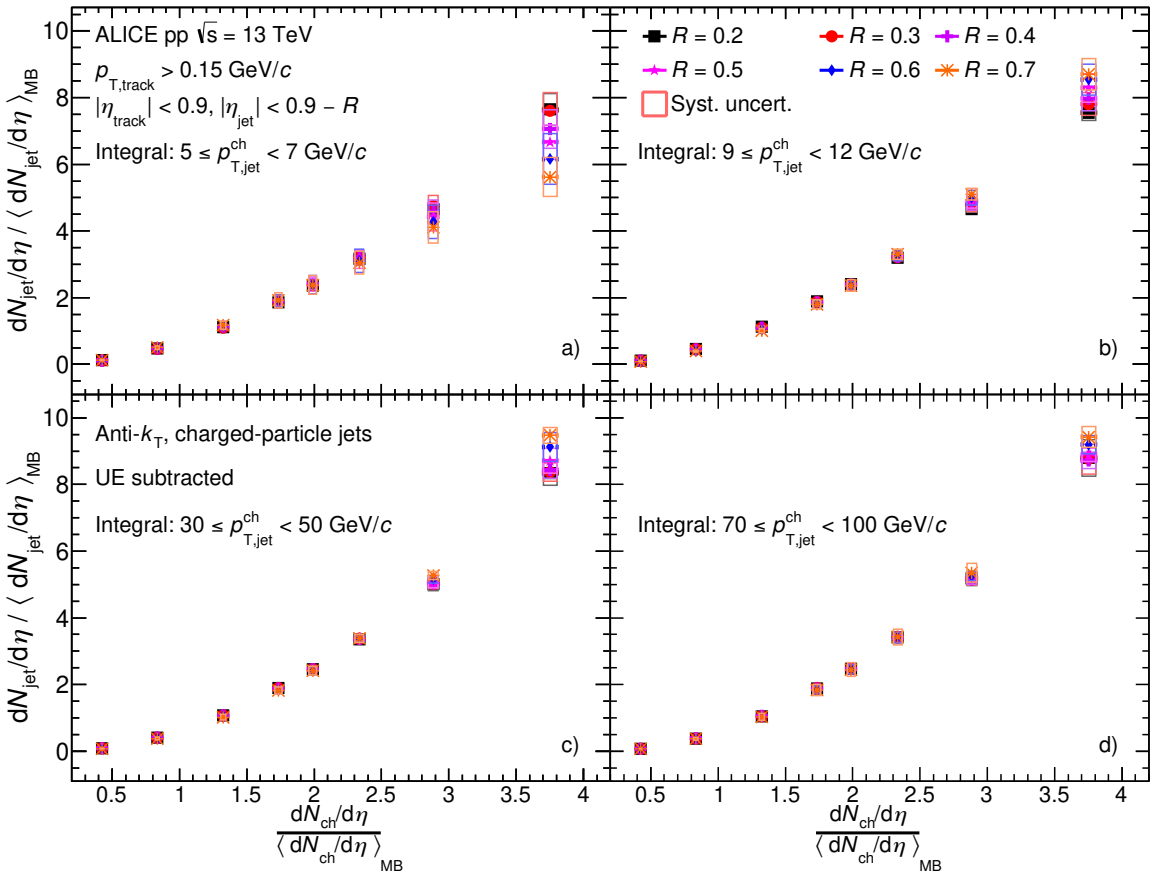

Figure 4.52: Self-normalised jet yields as a function of the self-normalised charged-particle multiplicity for different resolution parameters R varied from 0.2 to 0.7 in different jet p_T intervals: a) $5 \leq p^{ch}_{T,jet} < 7$ GeV/c, b) $9 \leq p^{ch}_{T,jet} < 12$ GeV/c, c) $30 \leq p^{ch}_{T,jet} < 50$ GeV/c, and d) $70 \leq p^{ch}_{T,jet} < 100$ GeV/c. The charged-particle multiplicities are taken from Ref. [29]. Statistical and systematic uncertainties are shown as vertical error bars and boxes around the data points, respectively.

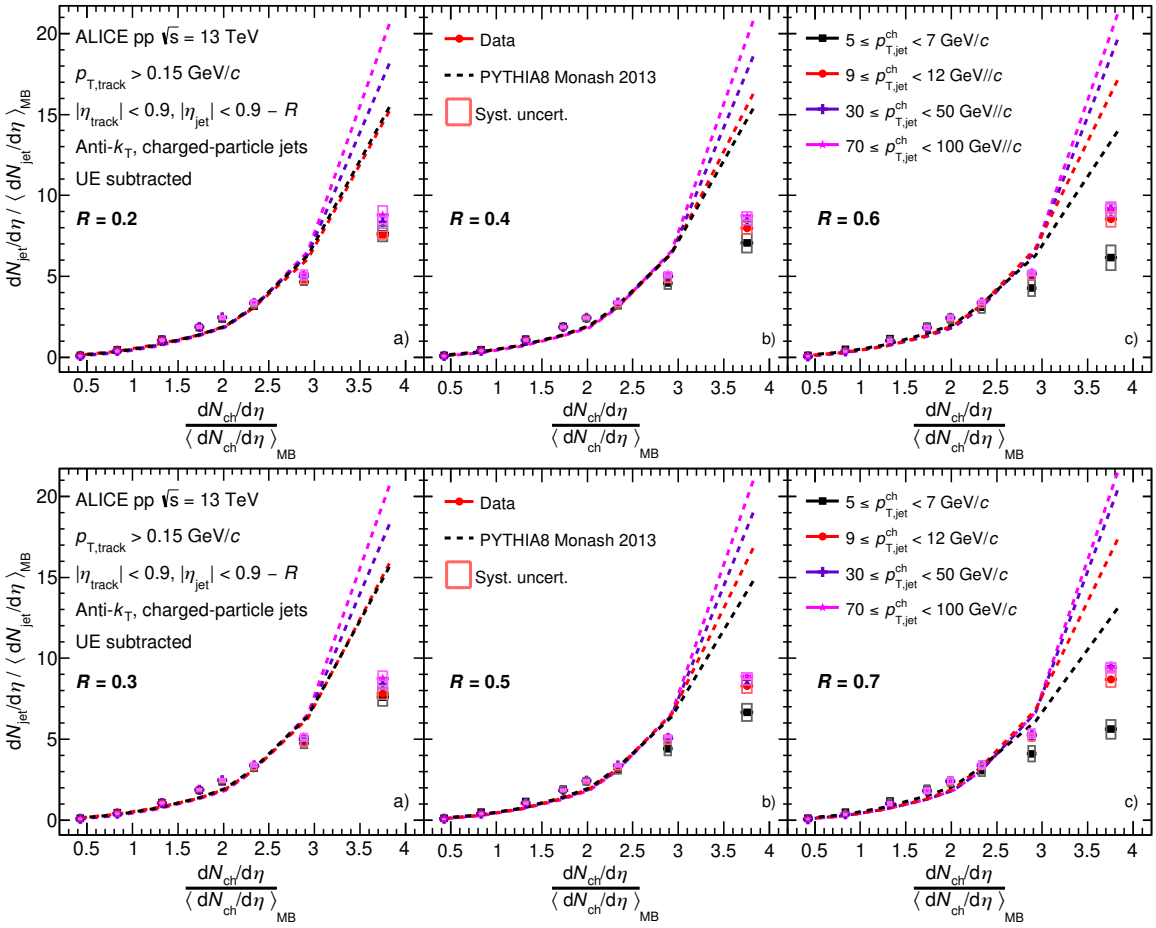

Figure 4.53: Comparison of self-normalised jet yields as a function of the self-normalised charged-particle multiplicity in four selected jet p_T intervals ($5 \le p_{T,jet}^{ch} < 7$ GeV/c, $9 \le p_{T,jet}^{ch} < 12$ GeV/c, $30 \le p_{T,jet}^{ch} < 50$ GeV/c, and $70 \le p_{T,jet}^{ch} < 100$ GeV/c) for all jet radii $R = 0.2 - 0.7$ between data and PYTHIA8 predictions, with the charged-particle multiplicities provided in Ref. [29]. Statistical and systematic uncertainties are shown as vertical error bars and boxes around the data points, respectively.

The jet production ratios measured at midrapidity increase with multiplicity in a similar way to the results presented in earlier publications for identified particles when using forward or midrapidity multiplicity estimators [215–217]. The increase is weaker for the lowest jet p_{T} in the highest multiplicity interval. In general, PYTHIA8 simulations predict the overall increasing trend, however, the absolute magnitude is overestimated by the PYTHIA8 MC, especially in the highest multiplicity interval.

5 Hadron-jet correlation measurements in pp collisions at $\sqrt{s} = 5.02$ TeV

Jet quenching is a necessary consequence of the QGP formation in heavy-ion collisions. Several common signatures of jet quenching are jet angular deflection and modification of jet substructure observed in heavy-ion collisions when compared to pp collisions. The measurement of reconstructed jets in heavy-ion collisions is challenging due to the large and non-uniform background. Initial studies of jet quenching therefore utilized high-p_{T} hadron production and correlations [218–220], which are more readily measurable with high precision in such an environment. Deeper insight into the mechanisms underlying jet quenching and the response of the QGP to the passage of energetic partons requires measurements incorporating reconstructed jets. Significant progress has been made over the past decade in the measurement of jets in heavy-ion collisions in terms of inclusive jet production, di-jet correlations, and trigger–jet coincidence observable [15, 82, 198, 221, 222]. Model studies incorporate both jet and hadronic observable, for a more comprehensive study of jet quenching [223, 224]. We report about new measurements of the semi-inclusive distribution of charged-particle jets recoiling from a high-p_{T} hadron ("h+jet") [15, 82] in pp and central Pb–Pb collisions $\sqrt{s_{\mathrm{NN}}} = 5.02$ TeV.

Measurements of medium-induced yield enhancement and acoplanarity broadening of low-p_{T} jets from measurements in pp and Pb–Pb collisions will help gaining unique insights into the properties of the QGP. Recoil jet yield distributions are measured as a function of jet p_{T} and acoplanarity $\Delta\varphi$, the azimuthal separation of the trigger hadron and recoil jet, for different jet resolution parameters $R = 0.2, 0.4, 0.5$. The uncorrelated background jet-yield in pp and central Pb–Pb collisions is corrected using the trigger p_{T}-differential statistical approach (data-driven method). This approach enables precise measurements of recoil jet distributions at low p_{T} and large jet radius R in central nucleus-nucleus collisions, a necessary input in the search for jet deflection effects over a broad phase space.

Similar to the multiplicity-dependent jet study in pp collisions at $\sqrt{s} = 13$ TeV, the analysis strategy of the h+jet correlation includes the following steps: selection of experimental data, event selection, track reconstruction, trigger track event selection, jet reconstruction, background subtraction, unfolding correction, systematic calculation and discussion of physical results.

5.1 Data and MC samples

The data for pp collisions at $\sqrt{s} = 5.02$ TeV were recorded during the 2015 and 2017 LHC running periods, with a MB trigger requiring a coincidence signal between V0A and V0C. The recorded data

comprise about 1.02×10^8 events from 2015 and about 9.3×10^8 events from the 2017 runs. Both datasets were found to be consist, so that they could be combined and analysed together. After applying all selection cuts, 1.04×10^9 pp events were accepted for further analysis. The MC datasets, to assess the detector response for the unfolding correction, correspond to jet-jet $p_{\mathrm{T,hard}}$ MC productions (PYTHIA8, Monash-2013 produced in 20 $p_{\mathrm{T,hard}}$ bins). Details of the data sets used are summarized in Table 5.1.

Table 5.1: Analyzed data samples and total number of events in each data sample for the pp analysis.

	period	N events (before selection)	N events (after selection)
data	LHC17p (Fast + CentwoSDD)	1.02×10^9	8.84×10^8
	LHC17q (Fast + CentwoSDD)	6.0×10^7	5.26×10^7
	LHC15n	1.17×10^8	1.02×10^8
total		1.20×10^9	1.04×10^9
MC	LHC18b8_fast (JJ)	5.2×10^6 / bin	4.7×10^6 / bin
	LHC18b8_centwoSDD (JJ)	2.8×10^6 / bin	2.6×10^6 / bin
total		8.0×10^6 / bin	7.3×10^6 / bin

The distributions of the recoil jets $\Delta\varphi$ and p_{T} were examined for each dataset, as shown in Fig. 5.1 and Fig. 5.2. confirm that the data samples can be combined before the analysis begins.

5.2 Event selection

We not only applied the event selection and track reconstruction as discussed in sections 3.1 and 3.2, but apply additional event selection requiring the presence of a high-p_{T} charged-hadron trigger particle within a defined p_{T} interval, $p_{\mathrm{T,low}} < p_{\mathrm{T}}^{\mathrm{trig}} < p_{\mathrm{T,high}}$ GeV/c, denoted as TT$\{p_{\mathrm{T,low}}, p_{\mathrm{T,high}}\}$ (referred to as ("Trigger Track"). Subsequently, jet reconstruction and background subtraction were performed as described in Section 3.2 and Section 3.3.

The principal analysis is carried out using charged-hadron triggers in TT$\{20, 50\}$ (signal distribution, denoted TT$_{\mathrm{sig}}$). The uncorrelated background yield is corrected using a lower-$p_{\mathrm{T}}^{\mathrm{trig}}$ interval, corresponding to TT$\{5, 7\}$ (reference distribution, denoted TT$_{\mathrm{ref}}$; see Section 5.4). The pp datasets are each divided randomly into two distinct subsets of unequal numbers of events. One subset is used for selecting the TT$_{\mathrm{sig}}$ population, while the other is designated for TT$_{\mathrm{ref}}$, as illustrated in Fig. 5.3, which compares the p_{T} spectrum of inclusive tracks and the selected trigger tracks. The relative fraction of the population in each subset is chosen to maximize the statistical precision of the corrected distributions. For the pp dataset, 90% of events are assigned to the TT$_{\mathrm{sig}}$ population and 10% are assigned to the TT$_{\mathrm{ref}}$ population. In addition, other signal trigger track intervals corresponding to $15 - 20$ GeV/c, $20 - 30$ GeV/c, $30 - 50$ GeV/c are also explored to study the TT-dependence of the recoil jet yield.

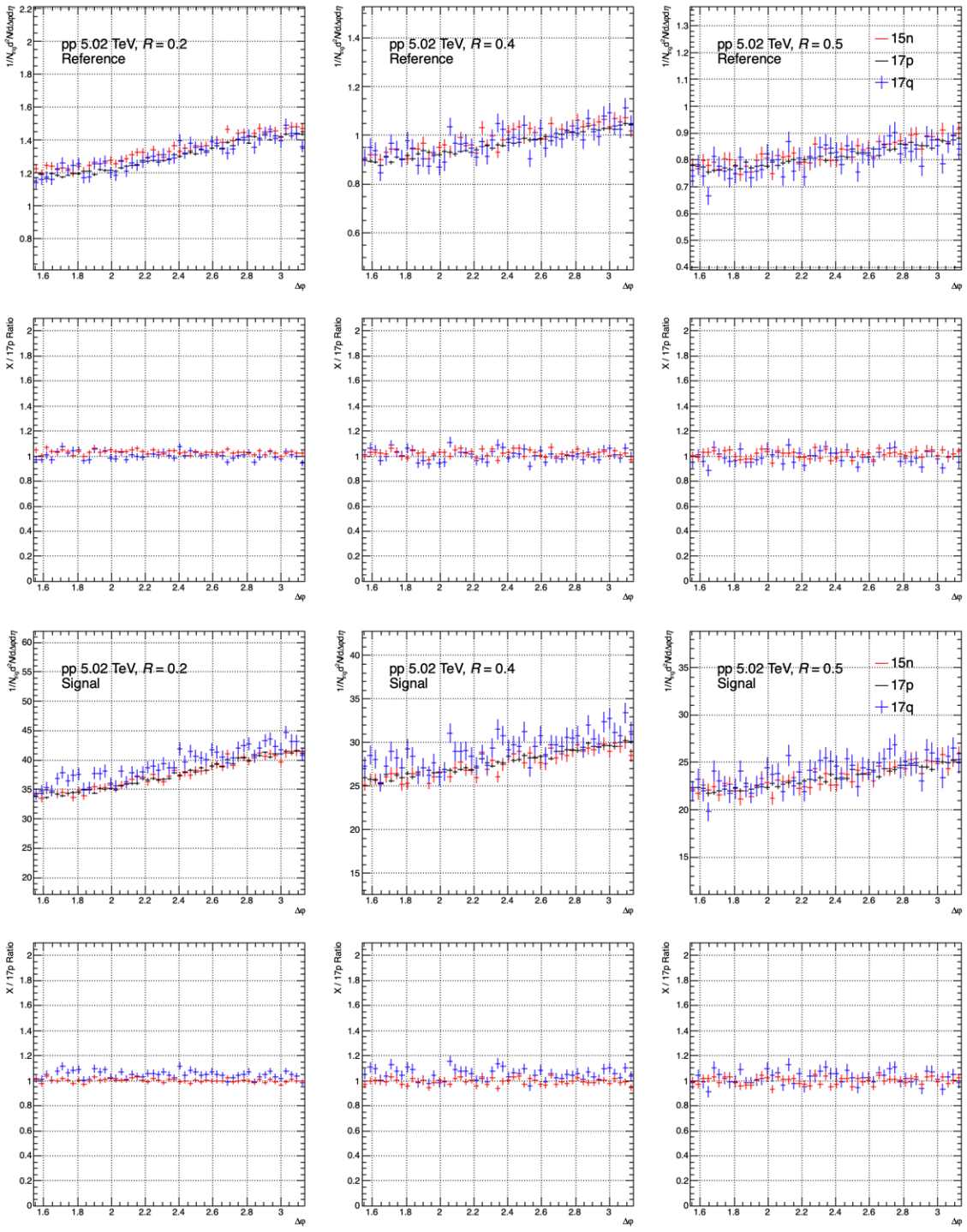

Figure 5.1: Comparison of the raw $\Delta\varphi$ distributions for the different data periods for the full p_{T} range in the reference (top) and signal (bottom) trigger track intervals, for $R = 0.2$ (left), $R = 0.4$ (middle) and $R = 0.5$ (right).

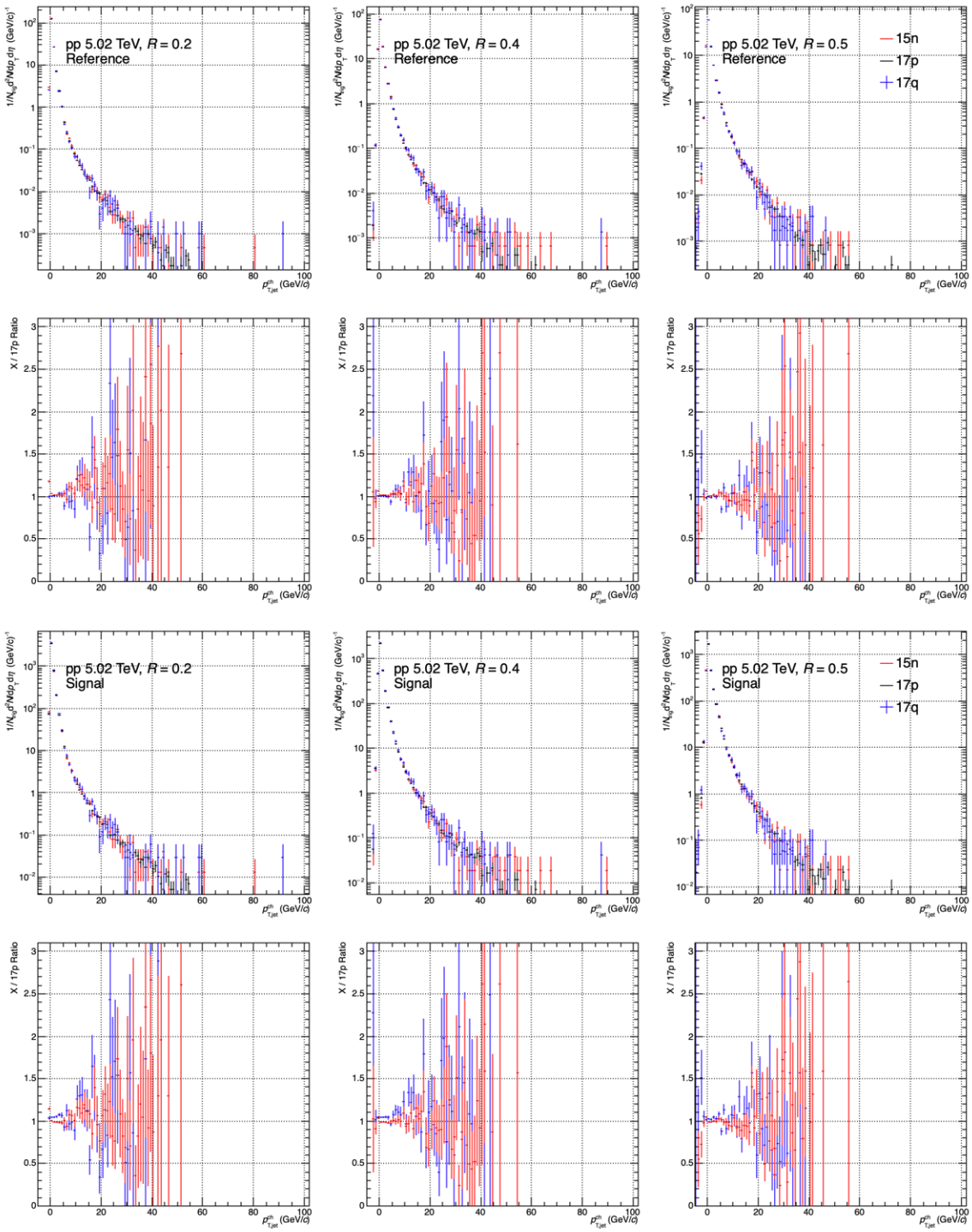

Figure 5.2: Comparison of the raw p_{T} distributions for the different data periods in the reference (top) and signal (bottom) TT intervals, for $R = 0.2$ (left), $R = 0.4$ (middle) and $R = 0.5$ (right).

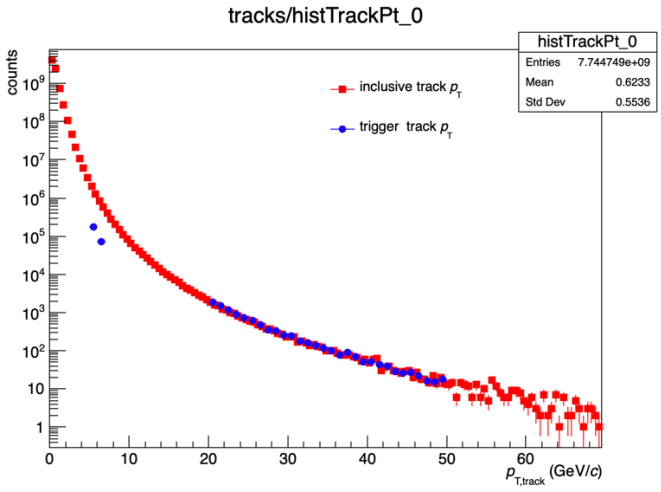

Figure 5.3: p_T distributions for inclusive charged tracks and chosen trigger tracks.

5.3 Semi-inclusive distributions

Jet reconstruction is carried out on TT-selected events. For each TT-selected event set, recoil jet candidates are tabulated in bins of $p_{T,ch\ jet}^{corr}$ and $\Delta\varphi$, and the distribution is normalized to the number of triggers N_{trig}. This normalized distribution is semi-inclusive, since event selection is based solely upon the presence of an inclusively-distributed high-p_T trigger track, without requiring the presence of jets with specific properties in the recoil region. It is therefore equivalent to the ratio of hard cross sections [15],

$$\frac{1}{N_{trig}}\frac{d^2N_{jet}^{corr}}{dp_{T,jet}d\Delta\varphi}\bigg|_{p_T^{trig}\in TT} = \left(\frac{1}{\sigma^{AA\to h}}\frac{d^2\sigma^{AA\to h+jet}}{dp_{T,jet}d\Delta\varphi}\right)\bigg|_{p_{T,h}\in TT}, \tag{5.1}$$

where $d^2N_{jet}^{corr}/dp_{T,jet}d\Delta\varphi$ represents the differential yield of recoil jets, AA denotes pp or Pb–Pb collisions, $\sigma^{AA\to h}$ is the cross section to generate a hadron within the p_T interval of the selected TT class, and $d^2\sigma^{AA\to h+jet}/dp_{T,jet}d\Delta\varphi$ is the differential cross section for coincidence production of a hadron in the TT interval and a recoil jet. Both cross sections in the ratio are perturbatively calculable in pp collisions [15, 225].

Figure 5.4 shows the trigger-normalized recoil-jet distributions for signal TT{20, 50} (left panel) and reference TT{5, 7} (right panel) in pp collisions at $\sqrt{s} = 5.02$ TeV for $R = 0.2$ (top), 0.4 (middle),0.5 (bottom). While the distributions are displayed over the full range in $\Delta\varphi$, it is notable that both distributions exhibit significant peaks at $\Delta\varphi = 0$ and $\Delta\varphi = \pi$. This analysis focuses on the recoil region $\pi/2 < \Delta\varphi < 3\pi/2$.

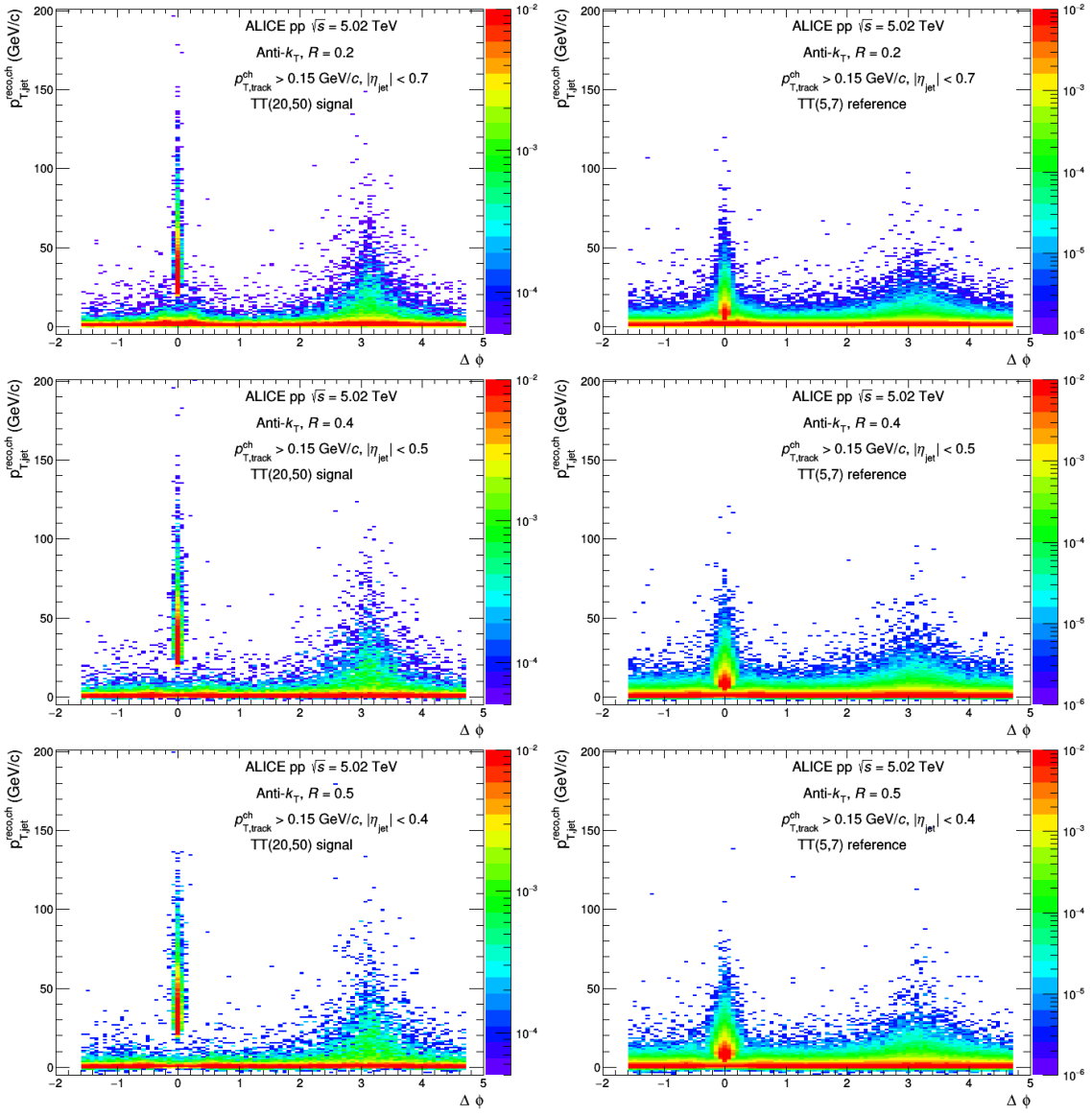

Figure 5.4: Trigger-normalized recoil jet distributions as a function of $\Delta\varphi$ and $p^{corr}_{T,ch\ jet}$ from signal and reference trigger track p_T intervals for jet radii R = 0.2, 0.4, 0.5 in pp collisions at $\sqrt{s}$ = 5.02 TeV.

5.4 Definition of the Δ_{recoil} observable

The goal of this analysis is to measure the trigger-normalized recoil jet distribution over a broad phase space, including low $p_{\text{T,jet}}$ and large R. However, in practice the semi-inclusive yield contains both trigger-correlated and uncorrelated contributions to the recoil jet yield. Uncorrelated background yield is especially large relative to correlated signal for low $p_{\text{T,jet}}$ and large R in central Pb–Pb than pp collisions. The uncorrelated background distribution cannot be modeled accurately, and a well-controlled background correction requires a fully data-driven approach.

The choice of observable for this analysis is motivated by the observation that, by definition, the trigger-normalized uncorrelated jet yield is independent of $p_{\text{T}}^{\text{trig}}$, and can therefore be removed by subtracting trigger-normalized recoil jet yields obtained with two different TT ranges. The observable Δ_{recoil} [15], designed for this purpose, is the difference between two semi-inclusive distributions with widely differing $p_{\text{T}}^{\text{trig}}$ ranges: the signal distribution, denoted TT_{sig}, and the reference distribution, denoted TT_{ref},

$$\Delta_{\text{recoil}}(p_{\text{T,ch jet}}, \Delta\varphi) = \frac{1}{N_{\text{trig}}} \frac{\mathrm{d}^2 N_{\text{ch,jet}}}{\mathrm{d}p_{\text{T,chjet}} \mathrm{d}\Delta\varphi}\bigg|_{p_{\text{T}}^{\text{trig}} \in \text{TT}_{\text{sig}}} - c_{\text{Ref}} \times \frac{1}{N_{\text{trig}}} \frac{\mathrm{d}^2 N_{\text{ch,jet}}}{\mathrm{d}p_{\text{T,chjet}} \mathrm{d}\Delta\varphi}\bigg|_{p_{\text{T}}^{\text{trig}} \in \text{TT}_{\text{ref}}}, \tag{5.2}$$

where c_{Ref} is a normalization factor which value is determined from the data. Scaling the TT_{ref} distribution by c_{Ref} is needed to account for the effect of the correlated recoil jet yield at large positive $p_{\text{T,ch jet}}^{\text{corr}}$, which is smaller in the TT_{ref} population, on the magnitude of the normalized distribution at small and negative $p_{\text{T,ch jet}}^{\text{corr}}$ [15]. The $\Delta_{\text{recoil}}(p_{\text{T,ch jet}}, \Delta\varphi)$ is normalized to unit η_{jet}.

While the subtraction in Δ_{recoil} removes the large uncorrelated jet yield, the TT_{ref} population contains an admixture of trigger-correlated yield which is also removed from the measurement by the subtraction. As noted in Sec. 5.2, the TT_{ref} p_{T}-range is $\text{TT}\{5, 7\}$. This p_{T}-interval is chosen to minimize the TT_{ref} correlated component, while still having high enough trigger p_{T} that its inclusive production cross section is perturbatively calculable in pp collisions. The Δ_{recoil} distribution is therefore not that of a single semi-inclusive recoil distribution, but rather the difference of two such distributions, both of which are perturbatively calculable; the Δ_{recoil} distribution is likewise perturbatively calculable.

In order to assess the effect of the subtraction of the TT_{ref} correlated yield for the choice $\text{TT}_{\text{ref}} = \text{TT}\{5, 7\}$, the analysis was also carried out with $\text{TT}_{\text{ref}} = \text{TT}\{8, 9\}$ (Results for $\text{TT}_{\text{ref}} = \text{TT}\{8, 9\}$ can be found in Appendix A.3). While small differences are observed in the central values of the physics results, all such differences are smaller than the systematic uncertainties of the measurement. This variation is however not an uncertainty; the choice of TT_{ref} defines the observable. This cross-check shows

rather that the physics conclusions from the analysis are not significantly dependent upon the specific choice of $\mathrm{TT}_{\mathrm{ref}}$.

We report the following projections of $\Delta_{\mathrm{recoil}}(p_{\mathrm{T,ch\ jet}}, \Delta\varphi)$:

- $\Delta_{\mathrm{recoil}}(p_{\mathrm{T,ch\ jet}})$: projection onto $p_{\mathrm{T,chjet}}$ for $|\Delta\varphi - \pi| < 0.6$;
- $\Delta_{\mathrm{recoil}}(\Delta\varphi)$: projection onto $\Delta\varphi$ for various intervals in $p_{\mathrm{T,chjet}}$ $(10 - 20 - 30 - 50 - 100\ \mathrm{GeV}/c)$ based on the statistics.

5.5 Measurement of Δ_{recoil} distributions

In this analysis, medium-induced effects are determined by comparing measurements of Pb–Pb collisions to those of pp collisions. The observable Δ_{recoil} was developed for precise, data-driven correction of the large background accompanying jet measurements in Pb–Pb collisions, whereas in pp collisions a more conventional approach could suffice. Nevertheless, for accurate comparison of the two systems, measurements of Δ_{recoil} and its projections are likewise reported for pp collisions. However, since the uncorrelated background is much smaller in pp than in central Pb–Pb collisions, the calibrations of c_{Ref} discussed are simpler, as shown below.

Scale factor c_{Ref} determination from the p_{T} distribution

Figure 5.5 shows the uncorrected distribution of semi-inclusive recoil jet p_{T} distributions for $\mathrm{TT}_{\mathrm{sig}}$ and $\mathrm{TT}_{\mathrm{ref}}$-selected populations, obtained by projection onto $p_{\mathrm{T,chjet}}$ from Fig. 5.4, in pp collisions at $\sqrt{s} = 5.02$ TeV for jet radii $R = 0.2$, 0.4 and 0.5. It also presents their ratio of $\mathrm{TT}_{\mathrm{sig}}$ to $\mathrm{TT}_{\mathrm{ref}}$ to determine the value of c_{Ref}. The ratio is seen to be close to unity at low $p^{\mathrm{corr}}_{\mathrm{T,ch\ jet}}$ and around $p^{\mathrm{corr}}_{\mathrm{T,ch\ jet}} = 5\ \mathrm{GeV}/c$ the ratio increases. The main value of c_{Ref} is determined using a linear pol0 fit in a narrow range around $p^{\mathrm{corr}}_{\mathrm{T,ch\ jet}} = 0$. The obtained value of c_{Ref} varies between 0.92 and 1.06, depending on jet R (for $R = 0.2$, $c_{\mathrm{Ref}} = 1.055 \pm 0.006$, $R = 0.4$, $c_{\mathrm{Ref}} = 0.977 \pm 0.007$ and $R = 0.5$, $c_{\mathrm{Ref}} = 0.926 \pm 0.009$). The dependence of c_{Ref} on $\Delta\varphi$ for the $\Delta_{\mathrm{recoil}}(\Delta\varphi)$ analysis is shown in Fig. 5.6. A comparison of the c_{Ref} results with and without $\Delta\varphi$ dependence indicates that the deviation between the two is very small, so that the same value of c_{Ref} can be used for all $\Delta\varphi$ bins for pp collisions. Differences in final results due a $\Delta\varphi$ dependent c_{Ref} are considered as uncertainties.

Scale factor c_{Ref} determination from the $\Delta\varphi$ distribution

Similar to previous recoil jet p_{T} ratios (see right Fig. 5.5), the c_{Ref} is also determined by the ratio of recoil jet $\Delta\varphi$ distribution between signal and reference TT intervals with p_{T} close to 0 GeV/c. Fig. 5.7 is shown these ratios for different radii and fitting the Signal/Reference ratios at $\Delta\varphi$ from 1 to 1.6 using

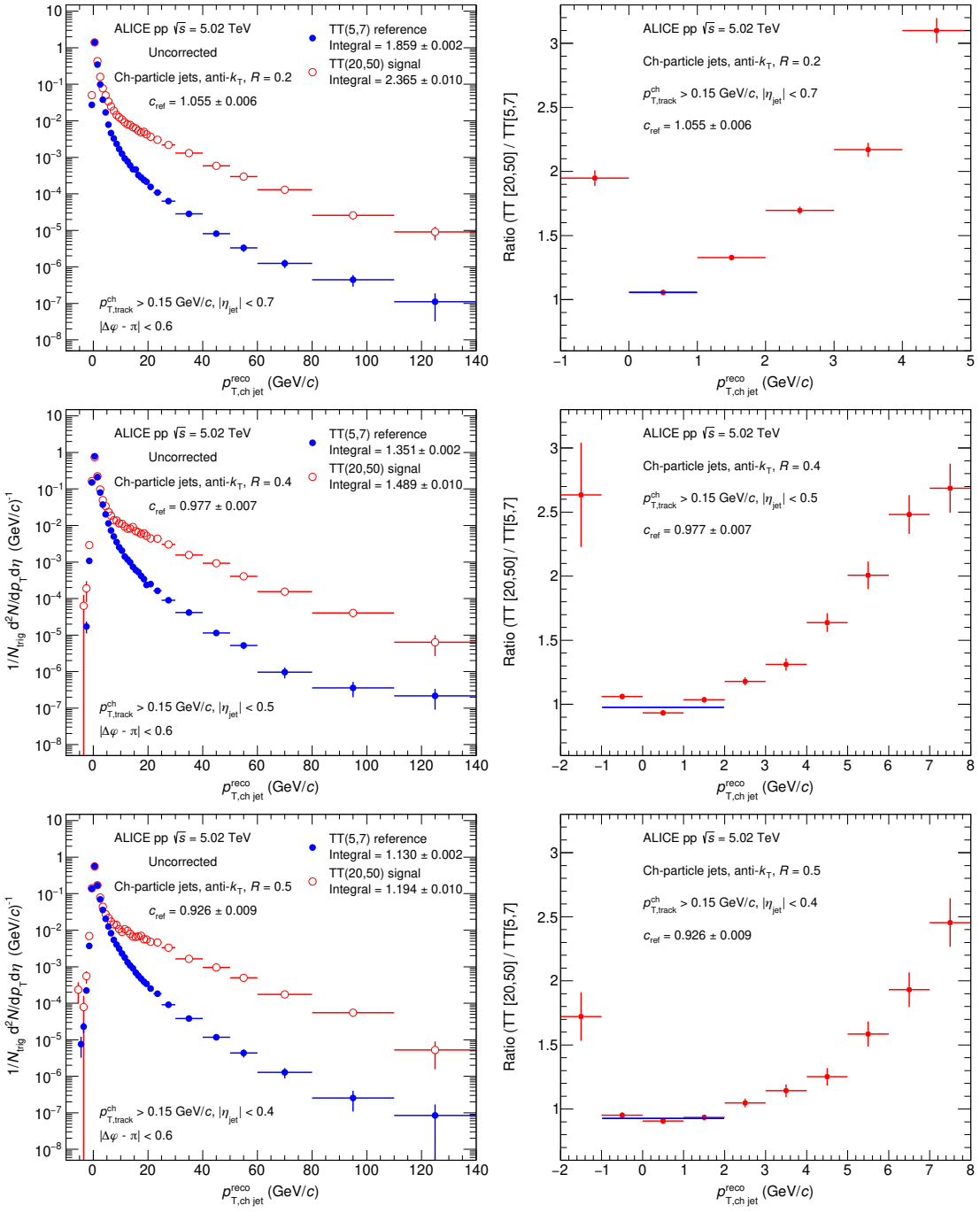

Figure 5.5: Left: trigger-normalized semi-inclusive recoil jet distributions with R = 0.2, 0.4, 0.5 for TT_{sig} and TT_{ref}-selected populations in pp collisions at $\sqrt{s}$ = 5.02 TeV; Right: ratio of the two distributions. The horizontal blue line indicates the fit to the ratio close to $p^{corr}_{T,ch\ jet}$ = 0 for the determination of c_{Ref}, the value of which is also given in the figures.

pol0 function. We use the fitting parameter as the c_{Ref} for Δ_{recoil} systematic analysis. From the fitting panel in Fig. 5.7, we can find the c_{ref} = 0.9992 for R = 0.2, c_{ref} = 0.9807 for R = 0.4 and c_{ref} = 0.9682

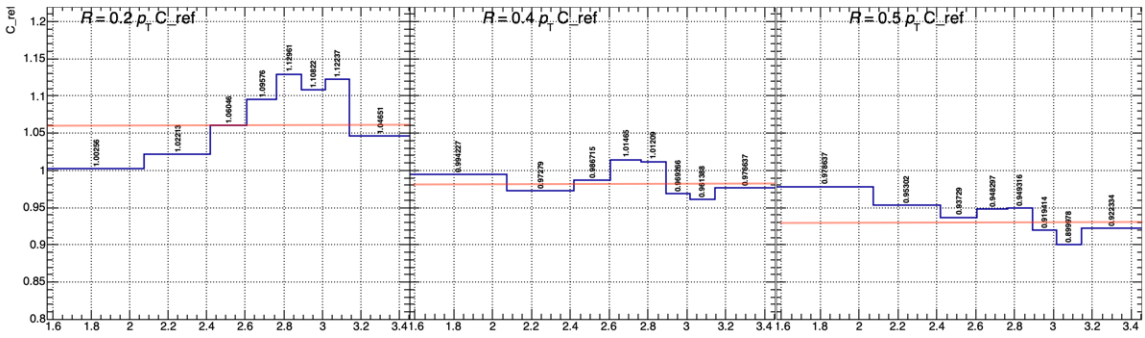

Figure 5.6: c_{Ref} distribution as a function of $\Delta\varphi$ for jet resolution parameters R = 0.2, 0.4 and 0.5.

for R = 0.5. These c_{Ref} results will also be considered as uncertainties.

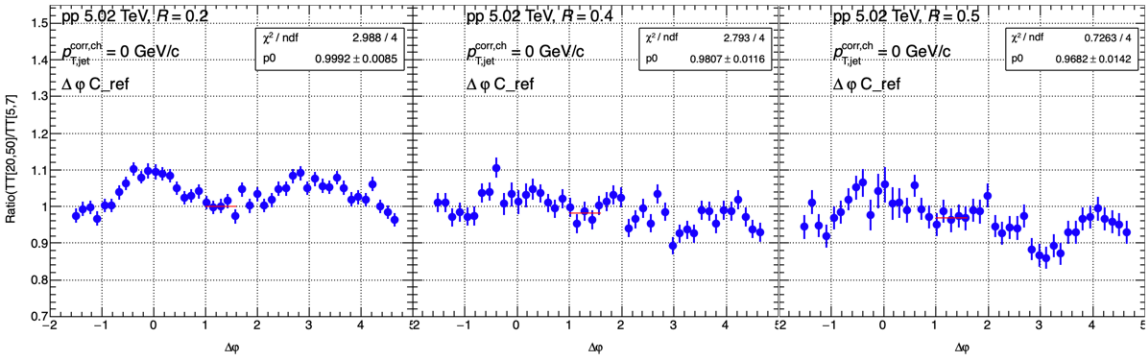

Figure 5.7: $\Delta\varphi$ ratios of distribution in signal TT{20, 50} to reference TT{5, 7} at p_{T} close to 0.

Once the c_{Ref} was obtained, the Δ_{recoil} distribution as a function of $\Delta\varphi$ and $p^{\mathrm{corr}}_{\mathrm{T,ch\ jet}}$ was calculated according to Eq. 5.2, as depicted in Fig. 5.8, for different jet resolution parameters R = 0.2, 0.4, and 0.5. These 2-dimensional distributions of Δ_{recoil} are used as input of the 2-dimensional unfolding correction.

Statistical reach

The measurement at high $p^{\mathrm{corr}}_{\mathrm{T,ch\ jet}}$ is limited by statistics. When unfolding a measured distribution to the particle level, a general rule ensuring a stable unfolding is that each bin of the measurement should contain at least 10 counts. To understand the optimal binning and kinematic reach of the measurement, the number of entries at high $p^{\mathrm{corr}}_{\mathrm{T,ch\ jet}}$ is investigated.

Statistical uncertainties in the raw distributions

The statistical uncertainties in the raw distributions take into account the statistical uncertainties from the signal and reference distributions. The uncertainty from the calculation of c_{Ref} is also included here, since the uncertainty from the fit to the ratio of the signal and reference distributions is statistical in

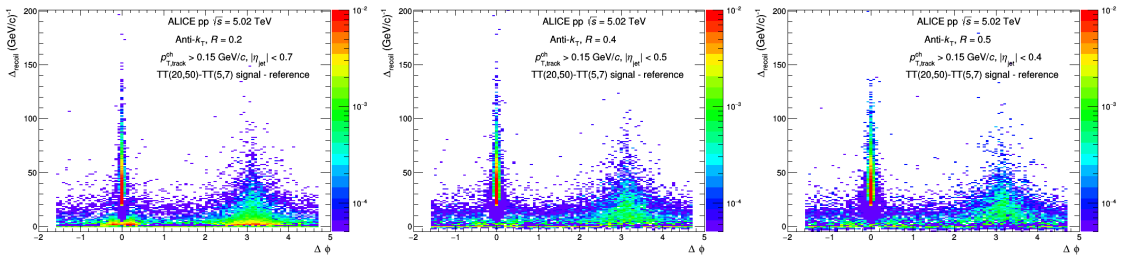

Figure 5.8: Δ_{recoil} distributions as a function of $\Delta\varphi$ and $p^{\text{corr}}_{\text{T,ch jet}}$ for jet radii $R = 0.2,\ 0.4,\ 0.5$ in pp collisions at $\sqrt{s} = 5.02$ TeV.

nature, and is calculated from the 1σ confidence interval of the fit. No statistical uncertainty on the number of trigger hadrons is assigned.

Expressing the bin content in a given bin for the observable Δ_{recoil} as B, the signal and reference counts as S and R, respectively, c_{Ref} as c and the number of triggers in the signal and reference class as T_R and T_S, respectively, then:

$$B = \frac{S}{T_S} - c\frac{R}{T_R} \tag{5.3}$$

The uncertainties on S, R and B are then

$$\Delta S^2 = S \tag{5.4}$$

$$\Delta R^2 = R \tag{5.5}$$

$$\Delta B^2 = \frac{S}{T_S^2} + (\frac{c}{T_R})^2 \times R + (\frac{R}{T_R})^2 \times \Delta c^2 \tag{5.6}$$

The statistical uncertainties in each bin of Δ_{recoil} are calculated in this way for both the pp and Pb–Pb analyses.

Figure 5.9 and Figure 5.10 show the trigger-normalized recoil jet distributions for TT_{sig} and TT_{ref}-selected populations, and the corresponding $\Delta_{\text{recoil}}(p^{\text{corr}}_{\text{T,ch jet}})$ and $\Delta_{\text{recoil}}(\Delta\varphi)$ distributions, for pp collisions at $\sqrt{s} = 5.02$ TeV. Figure 5.9 is presented distributions as functions of $p^{\text{corr}}_{\text{T,ch jet}}$ in the $\Delta\varphi$ acceptance of the $\Delta_{\text{recoil}}(p_{\text{T,ch jet}})$ analysis and Figure 5.10 is shown distributions as functions of $\Delta\varphi$ for $p^{\text{corr}}_{\text{T,ch jet}} \in [10, 20, 30, 50, 100]$ GeV/c. The TT_{ref} component is negligible except in a narrow region around $p^{\text{corr}}_{\text{T,ch jet}} = 0$, so that the Δ_{recoil} distributions closely match those of the TT_{sig}-selected population.

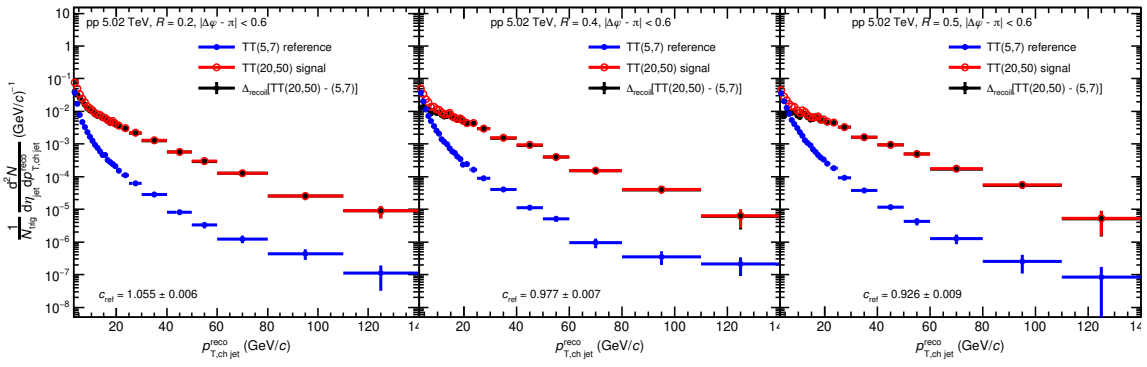

Figure 5.9: Trigger-normalized semi-inclusive recoil jet distributions for $\mathrm{TT}_{\mathrm{sig}}$ and $\mathrm{TT}_{\mathrm{ref}}$-selected populations in pp collisions at $\sqrt{s} = 5.02$ TeV, for $R = 0.2$ (left), 0.4 (middle), and 0.5 (right). The $\mathrm{TT}_{\mathrm{ref}}$ distribution is scaled by c_{Ref}. The resulting Δ_{recoil} distribution is also shown. Distributions as a function of $p_{\mathrm{T,ch\ jet}}^{\mathrm{corr}}$ in the $\Delta\varphi$ acceptance of the $\Delta_{\mathrm{recoil}}(p_{\mathrm{T,ch\ jet}})$ analysis. $\mathrm{TT}_{\mathrm{sig}}$ and $\mathrm{TT}_{\mathrm{ref}}$ distributions in left middle panel are the same as in Fig. 5.5, left panel.

After determining the default sets (reference: $\mathrm{TT}\{5,7\}$ GeV/c, signal: $\mathrm{TT}\{20,50\}$ GeV/c) for our main results, we also examine the other signal trigger track intervals. The reference TT interval is $\mathrm{TT}\{5,7\}$ GeV/c, while the signal trigger track intervals are $\mathrm{TT}\{15,20\}$ GeV/c, $\mathrm{TT}\{20,30\}$ GeV/c, and $\mathrm{TT}\{30,50\}$ GeV/c, which are then compared with the default sets. Fig. 5.11 illustrates the comparison of raw $\Delta_{\mathrm{recoil}}(p_{\mathrm{T,ch\ jet}})$ in different signal trigger track intervals.

5.6 Unfolding correction

Similar to the previous unfolding correction in Section 4.4 for multiplicity-dependent jet production, the semi-inclusive distributions should also be expressed at "truth" level to correct the instrumental effects and background fluctuations. The distributions reported here have two components: the high-p_{T} trigger hadron, which is used for event selection, and the reconstructed jets in the selected events. The corrections for each component are discussed next.

5.6.1 Trigger hadrons

As discussed in Ref. [15], high-p_{T} charged hadrons rather than jets are chosen as the trigger for this analysis because they are measured in pp and central Pb–Pb collisions with high precision event-by-event, without the need for corrections to the complex accompanying background. Tracking efficiency at high-p_{T} is independent of p_{T} [226], so that the loss of tracks due to inefficiency is equivalent to a reduction in integrated luminosity without imposing a bias on the hadron selection. Correction for the trigger hadron tracking efficiency is therefore not required. The effect of track momentum resolution on the selection of trigger hadrons near threshold was found to be negligible in Ref. [15], so is also not considered here.

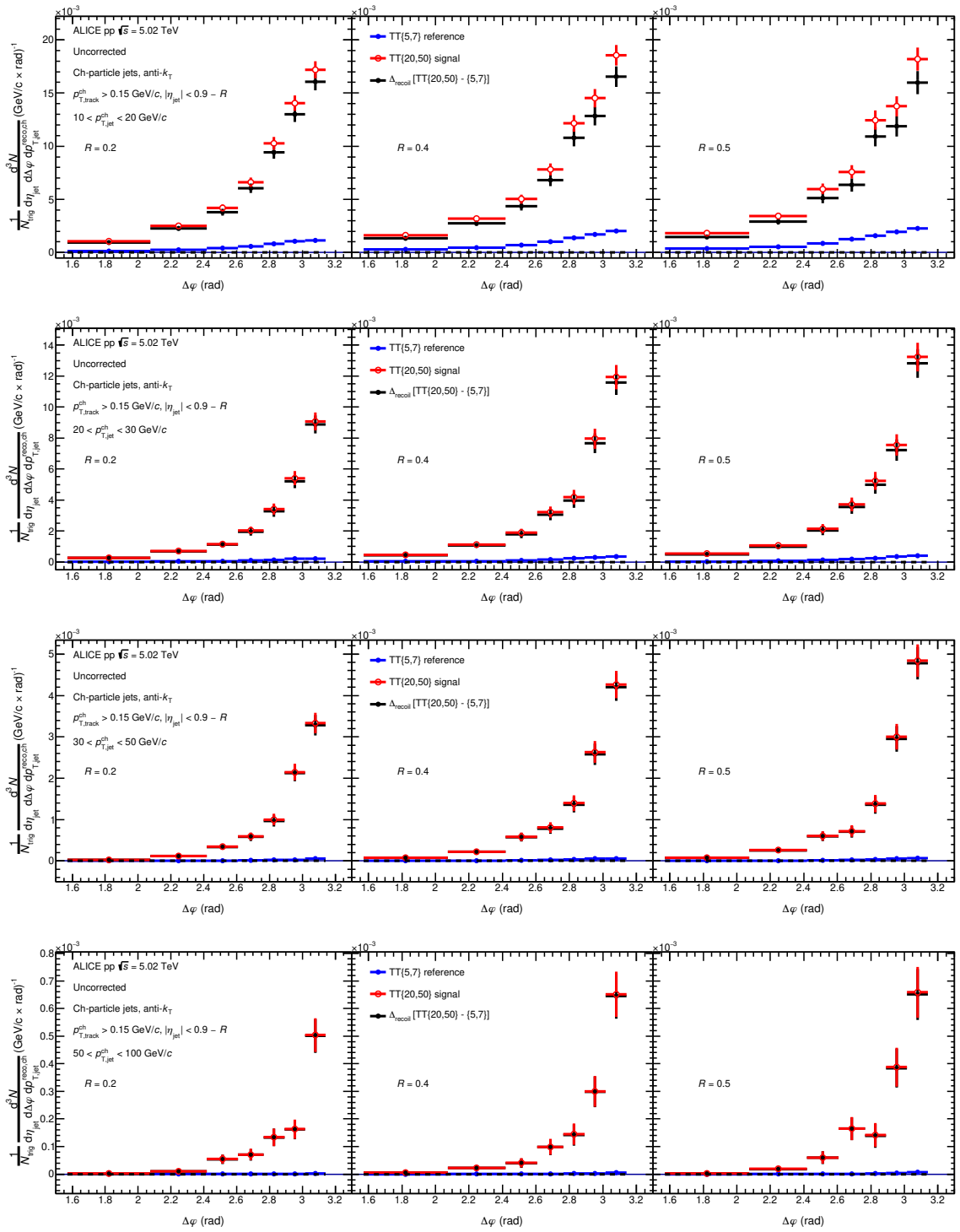

Figure 5.10: Trigger-normalized semi-inclusive recoil jet distributions for TT_{sig} and TT_{ref}-selected populations in pp collisions at $\sqrt{s}$ = 5.02 TeV, for R = 0.2 (left), 0.4 (middle), and 0.5 (right). The TT_{ref} distribution is scaled by c_{Ref}. The resulting Δ_{recoil} distribution is also shown. Distributions as a function of $\Delta\varphi$, for $p_{T,ch\ jet}^{corr} \in [10, 20, 30, 50, 100]$ GeV/c.

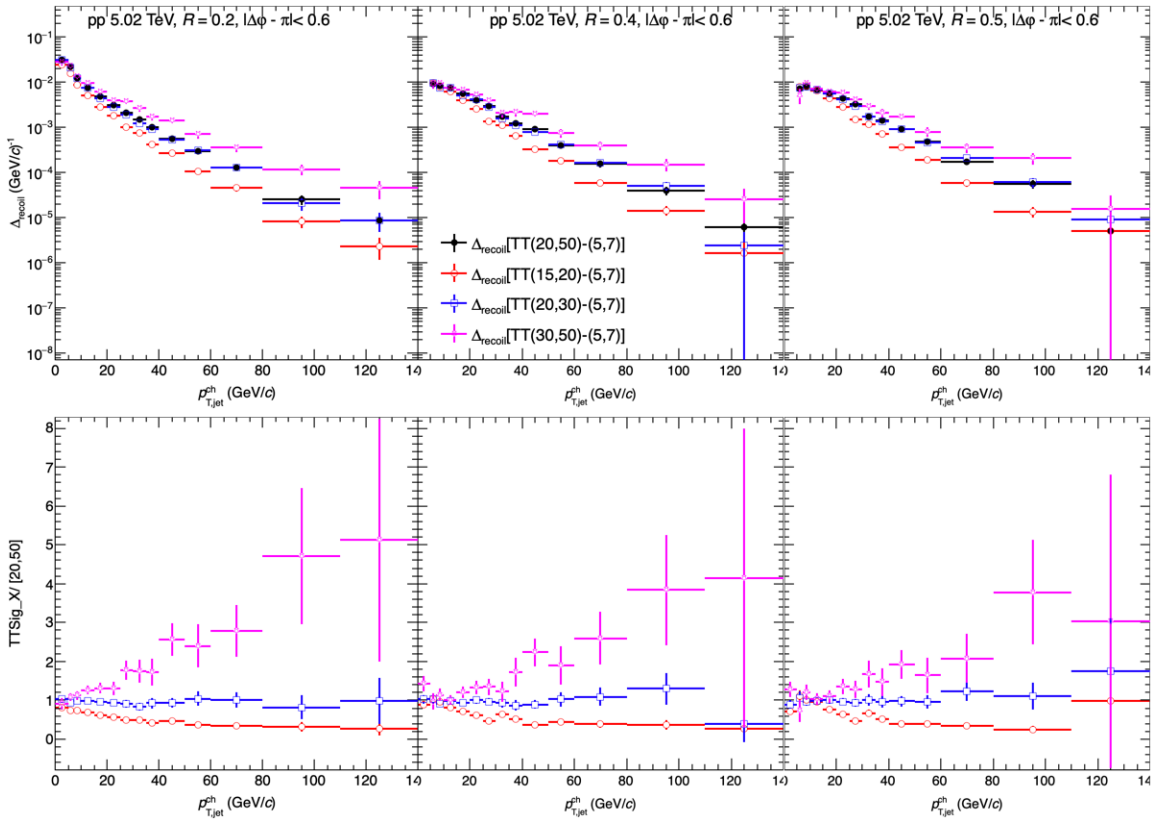

Figure 5.11: Comparison of raw $\Delta_{\text{recoil}}(p_{\text{T,ch jet}})$ distribution for TT$\{20,50\}$ and TT$\{15,20\}$, TT$\{20,30\}$, TT$\{30,50\}$ GeV/c for $R = 0.2$ (left) 0.4 (middle) 0.5 (right).

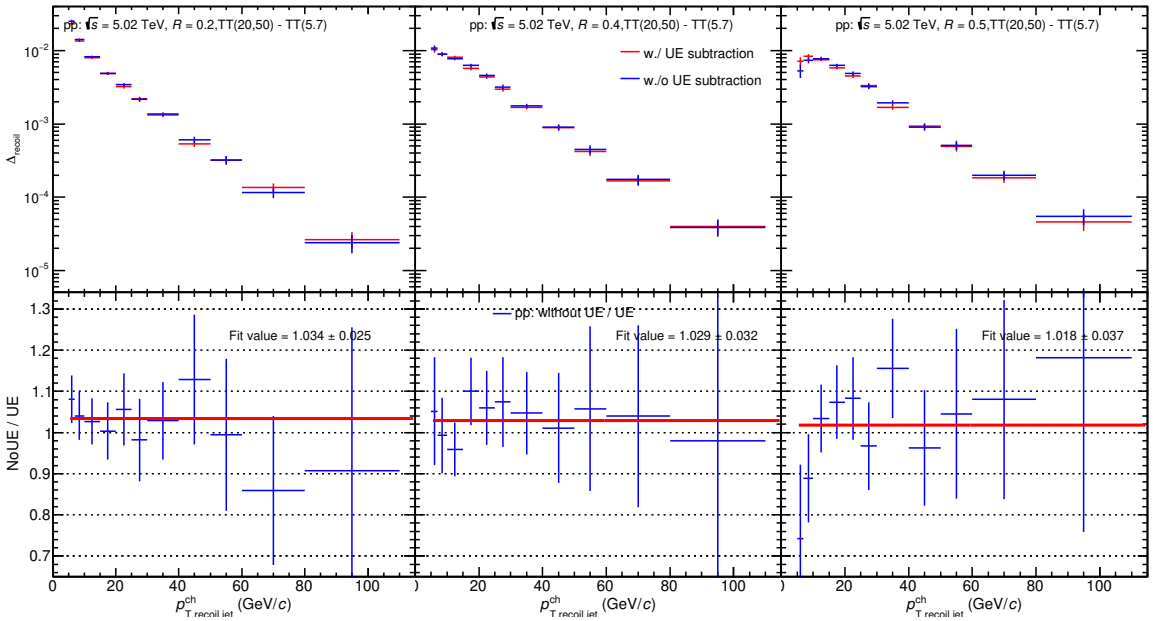

Figure 5.12: $\Delta_{\text{recoil}}(p_{\text{T,ch jet}})$ comparisons with and without UE subtraction for different jet radii $R = 0.2,\ 0.4$ and 0.5

The azimuthal angle (φ) resolution of charged tracks is better than 0.5 m rad for tracks with $p_{\text{T}} > 5$ GeV/c, and as such no correction for angular smearing of the trigger track is warranted.

5.6.2 Reconstructed jet distributions

The measured charged-particle jet distributions are corrected for the effects of both detector response and residual background fluctuations. The detector response corresponds to the effects of tracking inefficiencies, track p_{T}-resolution, and weak-decay background, all of which modify the jet momentum and axis when the jet is reconstructed.

Before the unfolding, we evaluated the impact of background fluctuations on Δ_{recoil} in pp collisions by comparing the Δ_{recoil} distributions with and without background subtraction. Fig. 5.12 compares the $\Delta_{\text{recoil}}(p_{\text{T,ch jet}})$ spectrum with and without background subtraction, Fig. 5.13 shows the $\Delta_{\text{recoil}}(\Delta\varphi)$ comparison. The ratios of distributions without and with UE subtraction for p_{T} and $\Delta\varphi$ revealed that the background minimally impacts Δ_{recoil}. This finding further validates the efficiency of the data-driven approach in mitigating background effects on Δ_{recoil} by computing the difference. So in this pp analysis, detector effects were corrected only through the detector response matrix, without consideration of the effect of background fluctuations. Fig. A.1 illustrates a significant disparity between the results when the inclusive jet spectrum is subtracted with background and when it is not.

Correction for detector response is carried out using an unfolding procedure. For the $\Delta_{\text{recoil}}(p_{\text{T,ch jet}})$

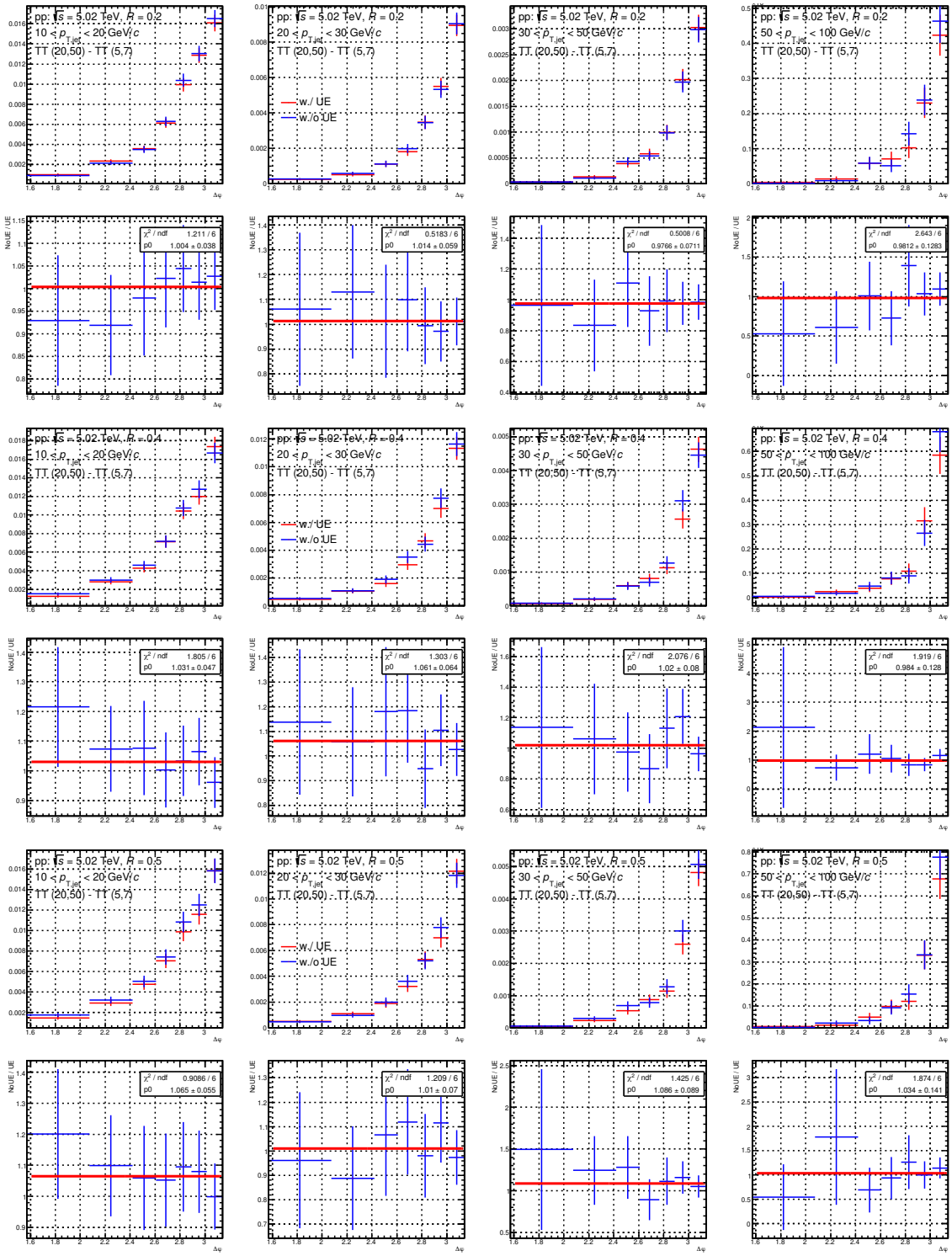

Figure 5.13: $\Delta_{\text{recoil}}(\Delta\varphi)$ comparisons with and without UE subtraction for different jet radii $R = 0.2,\ 0.4$ and 0.5

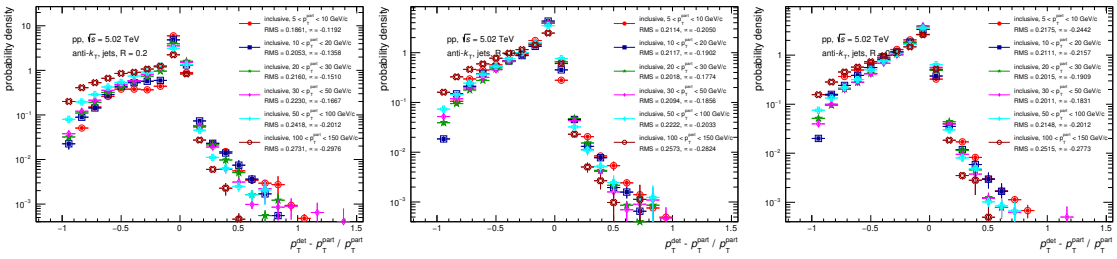

Figure 5.14: Residual distribution for $R = 0.2$, 0.4 and 0.5 for inclusive jets used to unfold in pp collisions at $\sqrt{s} = 5.02$ TeV.

analysis unfolding is performed in one dimension using Bayesian and SVD methods, $p_{\mathrm{T,jet}}$, with a 2-dimensional response matrix built from the detector-level and matched particle-level jets. While for the $\Delta_{\mathrm{recoil}}(\Delta\varphi)$ analysis unfolding is done in two dimensions using Bayesian approach, $p_{\mathrm{T,jet}}$ and $\Delta\varphi$, with a 4-dimensional response matrix built from detector-level jet $p_{\mathrm{T,jet}}$ and $\Delta\varphi$ to the particle level. $\Delta_{\mathrm{recoil}}(p_{\mathrm{T,ch\ jet}})$ for the two cases are consistent within experimental uncertainties for all R, when projected in a common $\Delta\varphi$ acceptance. Inclusive jets are used to fill the response matrix to reduce the influence of trigger track bias in this analysis. The resolution of inclusive and recoil jets has been checked and are seen to be very similar over all jet p_{T} relevant for this analysis.

While the unfolding procedure is carried out using the detector response matrices described below, key parameters that characterize the detector performance for jet reconstruction are summarized here for reference.

$p_{\mathrm{T,jet}}$ resolution and median $p_{\mathrm{T,jet}}$ shift: The detector effects which smear the $p_{\mathrm{T,jet}}$ distribution are characterized in pp simulations with the relative difference between the $p_{\mathrm{T,jet}}$ at detector level and particle level, as defined in Equation 4.4. Figure 5.14 displays the distributions of inclusive jet p_{T} resolution used for unfolding and Table 5.2 shows the corresponding width and median shift of this distribution for $R = 0.2$, 0.4 and 0.5 in selected $p^{\mathrm{part}}_{\mathrm{T,ch\ jet}}$ intervals. Since a value of $p^{\mathrm{det}}_{\mathrm{T,ch\ jet}}$ larger than $p^{\mathrm{part}}_{\mathrm{T,ch\ jet}}$ can only arise from $p_{\mathrm{T,jet}}$ resolution effects, and the distribution is not symmetric about zero, the $p_{\mathrm{T,jet}}$ resolution is determined by fitting a Gaussian function to the distribution for $(p^{\mathrm{det}}_{\mathrm{T,ch\ jet}} - p^{\mathrm{part}}_{\mathrm{T,ch\ jet}})/p^{\mathrm{part}}_{\mathrm{T,ch\ jet}} > 0$ (Right hand side, RHS) while fixing the mean of the fit to zero, since resolution effects are symmetric. The median relative $p^{\mathrm{part}}_{\mathrm{T,ch\ jet}}$ shift, which is non-zero due to detector inefficiencies, is also reported. These values are representative of the instrumental effects in pp collisions.

$\Delta\varphi$ resolution: The resolution in $\Delta\varphi$, denoted as $\sigma_{\Delta\varphi}$, is also the standard deviation of the difference between detector-level and truth-level jet values of $\Delta\varphi$. Figure 5.15 displays the distributions of inclusive jet $\Delta\varphi$ resolution used for unfolding, while Table 5.3 presents the corresponding $\sigma_{\Delta\varphi}$ values for $R = 0.2$,

Table 5.2: The resolution and median of the relative smearing of $p_{\mathrm{T,jet}}$ due to detector effects, JES as $S = (p^{\mathrm{det}}_{\mathrm{T,ch\ jet}} - p^{\mathrm{part}}_{\mathrm{T,ch\ jet}})/p^{\mathrm{part}}_{\mathrm{T,ch\ jet}}$, for $R = 0.2, 0.4$ and 0.5 in selected $p^{\mathrm{part}}_{\mathrm{T,ch\ jet}}$ intervals. Values are expressed in percentages.

	$R = 0.2$		$R = 0.4$		$R = 0.5$	
$p^{\mathrm{part}}_{\mathrm{T,ch\ jet}}$[GeV/$c$]	$\sigma^{\mathrm{RHS}}(S)$	median(S)	$\sigma^{\mathrm{RHS}}(S)$	median(S)	$\sigma^{\mathrm{RHS}}(S)$	median(S)
[5, 10]	0.19	−0.12	0.21	−0.21	0.22	−0.24
[50, 100]	0.24	−0.2	0.22	−0.20	0.21	−0.20

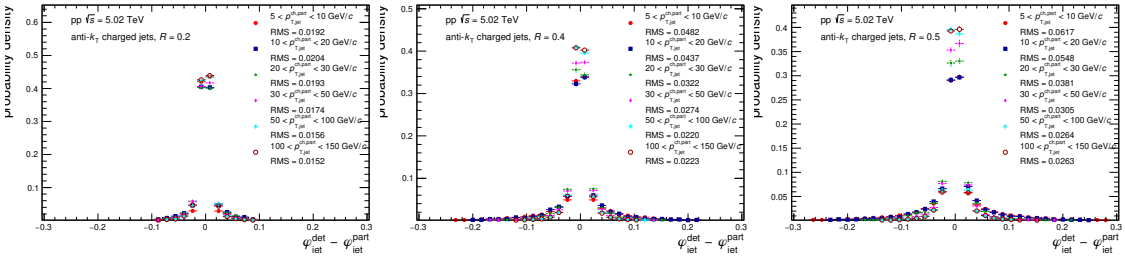

Figure 5.15: $\Delta\varphi$ resolution distribution for $R = 0.2$, 0.4 and 0.5 for inclusive jets used to unfold in pp collisions at $\sqrt{s} = 5.02$ TeV.

0.4, and 0.5 jets for selected intervals of $p_{\mathrm{T,jet}}$ in simulations of pp collisions. This resolution is due to detector effects and is finer for high $p^{\mathrm{part}}_{\mathrm{T,ch\ jet}}$ and small R. It is important to note that $\sigma_{\Delta\varphi}$ is typically smaller than the width of the $\Delta\varphi$ bins used in the analysis, and therefore corresponds to only a small correction in $\Delta\varphi$.

Table 5.3: Azimuthal difference resolution $\sigma_{\Delta\varphi}$ for $R = 0.2$ and 0.5 in pp collisions in selected $p^{\mathrm{part}}_{\mathrm{T,ch\ jet}}$ intervals. Values are expressed in radians.

	$R = 0.2$	$R = 0.4$	$R = 0.5$
$p^{\mathrm{part}}_{\mathrm{T,ch\ jet}}$[GeV/$c$]	$\sigma_{\Delta\varphi}$	$\sigma_{\Delta\varphi}$	$\sigma_{\Delta\varphi}$
[10, 20]	0.020	0.04	0.05
[50, 100]	0.015	0.02	0.03

Unfolding

In the pp analysis, the response matrix is also constructed from MC full simulations. pp collisions are generated using the PYTHIA8 generator (Monash2013 tune), and particles generated in these collisions are transported through the simulated ALICE detector using GEANT3. Detector-level jets are matched to particle-level jets based on their relative separation in rapidity and azimuth, $\Delta R = \sqrt{\Delta\eta^2 + \Delta\varphi^2}$, and requiring ΔR to be less than 0.15 for $R = 0.2$ jets, 0.25 for $R = 0.4$ jets, and 0.35 for $R = 0.5$. The response matrix for this analysis is depicted in Fig. 5.16, where the X-axis represents the detector-level jets, and the Y-axis represents the particle-level jets.

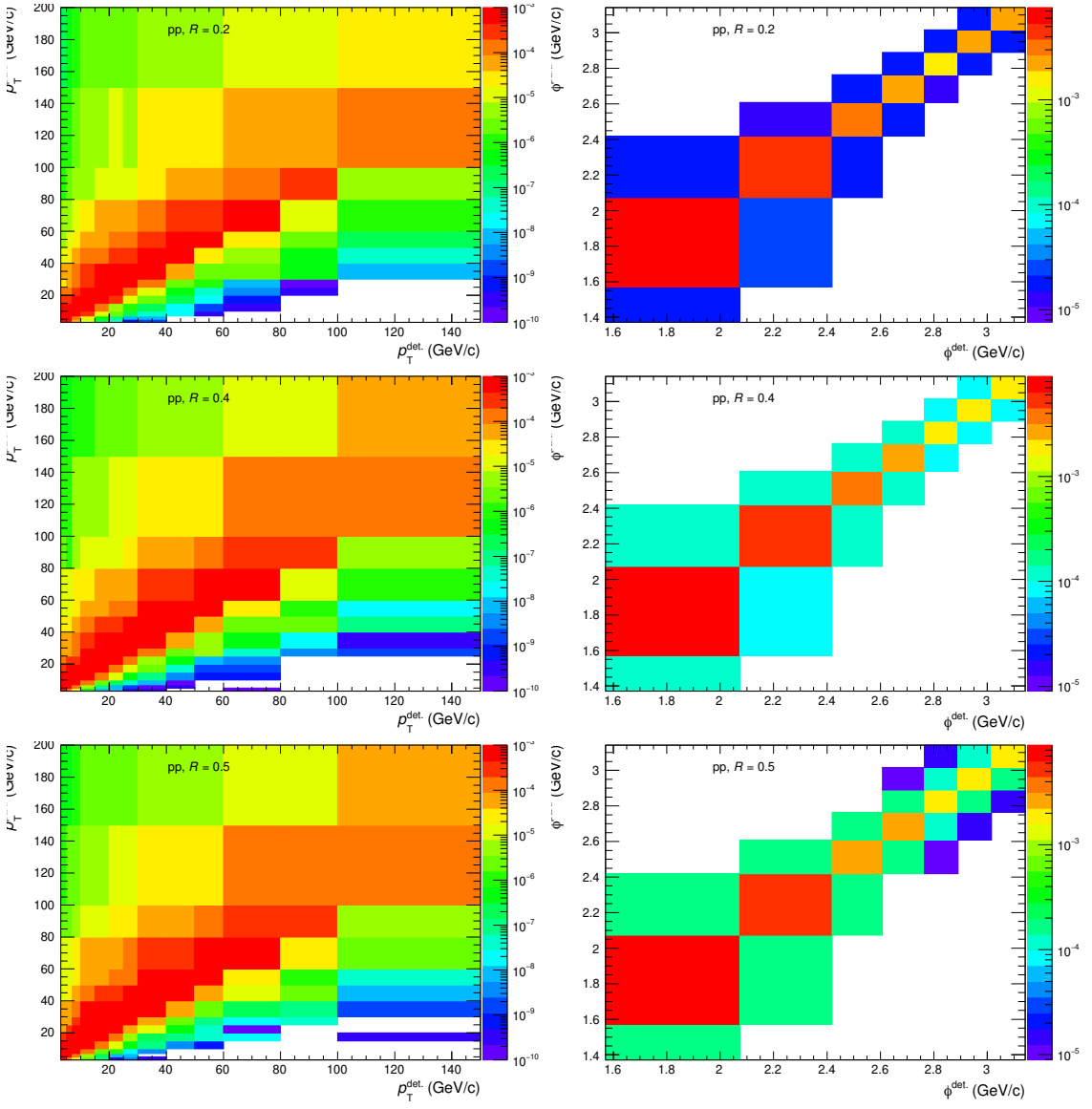

Figure 5.16: Inclusive p_T and $\Delta\varphi$ response matrix using the projection of 4-dimensional response matrix for jet R = 0.2, 0.4 and 0.5 in pp collisions at $\sqrt{s}$ = 5.02 TeV.

Unfolding is carried out using the iterative Bayesian algorithm implemented in the RooUnfold package [25]. For the $\Delta_{\text{recoil}}(p_{\text{T,ch jet}})$ analysis, unfolding is carried out in one dimension to correct $p^{\text{corr}}_{\text{T,ch jet}}$, taking advantage of the fact that the $\Delta\varphi$ resolution correction is small. For the $\Delta_{\text{recoil}}(\Delta\varphi)$ analysis, two-dimensional unfolding is used to correct both $p^{\text{corr}}_{\text{T,ch jet}}$ and $\Delta\varphi$. Crucial to this analysis is the ability to include the full $p^{\text{corr}}_{\text{T,ch jet}}$ range in the unfolding, which is enabled by the subtraction of the entire combinatorial background yield; the full Δ_{recoil} range shown in Figs. 5.9 and 5.10 is therefore used in the unfolding.

The regularization parameter, which for iterative Bayesian unfolding is the number of iterations, is optimized using both a consistency test between the raw and back-folded distributions, and the requirement that unfolded distributions from successive iterations have minimal variation. The optimal regularization parameters lie between 4 and 8, depending on collision system and jet R.

A key element of the unfolding procedure is the choice of prior. For the pp analysis the prior is based on the Δ_{recoil} distribution calculated with PYTHIA8. The distributions are fitted with a smooth function to remove the effect of finite statistical precision in the MC generation.

For the one-dimensional (1d) or two-dimensional (2d) $\Delta_{\text{recoil}}(p_{\text{T,ch jet}})$ analysis, The prior $P(p_{\text{T,jet}})$ corresponds to the true distribution $\Delta_{\text{recoil}}(p^{\text{part}}_{\text{T,ch jet}})$ generated by the PYTHIA MC and fitted using the exponential function $\Delta(p_{\text{T,jet}}) = p_0 \exp(-p_1 \times p_{\text{T,jet}}) + p_2 \times (p_{\text{T,jet}})^{p_3}$, where $p_{0,1,2,3}$ are the fitting parameters. For the $\Delta_{\text{recoil}}(\Delta\varphi)$ analysis, the $\Delta\varphi$ projections of the prior are parameterized with a function defined as $g(\Delta\varphi) = q_1 \times \exp(\frac{\Delta\varphi-\pi}{\sigma}) + q_2$, where $q_{1,2}$ and σ are fit parameters. The function $g(\Delta\varphi)$ is used to fit the $\Delta\varphi$ distribution for each $p_{\text{T,jet}}$ bin separately. The function $g(\Delta\varphi)$ in each $p_{\text{T,jet}}$ interval is then scaled such that the integral of $g(\Delta\varphi)$ in the region $|\Delta\varphi - \pi| < 0.6$ is equal to $P(p_{\text{T,jet}})$ in the same $p_{\text{T,jet}}$ region. The priors of $\Delta_{\text{recoil}}(p_{\text{T,ch jet}})$ and $\Delta_{\text{recoil}}(\Delta\varphi)$ are shown in Fig. 5.17 for different jet radii $R = 0.2, 0.4$ and 0.5. The $\Delta_{\text{recoil}}(\Delta\varphi)$ prior is displayed in each 5 GeV/c p_{T} binning. We vary the p_3 by ± 0.5 in $P(p_{\text{T,jet}})$ to modify the shape of the p_{T} spectrum, aiming to compute the systematic uncertainty caused by the choice of prior for Δ_{recoil} distribution.

Jet kinematic efficiency and jet-finding efficiency

An efficiency correction, which is a function of $p_{\text{T,ch jet}}$ and $\Delta\varphi$, is applied to the unfolded spectrum to account for the loss of jets outside the measured range due to smearing effects. This efficiency is also known as the kinematic efficiency and it is calculated using PYTHIA8 simulations in pp collisions. Figures 5.18 and 5.19 are shown the kinematic efficiency as function of $p_{\text{T,ch jet}}$ and $\Delta\varphi$ for different jet radii $R = 0.2, 0.4$ and 0.5, separately. For the $\Delta_{\text{recoil}}(p_{\text{T,ch jet}})$ analysis, the efficiency for all R is

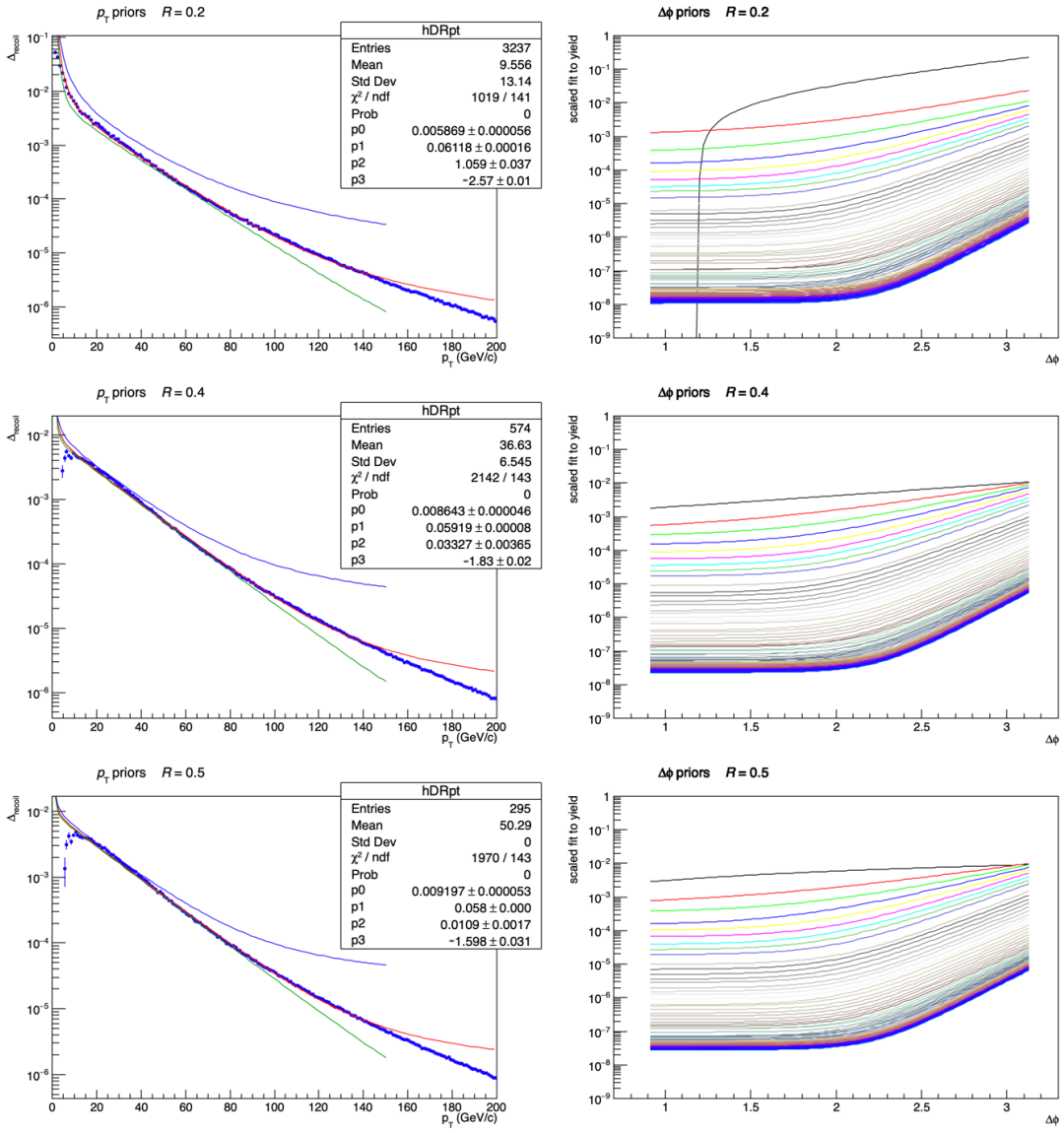

Figure 5.17: Priors of $\Delta_{\text{recoil}}(p_{\text{T,ch jet}})$ (left) and $\Delta_{\text{recoil}}(\Delta\varphi)$ (right) from the PYTHIA used for 1d and 2d unfolding with jet radii $R = 0.2$ (top),0.4 (middle) and 0.5 (bottom). In the left, red line is the fitting function for particle-level p_{T} distribution. Blue and green lines represent the vary the $p_3 \pm 0.5$ fitting functions. In right result, each function describes the $\Delta\varphi$ distribution in $p_{\text{T,jet}}$ bins of 5 GeV/c width, where the top-most line (black) is that in the region $0 < p_{\text{T}} < 5$ GeV/c and the bottom-most line is that in the region $295 < p_{\text{T}} < 300$ GeV/c. The integral of the function in $3\pi/4 < \Delta\varphi < \pi$ is scaled to the fit to the $p_{\text{T,ch jet}}$ distribution.

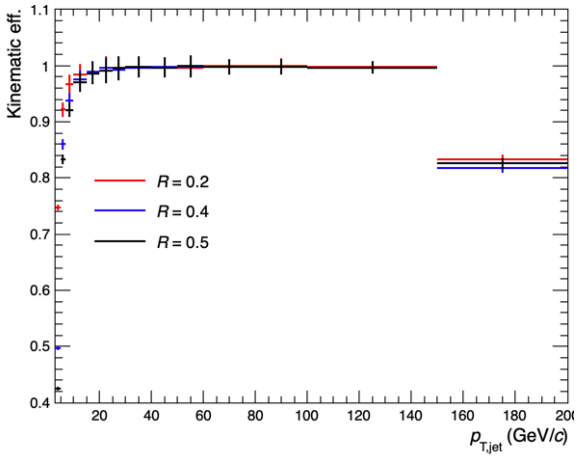

Figure 5.18: The kinematic efficiency of $\Delta_{\text{recoil}}(p_{\text{T,ch jet}})$ for R = 0.2, 0.4 and 0.5 in pp collisions at $\sqrt{s}$ = 5.02 TeV.

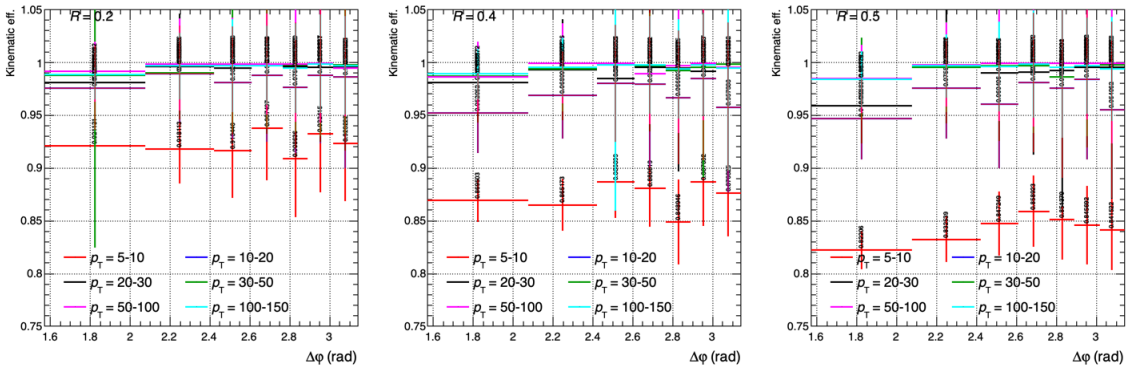

Figure 5.19: The kinematic efficiency of $\Delta_{\text{recoil}}(\Delta\varphi)$ for R = 0.2, 0.4 and 0.5 in selected $p_{\text{T,ch jet}}$ intervals in pp collisions at $\sqrt{s}$ = 5.02 TeV.

greater than 97% for $p_{\text{T,ch jet}} = 10$ GeV/c, and consistent with unity at $p_{\text{T,ch jet}} = 140$ GeV/c. For the $\Delta_{\text{recoil}}(\Delta\varphi)$ analysis, the efficiency is about 98% for $R = 0.2$ (96% for $R = 0.5$) at $\Delta\varphi \sim \pi/2$, increasing to 100% for $R = 0.2$ (99% for $R = 0.5$) at $\Delta\varphi \sim \pi$ in given $p_{\text{T,ch jet}} \in (20, 30)$ GeV/c.

An additional efficiency correction is applied after unfolding to account for the probability of reconstructing a particle-level jet, i.e. for the matching efficiency when constructing the response matrix. This factor is calculated using PYTHIA8 simulations of pp events, as the ratio of detector-level and particle-level jet yield. It is found to be independent of $\Delta\varphi$. In pp collisions, it is approximately 92% at $p_{\text{T,ch jet}} = 10$ GeV/c and 100% at $p_{\text{T,ch jet}} = 100$ GeV/c, as shown in Fig. 5.20.

Once we have the response matrix and prior, we can perform the unfolding correction with the following sets. The binning at the particle level and detector level is chosen based on the statistics in each region of $\Delta_{\text{recoil}}(p_{\text{T,ch jet}})$ and $\Delta_{\text{recoil}}(\Delta\varphi)$. The binning used for unfolding is as follows for 1d unfolding:

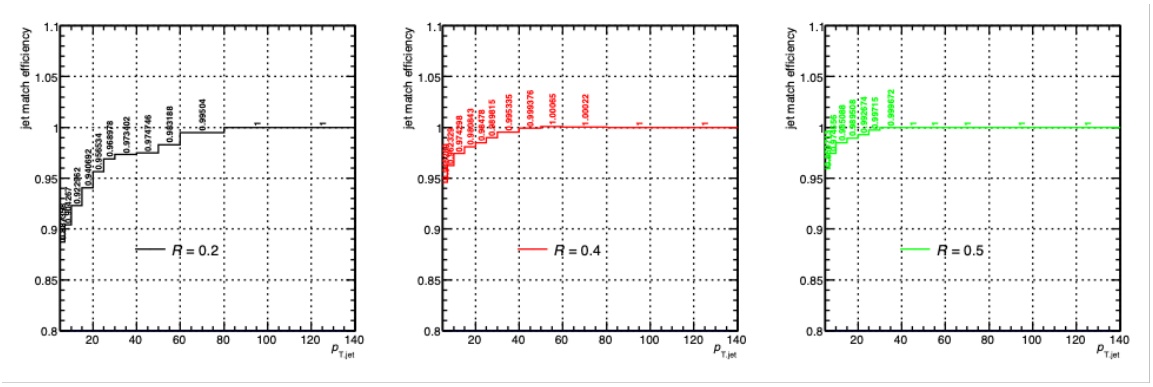

Figure 5.20: The jet reconstruction efficiency for $R = 0.2$, 0.4 and 0.5 in pp collisions at $\sqrt{s} = 5.02$ TeV.

- $p_{T,\text{ch jet}}$

  raw binning: $[2, 3, 5, 7, 10, 15, 20, 25, 30, 40, 50, 60, 80, 110, 140, 180]$ GeV/c;

  particle level binning: $[1, 2, 3, 5, 7, 10, 15, 20, 25, 30, 40, 50, 60, 80, 110, 140, 200]$ GeV/c;

In $\Delta_{\text{recoil}}(\Delta\varphi)$ where 2D unfolding is performed to correct both $\Delta\varphi$ and $p_{T,\text{ch jet}}$ the binning is as follows:

- $p_{T,\text{ch jet}}$

  projection binning for $\Delta\varphi$: $[0, 5, 10, 20, 30, 50, 100]$ GeV/c;

  raw binning: $[3, 5, 7, 10, 15, 20, 25, 30, 40, 50, 60, 80, 100, 150[$ GeV/c;

  particle level binning: $[2, 3, 5, 7, 10, 15, 20, 25, 30, 40, 50, 60, 80, 100, 150, 200]$ GeV/c;

- $\Delta\varphi$

  raw binning: $[\frac{50}{100}\pi, \frac{60}{100}\pi, \frac{66}{100}\pi, \frac{77}{100}\pi, \frac{83}{100}\pi, \frac{88}{100}\pi, \frac{92}{100}\pi, \frac{96}{100}\pi, \pi]$ rad;

  particle level binning: $[\frac{50}{100}\pi - 0.1, \frac{50}{100}\pi, \frac{60}{100}\pi, \frac{68}{100}\pi, \frac{76}{100}\pi, \frac{83}{100}\pi, \frac{88}{100}\pi, \frac{92}{100}\pi, \frac{96}{100}\pi, \pi]$ rad;

Unfolding for $\Delta_{\text{recoil}}(p_{T,\text{ch jet}})$ and $\Delta_{\text{recoil}}(\Delta\varphi)$

The unfolding process is validated by full closure tests in simulation. Bayesian unfolding is used for the nominal analysis to perform the unfolding process and obtain the unfolded and refolded results. We performed a closure test in MC to check the validity of the unfolding. Here the detector-level PYTHIA distribution is unfolded using the response matrix and compared to the truth-level PYTHIA distribution. The left panel in Fig. 5.21 shows the $\Delta_{\text{recoil}}(p_{T,\text{ch jet}})$ MC unfolding closure distribution for different iterations in the Bayesian method of 1-dimensional unfolding. The distributions are seen to agree well to within a few percent. For the MC unfolding we choose iterations are 4 for $R = 0.2$, $k = 6$ for $R = 0.4, 0.5$. We performed a refolding test to ensure stability of the 1-dimensional unfolding, where the unfolded result is refolded using the response matrix and compared to the measured distributions. Right panel of Fig. 5.21 shows the $\Delta_{\text{recoil}}(p_{T,\text{ch jet}})$ MC refolding closure distribution for different Bayesian

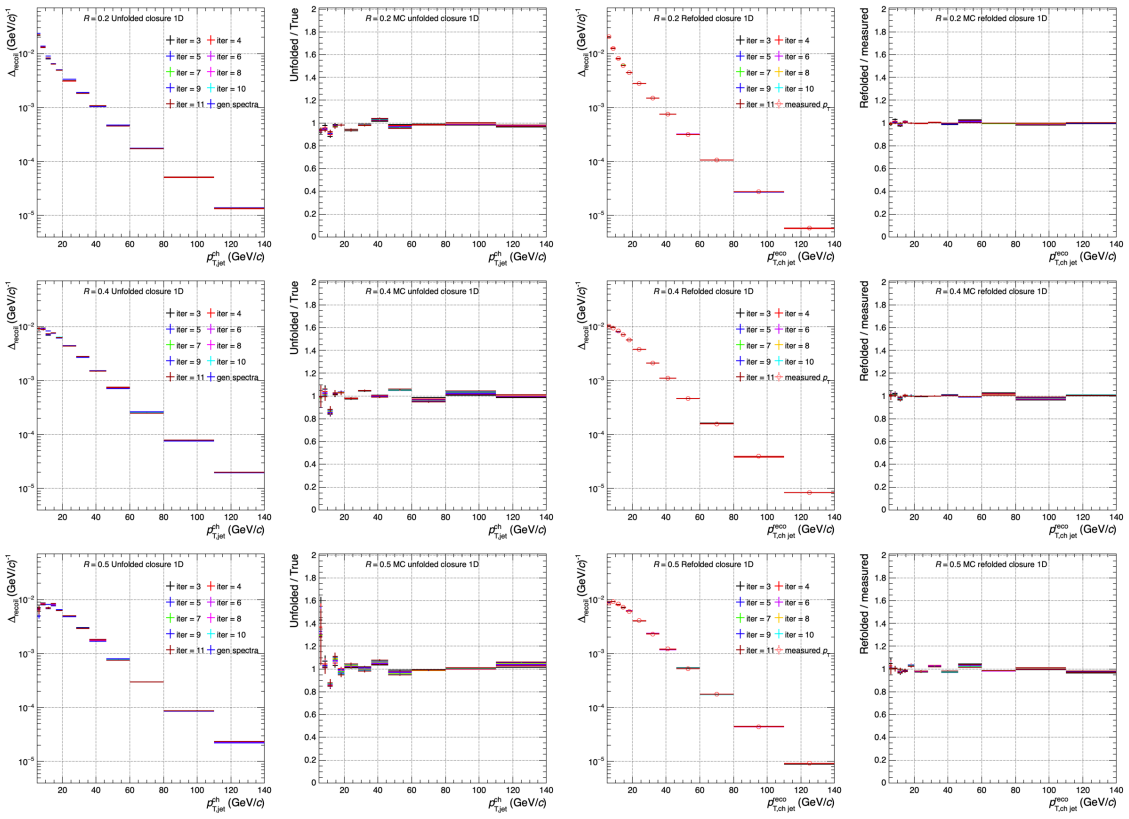

Figure 5.21: MC unfolding and refolding closure test of $\Delta_{\text{recoil}}(p_{\text{T,ch jet}})$ using Bayesian 1d unfolding method for $R = 0.2,\ 0.4,\ 0.5$ in pp collisions. First column: MC unfolded $\Delta_{\text{recoil}}(p_{\text{T,ch jet}})$ distributions for each iteration from 3 to 11. Second column: Ratio of the unfolded to true distribution for different iterations. Third column: MC refolded $\Delta_{\text{recoil}}(p_{\text{T,ch jet}})$ distribution as a function of the different iterations. Fourth column: Ratio of the refolded to raw distribution with $R = 0.2,\ 0.4,\ 0.5$.

iterations and the ratios are generally consistent unit.

The same unfolding closure and refolding checks are performed for the 2-dimensional unfolded analysis. Figure 5.22 shown the $\Delta_{\text{recoil}}(\Delta\varphi)$ MC closure in $p_{\text{T}} \in [10, 20]$ and $[30, 50]$ GeV/c intervals, for $R = 0.2$, 0.4 and 0.5, respectively. Convergence of the refolded spectra is obtained over the full $\Delta_{\text{recoil}}(\Delta\varphi)$ range after a few iterations to within a few percent within the statistical uncertainties of the raw distribution.

Next, the unfolding procedure is performed for measured $\Delta_{\text{recoil}}(p_{\text{T,ch jet}})$ and $\Delta_{\text{recoil}}(p_{\text{T,ch jet}}, \Delta\varphi)$ using Bayesian unfolding. Figure 5.23 shows the unfolded distributions for different iterations of the 1D Bayesian unfolding and the variation with respect to the previous iteration - it can be seen that the variation falls to within 1 – 2% within 4 iterations. The central selected iteration number is 8 for jet radii $R = 0.2,\ 0.4,\ 0.5$. The unfolded distributions are refolded and compared to raw $p_{\text{T,chjet}}$ distributions. The ratio of the refolded distributions over the raw $p_{\text{T,chjet}}$ distributions are shown in right two panels of

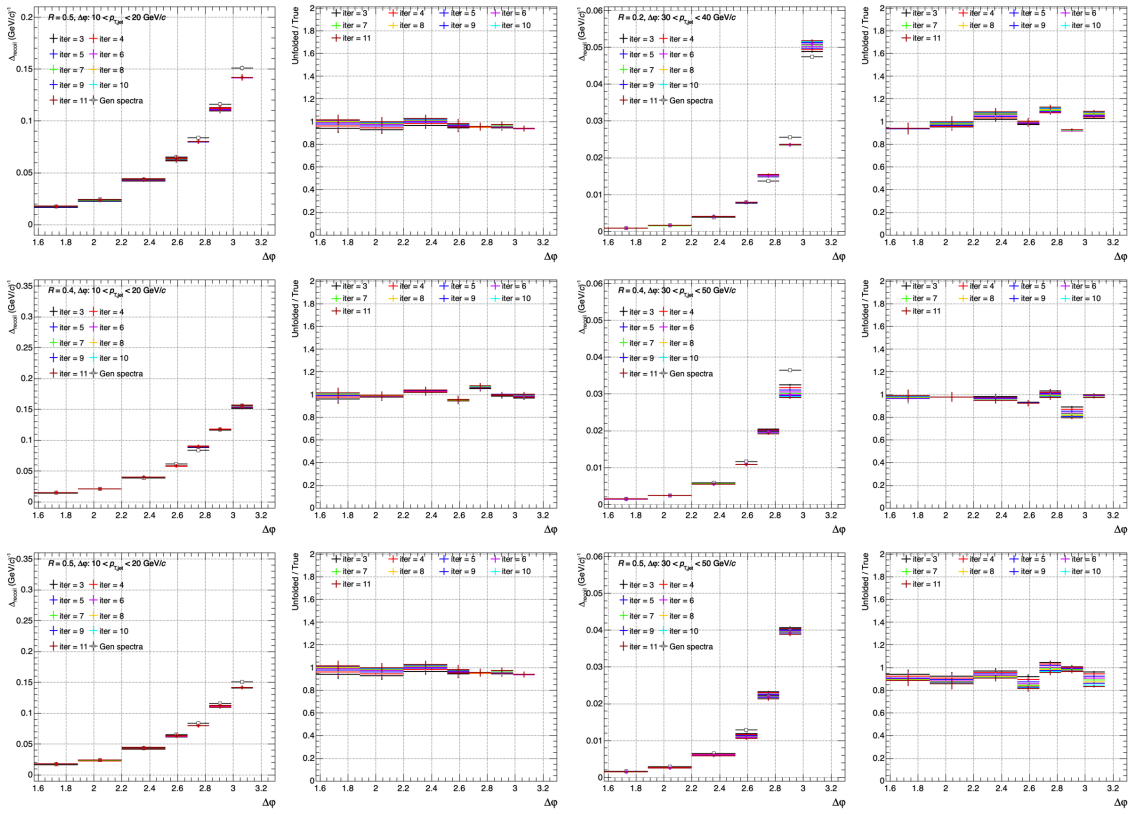

Figure 5.22: MC unfolded closure test distributions of $\Delta_{\text{recoil}}(\Delta\varphi)$ in different $p_{\text{T}} \in [10, 20]$ and $[30, 50]$ GeV/c intervals using Bayesian 2d unfolding method for $R = 0.2, 0.4, 0.5$. Left two panels are $p_{\text{T}} \in [10, 20]$ GeV/c results of unfolded results and ratios. Right panels are $p_{\text{T}} \in [30, 50]$ GeV/c results.

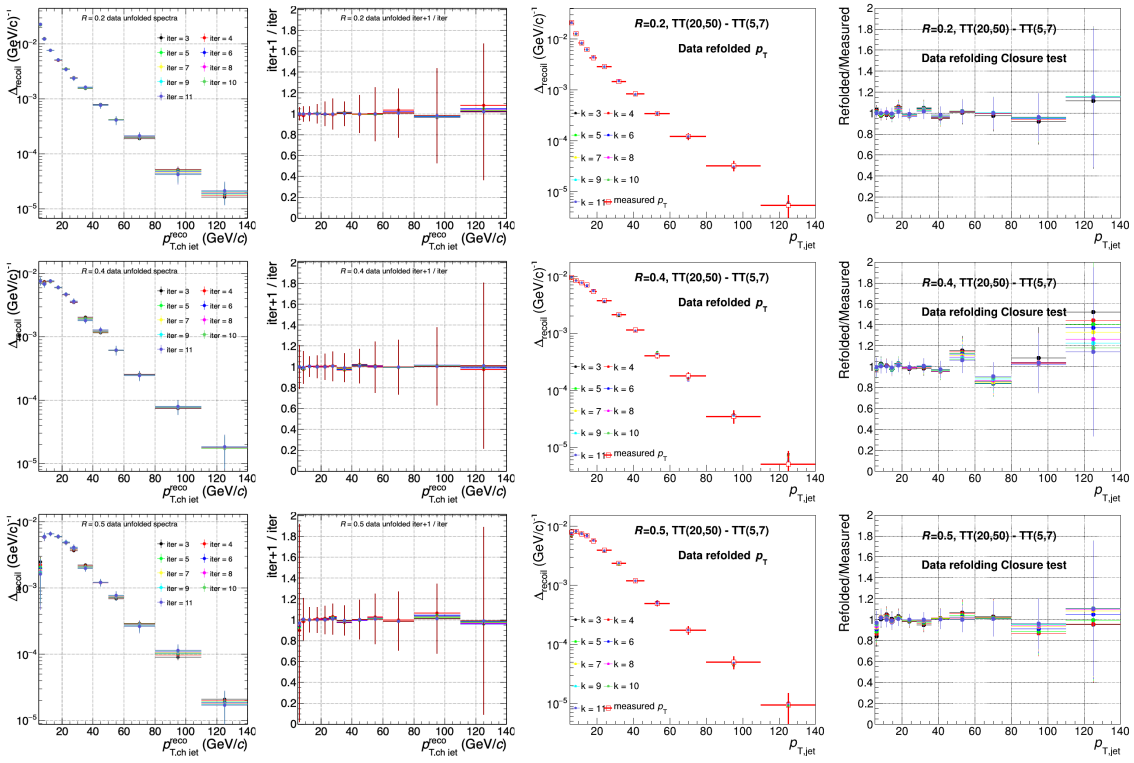

Figure 5.23: Data unfolding vs iteration for $R = 0.2, 0.4, 0.5$ analysis. First column: The unfolded $\Delta_{\text{recoil}}(p_{\text{T,ch jet}})$ distributions vs iteration from 3 to 11 for $R = 0.2, 0.4, 0.5$ analysis. Second column: The variation of unfolded distributions with respect to previous iteration. Three column: Refolded distribution compared to the raw distribution. Forth column: Ratio of the refolded distribution to the raw distribution.

Fig. 5.23. Convergence of the refolded spectra is obtained after a few iterations to within a few percent, and within the statistical uncertainties of the raw distribution.

The refolding check for 2D Bayesian unfolding is shown in Fig. 5.24, Fig. 5.25 and Fig. 5.26, where the unfolded distribution is refolded as a function of $\Delta\varphi$ in different p_{T} intervals and the ratio is taken with the initial raw distribution, for $R = 0.2$, 0.4 and 0.5. The refolded distributions are seen to agree with the raw distributions. Stable unfolding of the raw Δ_{recoil} distributions in $\Delta\varphi$ is possible for a range of jet R in pp collisions. The Bayesian regularisation parameter $iter = 8$ that has been chosen for the central points for all p_{T} intervals and all R. The unfolded $\Delta_{\text{recoil}}(\Delta\varphi)$ distributions from $\Delta_{\text{recoil}}(p_{\text{T,ch jet}}, \Delta\varphi)$ projected onto the $\Delta\varphi$ axis are shown in Fig. 5.27, Fig. 5.28 and Fig. 5.29 for $R = 0.2$, 0.4 and 0.5, respectively.

The two-dimensional unfolded $\Delta_{\text{recoil}}(p_{\text{T,ch jet}})$ results are compared with the one-dimensional unfolded results in Fig. 5.30, projecting in consistent p_{T} intervals. The distributions from the two different unfolding approaches are seen to be consistent within uncertainties.

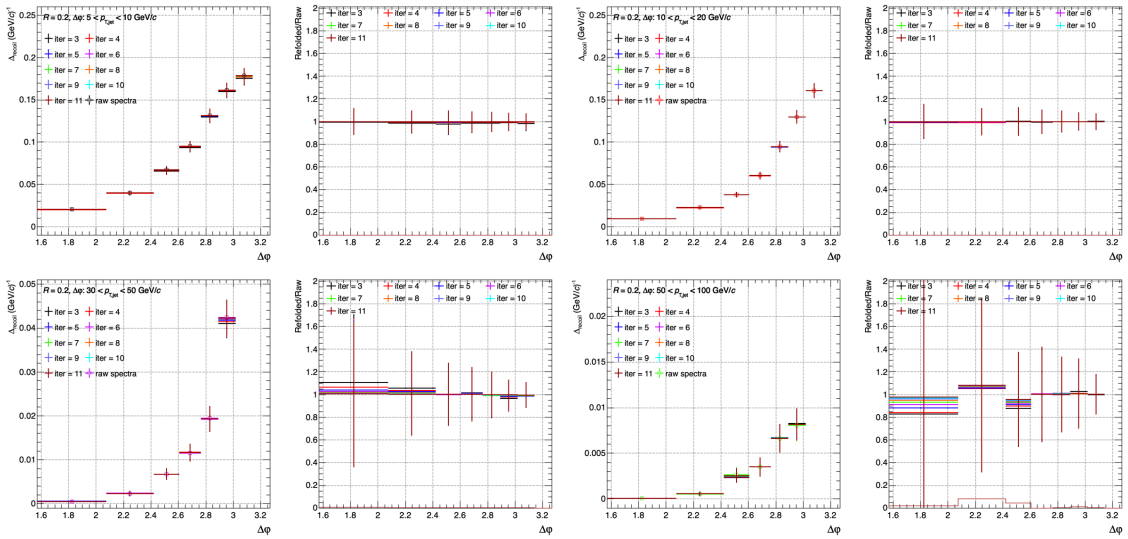

Figure 5.24: Data refolded closure distributions of $\Delta\varphi$ in selected p_{T} intervals ($p_{\mathrm{T}} \in [5,10]$, $[10,20]$, $[30,50]$, $[50,100]$ GeV/c) for $R = 0.2$.

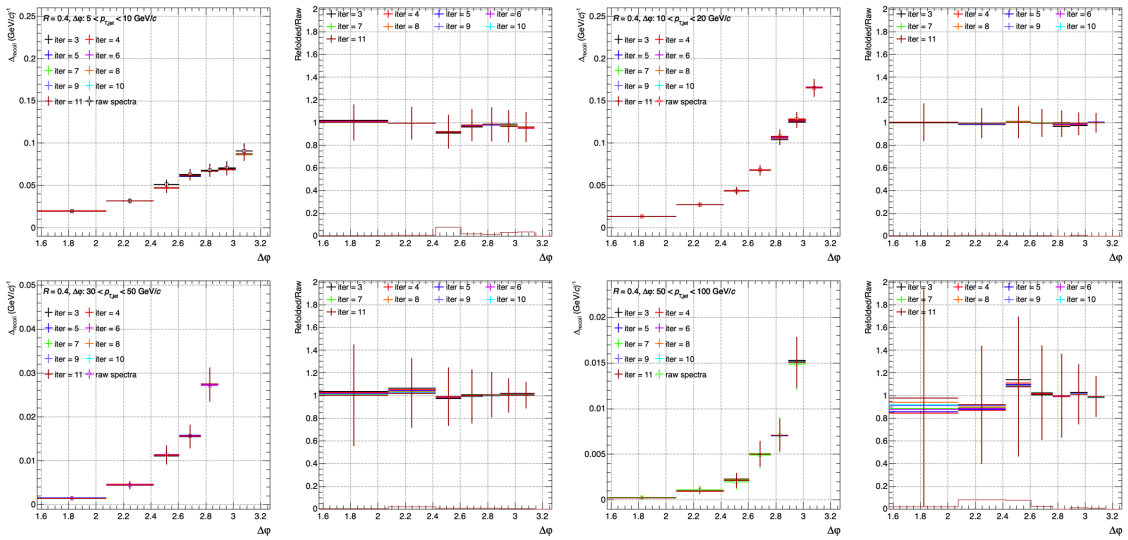

Figure 5.25: Data refolded closure distributions of $\Delta\varphi$ in selected p_{T} intervals ($p_{\mathrm{T}} \in [5,10]$, $[10,20]$, $[30,50]$, $[50,100]$ GeV/c) for $R = 0.4$.

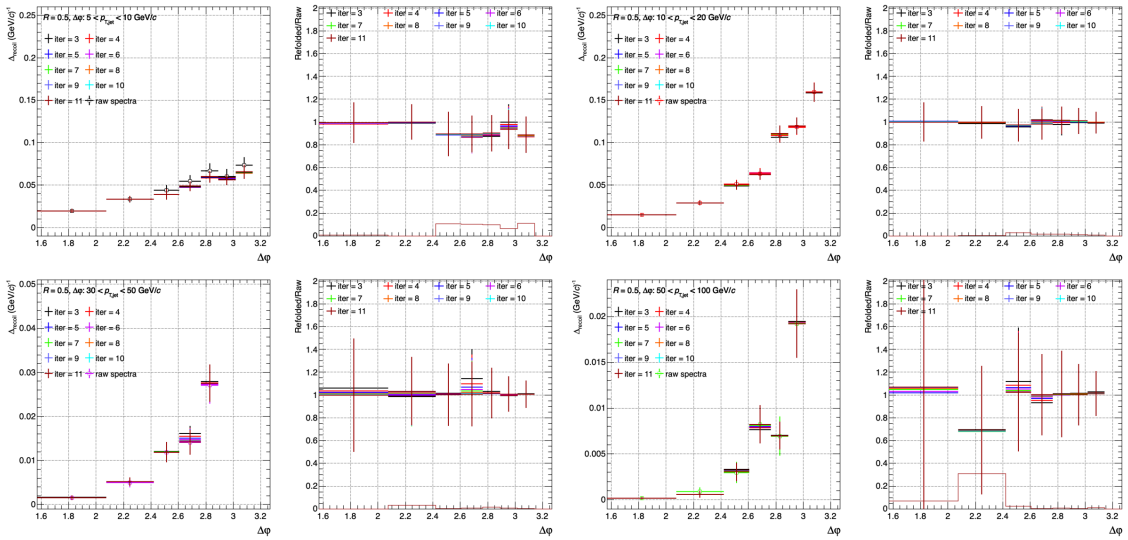

Figure 5.26: Data refolded closure distributions of $\Delta\varphi$ in selected p_{T} intervals ($p_{\mathrm{T}} \in [5,10]$, $[10,20]$, $[30,50]$, $[50,100]$ GeV/c) for $R = 0.5$.

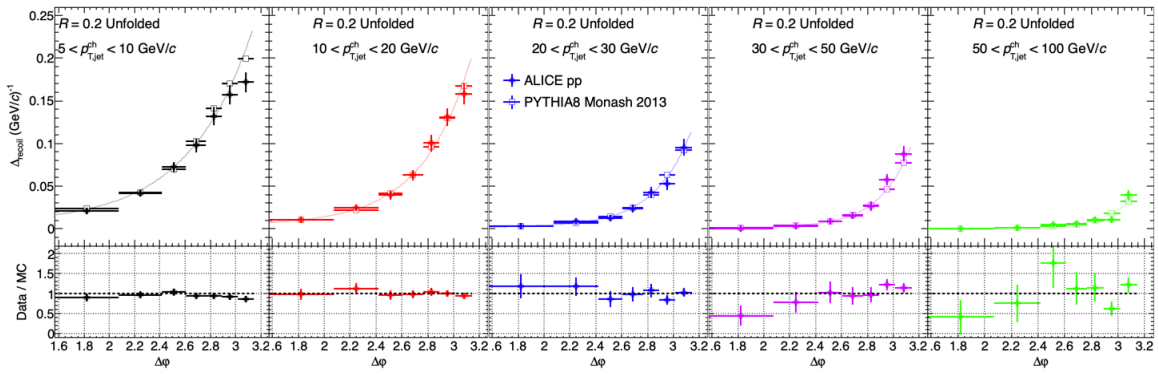

Figure 5.27: Top: Unfolded Δ_{recoil} distributions in different p_{T} intervals for jet $R = 0.2$ compared with true distribution from PYTHIA8 simulation. Bottom: Ratios of unfolded Δ_{recoil} to PYTHIA production.

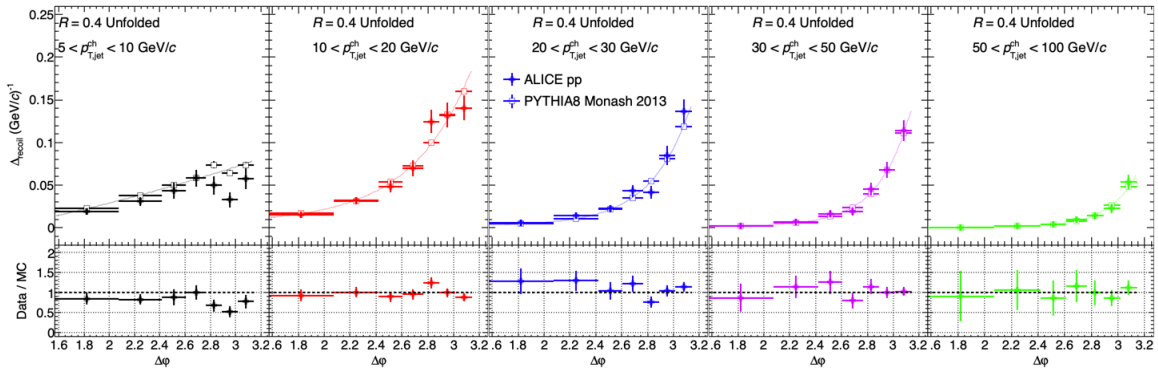

Figure 5.28: Top: Unfolded Δ_{recoil} distributions in different p_{T} intervals for jet $R = 0.4$ compared with true distribution from PYTHIA8 simulation. Bottom: Ratios of unfolded Δ_{recoil} to PYTHIA production.

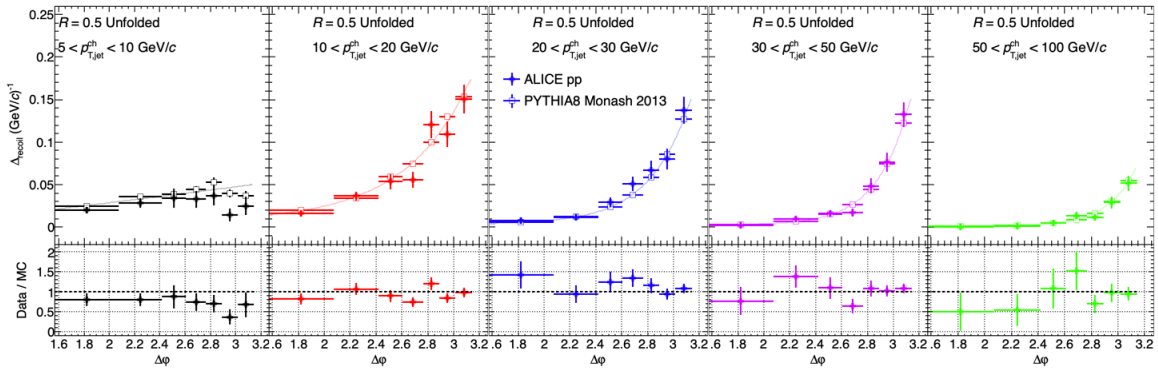

Figure 5.29: Top: Unfolded Δ_{recoil} distributions in different p_{T} intervals for jet R = 0.5 compared with true distribution from PYTHIA8 simulation. Bottom: Ratios of unfolded Δ_{recoil} to PYTHIA production.

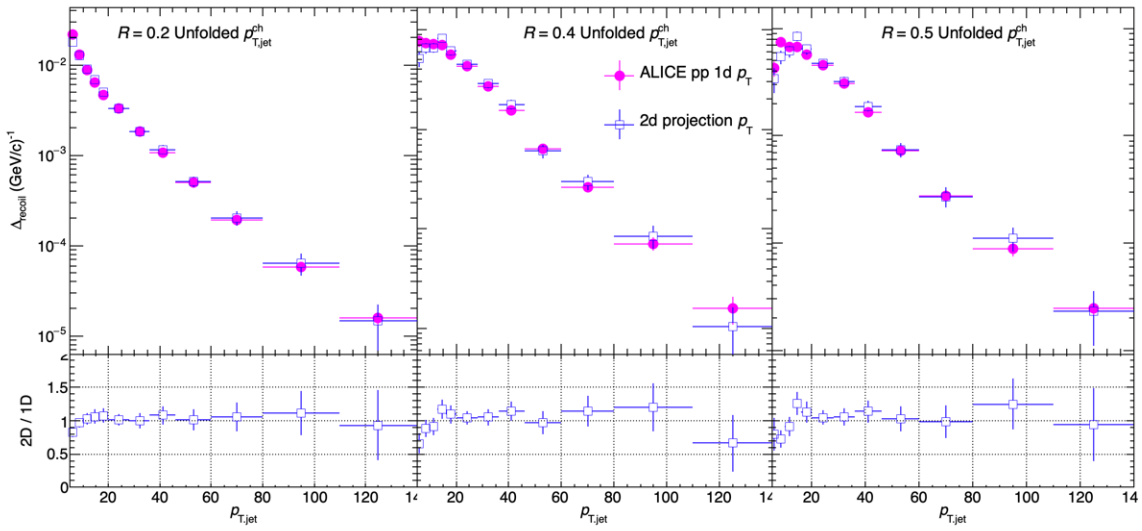

Figure 5.30: Comparison of $\Delta_{\text{recoil}}(p_{\text{T,ch jet}})$ distribution with using 2d and 1d unfolding procedure.

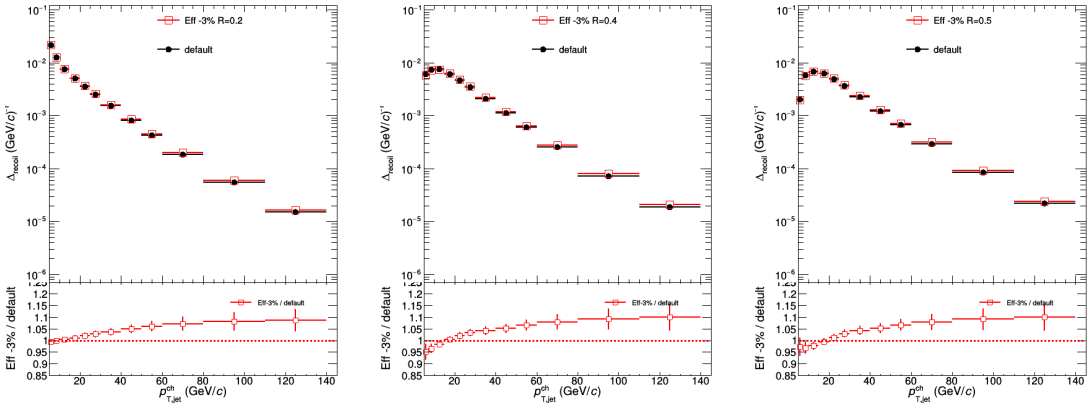

Figure 5.31: Systematic uncertainty of $\Delta_{\text{recoil}}(p_{\text{T,ch jet}})$ taken into by tracking efficiency for jet $R = 0.2, 0.4, 0.5$.

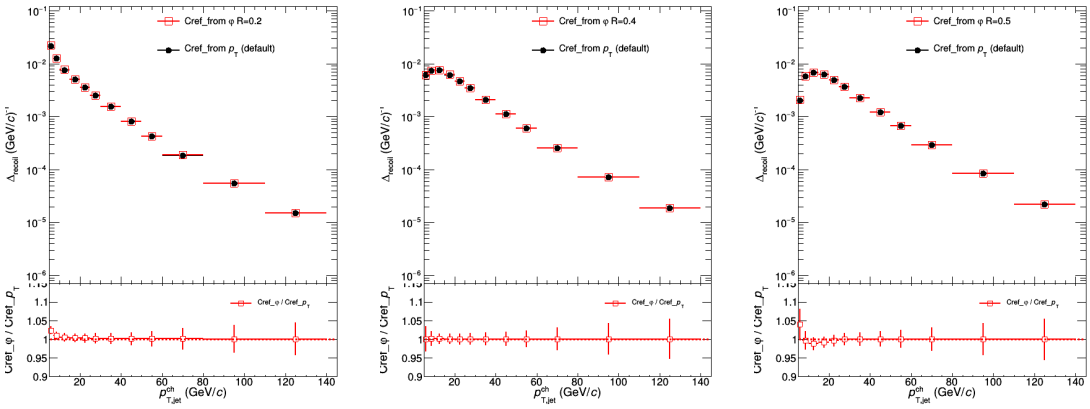

Figure 5.32: Systematic uncertainty of $\Delta_{\text{recoil}}(p_{\text{T,ch jet}})$ on scaling factor (c_{Ref}) by different method for jet $R = 0.2, 0.4, 0.5$.

5.7 Systematic uncertainties

For the h+jet correlations analyses, similar with previous analysis, the systematic uncertainty is mainly due to the tracking-efficiency uncertainty, the uncertainty on the scaling factor c_{Ref}, and the unfolding uncertainties, which include uncertainties due to the choice of prior, the choice of regularization parameter, the $p_{\text{T,jet}}$ binning choice, and the unfolding method.

TThe systematic uncertainty in the estimated tracking reconstruction efficiency, based on the variation of the cuts used in the track selection, is also 3% as in the previous inclusive jet analysis. The systematic uncertainty is the relative change in the unfolded result obtained with the modified response matrix with respect to the principal analysis, as shown in Figures 5.31 and 5.34. The dominant source of total systematic uncertainty comes from track reconstruction efficiency.

In pp collisions, the uncorrelated background is smaller and the fit range to extract c_{Ref} is narrower. The c_{Ref} uncertainty is evaluated by varying the range of $\Delta\varphi$ in the vicinity of $p_{\text{T}} = 0$ (see Section 5.5).

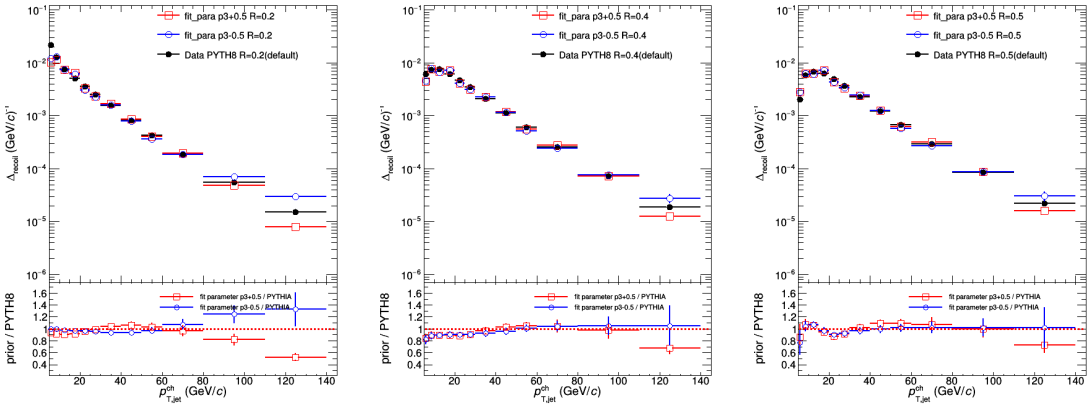

Figure 5.33: Systematic uncertainty of $\Delta_{\text{recoil}}(p_{\text{T,ch jet}})$ taken into by unfolding prior for jet $R = 0.2, 0.4, 0.5$.

The systematic uncertainty is presented in Figures 5.32 and 5.35. The uncertainty reduces as $p_{\text{T,ch jet}}^{\text{corr}}$ increases due to the fact that the subtraction of the TT_{ref}-selected distribution is a smaller relative correction at large $p_{\text{T,ch jet}}^{\text{corr}}$.

The uncertainties due to the unfolding are assessed by varying its configuration. The systematic uncertainty due to the prior utilized in the unfolding is determined by varying the value of the power in the functional form used to fit the prior. The uncertainty on the prior is assessed by varying the value of the parameters p_3 in Section 5.6.2 of prior creation and shows in Figures 5.33 and 5.36. The unfolding algorithm uncertainty is assessed by utilizing SVD as an alternative algorithm (where possible when performing 1-dimensional unfolding, see Fig. 5.37), and by varying the regularization parameter in the iterative Bayesian unfolding by ±2, the related uncertainty is shown in Figures 5.38 and 5.40. The uncertainty related to the binning choice was assessed by varying the detector-level $p_{\text{T,jet}}$ binning, and by varying the minimum and maximum particle-level $p_{\text{T,jet}}$ bin limits. The particle-level bin widths are halved in the full p_{T} range, the effect of which is negligible. The detector-level bin truncation is studied by changing the minimum p_{T} limit from 1 GeV/c to 2 GeV/c and the maximum p_{T} limit from 10 GeV/c to 20 GeV/c. The result of this can be seen in Figures 5.39 and 5.41. The relatively systematic uncertainties are below 2% for the $\Delta_{\text{recoil}}(p_{\text{T,ch jet}})$and below 5% for $\Delta_{\text{recoil}}(\Delta\varphi)$.

For the $\Delta_{\text{recoil}}(p_{\text{T,ch jet}})$ and $\Delta_{\text{recoil}}(\Delta\varphi)$ analyses in pp collisions the unfolding closure is successful for all $p_{\text{T,jet}}$ and $\Delta\varphi$, so no uncertainty is assigned.

In pp collisions, the effect of the underlying event subtraction is checked by performing the analysis with and without underlying event subtraction. For $p_{\text{T,ch jet}}^{\text{corr}} > 5$ GeV/c, the Δ_{recoil} distributions with and without this subtraction are fully consistent within the statistical uncertainties, and no uncertainty is

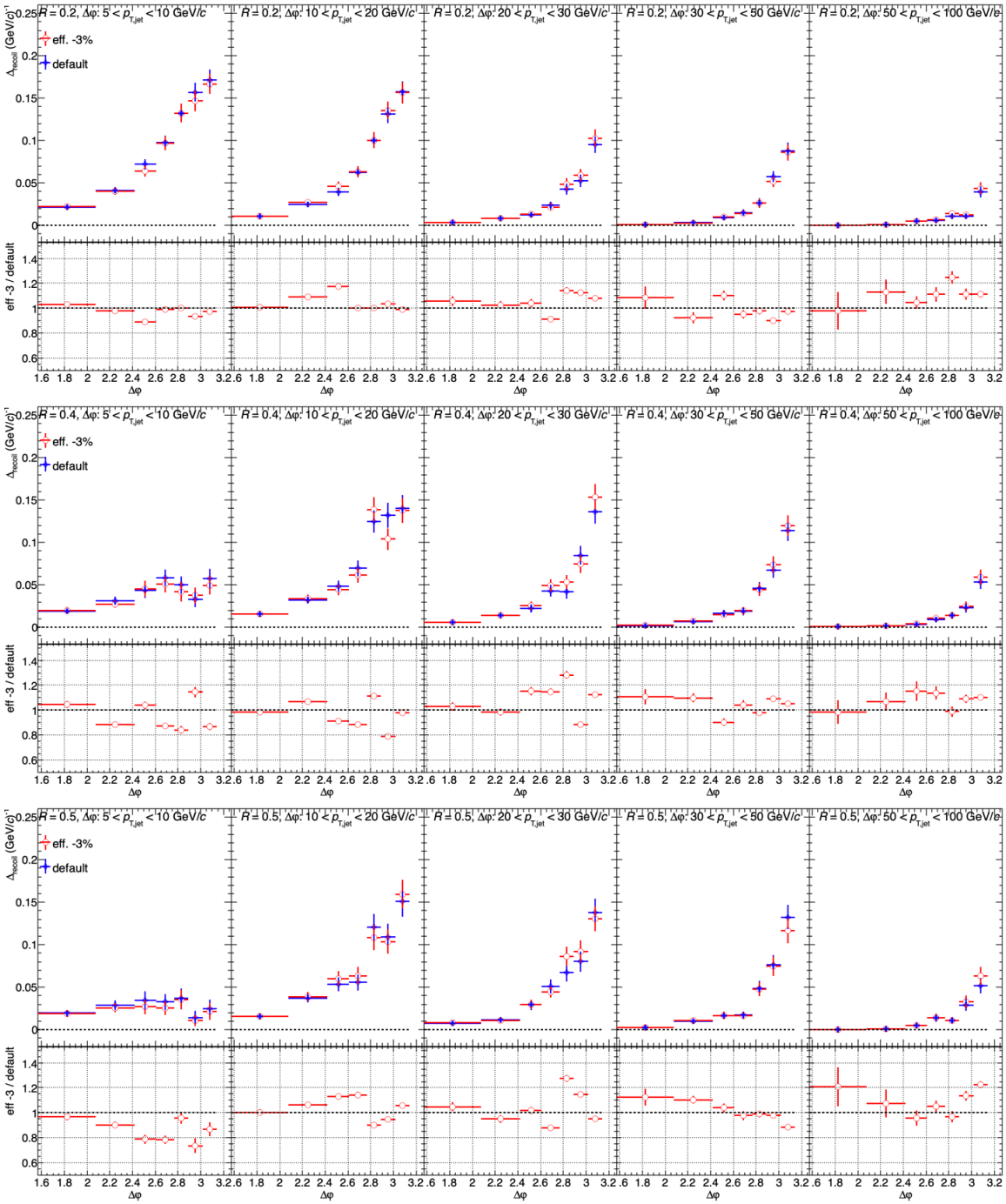

Figure 5.34: Systematic uncertainty of $\Delta_{\mathrm{recoil}}(\Delta\varphi)$ on tracking efficiency for jet $R = 0.2, 0.4, 0.5$.

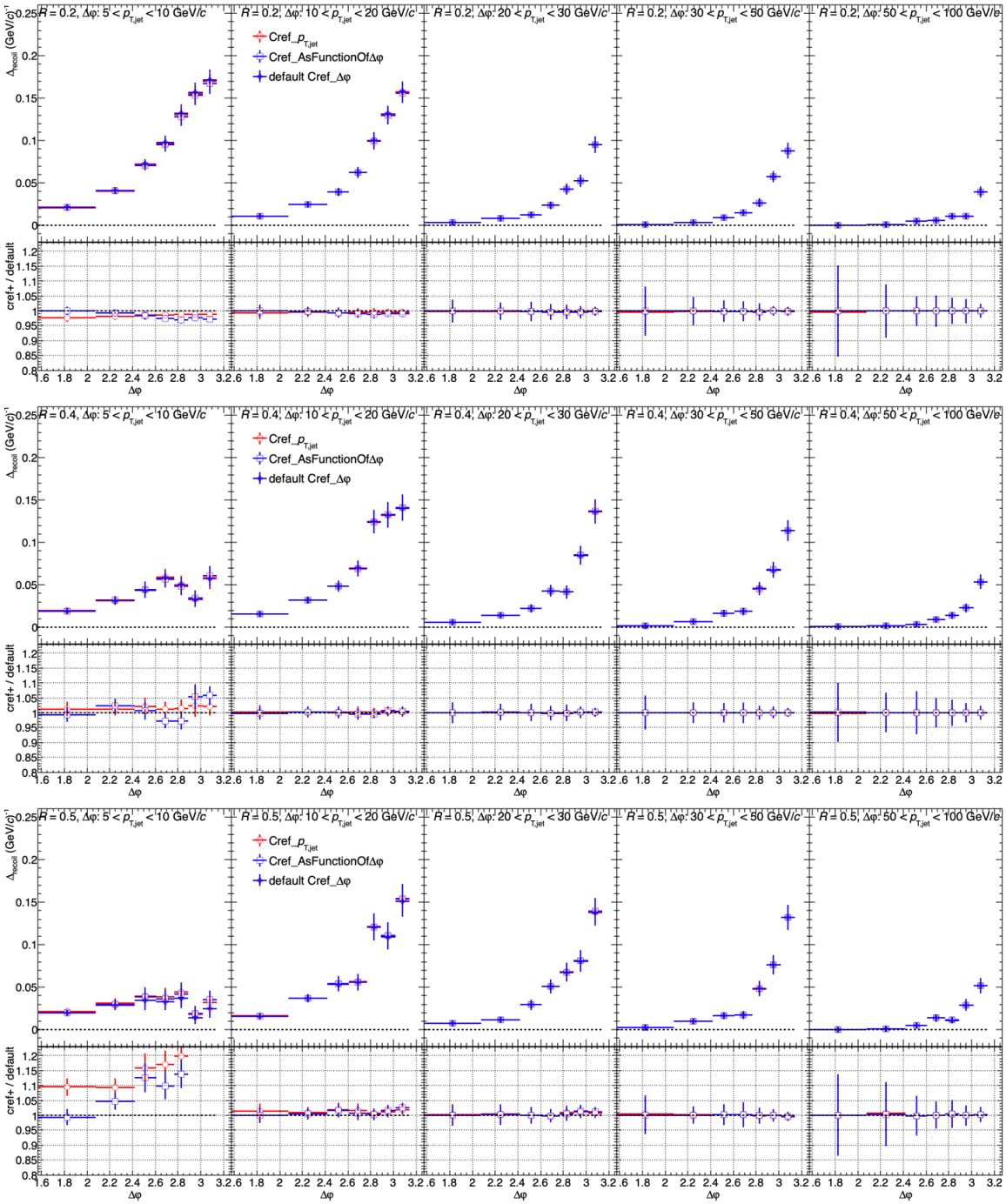

Figure 5.35: Systematic uncertainty of $\Delta_{\mathrm{recoil}}(\Delta\varphi)$ from c_{Ref} determination for jet $R = 0.2, 0.4, 0.5$.

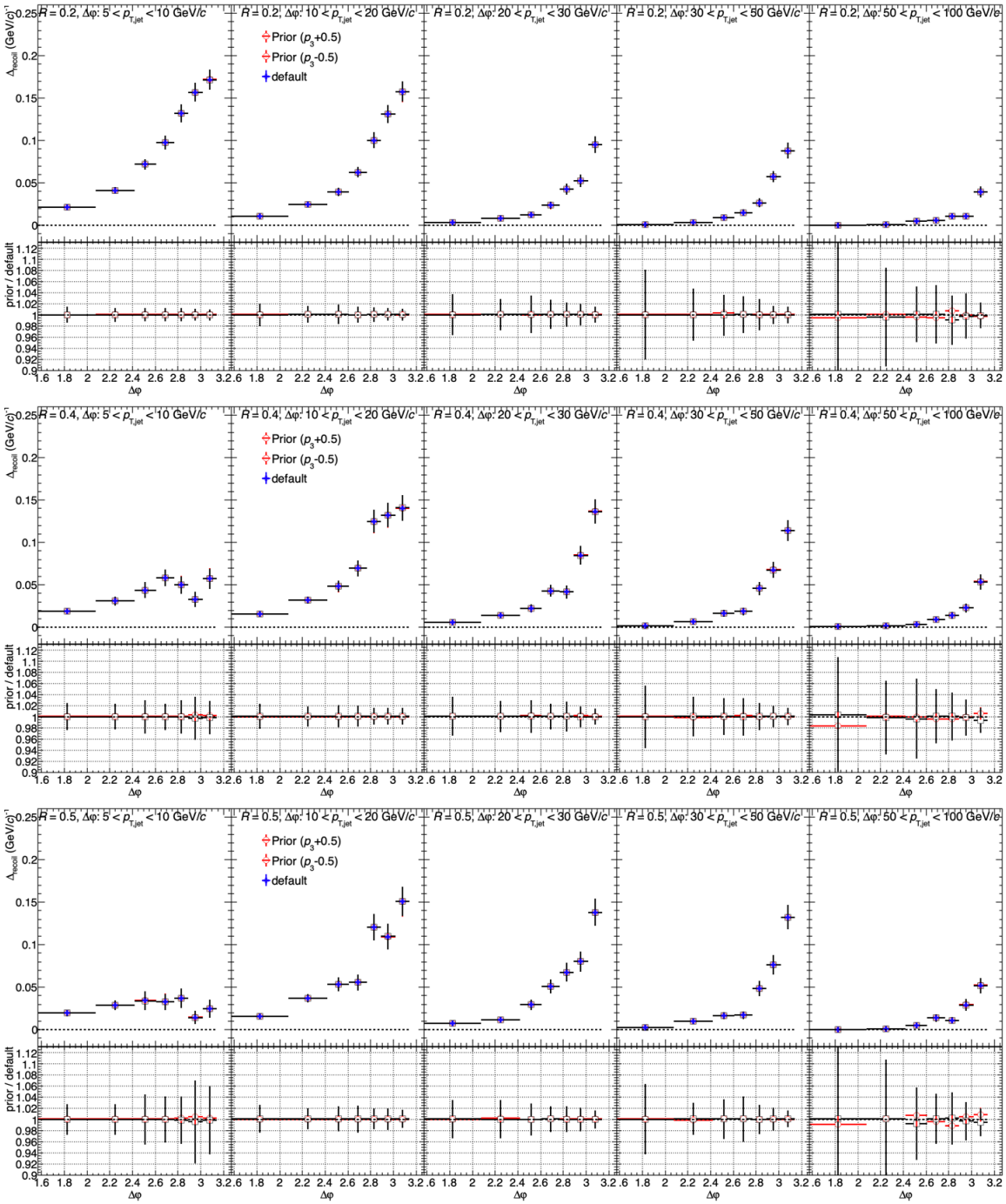

Figure 5.36: Systematic uncertainty of $\Delta_{\mathrm{recoil}}(\Delta\varphi)$ from unfolding prior for jet $R = 0.2, 0.4, 0.5$.

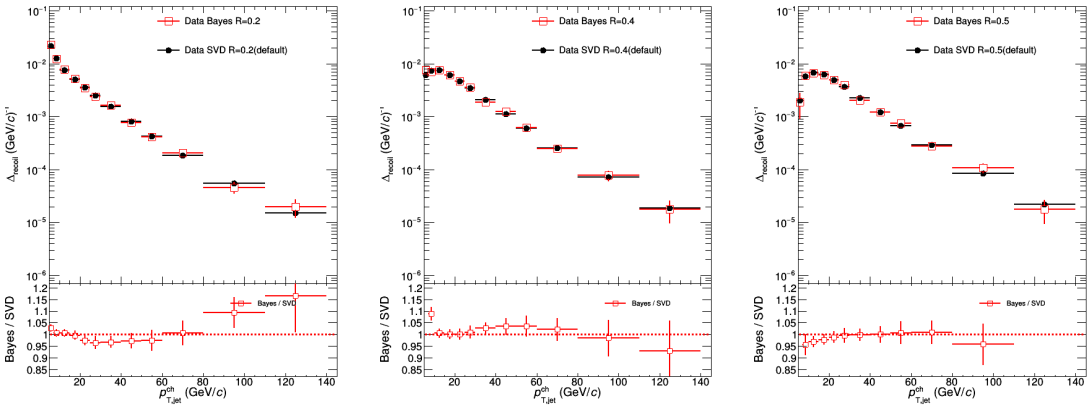

Figure 5.37: Systematic uncertainty of $\Delta_{\text{recoil}}(p_{\text{T,ch jet}})$ taken into by different unfolding method for jet $R = 0.2, 0.4, 0.5$.

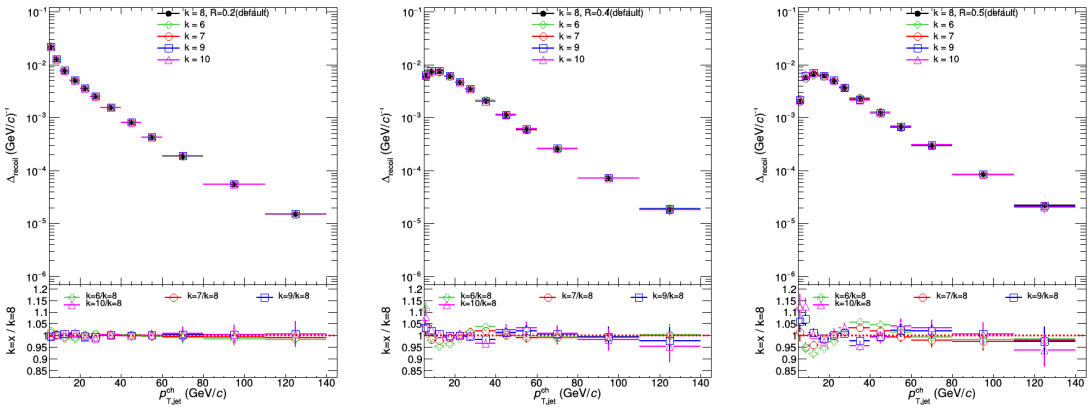

Figure 5.38: Systematic uncertainty of $\Delta_{\text{recoil}}(p_{\text{T,ch jet}})$ taken into by different unfolding iteration for jet $R = 0.2, 0.4, 0.5$.

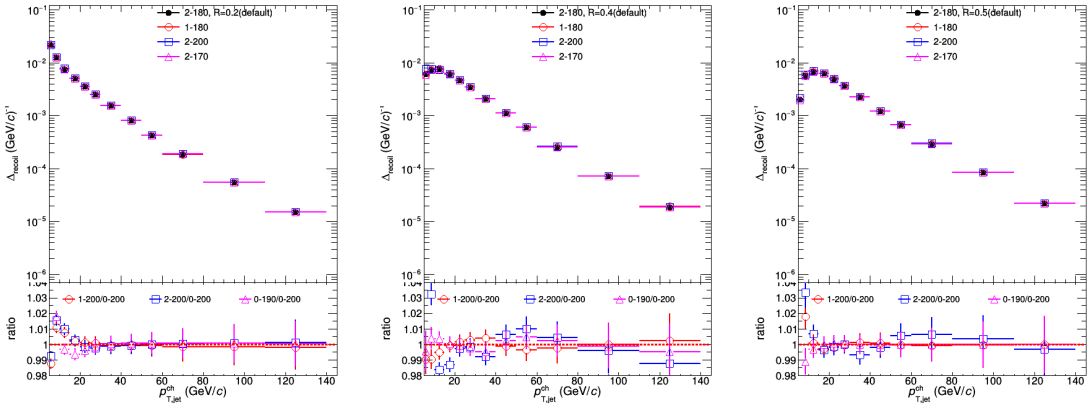

Figure 5.39: Systematic uncertainty of $\Delta_{\text{recoil}}(p_{\text{T,ch jet}})$ taken into by different unfolding binning for jet $R = 0.2, 0.4, 0.5$.

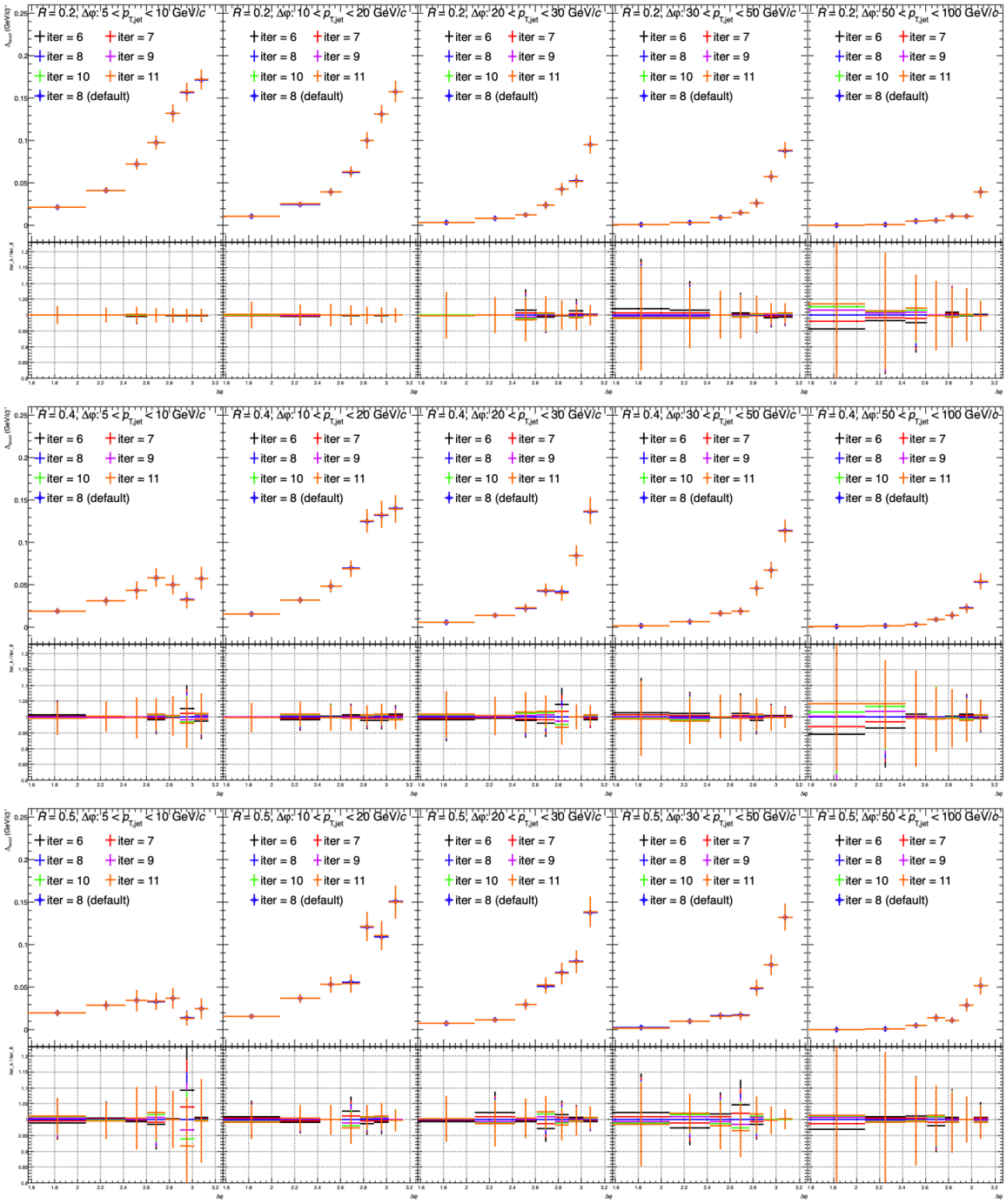

Figure 5.40: Systematic uncertainty of $\Delta_{\mathrm{recoil}}(\Delta\varphi)$ from unfolding iteration for jet $R = 0.2, 0.4, 0.5$.

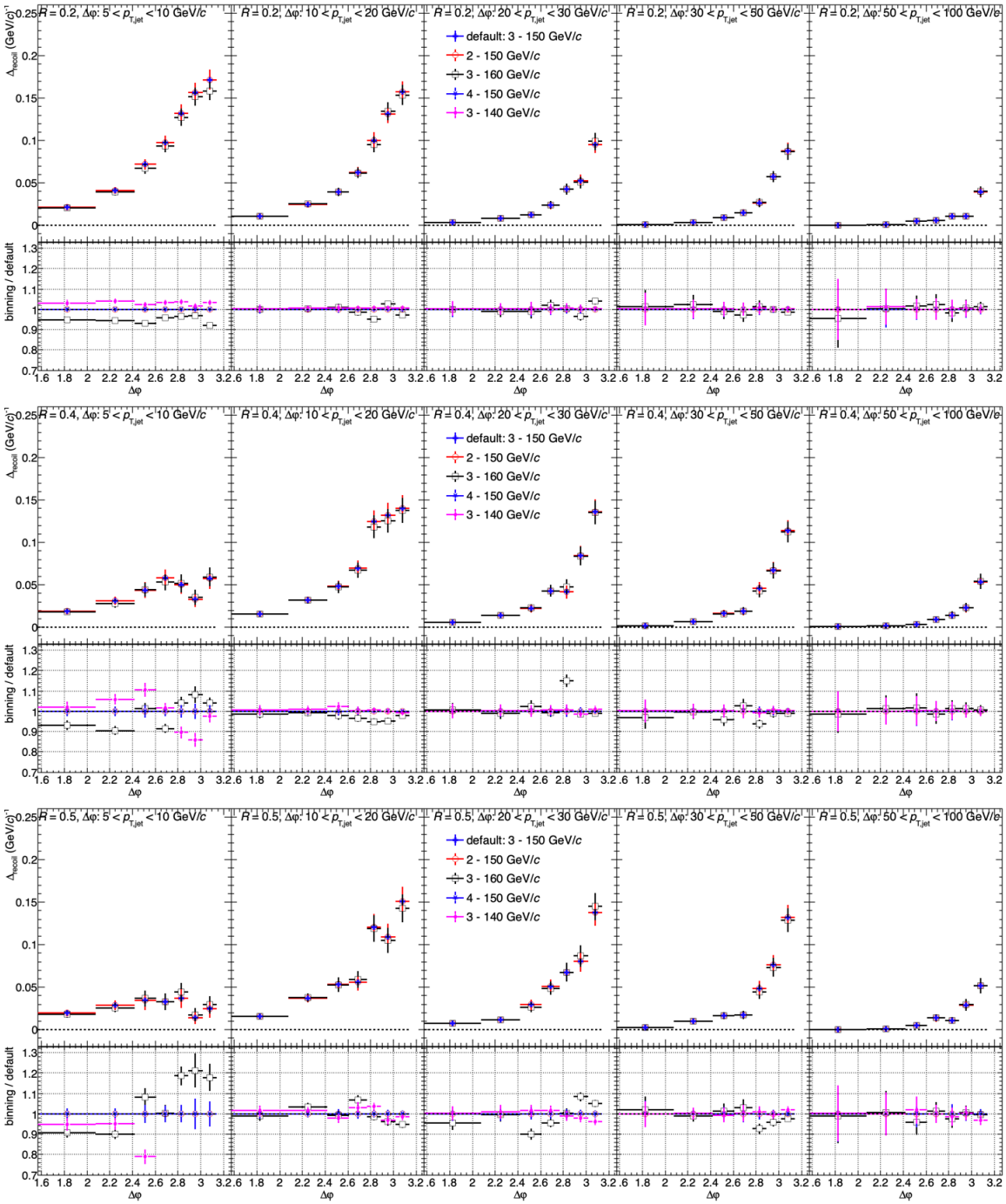

Figure 5.41: Systematic uncertainty of $\Delta_{\text{recoil}}(\Delta\varphi)$ from unfolding bin truncation for jet $R = 0.2, 0.4, 0.5$.

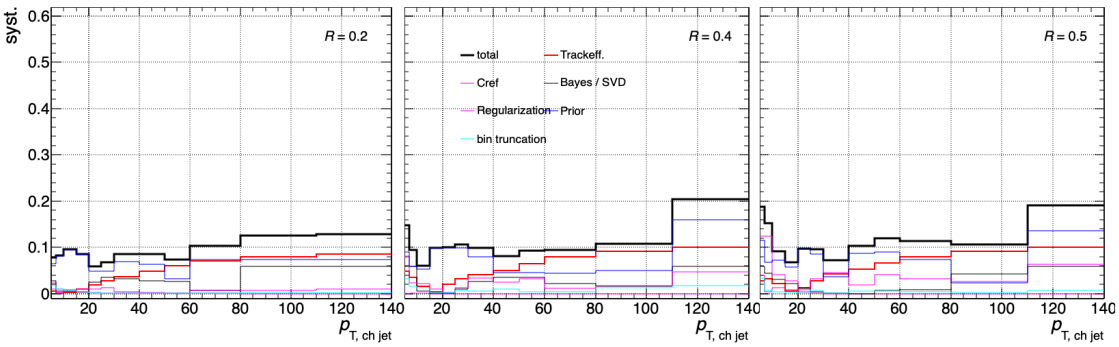

Figure 5.42: Total systematic uncertainty distribution of $\Delta_{\text{recoil}}(p_{\text{T,ch jet}})$ for jet $R = 0.2, 0.4, 0.5$.

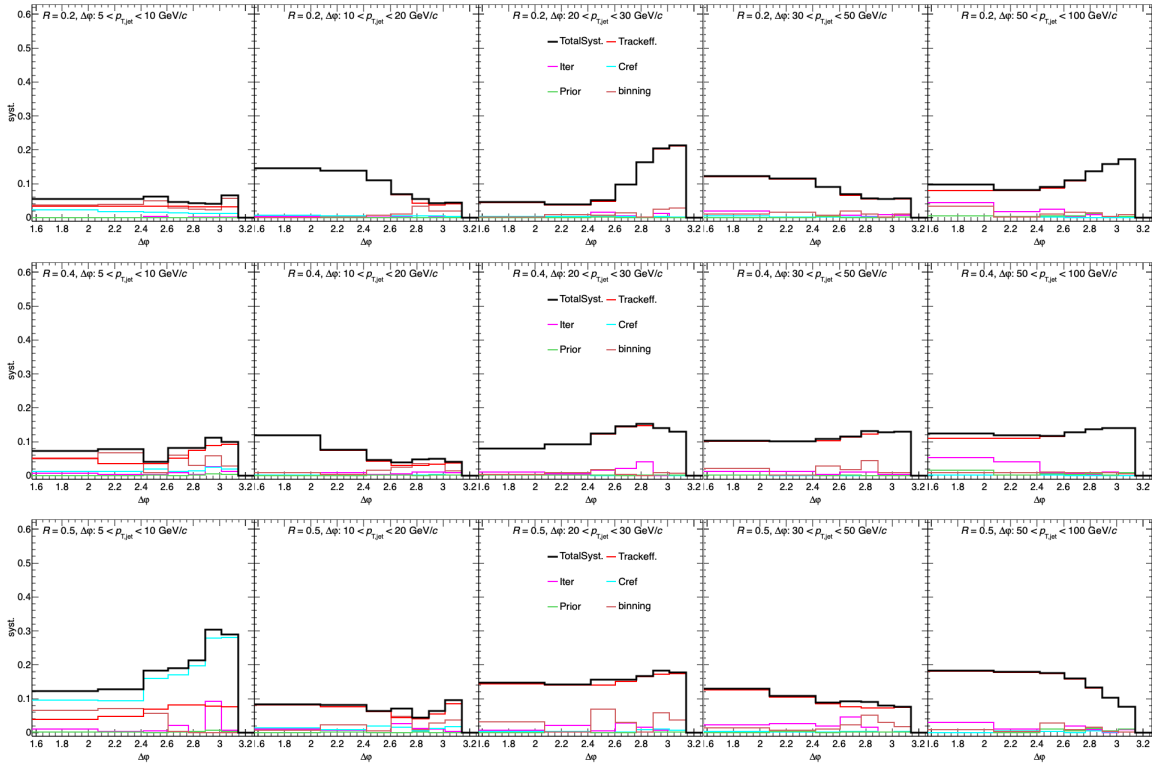

Figure 5.43: Total systematic uncertainty of $\Delta_{\text{recoil}}(\Delta\varphi)$ from all resources for jet $R = 0.2, 0.4, 0.5$.

therefore assigned.

In cases where the uncertainties are expected to vary smoothly bin-to-bin, the uncertainties are smoothed using the Smooth function in ROOT. The uncertainties from each source in each bin in $p_{\mathrm{T,jet}}$ and $\Delta\varphi$ are summed in quadrature to obtain the total systematic uncertainty. For the R-ratios, the uncertainties are considered uncorrelated between different R values, except for the tracking uncertainties with partially cancel in the ratio. A summary of the systematic uncertainty sources for the analysis vs p_{T} and $\Delta\varphi$ can be seen in Figures 5.42 and 5.43.

5.8 Results and discussion: Semi-inclusive jet production

5.8.1 Results in pp collisions

This section presents corrected $\Delta_{\text{recoil}}(p_{\text{T,ch jet}}, \Delta\varphi)$ distributions with systematic uncertainty for pp collisions at $\sqrt{s}$ = 5.02 TeV and compares them with the Pb–Pb results.

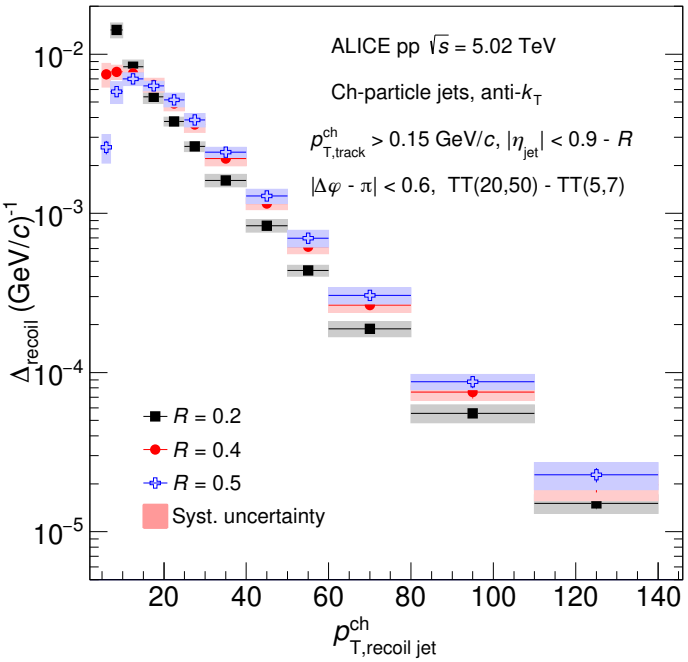

Figure 5.44: Full-corrected $\Delta_{\text{recoil}}(p_{\text{T,ch jet}})$ distribution for R = 0.2, 0.4 and 0.5 in pp collisions at $\sqrt{s}$ = 5.02 TeV.

Figure 5.44 shows **fully-corrected $\Delta_{\text{recoil}}(p_{\text{T,ch jet}})$ distributions** for R = 0.2, 0.4, and 0.5 measured in pp collisions at $\sqrt{s}$ = 5.02 TeV. In the upper panels of Figure 5.45 also display corrected $\Delta_{\text{recoil}}(p_{\text{T,ch jet}})$ distributions together with comparison to model calculations based on PYTHIA8 Monash 2013 tune [33, 34], JEWEL (vacuum) [32, 79], JETSCAPE (vacuum) [170], and POWHEG [168]. Figure 5.45, in the lower panels, show the ratio of the distributions in the upper panels to the fit of a smooth function to the data, in order to suppress fluctuations in the data for comparison purposes. The fitted function is consistent with the previous construction of the prior (Section 5.6.2). The same smoothing procedure is used in the lower panels of Figs. 5.48.

The PYTHIA8 and JETSCAPE calculations agree with the data within experimental uncertainties over the full $p_{\text{T,ch jet}}$ range. These calculations are related, since JETSCAPE utilizes PYTHIA8 for hard process generation and string fragmentation, with independent procedures for final-state parton showering and hadronization. These independent processes are expected to have little effect on jet distributions,

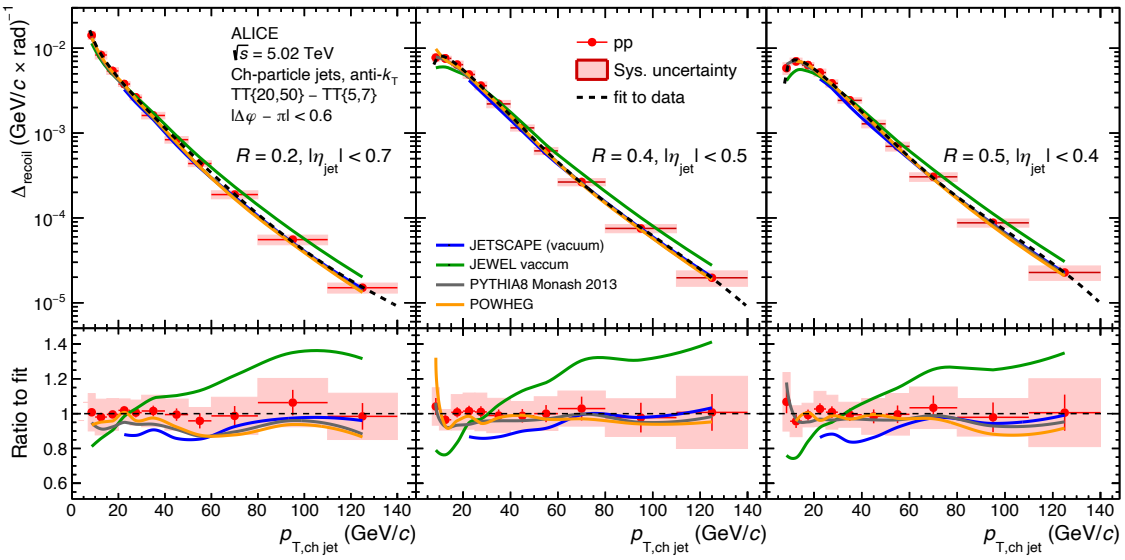

Figure 5.45: Upper panels: corrected $\Delta_{\text{recoil}}(p_{\text{T,ch jet}})$ distributions measured for $R = 0.2$ (left), 0.4 (middle), and 0.5 (right) in pp collisions at $\sqrt{s} = 5.02$ TeV, compared to calculations from JETSCAPE [30], JEWEL [31, 32], PYTHIA8 [33, 34], and POWHEG [35–38]. Lower panels: ratio of the data and calculations to a functional fit of the measured $\Delta_{\text{recoil}}(p_{\text{T,ch jet}})$ distributions.

however. The POWHEG calculations likewise describe the data well over the full $p_{\text{T,ch jet}}$ range. The JEWEL calculation does not describe $p_{\text{T,ch jet}}$-dependence of $\Delta_{\text{recoil}}(p_{\text{T,ch jet}})$ well, overestimating the data for $p_{\text{T,ch jet}} > 30$ GeV/c, with ~40% disagreement at high $p_{\text{T,ch jet}}$.

Jet shape modification: R-dependence of $\Delta_{\text{recoil}}(p_{\text{T,ch jet}})$ The ratio of inclusive jet cross sections or semi-inclusive jet yields at different values of R provides a precise probe of jet shape and collimation information, since there is significant cancellation of correlated uncertainties in the ratio for both experimental measurements and theoretical calculations [12, 227–229]. In pp collisions, R-dependent ratios are sensitive to high-order pQCD effects [12, 228, 230, 231]. In A–A collisions, such ratios provide experimentally robust probes of medium-induced modification of jet shapes over a broad kinematic range, including low $p_{\text{T,jet}}$ [15, 83, 84].

Figure 5.46 shows the ratio of $\Delta_{\text{recoil}}(p_{\text{T,ch jet}})$ distributions for $R = 0.2$ over that for $R = 0.4$ or $R = 0.5$ in pp collisions at $\sqrt{s} = 5.02$ TeV, using the data in Fig. 5.45. The ratio is below unity for $p_{\text{T,ch jet}} > 15$ GeV/c, consistent with the expected intra-jet energy distribution in which significant energy is carried at distances larger than 0.2 radians relative to the jet axis. The ratio rises towards low $p_{\text{T,ch jet}}$ and crossing unity at $p_{\text{T,ch jet}} \sim 10$ GeV/c. The measured distributions are well-reproduced by PYTHIA8 and JETSCAPE (vacuum) calculations. This $p_{\text{T,ch jet}}$-dependence and the good agreement of this observable

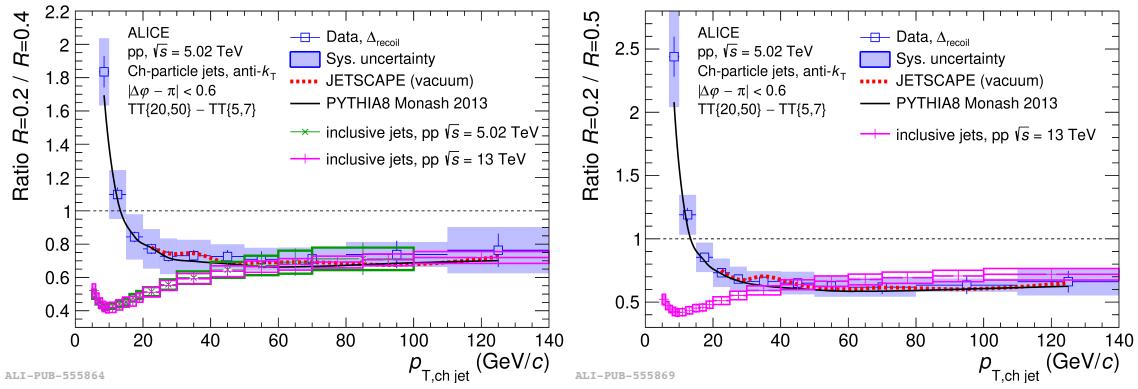

Figure 5.46: Ratio of $\Delta_{\mathrm{recoil}}(p_{\mathrm{T,ch\ jet}})$ distributions in pp collisions at $\sqrt{s}$ = 5.02 TeV using the data from Fig. 5.45, for $R = 0.2/R = 0.4$ (left) and $R = 0.2/R = 0.5$ (right), compared to calculations from PYTHIA8 and JETSCAPE. The corresponding ratios of cross sections for inclusive jets are also shown for pp collisions at $\sqrt{s}$ = 5.02 TeV [26] and $\sqrt{s}$ = 13 TeV [20]. The uncertainties in the ratio take into account the correlation of uncertainties between numerator and denominator.

with PYTHIA8 were also observed in Ref. [15], where a NLO pQCD calculation was likewise shown to reproduce the measured $p_{\mathrm{T,ch\ jet}}$-dependence of the ratio, although not its absolute magnitude.

Figure 5.46 also shows the ratios of the inclusive charged-jet cross sections for different values of R in pp collisions at $\sqrt{s}$ = 5.02 TeV [26] and $\sqrt{s}$ = 13 TeV (from Fig. 4.44) [20]. At high $p_{\mathrm{T,ch\ jet}}$, these ratios are consistent within uncertainties with the corresponding $\Delta_{\mathrm{recoil}}(p_{\mathrm{T,ch\ jet}})$ ratios. However, the observed increase in the $\Delta_{\mathrm{recoil}}(p_{\mathrm{T,ch\ jet}})$ ratio with decreasing $p_{\mathrm{T,ch\ jet}}$ is opposite to the behavior of the ratios for inclusive jet cross sections, which decrease with decreasing $p_{\mathrm{T,ch\ jet}}$. Note that the inclusive charged jet cross section ratios are also well-described by pQCD and Monte Carlo model calculations [20, 26]. Since PYTHIA8 accurately reproduces the R-dependent ratios for both populations, this difference evidently originates in QCD processes that are incorporated in PYTHIA8. Similar phenomenology of R-dependent yield ratios has also been observed in semi-inclusive measurements with direct photon and π^0 triggers in pp collisions at $\sqrt{s}$ = 200 GeV [232].

Figure 5.47 shows the R-dependent ratio of $\Delta_{\mathrm{recoil}}(p_{\mathrm{T,ch\ jet}})$ distributions measured in pp collisions compared to the same ratios in Pb–Pb collisions. For $R = 0.2$ in the numerator and $R = 0.4$ (left) or $R = 0.5$ (right) in the denominator, at intermediate values of $p_{\mathrm{T,ch\ jet}}$ the ratios for Pb–Pb collisions are lower than those for pp collisions, indicating significant medium-induced intra-jet broadening in that region. However, the results of JETSCAPE calculations incorporating jet quenching in Pb–Pb collisions are larger than those in pp collisions, in contrast to the data. This indicates that medium-induced intra-jet broadening is not accurately modeled in JETSCAPE.

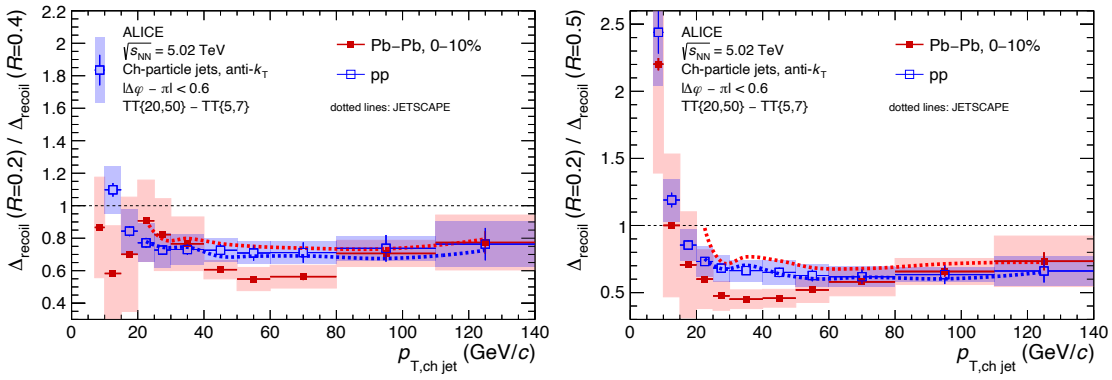

Figure 5.47: Ratio of $\Delta_{\text{recoil}}(p_{\text{T,ch jet}})$ distributions with different R for pp collisions at $\sqrt{s}$ = 5.02 TeV together with the ratios for Pb–Pb collisions, for $R = 0.2/R = 0.4$ (left) and $R = 0.2/R = 0.5$ (right). The uncertainty in the ratio takes into account the correlation of uncertainties between numerator and denominator. JETSCAPE calculations for pp and Pb–Pb collisions are also shown.

The medium-induced suppression of the R-dependent ratio in Fig. 5.47, corresponding to medium-induced intra-jet broadening, is in contrast to a similar measurement of the inclusive jet population [222] which finds medium-induced jet narrowing in a similar kinematic range. The jet populations of these two measurements differ, however, and they cannot be compared directly. Exploration of this difference requires the calculation of both observable within the same model framework.

Figure 5.48 shows **corrected $\Delta_{\text{recoil}}(\Delta\varphi)$ distributions** for R = 0.2, 0.4, and 0.5 measured in pp collisions at $\sqrt{s}$ = 5.02 TeV in various $p_{\text{T,ch jet}}$ bins, together with comparisons to theoretical calculations. The JETSCAPE calculation agrees with the data within uncertainties in all panels. The other calculations also agree with the data within uncertainties except for $\Delta\varphi \lesssim 2.5$ in the ranges $p_{\text{T,ch jet}} > 30$ GeV/c for R = 0.2 (PYTHIA8, POWHEG, JEWEL), and $p_{\text{T,ch jet}} > 50$ GeV/c for R = 0.5 (POWHEG, JEWEL). These pp data provide the reference for comparison to same distributions measured in Pb–Pb collisions, to explore medium-induced effects.

5.8.2 Comparison of $\Delta_{\text{recoil}}(p_{\text{T,ch jet}})$ in pp and Pb–Pb collisions - $I_{\text{AA}}(p_{\text{T,ch jet}})$

Medium-induced yield modification is measured by $I_{\text{AA}}(p_{\text{T,ch jet}}) = \Delta_{\text{recoil}}(\text{Pb–Pb})/\Delta_{\text{recoil}}(\text{pp})$, the ratio of the $\Delta_{\text{recoil}}(p_{\text{T,ch jet}})$ distributions measured in Pb–Pb and pp collisions. Fig. 5.49 shows $I_{\text{AA}}(p_{\text{T,ch jet}})$using the pp $\Delta_{\text{recoil}}(p_{\text{T,ch jet}})$ measurements as baseline. The $I_{\text{AA}}(p_{\text{T,ch jet}})$ distributions have significant dependence on $p_{\text{T,ch jet}}$ and R. For $p_{\text{T,ch jet}} < 20$ GeV/c, $I_{\text{AA}}(p_{\text{T,ch jet}})$ either increases above or is consistent with unity for all R. For R = 0.2 and 0.4, $I_{\text{AA}}(p_{\text{T,ch jet}})$ is lower than unity in the region $20 < p_{\text{T,ch jet}} < 60$ GeV/c, corresponding to medium-induced yield suppression due to energy loss, rising towards larger $p_{\text{T,ch jet}}$. In contrast, $I_{\text{AA}}(p_{\text{T,ch jet}})$ for R = 0.5 is consistent with unity over the

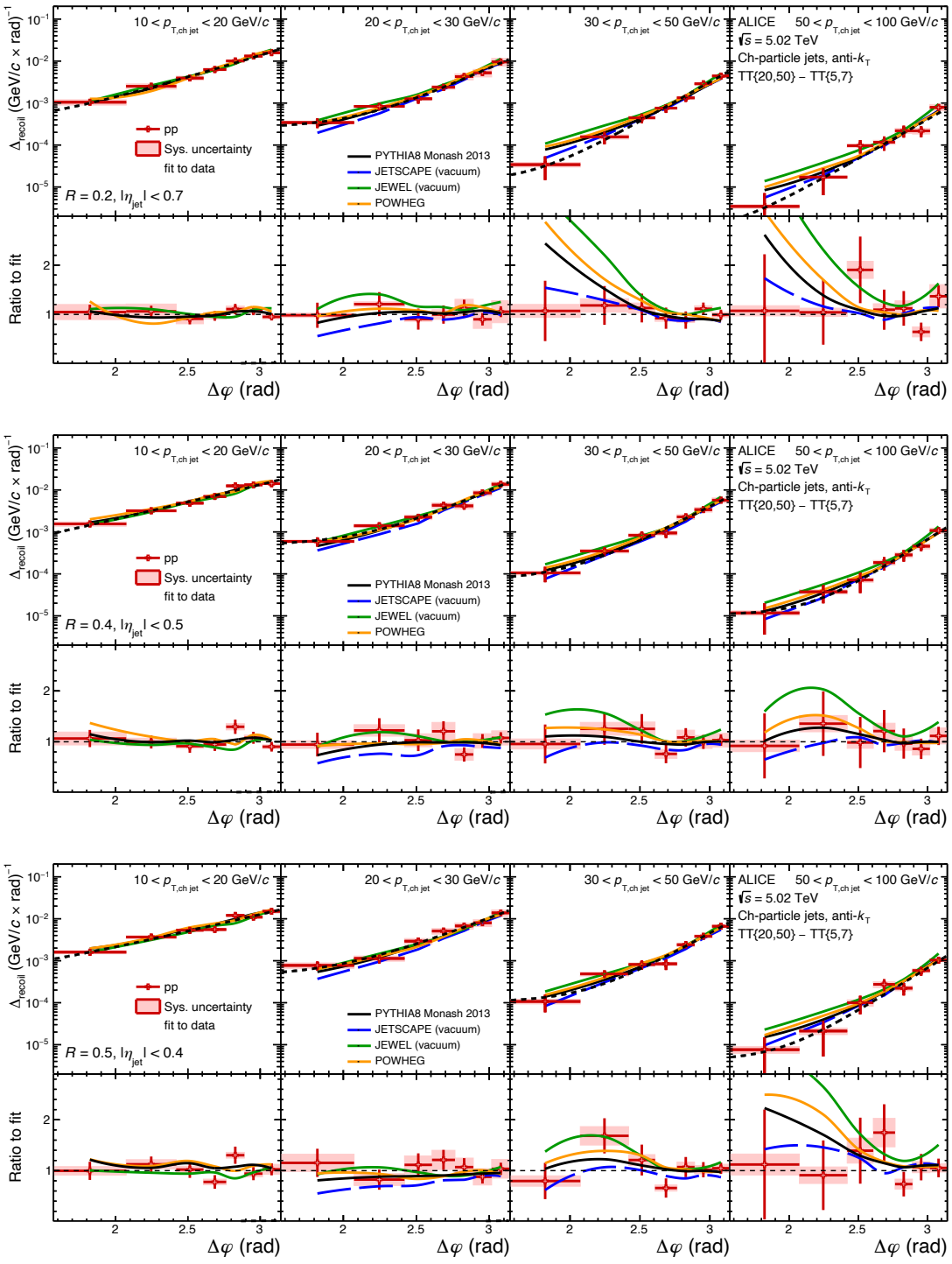

Figure 5.48: Corrected $\Delta_{\text{recoil}}(\Delta\varphi)$ distributions for pp collisions at $\sqrt{s}$ = 5.02 TeV for R = 0.2 (top), 0.4 (middle), and 0.5 (bottom) in $p_{\text{T,ch jet}}$ bins (left to right): [10,20], [20,30], [30,50], and [50,100] GeV/c. JETSCAPE, JEWEL, PYTHIA8, and POWHEG calculations are also shown. Upper sub-panels show the individual distributions, while lower sub-panels show their ratio to a functional fit of the measured data.

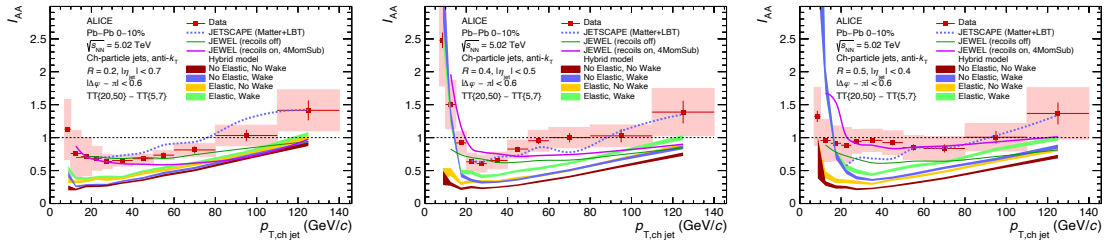

Figure 5.49: $I_{AA}(p_{T,ch\ jet})$ from the $\Delta_{recoil}(p_{T,ch\ jet})$ distributions measured for $R = 0.2$ (top), 0.4 (middle), and 0.5 (bottom) in central Pb–Pb and pp collisions (Fig. 5.45). JETSCAPE, JEWEL, and the Hybrid Model calculations are also shown.

range $7 < p_{T,ch\ jet} < 110$ GeV/c, indicating that the angular scale of medium-induced energy loss is less than 0.5 rad. Measurements of $I_{AA}(p_{T,ch\ jet})$ for central Au–Au collisions at $\sqrt{s_{NN}} = 200$ GeV with direct photon and π^0 triggers have recently been reported [221, 232], with a similar observation of less suppression for $R = 0.5$ than for $R = 0.2$, likewise indicating a similar angular scale of jet energy redistribution due to quenching at RHIC collision energies.

The JETSCAPE calculation describes well the measured $I_{AA}(p_{T,ch\ jet})$ distributions for $R = 0.2$ and 0.4 in $p_{T,ch\ jet} > 20$ GeV/c, including the rising trend for $p_{T,ch\ jet} > 60$ GeV/c. JETSCAPE predicts a similar $p_{T,ch\ jet}$-dependence of $I_{AA}(p_{T,ch\ jet})$ for $R = 0.5$, which however is not consistent with the measurement.

The JEWEL calculations, both recoils-off and recoils-on, describe the $I_{AA}(p_{T,ch\ jet})$ distribution for $R = 0.2$ at low $p_{T,ch\ jet}$, but do not capture the $p_{T,ch\ jet}$ dependence of the data and underpredict them at higher $p_{T,ch\ jet}$. For $R = 0.4$, both versions underestimate the data at high $p_{T,ch\ jet}$. For $R = 0.4$ and 0.5, JEWEL (recoils on) shows a significant increase in $I_{AA}(p_{T,ch\ jet})$ towards low $p_{T,ch\ jet}$ for $p_{T,ch\ jet} < 20$ GeV/c, similar to the trend in the data for $R = 0.4$. This increase is not seen for recoils-off. The larger value of $I_{AA}(p_{T,ch\ jet})$ in $20 < p_{T,ch\ jet} < 60$ GeV/c for $R = 0.5$ seen in the data is reproduced by JEWEL with recoils-on but not recoils-off. This R-dependence is due to the implementation of medium response in JEWEL, in which energy is carried by recoiling partons at large angles to the jet centroid [101].

Hybrid Model calculations of $I_{AA}(p_{T,ch\ jet})$ underestimate the magnitude of the data for all settings, although they do reproduce the rising trend with increasing $p_{T,ch\ jet}$ seen in the data for $p_{T,ch\ jet} > 20$ GeV/$c$for $R = 0.2$ and $R = 0.4$. The Hybrid Model with wake turned on likewise captures the sharply rising trend in the data with decreasing $p_{T,ch\ jet}$ at low $p_{T,ch\ jet}$ for $R = 0.4$, while no rising trend is seen when the wake is turned off, independent of the elastic scattering component. The model also exhibits a rising trend for $R = 0.5$, which in this case is not seen in the data within the experimental

uncertainties.

Overall, JETSCAPE most accurately describes both the magnitude and $p_{\mathrm{T,ch\ jet}}$ dependence of $I_{\mathrm{AA}}(p_{\mathrm{T,ch\ jet}})$ in the range $p_{\mathrm{T,ch\ jet}} > 20$ GeV/c for $R = 0.2$ and $R = 0.4$, while JEWEL most accurately describes it in the same $p_{\mathrm{T,ch\ jet}}$ region for $R = 0.5$. The rising trend in data towards low $p_{\mathrm{T,ch\ jet}}$ for $R = 0.4$ in $p_{\mathrm{T,ch\ jet}} < 20$ GeV/c is described by both the Hybrid Model and JEWEL, but only with the inclusion of medium-response effects. These models do not, however, describe the flatter trend seen for $R = 0.5$.

5.8.3 Comparison of $\Delta_{\mathrm{recoil}}(\Delta\varphi)$ in pp and Pb–Pb collisions - acoplanarity

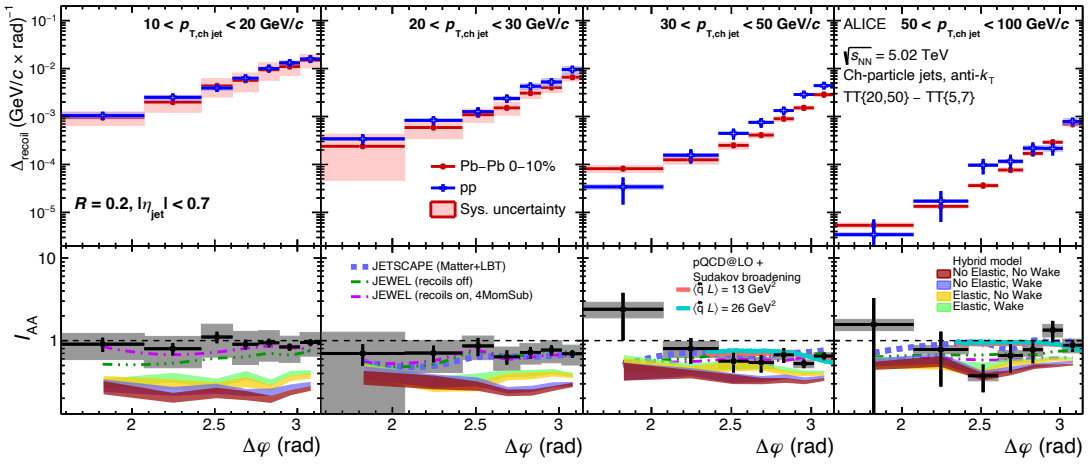

Figure 5.50: Distributions as a function of $\Delta\varphi$ for $R = 0.2$. Upper panels: $\Delta_{\mathrm{recoil}}(\Delta\varphi)$ in intervals of $p_{\mathrm{T,ch\ jet}}$ measured in pp and Pb–Pb collisions. Lower panels: $I_{\mathrm{AA}}(\Delta\varphi)$, the ratio of the pp and Pb–Pb distributions in the corresponding upper panel. Predictions from JETSCAPE, JEWEL, Hybrid model, and a pQCD calculation are also shown.

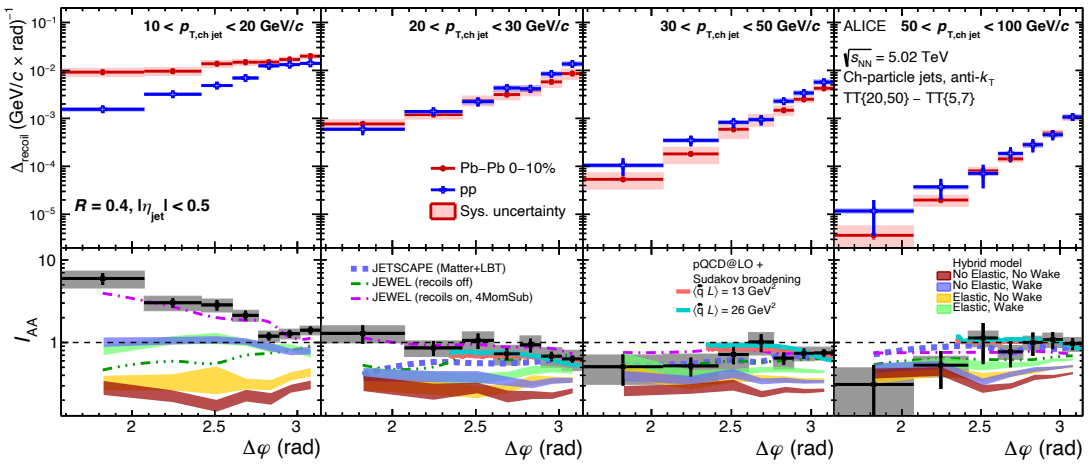

Figure 5.51: Same as Fig. 5.50, for $R = 0.4$.

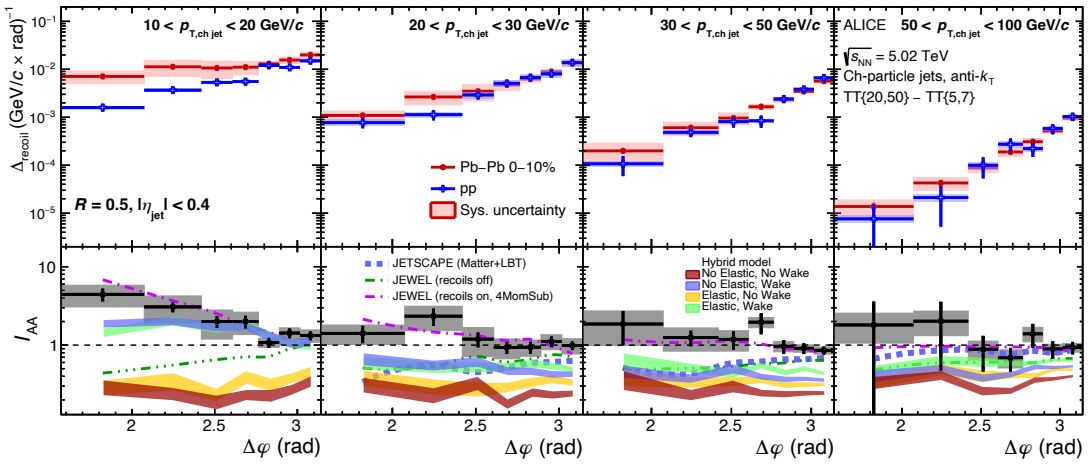

Figure 5.52: Same as Fig. 5.50, for $R = 0.5$.

Figures 5.50, 5.51, and 5.52, upper panels, show $\Delta_{\text{recoil}}(\Delta\varphi)$ (acoplanarity) distributions measured in different $p_{\text{T,ch jet}}$ intervals $[10, 20]$, $[20, 30]$, $[30, 50]$, $[50, 100]$ GeV/c for pp and Pb–Pb collisions. The lower panels show their ratio, $I_{\text{AA}}(\Delta\varphi)$, for $R = 0.2$, 0.4, and 0.5, respectively. The key physics conclusions from these results, including phenomenological discussion and model comparisons, are discussed below.

Suppression of $I_{\text{AA}}(\Delta\varphi)$ below unity can be seen in some $p_{\text{T,ch jet}}$ regions for $R = 0.2$ and 0.4, consistent with the yield suppression in Fig. 5.49. In the range $p_{\text{T,ch jet}} > 10$ GeV/c for $R = 0.2$, and the range $p_{\text{T,ch jet}} > 20$ GeV/c for $R = 0.4$ and $R = 0.5$, the shape of the Pb–Pb $\Delta_{\text{recoil}}(\Delta\varphi)$ distributions are consistent with that of the pp distributions in some $p_{\text{T,ch jet}}$ regions, corresponding to no significant in-medium acoplanarity broadening within the experimental uncertainties. In contrast, significant enhancement in $I_{\text{AA}}(\Delta\varphi)$ at $\Delta\varphi$ values far from π is observed in the region $10 < p_{\text{T,ch jet}} < 20$ GeV/c for $R = 0.4$ and 0.5, corresponding to medium-induced broadening of the acoplanarity distribution. Namely, the medium-induced acoplanarity broadening is seen only in the range $10 < p_{\text{T,ch jet}} < 20$ GeV/c, and only for $R = 0.4$ and 0.5. The value of $I_{\text{AA}}(\Delta\varphi)$ is either consistent with unity or suppressed at larger $p_{\text{T,ch jet}}$ for $R = 0.4$ and 0.5, and for all measured $p_{\text{T,jet}}$ for $R = 0.2$.

Figures 5.50, 5.51, and 5.52 also compare the measured $I_{\text{AA}}(\Delta\varphi)$ to theoretical calculations. The JETSCAPE calculation describes the $R = 0.2$ data for $p_{\text{T,ch jet}} > 20$ GeV/c, where the results of the calculation are available, while it underestimates the $R = 0.4$ data for $20 < p_{\text{T,ch jet}} < 30$ GeV/c and $R = 0.5$ data for $20 < p_{\text{T,ch jet}} < 50$ GeV/c, with larger discrepancy farther from $\Delta\varphi = \pi$. The JEWEL calculation also describes the $R = 0.2$ data for all $p_{\text{T,ch jet}}$ intervals, with minimal difference between recoils-on and

recoils-off. For larger R, JEWEL (recoils on) describes the data for all $p_{\mathrm{T,ch\ jet}}$ intervals and jet R, while JEWEL (recoils off) significantly underpredicts the data in the region $p_{\mathrm{T,jet}} < 20$ GeV/c for $R = 0.4$ and $p_{\mathrm{T,jet}} < 50$ GeV/c for $R = 0.5$, most significantly in the tails of the distributions. The Hybrid model underpredicts the magnitude of the $I_{\mathrm{AA}}(\Delta\varphi)$ for $R = 0.2$ and $R = 0.4$, for all model settings. The inclusion of wake effects increases the $I_{\mathrm{AA}}(\Delta\varphi)$ at low $p_{\mathrm{T,ch\ jet}}$ for $R = 0.2$ and $R = 0.4$, while the inclusion of elastic scattering moderately increases the prediction close to $\Delta\varphi = \pi$ in all $p_{\mathrm{T,ch\ jet}}$ intervals for $R = 0.2$, and for $p_{\mathrm{T,ch\ jet}} > 20$ GeV/c for $R = 0.4$ and $R = 0.5$, bringing the predictions closer to data. Similar to the JEWEL calculation, the significant azimuthal broadening seen at low $p_{\mathrm{T,ch\ jet}}$ for $R = 0.4$ and $R = 0.5$ is qualitatively reproduced when including wake effects in the Hybrid model, although the magnitude of the broadening is underpredicted for $R = 0.4$. The pQCD calculations at LO reproduce the measured $I_{\mathrm{AA}}(p_{\mathrm{T,ch\ jet}})$ distributions in the range $p_{\mathrm{T,ch\ jet}} > 20$ GeV/c for $R = 0.2$ and 0.4, though over a restricted range in acoplanarity, $2.4 < \Delta\varphi < \pi$. The data do not discriminate between the two values of quenching parameter in calculation, $\langle\hat{q}L\rangle = 13$ and 26 GeV^2. A higher-order calculation is required to extend the range of $\Delta\varphi$, with correspondingly greater discrimination of quenching parameters.

Overall, JEWEL (recoils on) describes both the data shape and magnitude well over the full R and $p_{\mathrm{T,ch\ jet}}$ range, including the significant azimuthal broadening for low $p_{\mathrm{T,ch\ jet}}$ and large R. However, none of the models considered successfully describes the full set of measured data.

A measurement of energetic di-jets in Pb–Pb collisions at $\sqrt{s_{\mathrm{NN}}} = 2.76$ TeV has also revealed significant broadening and softening of recoil-jet structure [233]. Such measurements, the results of this analysis, and inclusive jet production and jet substructure measurements, each probe a different aspect of the jet–medium interaction. A successful model of jet quenching must describe this full set of data correctly. A global analysis is required to ascertain whether a fully consistent description of all such data can be achieved by a suitable choice of model parameters, or whether the jet quenching mechanisms encoded in the model can be excluded by such a comprehensive comparison to multi-messenger jet quenching data.

6 Progress in heavy-flavour jet production in pp collisions at $\sqrt{s} = 13$ TeV

Heavy quarks, because of their large masses, are dominantly produced in hard scatterings at the initial stage of a collision, before the QGP formation, and their thermal production in the QGP is negligible. While traversing the medium, they lose part of their energy via collisional and radiative processes [234]. Therefore, heavy quarks are ideal tomographic probes of the QGP, allowing extraction of the medium transport properties [235]. Studies of production properties of heavy-flavour jets in pp collisions can set additional constraints on the heavy-quark energy loss mechanism and the medium properties as they provide insight into how the lost energy is radiated and dissipated in the medium. Heavy flavours can thus probe the entire space-time evolution of the system. They interact with the medium through gluon radiation and elastic scatterings. Correlating heavy-flavour particles with jets and studying particle production in jets compared to the production in underlying events will provide key information to understand the hadronization mechanism of heavy quarks.

We have studied the azimuthal correlations between charged-particle jet and heavy-flavour hadrons in pp collisions at $\sqrt{s} = 13$ TeV. We briefly describe the analysis strategy and the basic performances reached so far. The goal of this study is to measure the radial distribution of associated particles with respect to the jet axis and the baryon to meson ratio of the radial particle distribution for D meson and Λ_c baryon. In this analysis, the critical steps involve extracting the signal of heavy-flavor particles using machine learning techniques and applying mixed event correlations.

6.1 Analysis strategy

We measured the jet and heavy-flavour hadron (D^0, D^+, Λ_c^+) correlations in pp sample at $\sqrt{s} = 13$ TeV with a strategy similar to the one used in jet-hadron correlation [236, 237] studies. Jets and identified particles belonging to the same collision event are selected considering a trigger jet defined by the transverse momentum threshold $p_{\mathrm{T,trig}}^{\mathrm{jet}}$ and associated particles defined by $p_{\mathrm{T,assoc}}$. The analysis steps are as follows:

Reconstructed trigger jets

Reconstructed charged jets are utilized as a trigger in the correlation analysis. We used the Fastjet package with the anti-k_{T} algorithm and a resolution parameter of $R = 0.4$. Several low transverse momentum cuts were applied to the jet constituents, resulting in several different jet definitions. Jets with a higher minimum constituent cut are less sensitive to the underlying event. On the other hand,

they are also biased towards harder fragmentation. Only jets with a cone fully contained within the acceptance are accepted, limiting the pseudo-rapidity acceptance to $|\eta_{\rm jet}| < 0.5$. In addition, a jet area cut $A_{\rm jet} > 0.56\pi R^2$ is applied.

The transverse momentum of the reconstructed jets is corrected for the underlying event by the default $k_{\rm T}$ approach, details are in Section 3.3. It should be emphasized that this correction is applied to the jet transverse momentum only. It should not be confused with the correction of the correlation function itself.

Heavy-flavour hadron reconstruction

$\rm D^0$, $\rm D^+$ mesons and their anti-particles are reconstructed in the central rapidity region by exploiting their charged hadronic decay channels: $D^0 \rightarrow K^-\pi^+$ (branching ratio B.R. = (3.95 ± 0.03)%, and mean proper decay length $c\tau = 123\ \mu m$), $D^+ \rightarrow K^-\pi^+\pi^+$ (with B.R. = (9.13 ± 0.19)% and $c\tau = 312\ \mu m$). The selection of $\rm D^0$, $\rm D^+$ candidates is based on the reconstruction of the displaced secondary vertex topology, with a typical separation of $\sim 100 - 300\ \mu m$ from the interaction point due to their relatively large lifetime.

Λ_c^+ baryons and their anti-particles are reconstructed through the golden decay channel $\Lambda_c^+ \rightarrow p^+K^-\pi^+$ together with their charge conjugates with an overall branching ratio of B.R. = (6.28 ± 0.32)%. The reconstruction of Λ_c^+ candidates at central rapidity, exploits the displaced topology of the decay with respect to the collision primary vertex of interaction for the definition of topological variables. The Λ_c^+ baryon has, in fact, a mean proper decay length $c\tau = 60\ \mu m$ which causes its secondary vertex to be typically displaced by a few tens of μm from the primary vertex of the pp interaction. The daughter particles are then identified by the information provided by the TPC and TOF detectors helping in the reduction of the large combinatorial background.

The associated particle is then extracted by fitting the invariant mass distribution in each transverse momentum region with a function composed of Gaussian for the signal and an exponential term describing the combinatorial background. Details on the particle reconstruction are given in the next section.

Correlation of trigger jets with associated ($\rm D^0$, $\rm D^+$, Λ_c^+) candidates

Each jet is considered as the trigger axis and ($\rm D^0$, $\rm D^+$, Λ_c^+) candidates as associated particles. Correlations are, then, constructed in a specified $p_{\rm T,trig}^{\rm jet}$ and $p_{\rm T,assoc}$ range. The $\varphi_{\rm trig} - \varphi_{\rm assoc} = \Delta\varphi$ and the $\eta_{\rm trig} - \eta_{\rm assoc} = \Delta\eta$, as well $\Delta r = \sqrt{\Delta\varphi^2 + \Delta\eta^2}$ information are stored. $\Delta\eta$ and $\Delta\varphi$ are relative pseudo-rapidity and azimuthal angle with respect to the jet direction, as shown schematically in Fig. 6.1.

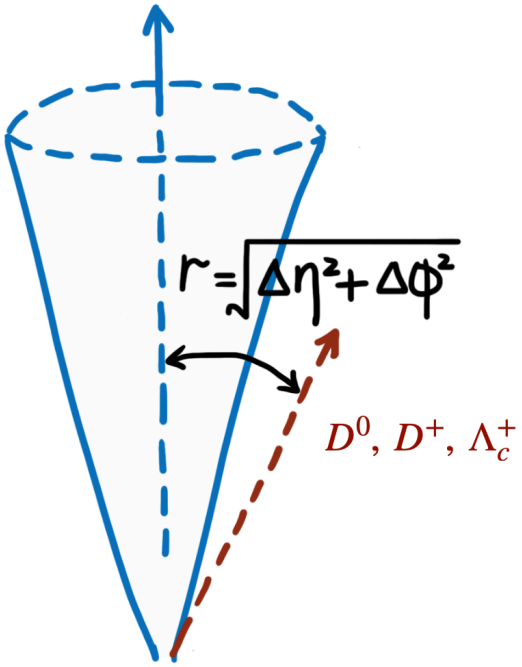

Figure 6.1: Schematic of jet-particle angular correlations.

Correction by Event Mixing technique

Structures in the angular correlation distribution may appear even for uncorrelated pair of particles due to the limited detector acceptance or angular inhomogeneities in the trigger jet and track reconstruction efficiency as a function of $\Delta\varphi$ and $\Delta\eta$. These effects are removed using the event mixing technique. The analysis is applied on the same data sample as the standard one (called "same event" analysis, SE), but the trigger particles found in each event were correlated to charged particles reconstructed in different events ("Mixed Events" analysis, ME) with similar features, in particular similar event multiplicity and z position of the primary vertex.

The differential yield of associated identified particles per trigger jet is obtained by

$$\frac{1}{N_{\text{jet}}}\frac{d^2N}{d\Delta\eta d\Delta\phi} = S(\Delta\eta,\Delta\phi)\frac{ME(0,0)}{ME(\Delta\eta,\Delta\phi)}. \tag{6.1}$$

Here, N is the total number of correlated jet-hadron pairs. The signal pair distribution $S(\Delta\eta,\Delta\phi)$ and the mixed-event pair distribution $ME(\Delta\eta,\Delta\phi)$ represent the per-trigger-jet yields of associated particles from the same and mixed events,

$$S(\Delta\eta,\Delta\phi) = \frac{1}{N_{\rm jet}}\frac{d^2N^{\rm same}}{d\Delta\eta d\Delta\phi}, ME(\Delta\eta,\Delta\phi) = \frac{1}{N_{\rm jet}}\frac{d^2N^{\rm mix}}{d\Delta\eta d\Delta\phi}.$$

The ratio $\frac{ME(0,0)}{ME(\Delta\eta,\Delta\phi)}$ is the normalized correction factor.

This is how far we could progress, several subsequent corrections and systematic calculation remain to be implemented. They include corrections via event mixing techniques, background contribution subtraction from signal correlations, correction for candidate and jet reconstruction efficiency, correction for secondary particle contamination and so on. Ultimately, our focus will shift towards studying the correlation properties.

6.2 Raw distributions

Candidate Selection and Invariant Mass plots

The strategy for the signal extraction from the large combinatorial background due to uncorrelated tracks is based on the reconstruction and selection of the secondary vertex topology that are significantly displaced with respect to the primary vertex. D^0, D^+ and Λ_c^+ candidates are formed by considering two, and triplets (triplets) charged tracks matching the correct charge combination, which also satisfy the following track quality criteria:

- ITS and TPC refit
- at least 70 (out of a maximum of 159) associated space points in the TPC
- ratio of crossed rows over findable clusters in the TPC larger than 0.8
- $\chi^2/\text{ndf} < 2$ in the TPC
- at least two (out of six) hits in the ITS, out of which at least one had to be in either of the two SPD layers
- $|\eta| < 0.8$
- $p_{\rm T} > 0.3$ GeV/c

These track selection criteria reduce the candidate (D^0, D^+, Λ_c^+) acceptance, which drops steeply to zero for $y_{\rm lab} > 0.5$ at low $p_{\rm T}$ and for $y_{\rm lab} > 0.8$ at high $p_{\rm T}$. A $p_{\rm T}$-dependent fiducial acceptance region was therefore defined as $y_{\rm lab} < y_{\rm fid}(p_{\rm T})$ increasing from 0.5 to 0.8 in the transverse momentum range $0 < p_{\rm T} < 5$ GeV/c according to a second-order polynomial function, and $y_{\rm fid} = 0.8$ for $p_{\rm T} > 5$ GeV/c. This strategy was adopted for all the previous D-meson and Λ_c^+ baryon analyses in ALICE [118, 126, 238–240].

To reduce the large combinatorial background and to separate the signal from background, a machine-

learning approach with binary classification, based on boosted decision trees (BDT), implemented in the XGBoost library [241, 242], was adopted. For the BDT training, prompt signal candidates from MC simulations based on the PYTHIA Monash event generator, while background samples were extracted from the candidate invariant-mass distributions inside the window of $5\sigma < |\Delta M| < 9\sigma$ in data, where ΔM is the difference between the candidate invariant mass and the mass of the hadron candidate, and σ is the invariant-mass resolution. Before the training, loose kinematic and topological selections were applied to the charm-hadron candidates and their decay topology along with the PID (Particle IDentification) information of decay product tracks. The PID selections were based on the difference between the measured and expected detector signals for a given particle specie hypothesis, in units of the detector resolution. Protons, pions and kaons were selected by requiring compatibility with the respective hypothesis within three standard deviations (3σ) for both the TPC specific energy loss (dE/dx) and the TOF time-of-flight. Tracks without TOF hits were relying on the particle identification information provided by the TPC only.

All the candidates that fulfil these requirements were considered for the analysis and used for machine learning based selection. Below are the specific details of the machine learning (ML).

Machine Learning selection and model optimization

The boosted decision tree algorithm, XGBoost is used to perform a binary classification between signal and combinatorial background. With this supervised machine learning algorithm, multiple selection criteria are used as features in the training. After the model is trained, all selection criteria are combined into one single response variable (BDT output score) for each candidate class. Then the trained model is applied to the full data sample. The model training and performance assessment are performed locally using the software developed in the hipe4ml package.

Model Training In order to obtain a ML algorithm able to make predictions, it is necessary to build the data sets on which the model training is performed and its performance is evaluated. These are called *training* and *test* sets and are constructed from MC and real data samples. In this analysis, the training and test sets are composed by two classes of candidates: prompt D mesons are taken from the MC sample, while combinatorial-background candidates are taken from real data. The examples for the combinatorial background are extracted from the data sample of real candidates, selecting D candidates in the sidebands of the D meson peak in the invariant-mass distribution. The idea behind this decision is to use real data, where feasible, to avoid a loss in the model predictive power caused by possible shortcomings of simulations in describing the real combinatorial background. The use of real background candidates is a well established procedure since it permitted to avoid biases in the real data

analysis, coming possibly from defects of the MC in reproducing the data. The number of signal and background candidates used to build the training and test set are reported, for the different p_{T} intervals in which the training is performed. In order to have a good training performance, to ratio of signal to background candidates is set to 1:2, if background sample is sufficient.

Choice of training variables Topological and kinematic variables are used in the model training together with the PID information of each candidate daughter. The topological variables adopted are variables typically used in other analyses of prompt D mesons performed without ML techniques [126]. Furthermore, in order to allow the model to better discriminate between signal and background and to keep the number of variables small and avoid overtraining the ML model, combinations of PID information from TPC and TOF are taken into account.

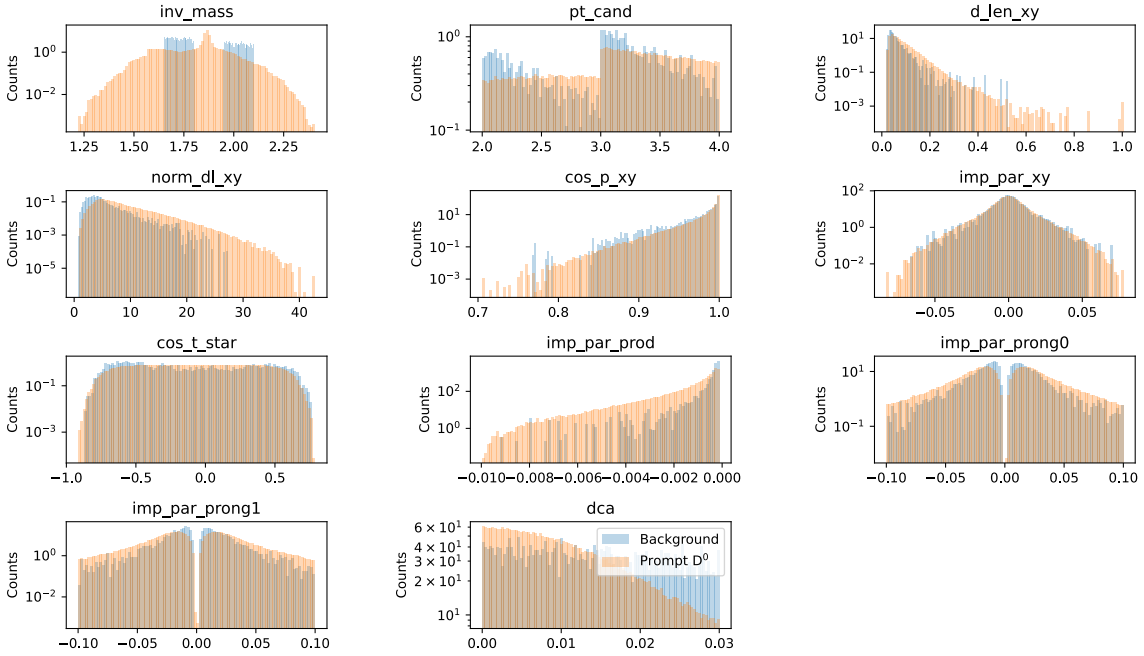

Figure 6.2: Distributions of training variables, invariant mass, and p_{T} for signal D^0 and combinatorial-background candidate variables in the $2 < p_{\mathrm{T}} < 4$ GeV/c interval.

The distributions of the training variables are shown in Fig. 6.2 for $2 < p_{\mathrm{T}} < 4$ GeV/c as an example. The linear correlations between the variables used in the training are reported in Fig. 6.3. Variables that carry the same physical information, such as those related to the decay length, are strongly correlated as expected. Moreover, there are some differences in the variable correlations between signal and background candidates, which could be exploited by the model to discriminate signal from background. It is also useful to control the presence of correlations between the training variables. When

choosing the variables, the model gains performance in class separation with an increasing number of variables, but also complexity. This can lead to over-training, which is visible in the difference between the performance of the training and test set. Therefore, only the variables that have large impact on the model performance should be included. The ranking of the impact - feature importance can be ordered by SHapley Additive exPlanations (SHAP) values, which is the average impact on the model output magnitude.

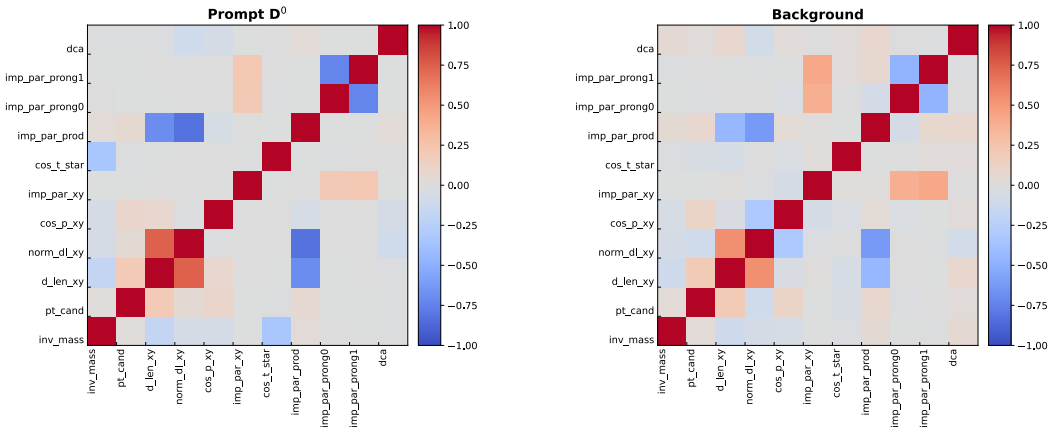

Figure 6.3: Linear correlations between the training variables, the invariant mass and the p_{T}, for prompt D^0 meson (left) and combinatorial background(right) in the $2 < p_{\mathrm{T}} < 4$ GeV/c. The correlation value is represented with colours: from red (fully correlated) to blue (fully anti-correlated).

Model optimization The hyper-parameter configuration used for training, in the different p_{T} intervals, was chosen with Optuna optimisation procedure along with a 5-fold cross validation implemented in the hipe4ml package.

After the training phase, the model is applied to both training and test sets in order to extract the ML score distributions and verify the level of agreement between the two samples. In binary classification cases, one score is provided by the model, representing the probability for a candidate to be signal or background. By construction, for each candidates, these probabilities/scores sum to unity. Figures 6.4 show example of ML score distribution for background and signal candidates in different p_{T} intervals. Small deviations, though with large statistical uncertainties, are observed between the training and the test sample, for both signal and background candidates, becoming more evident especially in the tails of the distributions.

To access the performance of the model, the area under the Receiver Operating Characteristic curve

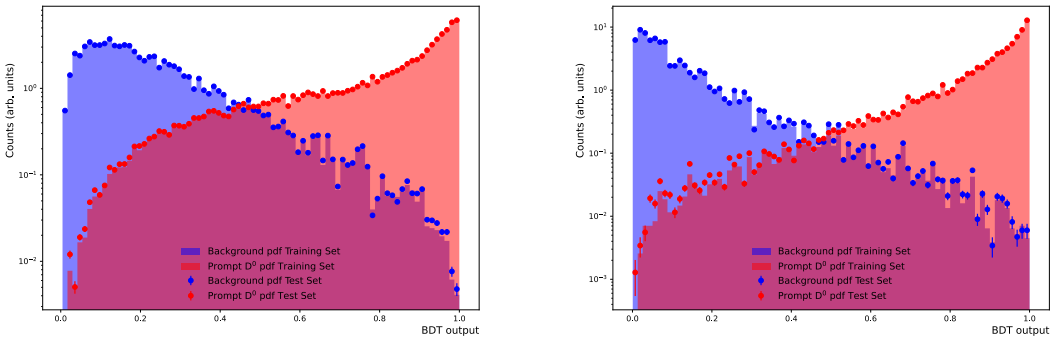

Figure 6.4: Distributions of ML output scores for combinatorial background (blue) candidates and prompt D^0 meson (red) for training (shaded area) and test sample (data point) in two transverse momentum intervals, $2 < p_T < 4$ GeV/c (left) and $4 < p_T < 6$ GeV/c (right).

(ROC AUC) is considered. This is obtained by evaluating the True Positive Rate, the signal efficiency, as function of the False Positive Rate, the background selection efficiency, for various threshold settings on the ML score. Generally, the ROC AUC values are comprehended between one half, corresponding to a random classifier, and 1 meaning a perfect recognition of signal and background candidates. The obtained ROC AUC are all about 90% meaning that a good discrimination power was achieved with the training of the models. Figures 6.5 show the ROC distributions for training and test sample in two transverse momentum $2 < p_T < 4$ GeV/c (left) and $4 < p_T < 6$ GeV/c intervals of D^0 meson.

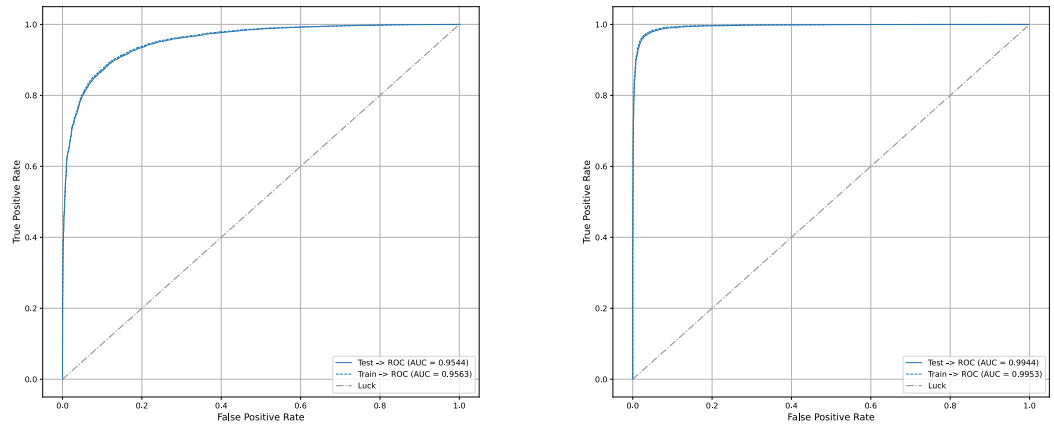

Figure 6.5: ROC curves for the models trained for D^0 meson in the $2 < p_T < 4$ GeV/c (left) and $4 < p_T < 6$ GeV/c (right) intervals for the binary-classification.

ML Working point The choice of the ML output scores to be applied for candidate selection on data was

performed by estimating the expected significance ($S/\sqrt{S+B}$) and the efficiency × acceptance factor ($\epsilon \times A_{cc}$) for D^0 meson as function of the ML output score. The expected signal per event needed for the computation of the expected significance and signal-to-background ratio was estimated as:

$$S_{\text{ML score}} = 2 \cdot \frac{d\sigma^{\text{FONLL}}}{\sigma^{\text{pp}}_{\text{MB}} dp_{\text{T}} dy} \cdot \Delta p_{\text{T}} \Delta y \cdot BR \cdot (\epsilon \times A_{cc})_{\text{ML score}} \tag{6.2}$$

where the factor 2 takes in account the particle-antiparticle reconstruction, $\sigma^{\text{pp}}_{\text{MB}}$ is the minimum-bias inelastic cross-section. Δp_{T} is the width of the p_{T} interval, Δy is the correction factor for the rapidity coverage, BR is the branching ratio. The expected background under the signal peak was instead evaluated from a fraction of the data by fitting the sidebands of the invariant-mass distribution, and subsequently scaling it to match the one in the full data sample.

Invariant mass plot extraction

The Machine Learning selection was then applied to data: the extracted invariant mass distributions are represented in Fig. 6.6. These are fitted with an exponential and a Gaussian term to properly reproduce the combinatorial background and the signal shape respectively. Currently, we have only utilized the LHC16k statistics, representing one-tenth of the total dataset. With an increase in statistics, the is a potential for improving and optimizing the current results.

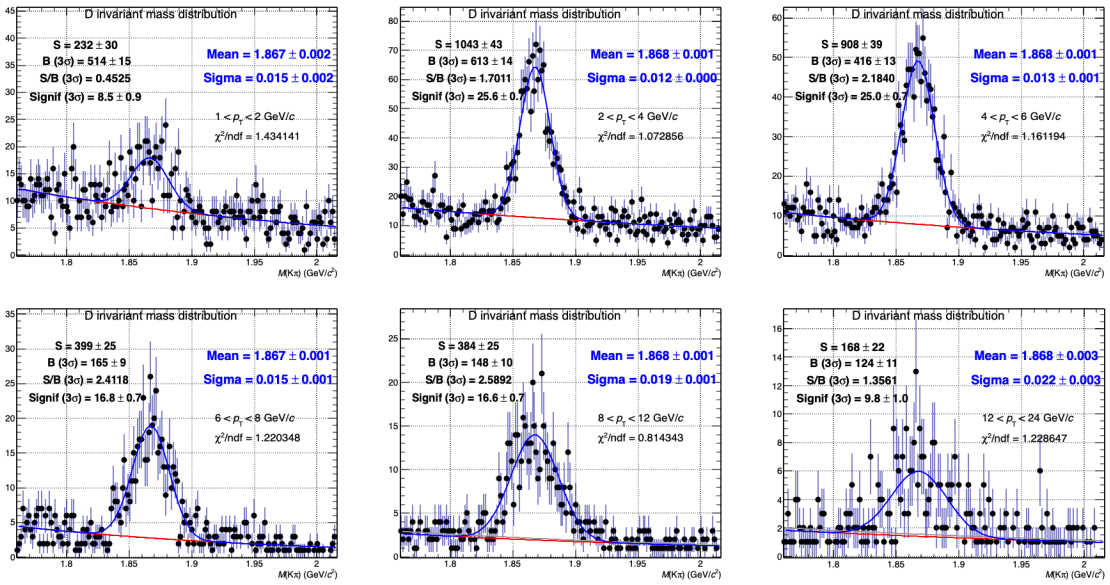

Figure 6.6: Fits to the invariant-mass distributions of D^0 candidates in different p_{T} intervals from 1 to 24 GeV/c before efficiency correction. The blue curve represents the total fit function and the red curve the represents the combinatorial background.

Jet-particle correlations

At the present stage of this analysis, we have obtained the raw two-dimensional distributions of $\Delta\eta - \Delta\phi$ in different D^0 p_T intervals with $p_{T,trig}^{jet} > 1$ GeV/c from same event, as illustrated in Fig. 6.7. These raw results are statistically deficient because not all statistics are currently used. The raw $\Delta\phi$ distribution of D^0 meson, derived from the projection of Fig. 6.7, is depicted in Fig. 6.8. Currently, these results lack physical significance, merely serving as rough performance plots.

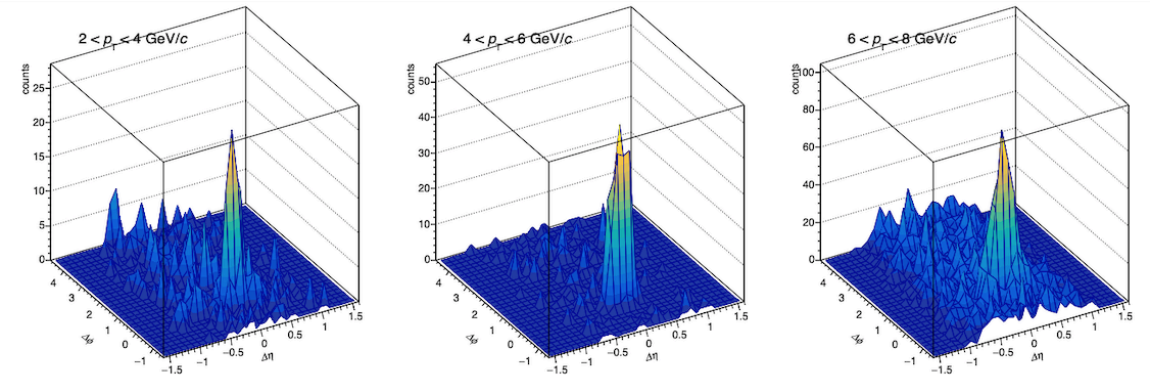

Figure 6.7: Raw $\Delta\eta - \Delta\phi$ distributions in D^0 p_T $[2,4]$, $[4,6]$, $[6,8]$ GeV/c intervals without normalization from same event.

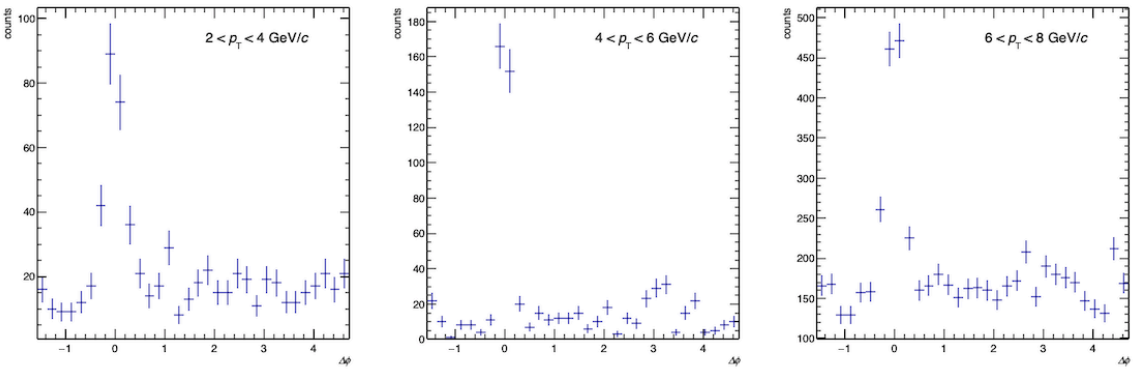

Figure 6.8: Raw $\Delta\phi$ distributions in D^0 p_T $[2,4]$, $[4,6]$, $[6,8]$ GeV/c intervals projected by Fig. 6.7.

Our primary task was to finalize the basic event analysis code for heavy flavor particles, aimed at signal extraction through machine learning techniques. We thus gained a comprehensive understanding of the machine learning techniques tailored to the identification of heavy flavor particles. The two-dimensional correlation function has so far been obtained only for D^0 particles. The analysis code for implementing the mixed event technique is presently under development. The immediate goal is to obtain the two-dimensional correlation functions for D^0, D^+, and Λ_c^+ particles, both in the same and mixed events. Subsequently, the distribution of radial ΔR values will be examined, followed by an investigation into the radial ΔR dependence of the baryon-to-meson ratio. This is similar to the approach in the theoretical

analysis [237].

7 Conclusions and Outlook

We have reported about the cross sections of the inclusive charged-particle jet production with transverse momentum from 5 GeV/c to 140 GeV/c measured in pp collisions at $\sqrt{s}$ = 13 TeV. We have used the anti-k_{T} jet finding algorithm with different resolution parameters R varied from 0.2 to 0.7 and the pseudorapidity range $|\eta_{\mathrm{jet}}| < 0.9-R$. We have compared the inclusive charged-particle jet cross sections to LO PYTHIA and NLO POWHEG pQCD calculations. As expected, a better agreement between data and MC is observed for the NLO predictions, although the NLO prediction overestimates the jet yield below 20 GeV/c. We have also studied the cross section ratios for different resolution parameters. These cross-section ratios for smaller jet R over larger R increase with jet p_{T} and saturate at the high end of the jet p_{T} range, indicating an increasingly stronger collimation of high-momentum jets.

We have presented a study on the multiplicity dependence of jet production for different jet resolution parameters where we used the forward V0 multiplicity estimator. A higher (lower) jet yield is observed in higher (lower) multiplicity classes. Jet production in different multiplicity intervals compared to MB has a weak p_{T} and jet resolution parameter dependence. Furthermore, we have measured the self-normalised jet production yields and average jet p_{T} as a function of the self-normalised charged-particle multiplicity. The integrated jet yields and $\langle p_{\mathrm{T}} \rangle$ in the integrated p_{T} interval between 5 and 100 GeV/c increase with the self-normalised charged-particle multiplicity. No strong dependence of jet p_{T} and the resolution parameter R are observed except at low transverse momentum in the highest multiplicity percentile interval. We performed a similar analysis using the mid-rapidity SPD multiplicity estimator and found that the jet yield also increases with multiplicity, being consistent with those obtained with the V0 multiplicity estimator. A similar multiplicity dependence has also been reported for prompt D mesons in p–Pb collisions at $\sqrt{s_{\mathrm{NN}}}$ = 5.02 TeV and non-prompt J/ψ (from B hadron decays) production in pp collisions at $\sqrt{s}$ = 7 TeV when using the forward multiplicity estimator. Current MC event generators can only predict the rising trend but cannot describe the absolute yields, especially in the highest multiplicity class.

The measurements in small system presented in this analysis provide further insight into the interplay between soft particle production and hard processes. Detailed comparisons of models with data will help to elucidate the relationship between jet production mechanisms and high-multiplicity events in small systems, particularly at LHC energies.

We have reported about our measurements of semi-inclusive distributions of charged-particle jets re-

coiling from a high-p_{T} hadron trigger in pp collisions at $\sqrt{s} = 5.02$ TeV, using the large data samples recorded with the ALICE detector during LHC Run 2. The results have been presented as a function of both $p_{\mathrm{T,ch\ jet}}$, the recoil jet transverse momentum, and $\Delta\varphi$, the azimuthal separation between the trigger and recoil jet. We have used a statistical, data-driven method previously developed by the ALICE Collaboration to mitigate the large uncorrelated background jet yield in central Pb–Pb collisions, enabling measurements of jet quenching in a kinematic region previously unexplored by reconstructed jets at the LHC, including low $p_{\mathrm{T,ch\ jet}} \sim 10$ GeV/c with jet resolution parameter $R = 0.5$. The observed phenomena explore several different aspects of jet production in pp compared with Pb–Pb collisions.

The $p_{\mathrm{T,ch\ jet}}$ and azimuthal distributions measured in pp collisions provide a precise reference to explore medium-induced modifications to jet production in central Pb–Pb collisions, and are well described by pQCD-based calculations over the entire measured ranges. The ratio of recoil jet yields in pp collisions for $R = 0.2$ to that for $R = 0.4$ or 0.5 is below unity at high p_{T}, reflecting the well-established transverse profile of energy within a jet in vacuum. However, this ratio is observed to increase as $p_{\mathrm{T,ch\ jet}}$ is reduced below the value of $p_{\mathrm{T}}^{\mathrm{trig}}$, the trigger hadron p_{T}, in marked contrast to the behavior of a similar ratio measured for inclusive jet cross sections. Both sets of measurements are well described by pQCD calculations, suggesting that these opposing effects may arise from different jet production mechanisms, in particular suppression of leading order processes for the semi-inclusive population of jets recoiling from a high-p_{T} hadron trigger, in which $p_{\mathrm{T}}^{\mathrm{trig}}$ provides an additional scale of fragmentation.

The measured values of $I_{\mathrm{AA}}(p_{\mathrm{T,ch\ jet}})$, the ratio of recoil yield for Pb–Pb and pp collisions for the same jet R as a function of $p_{\mathrm{T,ch\ jet}}$, exhibit a dependence on $p_{\mathrm{T,ch\ jet}}$ and R. For $R = 0.5$, the ratio is consistent with unity within uncertainties over the entire measured range, indicating that medium-induced jet modifications as probed by this observable are largely constrained to angular scales less than 0.5 radians. The ratio of recoil jet yield in Pb–Pb collisions for $R = 0.2$ to that for $R = 0.4$ or 0.5 is below that for pp collisions at intermediate $p_{\mathrm{T,ch\ jet}}$, indicating medium-induced intra-jet broadening within this angular scale. For $R = 0.2$ and 0.4, the value of $I_{\mathrm{AA}}(p_{\mathrm{T,ch\ jet}})$ is below unity at intermediate $p_{\mathrm{T,ch\ jet}}$, increasing to unity at both lower and higher $p_{\mathrm{T,ch\ jet}}$. For $R = 0.4$, $I_{\mathrm{AA}}(p_{\mathrm{T,ch\ jet}})$ exceeds unity at the lowest value of $p_{\mathrm{T,ch\ jet}}$ reported here. Comparison to models indicate that the low-$p_{\mathrm{T,ch\ jet}}$ behavior may be due to the recovery of energy lost to the medium by higher-$p_{\mathrm{T,ch\ jet}}$ jets that are likewise correlated with the trigger. The high-$p_{\mathrm{T,ch\ jet}}$ behavior may arise from the interplay between the energy loss due to jet quenching and the geometric bias induced by using a hadron trigger.

The measured values of $I_{\mathrm{AA}}(\Delta\varphi)$, the ratio of recoil yield for Pb–Pb and pp collisions for the same jet R as a function of $\Delta\varphi$, provide the first measurement of significant in-medium jet acoplanarity broadening

in Pb–Pb collisions, for R = 0.4 and 0.5 at low $p_{\mathrm{T,ch\ jet}}$.

Current model calculations incorporating jet quenching do not reproduce all of these observations. Further modeling developments, and their comparison to these and similar data, promise significant new understanding of the mechanisms governing energy transport and the dynamics of the QGP. In the meantime, more precise and detailed measurements of semi-inclusive jet profiles and substructures with higher statistics from LHC RUN3 are anticipated to be pursued to unravel the possible origins of the physical results obtained above.

A feasibility study on the production of heavy-flavour jets (jet-D^0/D^+/Λc^+) in pp collisions at $\sqrt{s}$ = 13 TeV will be reported. The ($\Delta\eta$, $\Delta\phi$) distribution of baryons and mesons with respect to the triggered jet direction will be calculated to investigate the hadronization mechanisms.

References

[1] W. Commons, "Standard model of elementary particles", 2023. https://en.wikipedia.org/wiki/File:Standard_Model_of_Elementary_Particles.svg. XIV, 3

[2] P. D. Group and Z. et al, "Review of particle physics", *Progress of Theoretical and Experimental Physics* **2020** (08, 2020) 083C01. https://doi.org/10.1093/ptep/ptaa104. XIV, 6

[3] **NNPDF** Collaboration, R. D. Ball *et al.*, "The path to proton structure at 1% accuracy", *Eur. Phys. J. C* **82** (2022) 428, arXiv:2109.02653 [hep-ph]. XIV, 8

[4] H. Caines, "The search for C=critical behavior and other features of the QCD phase diagram – current status and future prospects", *Nucl. Phys. A* **967** (2017) 121–128. XIV, 10

[5] T. Pierog, I. Karpenko, J. M. Katzy, E. Yatsenko, and K. Werner, "EPOS LHC: Test of collective hadronization with data measured at the CERN Large Hadron Collider", *Phys. Rev. C* **92** (2015) 034906, arXiv:1306.0121 [hep-ph]. XIV, 12, 86

[6] **LHCb** Collaboration, R. Aaij *et al.*, "Centrality determination in heavy-ion collisions with the LHCb detector", *JINST* **17** (2022) P05009, arXiv:2111.01607 [nucl-ex]. XIV, 15

[7] **ALICE** Collaboration, "Centrality determination in heavy ion collisions", Tech. Rep. ALICE-PUBLIC-2018-011, Aug, 2018. https://cds.cern.ch/record/2636623. XIV, 16

[8] U. W. Heinz, "The strongly coupled quark-gluon plasma created at RHIC", *J. Phys. A* **42** (2009) 214003, arXiv:0810.5529 [nucl-th]. XIV, 17

[9] Z. Qiu, *Event-by-event Hydrodynamic Simulations for Relativistic Heavy-ion Collisions*. PhD thesis, Ohio State U., Columbus, 2013. arXiv:1308.2182 [nucl-th]. XIV, 18

[10] **ALICE** Collaboration, S. Acharya *et al.*, "Transverse momentum spectra and nuclear modification factors of charged particles in pp, p–Pb and Pb–Pb collisions at the LHC", *JHEP* **11** (2018) 013, arXiv:1802.09145 [nucl-ex]. XV, 23

[11] **CMS** Collaboration, V. Khachatryan *et al.*, "Charged-particle nuclear modification factors in Pb–Pb and p–Pb collisions at $\sqrt{s_{\mathrm{NN}}}$ = 5.02 TeV", *JHEP* **04** (2017) 039, arXiv:1611.01664 [nucl-ex]. XV, 23

[12] **ALICE** Collaboration, S. Acharya *et al.*, "Measurements of inclusive jet spectra in pp and central Pb–Pb collisions at $\sqrt{s_{\rm NN}}$ = 5.02 TeV", *Phys. Rev. C* **101** (2020) 034911, arXiv:1909.09718 [nucl-ex]. XV, 23, 24, 166

[13] **ATLAS** Collaboration, M. Aaboud *et al.*, "Measurement of the nuclear modification factor for inclusive jets in Pb+Pb collisions at $\sqrt{s_{\rm NN}}$ = 5.02 TeV with the ATLAS detector", *Phys. Lett. B* **790** (2019) 108–128, arXiv:1805.05635 [nucl-ex]. XV, 23, 24

[14] **ALICE** Collaboration, S. Acharya *et al.*, "Measurement of the groomed jet radius and momentum splitting fraction in pp and Pb–Pb collisions at $\sqrt{s_{NN}}$ = 5.02 TeV", *Phys. Rev. Lett.* **128** (2022) 102001, arXiv:2107.12984 [nucl-ex]. XV, 27

[15] **ALICE** Collaboration, J. Adam *et al.*, "Measurement of jet quenching with semi-inclusive hadron-jet distributions in central Pb–Pb collisions at $\sqrt{s_{\rm NN}}$ = 2.76 TeV", *JHEP* **09** (2015) 170, arXiv:1506.03984 [nucl-ex]. XV, 24, 27, 28, 59, 126, 130, 132, 137, 166, 167, 223

[16] https://home.cern/news/press-release/cern/new-state-matter-created-cern. XV, 11, 28

[17] **CMS** Collaboration, V. Khachatryan *et al.*, "Measurement of long-range near-side two-particle angular correlations in pp collisions at $\sqrt{s}$ =13 TeV", *Phys. Rev. Lett.* **116** (2016) 172302, arXiv:1510.03068 [nucl-ex]. XV, XVI, 30, 58

[18] J. Haffner, "The CERN accelerator complex. Complexe des accélérateurs du CERN",. https://cds.cern.ch/record/1621894. General Photo. XV, 33, 34

[19] A. Tauro, "ALICE Schematics." General Photo, 2017. XV, 36

[20] **ALICE** Collaboration, S. Acharya *et al.*, "Multiplicity dependence of charged-particle jet production in pp collisions at $\sqrt{\mathbf{s}}$ = **13 TeV**", *Eur. Phys. J. C* **82** (2022) 514, arXiv:2202.01548 [nucl-ex]. XV, XXV, 38, 167

[21] J. Alme *et al.*, "The ALICE TPC, a large 3-dimensional tracking device with fast readout for ultra-high multiplicity events", *Nucl. Instrum. Meth. A* **622** (2010) 316–367, arXiv:1001.1950 [physics.ins-det]. XV, 38, 39

[22] **ALICE** Collaboration, S. Acharya *et al.*, "Production of light-flavor hadrons in pp collisions at $\sqrt{s}$ = 7 and $\sqrt{s}$ = 13 TeV", *Eur. Phys. J. C* **81** (2021) 256, arXiv:2005.11120 [nucl-ex]. XV, 41

[23] B. R. Webber, "Fragmentation and hadronization", *Int. J. Mod. Phys. A* **15S1** (2000) 577–606, arXiv:hep-ph/9912292. XV, 45

[24] G. C. Blazey *et al.*, "Run II jet physics", in *Physics at Run II: QCD and Weak Boson Physics Workshop: Final General Meeting*, pp. 47–77. 5, 2000. arXiv:hep-ex/0005012. XVI, 48, 57

[25] T. Adye, "Unfolding algorithms and tests using RooUnfold", in *PHYSTAT 2011*, pp. 313–318. CERN, Geneva, 2011. arXiv:1105.1160 [physics.data-an]. XVII, 65, 67, 145

[26] **ALICE** Collaboration, S. Acharya *et al.*, "Measurement of charged jet cross section in pp collisions at $\sqrt{s}$ = 5.02 TeV", *Phys. Rev. D* **100** (2019) 092004, arXiv:1905.02536 [nucl-ex]. XX, XXV, XXVII, 53, 117, 167, 214

[27] **ALICE** Collaboration, B. Abelev *et al.*, "Charged jet cross sections and properties in proton–proton collisions at $\sqrt{s}$ = 7 TeV", arXiv:1411.4969 [nucl-ex]. XX, 102, 117

[28] **ALICE** Collaboration, J. Adam *et al.*, "Measurement of charged jet production cross sections and nuclear modification in p–Pb collisions at $\sqrt{s_{\mathrm{NN}}}$ = 5.02 TeV", *Phys. Lett.* **B749** (2015) 68–81, arXiv:1503.00681 [nucl-ex]. XX, 117

[29] **ALICE** Collaboration, S. Acharya *et al.*, "Pseudorapidity distributions of charged particles as a function of mid- and forward rapidity multiplicities in pp collisions at $\sqrt{s}$ = 5.02, 7 and 13 TeV", *Eur. Phys. J. C* **81** (2021) 630, arXiv:2009.09434 [nucl-ex]. XXI, XXII, XXIX, 72, 74, 75, 122, 123, 124, 210, 211

[30] J. H. Putschke *et al.*, "The JETSCAPE framework", arXiv:1903.07706 [nucl-th]. XXV, 46, 48, 166

[31] K. Zapp, G. Ingelman, J. Rathsman, J. Stachel, and U. A. Wiedemann, "A Monte Carlo Model for "Jet Quenching"", *Eur. Phys. J. C* **60** (2009) 617–632, arXiv:0804.3568 [hep-ph]. XXV, 24, 48, 166

[32] K. C. Zapp, "JEWEL 2.0.0: directions for use", *Eur. Phys. J. C* **74** (2014) 2762, arXiv:1311.0048 [hep-ph]. XXV, 48, 165, 166, 227

[33] T. Sjöstrand *et al.*, "An introduction to PYTHIA 8.2", *Comput. Phys. Commun.* **191** (2015) 159–177, arXiv:1410.3012 [hep-ph]. XXV, 42, 43, 45, 165, 166, 227

[34] P. Skands, S. Carrazza, and J. Rojo, "Tuning PYTHIA 8.1: the Monash 2013 Tune", *Eur. Phys. J. C* **74** (2014) 3024, arXiv:1404.5630 [hep-ph]. XXV, 43, 46, 165, 166, 227

[35] P. Nason, "A New method for combining NLO QCD with shower Monte Carlo algorithms", *JHEP* **11** (2004) 040, arXiv:hep-ph/0409146. XXV, 46, 166

[36] S. Frixione, P. Nason, and C. Oleari, "Matching NLO QCD computations with Parton Shower simulations: the POWHEG method", *JHEP* **0711** (2007) 070, arXiv:0709.2092 [hep-ph].

[37] S. Alioli, P. Nason, C. Oleari, and E. Re, "A general framework for implementing NLO calculations in shower Monte Carlo programs: the POWHEG BOX", *JHEP* **06** (2010) 043, arXiv:1002.2581 [hep-ph].

[38] A. Buckley and D. Bakshi Gupta, "Powheg-Pythia matching scheme effects in NLO simulation of dijet events", arXiv:1608.03577 [hep-ph]. XXV, 46, 166

[39] S. Braibant and G. Giacomelli, *Particles and fundamental interactions: An introduction to particle physics*. Undergraduate lecture notes in physics. Springer, Dordrecht, Netherlands, 2012. 2

[40] F. Halzen and A. D. Martin, *QUARKS AND LEPTONS: AN INTRODUCTORY COURSE IN MODERN PARTICLE PHYSICS*. 1984. 2

[41] J. R. Forshaw, "An introduction to quantum electrodynamics and quantum chromodynamics", in *School for Young High-Energy Physicists*, pp. 47–102. 8, 1997. 4

[42] K. Melnikov, "Lectures on QCD for hadron colliders", *CERN Yellow Rep. School Proc.* **3** (2018) 37–82. 4

[43] M. E. Peskin and D. V. Schroeder, *An Introduction to quantum field theory*. Addison-Wesley, Reading, USA, 1995. 4, 5

[44] C. Y. Wong, *Introduction to high-energy heavy ion collisions*. 1995. 5

[45] J.-W. Qiu, F. Ringer, N. Sato, and P. Zurita, "Factorization of jet cross sections in heavy-ion collisions", *Phys. Rev. Lett.* **122** (2019) 252301, arXiv:1903.01993 [hep-ph]. 6

[46] Y. L. Dokshitzer, "Calculation of the structure functions for deep inelastic scattering and e^+e^- annihilation by perturbation theory in quantum chromodynamics.", *Sov. Phys. JETP* 46 (1977) 641–653. 7

[47] V. N. Gribov and L. N. Lipatov, "Deep inelastic e p scattering in perturbation theory", *Sov. J. Nucl. Phys.* **15** (1972) 438–450.

[48] G. Altarelli and G. Parisi, "Asymptotic freedom in parton language", *Nucl. Phys. B* **126** (1977) 298–318. 7

[49] E. Iancu and R. Venugopalan, *The Color glass condensate and high-energy scattering in QCD*, pp. 249–3363. 3, 2003. arXiv:hep-ph/0303204. 8

[50] A. Accardi *et al.*, "Electron Ion Collider: The Next QCD Frontier: Understanding the glue that binds us all", *Eur. Phys. J. A* **52** (2016) 268, arXiv:1212.1701 [nucl-ex]. 8

[51] J. Casalderrey-Solana, H. Liu, D. Mateos, K. Rajagopal, and U. A. Wiedemann, *Gauge/String Duality, Hot QCD and Heavy Ion Collisions*. Cambridge University Press, 2014. arXiv:1101.0618 [hep-th]. 9

[52] C. W. Bauer, S. Fleming, D. Pirjol, and I. W. Stewart, "An Effective field theory for collinear and soft gluons: Heavy to light decays", *Phys. Rev. D* **63** (2001) 114020, arXiv:hep-ph/0011336. 9

[53] **STAR** Collaboration, J. Adams *et al.*, "Experimental and theoretical challenges in the search for the quark gluon plasma: The STAR Collaboration's critical assessment of the evidence from RHIC collisions", *Nucl. Phys. A* **757** (2005) 102–183, arXiv:nucl-ex/0501009. 9

[54] **ALICE** Collaboration, K. Aamodt *et al.*, "The ALICE experiment at the CERN LHC", *JINST* **3** (2008) S08002. 9, 33, 34, 35, 51

[55] H.-T. Ding, F. Karsch, and S. Mukherjee, "Thermodynamics of strong-interaction matter from Lattice QCD", *Int. J. Mod. Phys. E* **24** (2015) 1530007, arXiv:1504.05274 [hep-lat]. 9

[56] G. Martinez, "Advances in Quark Gluon Plasma", 4, 2013. arXiv:1304.1452 [nucl-ex]. 9

[57] M. G. Alford, A. Schmitt, K. Rajagopal, and T. Schäfer, "Color superconductivity in dense quark matter", *Rev. Mod. Phys.* **80** (2008) 1455–1515, arXiv:0709.4635 [hep-ph]. 10

[58] **HotQCD** Collaboration, A. Bazavov *et al.*, "Chiral crossover in QCD at zero and non-zero chemical potentials", *Phys. Lett. B* **795** (2019) 15–21, arXiv:1812.08235 [hep-lat]. 10

[59] S. Borsanyi, "Thermodynamics of the QCD transition from lattice", *Nucl. Phys. A* **904-905** (2013) 270c–277c, arXiv:1210.6901 [hep-lat]. 10

[60] **STAR** Collaboration, K. H. Ackermann *et al.*, "Elliptic flow in Au + Au collisions at $\sqrt{s_{NN}}$ = 130 GeV", *Phys. Rev. Lett.* **86** (2001) 402–407, arXiv:nucl-ex/0009011. 11

[61] E. Iancu, "QCD in heavy ion collisions", in *2011 European School of High-Energy Physics*, pp. 197–266. 2014. arXiv:1205.0579 [hep-ph]. 13

[62] A. Jaiswal and V. Roy, "Relativistic hydrodynamics in heavy-ion collisions: general aspects and recent developments", *Adv. High Energy Phys.* **2016** (2016) 9623034, arXiv:1605.08694 [nucl-th]. 13

[63] J. Xu and C. M. Ko, "Chemical freeze-out in relativistic heavy-ion collisions", *Phys. Lett. B* **772** (2017) 290–293, arXiv:1704.04934 [nucl-th]. 14

[64] M. L. Miller, K. Reygers, S. J. Sanders, and P. Steinberg, "Glauber modeling in high energy nuclear collisions", *Ann. Rev. Nucl. Part. Sci.* **57** (2007) 205–243, arXiv:nucl-ex/0701025. 15, 21

[65] J. L. Nagle and W. A. Zajc, "Small system collectivity in relativistic hadronic and nuclear collisions", *Ann. Rev. Nucl. Part. Sci.* **68** (2018) 211–235, arXiv:1801.03477 [nucl-ex]. 16, 31

[66] **ALICE** Collaboration, B. B. Abelev *et al.*, "Multi-strange baryon production at mid-rapidity in Pb–Pb collisions at $\sqrt{s_{NN}}$ = 2.76 TeV", *Phys. Lett. B* **728** (2014) 216–227, arXiv:1307.5543 [nucl-ex]. [Erratum: Phys.Lett.B 734, 409–410 (2014)]. 17, 19

[67] K. Fukushima, D. E. Kharzeev, and H. J. Warringa, "The chiral magnetic effect", *Phys. Rev. D* **78** (2008) 074033, arXiv:0808.3382 [hep-ph]. 18

[68] J. Rafelski, "Strangeness and Quark–Gluon Plasma", *Acta Phys. Polon. B* **43** (2012) 829, arXiv:1112.4890 [nucl-th]. 18

[69] O. Kaczmarek and F. Zantow, "Static quark anti-quark interactions in zero and finite temperature QCD. I. Heavy quark free energies, running coupling and quarkonium binding", *Phys. Rev. D* **71** (2005) 114510, arXiv:hep-lat/0503017. 18

[70] A. Tounsi and K. Redlich, "Strangeness enhancement and canonical suppression", arXiv:hep-ph/0111159. 19

[71] **NA57** Collaboration, F. Antinori *et al.*, "Enhancement of hyperon production at central rapidity in 158-A-GeV/c Pb–Pb collisions", *J. Phys. G* **32** (2006) 427–442, arXiv:nucl-ex/0601021. 19

[72] **STAR** Collaboration, B. I. Abelev *et al.*, "Enhanced strange baryon production in Au + Au collisions compared to p + p at $\sqrt{s_{NN}}$ = 200 GeV", *Phys. Rev. C* **77** (2008) 044908, arXiv:0705.2511 [nucl-ex]. 19

[73] **ALICE** Collaboration, J. Adam *et al.*, "Enhanced production of multi-strange hadrons in high-multiplicity proton-proton collisions", *Nature Phys.* **13** (2017) 535–539, arXiv:1606.07424 [nucl-ex]. 19, 31, 70, 222

[74] U. W. Heinz, R. Chatterjee, E. S. Frodermann, C. Gale, and D. K. Srivastava, "Elliptic flow of thermal photons and dileptons", *Nucl. Phys. A* **783** (2007) 379–386, arXiv:nucl-th/0610014. 20

[75] **ALICE** Collaboration, "The ALICE experiment – A journey through QCD", arXiv:2211.04384 [nucl-ex]. 20, 25

[76] Y. L. Dokshitzer and D. E. Kharzeev, "Heavy quark colorimetry of QCD matter", *Phys. Lett. B* **519** (2001) 199–206, arXiv:hep-ph/0106202. 22

[77] **JETSCAPE** Collaboration, S. Cao *et al.*, "Determining the jet transport coefficient $\hat{q}$ from inclusive hadron suppression measurements using Bayesian parameter estimation", *Phys. Rev. C* **104** (2021) 024905, arXiv:2102.11337 [nucl-th]. 24

[78] K. C. Zapp, F. Krauss, and U. A. Wiedemann, "Explaining jet quenching with perturbative QCD alone", arXiv:1111.6838 [hep-ph]. 24

[79] K. C. Zapp, F. Krauss, and U. A. Wiedemann, "A perturbative framework for jet quenching", *JHEP* **03** (2013) 080, arXiv:1212.1599 [hep-ph]. 24, 48, 165, 227

[80] **CMS** Collaboration, A. M. Sirunyan *et al.*, "Measurement of the groomed jet mass in Pb–Pb and pp collisions at $\sqrt{s_{\mathrm{NN}}}$ = 5.02 TeV", *JHEP* **10** (2018) 161, arXiv:1805.05145 [hep-ex]. 24

[81] J. Casalderrey-Solana, D. Gulhan, G. Milhano, D. Pablos, and K. Rajagopal, "Angular structure of jet quenching within a Hybrid strong/Weak coupling model", *JHEP* **03** (2017) 135, arXiv:1609.05842 [hep-ph]. 24

[82] **ALICE** Collaboration, S. Acharya *et al.*, "Constraints on jet quenching in p–Pb collisions at $\sqrt{s_{NN}}$ = 5.02 TeV measured by the event-activity dependence of semi-inclusive hadron-jet distributions", *Phys. Lett.* **B783** (2018) 95–113, arXiv:1712.05603 [nucl-ex]. 24, 126, 223

[83] **STAR** Collaboration, L. Adamczyk *et al.*, "Measurements of jet quenching with semi-inclusive hadron+jet distributions in Au+Au collisions at $\sqrt{s_{NN}}$ = 200 GeV", *Phys. Rev. C* **96** (2017) 024905, arXiv:1702.01108 [nucl-ex]. 27, 166

[84] **STAR** Collaboration, J. Adam *et al.*, "Measurement of inclusive charged-particle jet production in Au + Au collisions at $\sqrt{s_{NN}}$ =200 GeV", *Phys. Rev. C* **102** (2020) 054913, arXiv:2006.00582 [nucl-ex]. 24, 166

[85] **ALICE** Collaboration, S. Acharya *et al.*, "Exploration of jet substructure using iterative declustering in pp and Pb–Pb collisions at LHC energies", *Phys. Lett. B* **802** (2020) 135227, arXiv:1905.02512 [nucl-ex]. 24, 26

[86] **ALICE** Collaboration, S. Acharya *et al.*, "Medium modification of the shape of small-radius jets in central Pb–Pb collisions at $\sqrt{s_{\mathrm{NN}}}$ = 2.76 TeV", *JHEP* **10** (2018) 139, arXiv:1807.06854 [nucl-ex].

[87] **CMS** Collaboration, S. Chatrchyan *et al.*, "Modification of jet shapes in Pb–Pb collisions at $\sqrt{s_{NN}}$ = 2.76 TeV", *Phys. Lett. B* **730** (2014) 243–263, arXiv:1310.0878 [nucl-ex].

[88] **CMS** Collaboration, A. M. Sirunyan *et al.*, "Measurement of the splitting function in pp and Pb–Pb collisions at $\sqrt{s_{\mathrm{NN}}}$ = 5.02 TeV", *Phys. Rev. Lett.* **120** (2018) 142302, arXiv:1708.09429 [nucl-ex]. 26

[89] **CMS** Collaboration, A. M. Sirunyan *et al.*, "Measurement of quark- and gluon-like jet fractions using jet charge in Pb–Pb and pp collisions at 5.02 TeV", *JHEP* **07** (2020) 115, arXiv:2004.00602 [hep-ex]. 24

[90] A. J. Larkoski, I. Moult, and B. Nachman, "Jet substructure at the Large Hadron Collider: A review of recent advances in theory and machine learning", *Phys. Rept.* **841** (2020) 1–63, arXiv:1709.04464 [hep-ph]. 24

[91] M. Dasgupta, A. Fregoso, S. Marzani, and G. P. Salam, "Towards an understanding of jet substructure", *JHEP* **09** (2013) 029, arXiv:1307.0007 [hep-ph]. 25

[92] F. A. Dreyer, G. P. Salam, and G. Soyez, "The lund jet plane", *JHEP* **12** (2018) 064, arXiv:1807.04758 [hep-ph].

[93] Z.-B. Kang, K. Lee, X. Liu, D. Neill, and F. Ringer, "The soft drop groomed jet radius at NLL", *JHEP* **02** (2020) 054, arXiv:1908.01783 [hep-ph]. 24

[94] Y. Mehtar-Tani and K. Tywoniuk, "Groomed jets in heavy-ion collisions: sensitivity to medium-induced bremsstrahlung", *JHEP* **04** (2017) 125, arXiv:1610.08930 [hep-ph]. 24

[95] J. Casalderrey-Solana, Y. Mehtar-Tani, C. A. Salgado, and K. Tywoniuk, "New picture of jet quenching dictated by color coherence", *Phys. Lett. B* **725** (2013) 357–360, arXiv:1210.7765 [hep-ph].

[96] H. A. Andrews *et al.*, "Novel tools and observables for jet physics in heavy-ion collisions", *J. Phys. G* **47** (2020) 065102, arXiv:1808.03689 [hep-ph].

[97] F. Ringer, B.-W. Xiao, and F. Yuan, "Can we observe jet P_T-broadening in heavy-ion collisions at the LHC?", *Phys. Lett. B* **808** (2020) 135634, arXiv:1907.12541 [hep-ph].

[98] Z. Hulcher, D. Pablos, and K. Rajagopal, "Resolution effects in the Hybrid strong/Weak coupling model", *JHEP* **03** (2018) 010, arXiv:1707.05245 [hep-ph].

[99] J. Casalderrey-Solana, G. Milhano, D. Pablos, and K. Rajagopal, "Modification of jet substructure in heavy ion collisions as a probe of the resolution length of quark-gluon plasma", *JHEP* **01** (2020) 044, arXiv:1907.11248 [hep-ph].

[100] G. Milhano, U. A. Wiedemann, and K. C. Zapp, "Sensitivity of jet substructure to jet-induced medium response", *Phys. Lett. B* **779** (2018) 409–413, arXiv:1707.04142 [hep-ph].

[101] R. Kunnawalkam Elayavalli and K. C. Zapp, "Medium response in JEWEL and its impact on jet shape observables in heavy ion collisions", *JHEP* **07** (2017) 141, arXiv:1707.01539 [hep-ph]. 24, 49, 170

[102] **ATLAS** Collaboration, M. Aaboud *et al.*, "Measurement of jet fragmentation in Pb+Pb and pp collisions at $\sqrt{s_{NN}}$ = 5.02 TeV with the ATLAS detector", *Phys. Rev. C* **98** (2018) 024908, arXiv:1805.05424 [nucl-ex]. 25

[103] **CMS** Collaboration, A. M. Sirunyan *et al.*, "Observation of medium-Induced modifications of jet fragmentation in Pb–Pb collisions at $\sqrt{s_{NN}}$ = 5.02 TeV using isolated photon-tagged jets", *Phys. Rev. Lett.* **121** (2018) 242301, arXiv:1801.04895 [hep-ex].

[104] **CMS** Collaboration, S. Chatrchyan *et al.*, "Measurement of jet fragmentation in Pb–Pb and pp collisions at $\sqrt{s_{NN}}$ = 2.76 TeV", *Phys. Rev. C* **90** (2014) 024908, arXiv:1406.0932 [nucl-ex]. 25

[105] **ATLAS** Collaboration, G. Aad *et al.*, "Measurement of angular and momentum distributions of charged particles within and around jets in Pb–Pb and pp collisions at $\sqrt{s_{\mathrm{NN}}}$ = 5.02 TeV with the ATLAS detector", *Phys. Rev. C* **100** (2019) 064901, arXiv:1908.05264 [nucl-ex]. [Erratum: Phys.Rev.C 101, 059903 (2020)]. 25

[106] **CMS** Collaboration, S. Chatrchyan *et al.*, "Modification of jet shapes in Pb–Pb collisions at $\sqrt{s_{NN}}$ = 2.76 TeV", *Phys. Lett. B* **730** (2014) 243–263, arXiv:1310.0878 [nucl-ex]. 25

[107] **CMS** Collaboration, A. M. Sirunyan *et al.*, "Jet properties in Pb–Pb and pp collisions at $\sqrt{s_{\mathrm{N\,N}}}$ = 5.02 TeV", *JHEP* **05** (2018) 006, arXiv:1803.00042 [nucl-ex]. 25

[108] **CMS** Collaboration, A. M. Sirunyan *et al.*, "Jet shapes of isolated photon-tagged jets in Pb–Pb and pp collisions at $\sqrt{s_{\mathrm{NN}}}$ = 5.02 TeV", *Phys. Rev. Lett.* **122** (2019) 152001, arXiv:1809.08602 [hep-ex]. 25

[109] **CMS** Collaboration, A. M. Sirunyan *et al.*, "Studies of charm quark diffusion inside jets using Pb–Pb and pp collisions at $\sqrt{s_{\mathrm{NN}}}$ = 5.02 TeV", *Phys. Rev. Lett.* **125** (2020) 102001, arXiv:1911.01461 [hep-ex]. 25

[110] A. J. Larkoski, S. Marzani, G. Soyez, and J. Thaler, "Soft Drop", *JHEP* **05** (2014) 146, arXiv:1402.2657 [hep-ph]. 25

[111] A. J. Larkoski, S. Marzani, and J. Thaler, "Sudakov safety in perturbative QCD", *Phys. Rev. D* **91** (2015) 111501, arXiv:1502.01719 [hep-ph]. 25

[112] J. Mulligan and M. Ploskon, "Identifying groomed jet splittings in heavy-ion collisions", *Phys. Rev. C* **102** (2020) 044913, arXiv:2006.01812 [hep-ph]. 26

[113] L. Chen, G.-Y. Qin, S.-Y. Wei, B.-W. Xiao, and H.-Z. Zhang, "Probing transverse momentum broadening via dihadron and hadron-jet angular correlations in relativistic heavy-ion collisions", *Phys. Lett. B* **773** (2017) 672–676, arXiv:1607.01932 [hep-ph]. 27, 49

[114] M. Gyulassy, P. Levai, J. Liao, S. Shi, F. Yuan, and X. N. Wang, "Precision dijet acoplanarity tomography of the chromo structure of perfect QCD fluids", *Nucl. Phys. A* **982** (2019) 627–630, arXiv:1808.03238 [hep-ph]. 27

[115] M. Gyulassy, P. M. Jacobs, J. Liao, S. Shi, X. N. Wang, and F. Yuan, "Dijet acoplanarity in CUJET3 as a probe of the nonperturbative color structure of QCD perfect fluids", *Nucl. Phys. A* **1005** (2021) 121938, arXiv:2012.06151 [hep-ph]. 27

[116] F. D'Eramo, M. Lekaveckas, H. Liu, and K. Rajagopal, "Momentum broadening in weakly coupled quark-gluon plasma (with a view to finding the quasiparticles within liquid quark-gluon plasma)", *JHEP* **05** (2013) 031, arXiv:1211.1922 [hep-ph]. 27, 28

[117] F. D'Eramo, K. Rajagopal, and Y. Yin, "Molière scattering in quark-gluon plasma: finding point-like scatterers in a liquid", *JHEP* **01** (2019) 172, arXiv:1808.03250 [hep-ph]. 27, 28, 49

[118] **ALICE** Collaboration, S. Acharya *et al.*, "Study of flavor dependence of the baryon-to-meson ratio in proton-proton collisions at s=13 TeV", *Phys. Rev. D* **108** (2023) 112003, arXiv:2308.04873 [hep-ex]. 29, 177

[119] **ALICE** Collaboration, S. Acharya *et al.*, "Investigations of anisotropic flow using multiparticle azimuthal correlations in pp, p–Pb, Xe–Xe, and Pb–Pb collisions at the LHC", *Phys. Rev. Lett.* **123** (2019) 142301, arXiv:1903.01790 [nucl-ex]. 70

[120] **CMS** Collaboration, V. Khachatryan *et al.*, "Evidence for Collective Multiparticle Correlations in p–Pb Collisions", *Phys. Rev. Lett.* **115** (2015) 012301, arXiv:1502.05382 [nucl-ex].

[121] **ALICE** Collaboration, J. Adam *et al.*, "Multi-strange baryon production in p–Pb collisions at $\sqrt{s_{\mathrm{NN}}}$ = 5.02 TeV", *Phys. Lett. B* **758** (2016) 389–401, arXiv:1512.07227 [nucl-ex].

[122] **ATLAS** Collaboration, G. Aad *et al.*, "Observation of long-range elliptic azimuthal anisotropies in $\sqrt{s}$ =13 and 2.76 TeV pp collisions with the ATLAS detector", *Phys. Rev. Lett.* **116** (2016) 172301, arXiv:1509.04776 [hep-ex]. 70, 222

[123] **ALICE** Collaboration, B. B. Abelev *et al.*, "$K^*(892)^0$ and (1020) production in Pb–Pb collisions at $\sqrt{s_{\mathrm{NN}}}$ = 2.76 TeV", *Phys. Rev. C* **91** (2015) 024609, arXiv:1404.0495 [nucl-ex].

[124] **ALICE** Collaboration, B. B. Abelev *et al.*, "Long-range angular correlations of π, K and p in p–Pb collisions at $\sqrt{s_{\mathrm{NN}}}$ = 5.02 TeV", *Phys. Lett. B* **726** (2013) 164–177, arXiv:1307.3237 [nucl-ex].

[125] **ALICE** Collaboration, B. Abelev *et al.*, "Long-range angular correlations on the near and away side in p-Pb collisions at $\sqrt{s_{\rm NN}}$ = 5.02 TeV", *Phys. Lett. B* **719** (2013) 29–41, arXiv:1212.2001 [nucl-ex]. 29

[126] **ALICE** Collaboration, S. Acharya *et al.*, "Observation of a multiplicity dependence in the $p_{\rm T}$-differential charm baryon-to-meson ratios in proton–proton collisions at $\sqrt{s}$ = 13 TeV", *Phys. Lett. B* **829** (2022) 137065, arXiv:2111.11948 [nucl-ex]. 29, 31, 177, 179

[127] **ALICE** Collaboration, S. Acharya *et al.*, "Search for jet quenching effects in high-multiplicity pp collisions at $\sqrt{s}$ = 13 TeV via di-jet acoplanarity", arXiv:2309.03788 [hep-ex].

[128] **ALICE** Collaboration, S. Acharya *et al.*, "Multiplicity dependence of charged-particle intra-jet properties in pp collisions at $\sqrt{s}$ = 13 TeV", arXiv:2311.13322 [hep-ex]. 29

[129] **ALICE** Collaboration, S. Acharya *et al.*, "Multiplicity dependence of light-flavor hadron production in pp collisions at $\sqrt{s}$ = 7 TeV", *Phys. Rev. C* **99** (2019) 024906, arXiv:1807.11321 [nucl-ex]. 31

[130] **CMS** Collaboration, V. Khachatryan *et al.*, "Multiplicity and rapidity dependence of strange hadron production in pp, pPb, and Pb–Pb collisions at the LHC", *Phys. Lett. B* **768** (2017) 103–129, arXiv:1605.06699 [nucl-ex]. 70, 222

[131] **ALICE** Collaboration, B. B. Abelev *et al.*, "K^0_S and Λ production in Pb–Pb collisions at $\sqrt{s_{NN}}$ = 2.76 TeV", *Phys. Rev. Lett.* **111** (2013) 222301, arXiv:1307.5530 [nucl-ex]. 31

[132] R. D. Weller and P. Romatschke, "One fluid to rule them all: viscous hydrodynamic description of event-by-event central pp, p–Pb and Pb–Pb collisions at $\sqrt{s}$ = 5.02 TeV", *Phys. Lett. B* **774** (2017) 351–356, arXiv:1701.07145 [nucl-th]. 31

[133] B. Blok, C. D. Jäkel, M. Strikman, and U. A. Wiedemann, "Collectivity from interference", *JHEP* **12** (2017) 074, arXiv:1708.08241 [hep-ph]. 31

[134] A. Dumitru, K. Dusling, F. Gelis, J. Jalilian-Marian, T. Lappi, and R. Venugopalan, "The ridge in proton-proton collisions at the LHC", *Phys. Lett. B* **697** (2011) 21–25, arXiv:1009.5295 [hep-ph]. 31

[135] A. Ortiz Velasquez, P. Christiansen, E. Cuautle Flores, I. Maldonado Cervantes, and G. Paić, "Color reconnection and flowlike patterns in pp collisions", *Phys. Rev. Lett.* **111** (2013) 042001, arXiv:1303.6326 [hep-ph]. 31

[136] C. Bierlich, "Rope hadronization and strange particle production", *EPJ Web Conf.* **171** (2018) 14003, arXiv:1710.04464 [nucl-th]. 32

[137] C. Bierlich, G. Gustafson, and L. Lönnblad, "A shoving model for collectivity in hadronic collisions", arXiv:1612.05132 [hep-ph]. 32

[138] N. Angert *et al.*, "CERN heavy ion facility design report",. 33

[139] K. Schindl, "The injector chain for the LHC; rev. version",. https://cds.cern.ch/record/384396. 33

[140] **ATLAS** Collaboration, G. Aad *et al.*, "The ATLAS Experiment at the CERN Large Hadron Collider", *JINST* **3** (2008) S08003. 33

[141] **CMS** Collaboration, S. Chatrchyan *et al.*, "The CMS Experiment at the CERN LHC", *JINST* **3** (2008) S08004. 33

[142] **LHCb** Collaboration, A. A. Alves, Jr. *et al.*, "The LHCb Detector at the LHC", *JINST* **3** (2008) S08005. 33

[143] **ALICE** Collaboration, S. Acharya *et al.*, "Pseudorapidity distributions of charged particles as a function of mid- and forward rapidity multiplicities in pp collisions at $\sqrt{s}$ = 5.02, 7 and 13 TeV", *Eur. Phys. J. C* **81** (2021) 630, arXiv:2009.09434 [nucl-ex]. 35

[144] **ALICE** Collaboration, J. Adam *et al.*, "Centrality dependence of the charged-particle multiplicity density at midrapidity in Pb–Pb collisions at $\sqrt{s_{\mathrm{NN}}}$ = 5.02 TeV", *Phys. Rev. Lett.* **116** (2016) 222302, arXiv:1512.06104 [nucl-ex]. 35

[145] **ALICE** Collaboration, E. Abbas *et al.*, "Performance of the ALICE VZERO system", *JINST* **8** (2013) P10016, arXiv:1306.3130 [nucl-ex]. 37

[146] **ALICE** Collaboration, K. Aamodt *et al.*, "Alignment of the ALICE Inner Tracking System with cosmic-ray tracks", *JINST* **5** (2010) P03003, arXiv:1001.0502 [physics.ins-det]. 37

[147] C. Lippmann, "Performance of the ALICE Time Projection Chamber", *Phys. Procedia* **37** (2012) 434–441. 38

[148] **ALICE** Collaboration, Y. Belikov, K. Safarík, and B. Batyunya, "Kalman filtering application for track recognition and reconstruction in ALICE tracking system",. 39

[149] **ALICE** Collaboration, G. Dellacasa *et al.*, "ALICE technical design report of the time-of-flight system (TOF)",. 40

[150] R. Forty and O. Ullaland, *Particle Identification: Time-of-Flight, Cherenkov and Transition Radiation Detectors*, pp. 281–335. Springer, Cham, 2020. 41

[151] **ALICE** Collaboration, "ALICE Off-line Project",. https://alice-offline.web.cern.ch/. 42

[152] **ALICE** Collaboration, "AliPhysics Framework",. https://github.com/alisw/AliPhysics. 42

[153] R. Brun, F. Rademakers, and S. Panacek, "ROOT, an object oriented data analysis framework",. https://cds.cern.ch/record/491486. 42

[154] T. Sjostrand, S. Mrenna, and P. Z. Skands, "PYTHIA 6.4 Physics and Manual", *JHEP* **0605** (2006) 026, arXiv:hep-ph/0603175 [hep-ph]. 42, 45, 48

[155] X.-N. Wang and M. Gyulassy, "HIJING: A Monte Carlo model for multiple jet production in pp, px A and AA collisions", *Phys.Rev.* **D44** (1991) 3501–3516. 42

[156] R. Brun *et al.*, "GEANT: Detector description and simulation tool; Oct 1994",. http://cds.cern.ch/record/1082634. Long Writeup W5013. 42, 43

[157] **GEANT4** Collaboration, S. Agostinelli *et al.*, "GEANT4–a simulation toolkit", *Nucl. Instrum. Meth. A* **506** (2003) 250–303. 42

[158] A. Ferrari, P. R. Sala, A. Fassò, and J. Ranft, "FLUKA: A multi-particle transport code (program version 2005)",. https://cds.cern.ch/record/898301. 42

[159] **CERN** Collaboration, "WORLDWIDE LHC COMPUTING GRID",. https://wlcg-public.web.cern.ch/. 42

[160] K. Bos, *et al.*, *LHC computing Grid: Technical Design Report. Version 1.06 (20 Jun 2005)*. Technical design report. LCG. CERN, Geneva, 2005. https://cds.cern.ch/record/840543. 42

[161] **ALICE** Collaboration, "JAliEn - ALICE Environment Grid Framework",. https://alien.web.cern.ch/. 42

[162] **ALICE** Collaboration, P. Saiz, L. Aphecetche, P. Buncic, R. Piskac, J. E. Revsbech, and V. Sego, "AliEn - ALICE environment on the GRID", *Nucl. Instrum. Meth. A* **502** (2003) 437–440. 42

[163] B. R. Webber, "Hadronization", in *Summer School on Hadronic Aspects of Collider Physics*, pp. 49–77. 11, 1994. arXiv:hep-ph/9411384. 44

[164] B. R. Webber, "A QCD model for jet fragmentation including soft gluon interference", *Nucl. Phys. B* **238** (1984) 492–528. 44

[165] B. Andersson, G. Gustafson, G. Ingelman, and T. Sjostrand, "Parton fragmentation and string dynamics", *Phys. Rept.* **97** (1983) 31–145. 44

[166] **NNPDF** Collaboration, R. D. Ball and Bothers, "Parton distributions with QED corrections", *Nucl. Phys. B* **877** (2013) 290–320, arXiv:1308.0598 [hep-ph]. 46

[167] S. Dulat, T.-J. Hou, J. Gao, M. Guzzi, J. Huston, P. Nadolsky, J. Pumplin, C. Schmidt, D. Stump, and C. P. Yuan, "New parton distribution functions from a global analysis of quantum chromodynamics", *Phys. Rev. D* **93** (2016) 033006, arXiv:1506.07443 [hep-ph]. 46

[168] S. Alioli, K. Hamilton, P. Nason, C. Oleari, and E. Re, "Jet pair production in POWHEG", *JHEP* **04** (2011) 081, arXiv:1012.3380 [hep-ph]. 46, 165, 227

[169] **CMS** Collaboration, S. Chatrchyan *et al.*, "Measurement of jet fragmentation into charged particles in pp and Pb–Pb Collisions at $\sqrt{s_{\mathrm{NN}}} = 2.76$ TeV", *JHEP* **10** (2012) 087, arXiv:1205.5872 [nucl-ex]. 46

[170] **JETSCAPE** Collaboration, A. Kumar *et al.*, "JETSCAPE framework: $p + p$ results", *Phys. Rev. C* **102** (2020) 054906, arXiv:1910.05481 [nucl-th]. 47, 165, 227

[171] S. Cao and A. Majumder, "Nuclear modification of leading hadrons and jets within a virtuality ordered parton shower", *Phys. Rev. C* **101** (2020) 024903, arXiv:1712.10055 [nucl-th]. 47

[172] B. G. Zakharov, "Radiative energy loss of high-energy quarks in finite size nuclear matter and quark - gluon plasma", *JETP Lett.* **65** (1997) 615–620, arXiv:hep-ph/9704255. 47

[173] B. G. Zakharov, "Fully quantum treatment of the Landau-Pomeranchuk-Migdal effect in QED and QCD", *JETP Lett.* **63** (1996) 952–957, arXiv:hep-ph/9607440. 47

[174] P. B. Arnold, G. D. Moore, and L. G. Yaffe, "Photon emission from ultrarelativistic plasmas", *JHEP* **11** (2001) 057, arXiv:hep-ph/0109064. 47

[175] U. A. Wiedemann, "Gluon radiation off hard quarks in a nuclear environment: Opacity expansion", *Nucl. Phys. B* **588** (2000) 303–344, arXiv:hep-ph/0005129. 47

[176] X.-N. Wang and X.-f. Guo, "Multiple parton scattering in nuclei: Parton energy loss", *Nucl. Phys. A* **696** (2001) 788–832, arXiv:hep-ph/0102230. 47

[177] M. Gyulassy, P. Levai, and I. Vitev, "Jet quenching in thin quark gluon plasmas. 1. Formalism", *Nucl. Phys. B* **571** (2000) 197–233, arXiv:hep-ph/9907461. 47

[178] D. d'Enterria, "Jet quenching", *Landolt-Bornstein* **23** (2010) 471, arXiv:0902.2011 [nucl-ex]. 47

[179] **JETSCAPE** Collaboration, A. Kumar *et al.*, "Inclusive jet and hadron suppression in a multistage approach", *Phys. Rev. C* **107** (2023) 034911, arXiv:2204.01163 [hep-ph]. 48

[180] A. Majumder, "Incorporating space-time within medium-modified jet event generators", *Phys. Rev. C* **88** (2013) 014909, arXiv:1301.5323 [nucl-th]. 48

[181] A. Majumder, "The in-medium scale evolution in jet modification", arXiv:0901.4516 [nucl-th]. 48

[182] Y. He, T. Luo, X.-N. Wang, and Y. Zhu, "Linear boltzmann transport for jet propagation in the quark-gluon plasma: elastic processes and medium recoil", *Phys. Rev. C* **91** (2015) 054908, arXiv:1503.03313 [nucl-th]. [Erratum: Phys.Rev.C 97, 019902 (2018)]. 48

[183] X.-N. Wang and Y. Zhu, "Medium modification of γ-jets in high-energy heavy-ion collisions", *Phys.Rev.Lett.* **111** (2013) 062301, arXiv:1302.5874 [hep-ph]. 48

[184] J. Casalderrey-Solana, D. C. Gulhan, J. G. Milhano, D. Pablos, and K. Rajagopal, "A Hybrid strong/weak coupling approach to jet quenching", *JHEP* **10** (2014) 019, arXiv:1405.3864 [hep-ph]. [Erratum: JHEP 09, 175 (2015)]. 49

[185] A. H. Mueller, B. Wu, B.-W. Xiao, and F. Yuan, "Probing transverse momentum broadening in heavy ion collisions", *Phys. Lett. B* **763** (2016) 208–212, arXiv:1604.04250 [hep-ph]. 49

[186] A. H. Mueller, B. Wu, B.-W. Xiao, and F. Yuan, "Medium induced transverse momentum broadening in hard processes", *Phys. Rev. D* **95** (2017) 034007, arXiv:1608.07339 [hep-ph]. 49

[187] **ALICE** Collaboration, C. W. Fabjan *et al.*, "ALICE: Physics performance report", *J. Phys. G* **32** (2006) 1295–2040. 50

[188] R. Fruehwirth, "Application of halman filtering to Track fitting in the DELPHI detector",. 51

[189] **ALICE** Collaboration, B. B. Abelev *et al.*, "Performance of the ALICE Experiment at the CERN LHC", *Int. J. Mod. Phys. A* **29** (2014) 1430044, arXiv:1402.4476 [nucl-ex]. 53

[190] G. P. Salam, "Towards Jetography", *Eur. Phys. J. C* **67** (2010) 637–686, arXiv:0906.1833 [hep-ph]. 56

[191] M. Cacciari, G. P. Salam, and G. Soyez, "The anti-k_t jet clustering algorithm", *JHEP* **04** (2008) 063, arXiv:0802.1189 [hep-ph]. 56

[192] M. Cacciari, G. P. Salam, and G. Soyez, "FastJet User Manual", *Eur. Phys. J. C* **72** (2012) 1896, arXiv:1111.6097 [hep-ph]. 56

[193] Y. L. Dokshitzer, G. D. Leder, S. Moretti, and B. R. Webber, "Better jet clustering algorithms", *JHEP* **08** (1997) 001, arXiv:hep-ph/9707323. 56, 58

[194] M. Cacciari, G. P. Salam, and G. Soyez, "The anti-k_t jet clustering algorithm", *JHEP* **04** (2008) 063, arXiv:0802.1189 [hep-ph]. 56

[195] S. D. Ellis and D. E. Soper, "Successive combination jet algorithm for hadron collisions", *Phys. Rev. D* **48** (1993) 3160–3166, arXiv:hep-ph/9305266. 56, 58

[196] M. Cacciari, G. P. Salam, and G. Soyez, "The Catchment area of jets", *JHEP* **04** (2008) 005, arXiv:0802.1188 [hep-ph]. 58, 62

[197] **ATLAS** Collaboration, G. Aad *et al.*, "Properties of jets measured from tracks in proton-proton collisions at center-of-mass energy $\sqrt{s}$ = 7 TeV with the ATLAS detector", *Phys. Rev. D* **84** (2011) 054001, arXiv:1107.3311 [hep-ex]. 60

[198] **ALICE** Collaboration, B. Abelev *et al.*, "Measurement of charged jet suppression in Pb–Pb collisions at $\sqrt{s_{\mathrm{NN}}}$ = 2.76 TeV", *JHEP* **03** (2014) 013, arXiv:1311.0633 [nucl-ex]. 60, 75, 81, 126, 223

[199] M. Cacciari and G. P. Salam, "Pileup subtraction using jet areas", *Phys. Lett.* **B659** (2008) 119–126, arXiv:0707.1378 [hep-ph]. 60, 62, 63

[200] M. Verweij, *Modelling and measurement of jet quenching in relativistic heavy-ion collisions at the LHC*. PhD thesis, Utrecht U., 2013. 62

[201] **CMS** Collaboration, S. Chatrchyan *et al.*, "Measurement of the underlying event activity in pp collisions at $\sqrt{s}$ = 0.9 and 7 TeV with the novel jet-area/median approach", *JHEP* **08** (2012) 130, arXiv:1207.2392 [hep-ex]. 63

[202] H. B. Prosper and L. Lyons, eds., *Proceedings, PHYSTAT 2011 Workshop on Statistical Issues Related to Discovery Claims in Search Experiments and Unfolding, CERN,Geneva, Switzerland 17-20 January 2011*, CERN Yellow Reports: Conference Proceedings. CERN, Geneva, 1, 2011. 65

[203] A. Hocker and V. Kartvelishvili, "SVD approach to data unfolding", *Nucl. Instrum. Meth. A* **372** (1996) 469–481, arXiv:hep-ph/9509307. 67, 86

[204] L. Brenner, R. Balasubramanian, C. Burgard, W. Verkerke, G. Cowan, P. Verschuuren, and V. Croft, "Comparison of unfolding methods using RooFitUnfold", *Int. J. Mod. Phys. A* **35** (2020) 2050145, arXiv:1910.14654 [physics.data-an]. 65

[205] G. D'Agostini, "A multidimensional unfolding method based on Bayes' theorem", *Nucl.Instrum.Meth.* **A362** (1995) 487–498. 67

[206] **ALICE** Collaboration, B. Abelev *et al.*, "Performance of the ALICE Experiment at the CERN LHC", *Int. J. Mod. Phys. A* **29** (2014) 1430044, arXiv:1402.4476 [nucl-ex]. 70

[207] V. Balagura, "Notes on van der Meer scan for absolute luminosity measurement", *Nucl. Instrum. Meth. A* **654** (2011) 634, arXiv:1103.1129 [physics.ins-det]. 70

[208] S. van der Meer, "Calibration of the effective beam height in the ISR", tech. rep., CERN, Geneva, 1968. https://cds.cern.ch/record/296752. 70

[209] **ALICE Collaboration** Collaboration, "ALICE 2016-2017-2018 luminosity determination for pp collisions at $\sqrt{s}$ = 13 TeV",. https://cds.cern.ch/record/2776672. 70, 111

[210] **ALICE** Collaboration, B. Abelev *et al.*, "Measurement of event background fluctuations for charged particle jet reconstruction in Pb–Pb collisions at $\sqrt{s_{\mathrm{NN}}}$ = 2.76 TeV", *JHEP* **03** (2012) 053, arXiv:1201.2423 [hep-ex]. 76

[211] **ALICE** Collaboration, S. Acharya *et al.*, "Measurement of inclusive charged-particle b-jet production in pp and p–Pb collisions at $\sqrt{s_{\mathrm{NN}}}$ = 5.02 TeV", *JHEP* **01** (2022) 178, arXiv:2110.06104 [nucl-ex]. 76

[212] **ALICE Collaboration** Collaboration, "The ALICE definition of primary particles",. https://cds.cern.ch/record/2270008. 81

[213] M. Dasgupta, L. Magnea, and G. P. Salam, "Non-perturbative QCD effects in jets at hadron colliders", *JHEP* **02** (2008) 055, arXiv:0712.3014 [hep-ph]. 114

[214] **ALICE** Collaboration, S. Acharya *et al.*, "Charged jet cross section and fragmentation in proton-proton collisions at $\sqrt{s}$ = 7 TeV", *Phys. Rev. D* **99** (2018) 012016, arXiv:1809.03232 [nucl-ex]. 114

[215] **ALICE** Collaboration, B. Abelev *et al.*, "J/ψ production as a function of charged particle multiplicity in pp collisions at $\sqrt{s}$ = 7 TeV", *Phys. Lett.* **B712** (2012) 165–175, arXiv:1202.2816 [hep-ex]. 125, 227

[216] **ALICE** Collaboration, S. Acharya *et al.*, "Multiplicity dependence of J/ψ production at midrapidity in pp collisions at $\sqrt{s}$ = 13 TeV", *Phys. Lett. B* **810** (2020) 135758, arXiv:2005.11123 [nucl-ex].

[217] **ALICE** Collaboration, S. Acharya *et al.*, "J/ψ production as a function of charged-particle multiplicity in p–Pb collisions at $\sqrt{s_{\rm NN}}$ = 8.16 TeV", *JHEP* **09** (2020) 162, arXiv:2004.12673 [nucl-ex]. 125, 227

[218] **PHENIX** Collaboration, K. Adcox *et al.*, "Suppression of hadrons with large transverse momentum in central Au+Au collisions at $\sqrt{s_{NN}}$ = 130 GeV", *Phys. Rev. Lett.* **88** (2002) 022301, arXiv:nucl-ex/0109003. 126, 223

[219] **STAR** Collaboration, C. Adler *et al.*, "Centrality dependence of high $p_{\rm T}$ hadron suppression in Au+Au collisions at $\sqrt{s_{\rm NN}}$ = 130 GeV", *Phys. Rev. Lett.* **89** (2002) 202301, arXiv:nucl-ex/0206011.

[220] **STAR** Collaboration, J. Adams *et al.*, "Direct observation of dijets in central Au+Au collisions at $\sqrt{s_{NN}}$ = 200 GeV", *Phys. Rev. Lett.* **97** (2006) 162301, arXiv:nucl-ex/0604018. 126, 223

[221] **STAR** Collaboration, "Measurement of in-medium jet modification using direct photon+jet and π^0+jet correlations in $p + p$ and central Au+Au collisions at $\sqrt{s_{\rm NN}}$ = 200 GeV", arXiv:2309.00156 [nucl-ex]. 126, 170, 223, 228

[222] **ALICE** Collaboration, S. Acharya *et al.*, "Measurement of the radius dependence of charged-particle jet suppression in Pb–Pb collisions at $\sqrt{s_{\mathrm{NN}}}$ = 5.02 TeV", *Phys. Lett. B* **849** (2024) 138412, arXiv:2303.00592 [nucl-ex]. 126, 168, 223

[223] J. Casalderrey-Solana, Z. Hulcher, G. Milhano, D. Pablos, and K. Rajagopal, "Simultaneous description of hadron and jet suppression in heavy-ion collisions", *Phys. Rev. C* **99** (2019) 051901, arXiv:1808.07386 [hep-ph]. 126, 223

[224] **JETSCAPE** Collaboration, R. Ehlers, "Bayesian Analysis of QGP Jet Transport Using Multi-scale Modeling Applied to Inclusive Hadron and Reconstructed Jet Data", *Acta Phys. Polon. Supp.* **16** (2023) 62, arXiv:2208.07950 [hep-ph]. 126, 223

[225] D. de Florian, "Next-to-leading order QCD corrections to hadron+jet production in pp collisions at RHIC", *Phys.Rev.* **D79** (2009) 114014, arXiv:0904.4402 [hep-ph]. 130

[226] **ALICE** Collaboration, S. Acharya *et al.*, "Transverse momentum spectra and nuclear modification factors of charged particles in pp, p–Pb and Pb–Pb collisions at the LHC", *JHEP* **11** (2018) 013, arXiv:1802.09145 [nucl-ex]. 137

[227] G. Soyez, "A Simple description of jet cross-section ratios", *Phys. Lett. B* **698** (2011) 59–62, arXiv:1101.2665 [hep-ph]. 166

[228] **ALICE** Collaboration, B. Abelev *et al.*, "Measurement of the inclusive differential jet cross section in pp collisions at $\sqrt{s}$ = 2.76 TeV", *Phys. Lett. B* **722** (2013) 262–272, arXiv:1301.3475 [nucl-ex]. 166

[229] M. Dasgupta, F. Dreyer, G. P. Salam, and G. Soyez, "Small-radius jets to all orders in QCD", *JHEP* **04** (2015) 039, arXiv:1411.5182 [hep-ph]. 166

[230] **CMS** Collaboration, S. Chatrchyan *et al.*, "Measurement of the ratio of inclusive jet cross sections using the Anti-k_T algorithm with radius parameters R = 0.5 and 0.7 in pp collisions at $\sqrt{s}$ = 7 TeV", *Phys. Rev. D* **90** (2014) 072006, arXiv:1406.0324 [hep-ex]. 166

[231] M. Dasgupta, F. A. Dreyer, G. P. Salam, and G. Soyez, "Inclusive jet spectrum for small-radius jets", *JHEP* **06** (2016) 057, arXiv:1602.01110 [hep-ph]. 166

[232] **STAR** Collaboration, "Semi-inclusive direct photon+jet and π^0+jet correlations measured in $p+p$ and central Au+Au collisions at $\sqrt{s_{\mathrm{NN}}}$ = 200 GeV", arXiv:2309.00145 [nucl-ex]. 167, 170, 228

[233] **CMS** Collaboration, S. Chatrchyan *et al.*, "Observation and studies of jet quenching in Pb–Pb collisions at nucleon-nucleon center-of-mass energy $\sqrt{s_{\mathrm{NN}}}$ = 2.76 TeV", *Phys.Rev.* **C84** (2011) 024906, arXiv:1102.1957 [nucl-ex]. 173, 229

[234] J. Aichelin, P. B. Gossiaux, and T. Gousset, "Radiative and collisional energy loss of heavy quarks in deconfined matter", *Acta Phys. Polon.* **B43** (2012) 655–662, arXiv:1201.4192 [nucl-th]. 174, 223

[235] **ALICE** Collaboration, S. Acharya *et al.*, "Measurement of D^0, D^+, D^{*+} and D_s^+ production in Pb–Pb collisions at $\sqrt{s_{\mathrm{NN}}}$ = 5.02 TeV", *JHEP* **10** (2018) 174, arXiv:1804.09083 [nucl-ex]. 174, 223

[236] **ALICE** Collaboration, S. Acharya *et al.*, "Measurement of jet radial profiles in Pb–Pb collisions at $\sqrt{s_{\mathrm{NN}}}$ = 2.76 TeV", *Phys. Lett. B* **796** (2019) 204–219, arXiv:1904.13118 [nucl-ex]. 174

[237] A. Luo, Y.-X. Mao, G.-Y. Qin, E.-K. Wang, and H.-Z. Zhang, "Enhancement of baryon-to-meson ratios around jets as a signature of medium response", *Phys. Lett. B* **837** (2023) 137638, arXiv:2109.14314 [hep-ph]. 174, 184

[238] **ALICE** Collaboration, S. Acharya *et al.*, "Measurement of D^0 , D^+ , D^{*+} and D_s^+ production in pp collisions at $\sqrt{s}$ = 5.02 TeV with ALICE", *Eur. Phys. J. C* **79** (2019) 388, arXiv:1901.07979 [nucl-ex]. 177

[239] **ALICE** Collaboration, S. Acharya *et al.*, "Λ_c^+ production in pp and in p–Pb collisions at $\sqrt{s_{\mathrm{NN}}}$=5.02 TeV", *Phys. Rev. C* **104** (2021) 054905, arXiv:2011.06079 [nucl-ex].

[240] **ALICE** Collaboration, S. Acharya *et al.*, "Measurement of beauty production via non-prompt D^0 mesons in Pb–Pb collisions at $\sqrt{s_{\mathrm{NN}}}$= 5.02 TeV", *JHEP* **12** (2022) 126, arXiv:2202.00815 [nucl-ex]. 177

[241] T. Chen and C. Guestrin, "XGBoost: A Scalable Tree Boosting System", arXiv:1603.02754 [cs.LG]. 178

[242] L. Barioglio, F. Catalano, M. Concas, P. Fecchio, F. Grosa, F. Mazzaschi, and M. Puccio, "hipe4ml/hipe4ml", Nov., 2021. https://doi.org/10.5281/zenodo.5734093. 178

[243] W. Busza, K. Rajagopal, and W. van der Schee, "Heavy Ion Collisions: The Big Picture, and the Big Questions", *Ann. Rev. Nucl. Part. Sci.* **68** (2018) 339–376, arXiv:1802.04801 [hep-ph]. 222

[244] L. Cunqueiro and A. M. Sickles, “Studying the QGP with Jets at the LHC and RHIC”, *Prog. Part. Nucl. Phys.* **124** (2022) 103940, arXiv:2110.14490 [nucl-ex]. 222

Appendix A Multiplicity-dependent jet production and semi-inclusive jet yields

A.1 Charged-particle jet cross section and ratios without UE subtraction

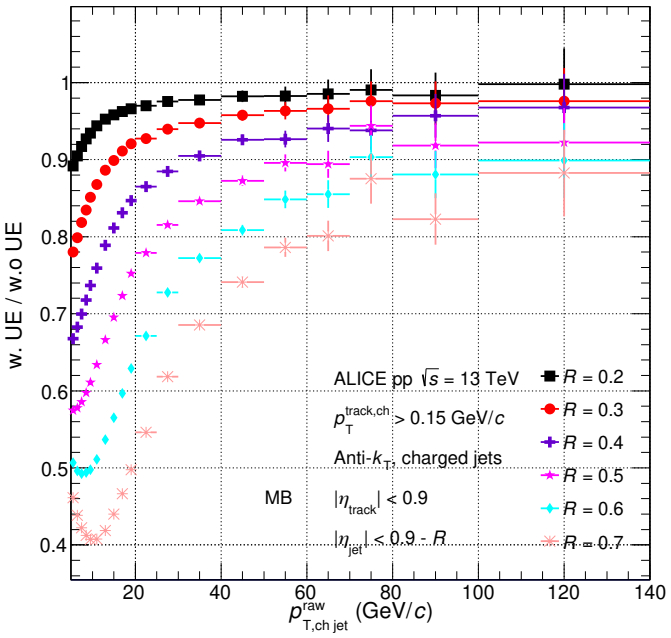

Figure A.1: Comparison of raw inclusive charged-particle jet yield between without and with UE subtraction in pp collisions at $\sqrt{s}$ = 13 TeV.

The fully corrected inclusive charged-particle jet cross sections and cross section ratios without UE corrections in pp collisions at $\sqrt{s}$ = 13 TeV are presented in this section. Fig. A.2 shows the jet cross section for different resolution parameters R varied from 0.2 to 0.7 without UE subtraction. The comparisons with LO and NLO theoretical calculations are shown in Fig. A.3. Fig. A.4 and A.5 show the jet cross section ratios without UE subtraction, in addition to comparison with theoretical calculations between different collision energies, respectively.

A.2 Multiplicity dependence of jet production using SPD tracklets estimator

As a cross-check, jet production dependent on multiplicity was measured and obtained using the SPD tracklets estimator, as depicted from Fig.A.6 to Fig.A.10. To facilitate citation and comparison with publicly available results $\langle \mathrm{d}N_{\mathrm{ch}}/\mathrm{d}\eta \rangle_{|\eta|<1}$ [29], the event data were classified into 10 SPD multiplicity

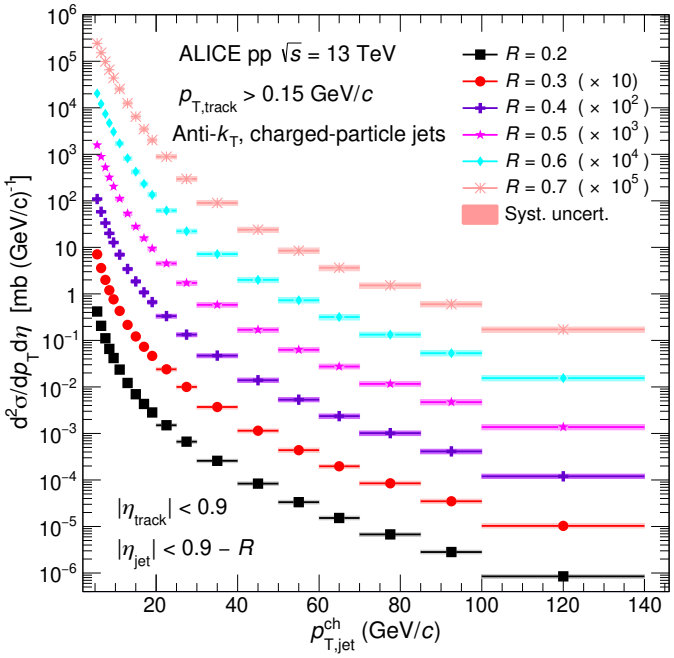

Figure A.2: Inclusive charged-particle jet cross sections in pp collisions at $\sqrt{s}$ = 13 TeV using the anti-k_T algorithm for different resolution parameters R varied from 0.2 to 0.7, without UE subtraction. Statistical uncertainties are displayed as vertical error bars. The total systematic uncertainties are shown as solid boxes around the data points.

classes, as shown in Table A.1, leading to a decrease in the statistics of events with lower multiplicities. From Fig. A.7, it is evident that the production ratio of $R = 0.2$ to other radii at $p_T > 60$ GeV/c is unreliable for the last three multiplicity classes. All the results presented here and descriptions of figures are similar to those in Section 4.6.2.

Table A.1: Average charged-particle pseudorapidity densities at midrapidity $\langle dN_{ch}/d\eta \rangle$ from data for inclusive events and different SPD tracklets multiplicity classes [29].

Class	SPD tracklets percentile	$\langle dN_{ch}/d\eta \rangle_{\|\eta\|<1}$
MB	0–100%	6.93 ± 0.09
I	0–1%	32.70 ± 0.67
II	1–5%	23.21 ± 0.45
III	5–10%	18.03 ± 0.37
IV	10–15%	14.94 ± 0.30
V	15–20%	12.69 ± 0.27
VI	20–30%	10.33 ± 0.22
VII	30–40%	8.03 ± 0.18
VIII	40–50%	6.18 ± 0.13
IX	50–70%	4.05 ± 0.09
X	70–100%	1.80 ± 0.05

Comparison of jet production between using V0M and SPD multiplicity estimators

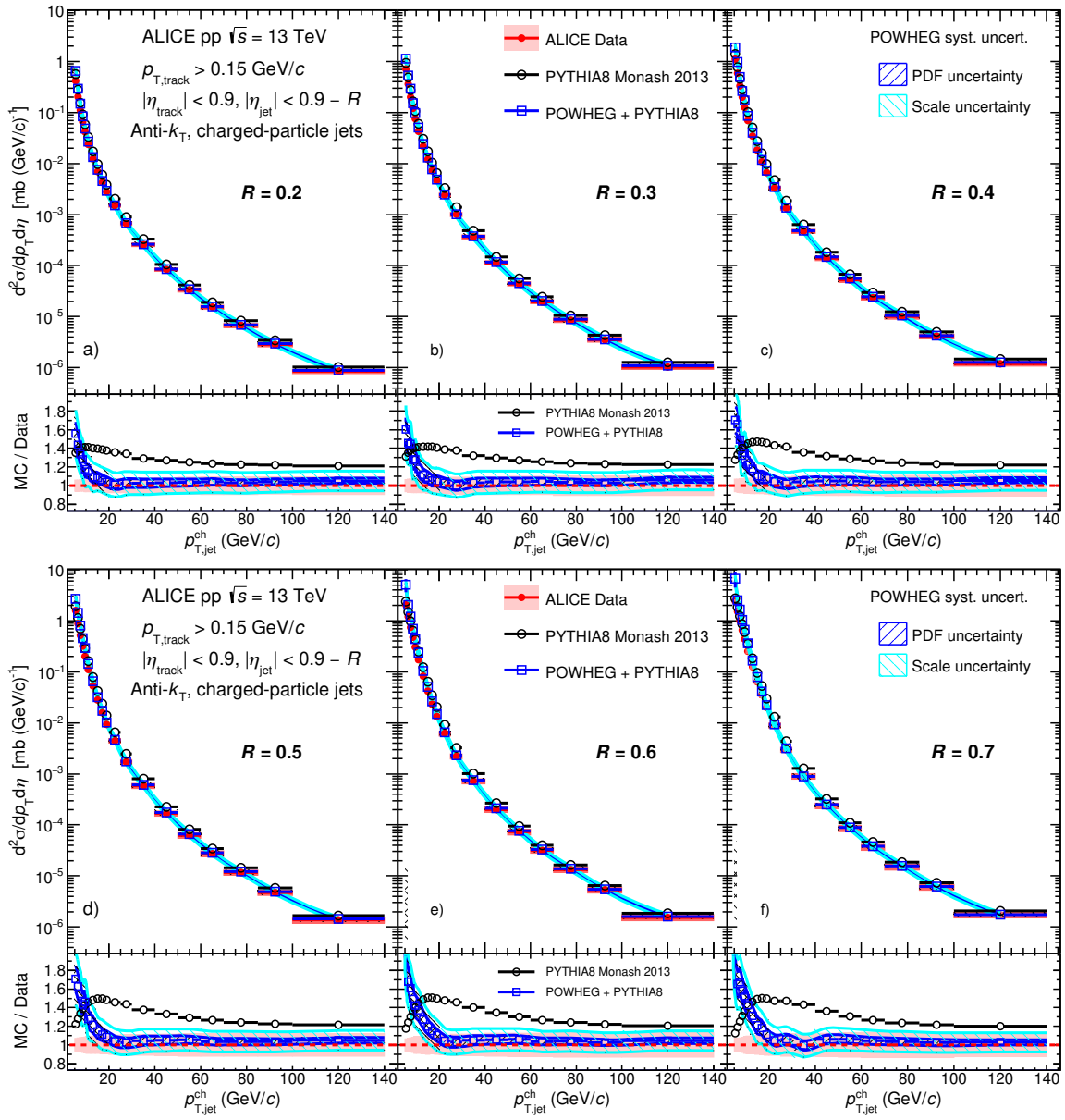

Figure A.3: Inclusive charged-particle jet cross sections in pp collisions at $\sqrt{s}$ = 13 TeV without UE subtraction and compared to LO and NLO MC predictions with different resolution parameters R varied from 0.2 to 0.7. The statistical uncertainties are displayed as vertical error bars. The systematic uncertainties on the data are indicated by shaded boxes in the top panels and shaded bands drawn around unity in the bottom panels. The red dashed lines in the ratio correspond to unity.

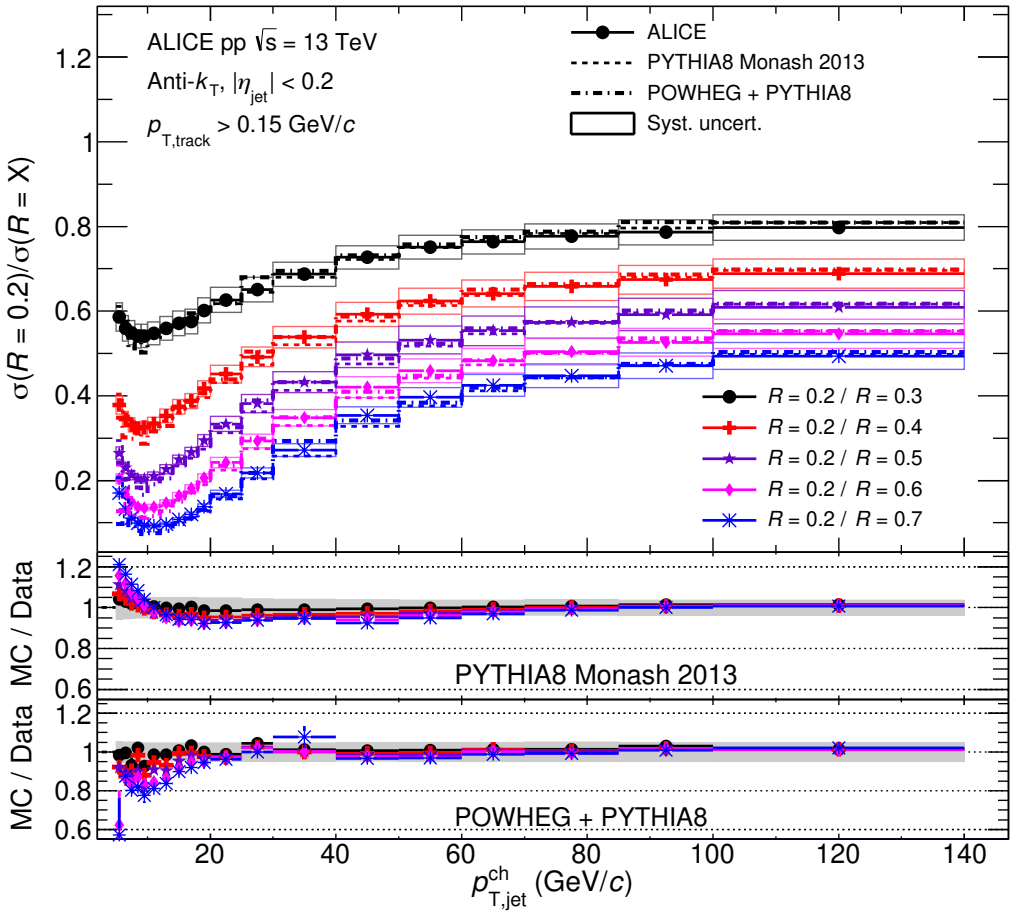

Figure A.4: Ratio of charged-particle jet cross section for resolution parameter $R = 0.2$ to other radii $R = X$, with X ranging from 0.3 to 0.7, without UE subtraction, and the comparison of calculations from LO (PYTHIA) and NLO event generators (POWHEG+PYTHIA8). The systematic uncertainties of the cross section ratios from data are indicated by solid boxes around data points in the upper panels, and shaded bands around unity in the lower panels. No uncertainties are shown for theoretical predictions for better visibility.

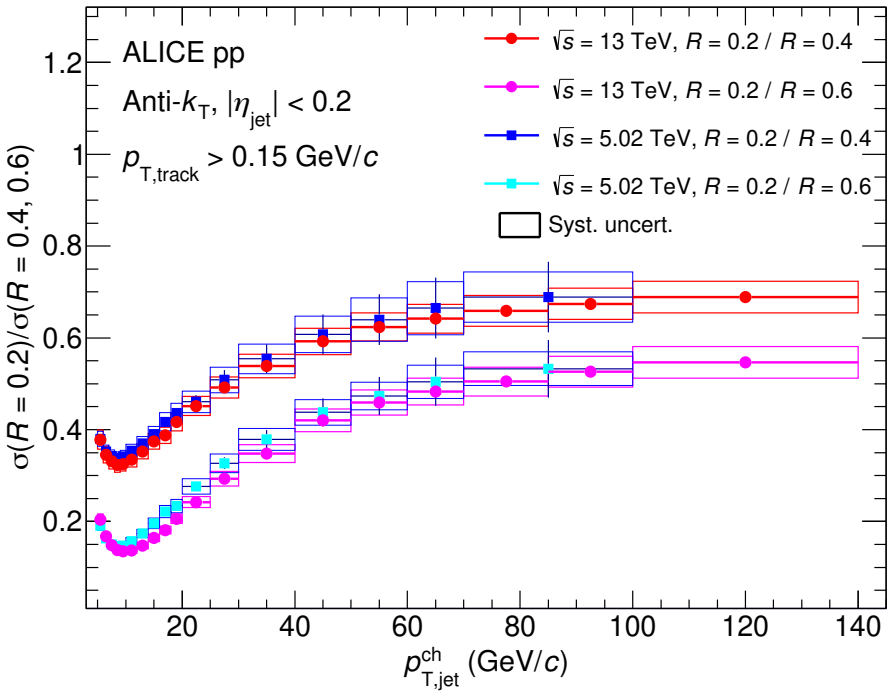

Figure A.5: Comparison of charged-particle jet cross section ratios for $\sigma(R = 0.2)/\sigma(R = 0.4)$ and $\sigma(R = 0.2)/\sigma(R = 0.6)$ without UE subtraction in pp collisions at $\sqrt{s}$ = 13 and 5.02 TeV [26].

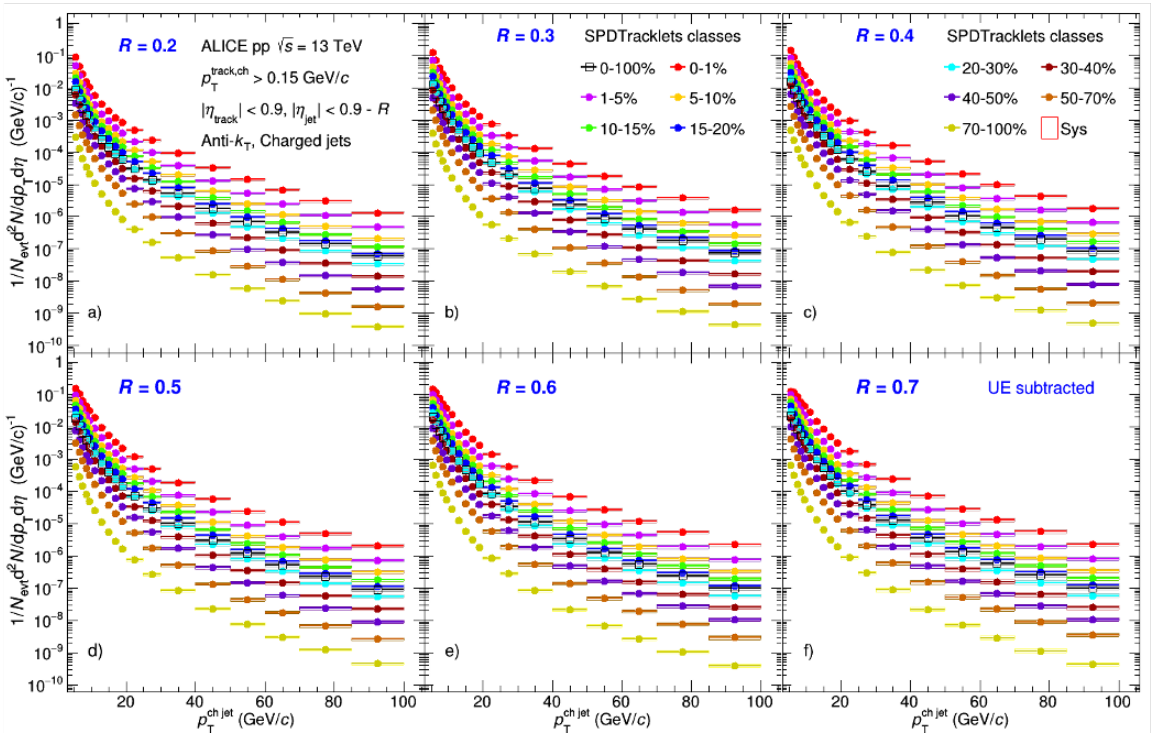

Figure A.6: Jet p_T distribution for different multiplicity bins with R = 0.2 – 0.7 using SPD tracklets estimator

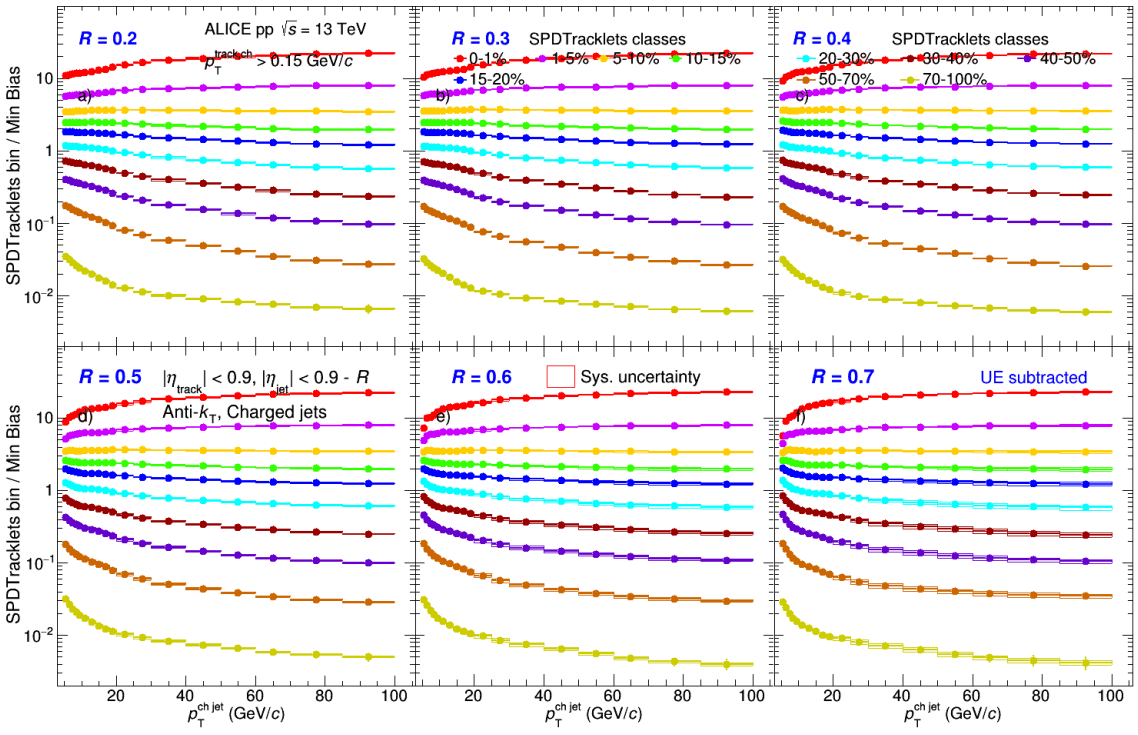

Figure A.7: Jet p_{T} production ratio of different multiplicity bins to MB one with $R = 0.2 - 0.7$ using SPD tracklets estimator

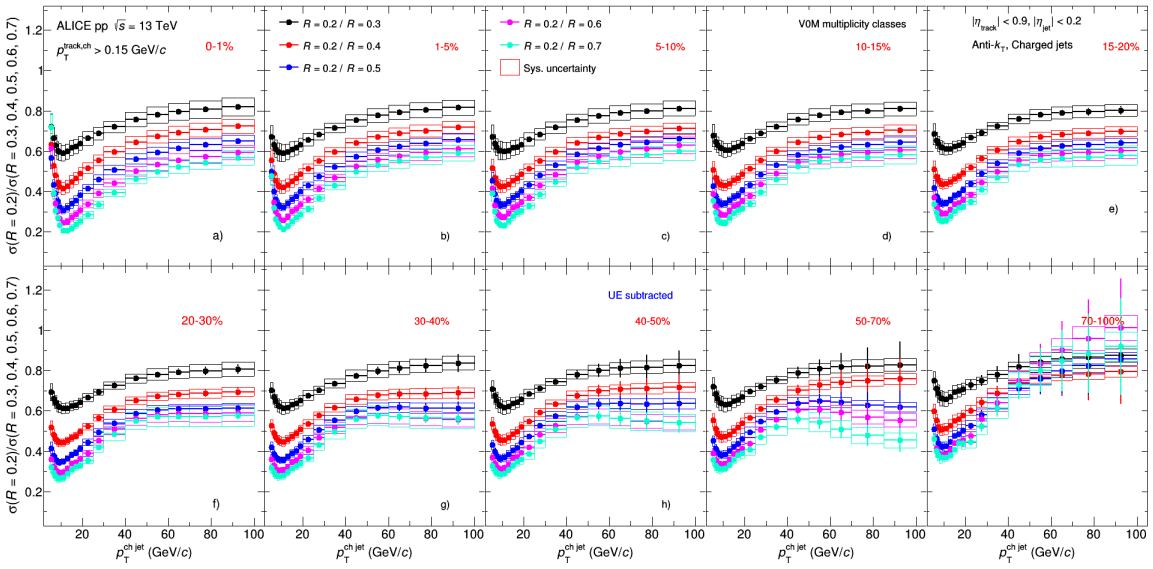

Figure A.8: The charged jet production ratio of $R = 0.2$ to $R = X$ for different multiplicity bins and MB one using SPD tracklets estimator.

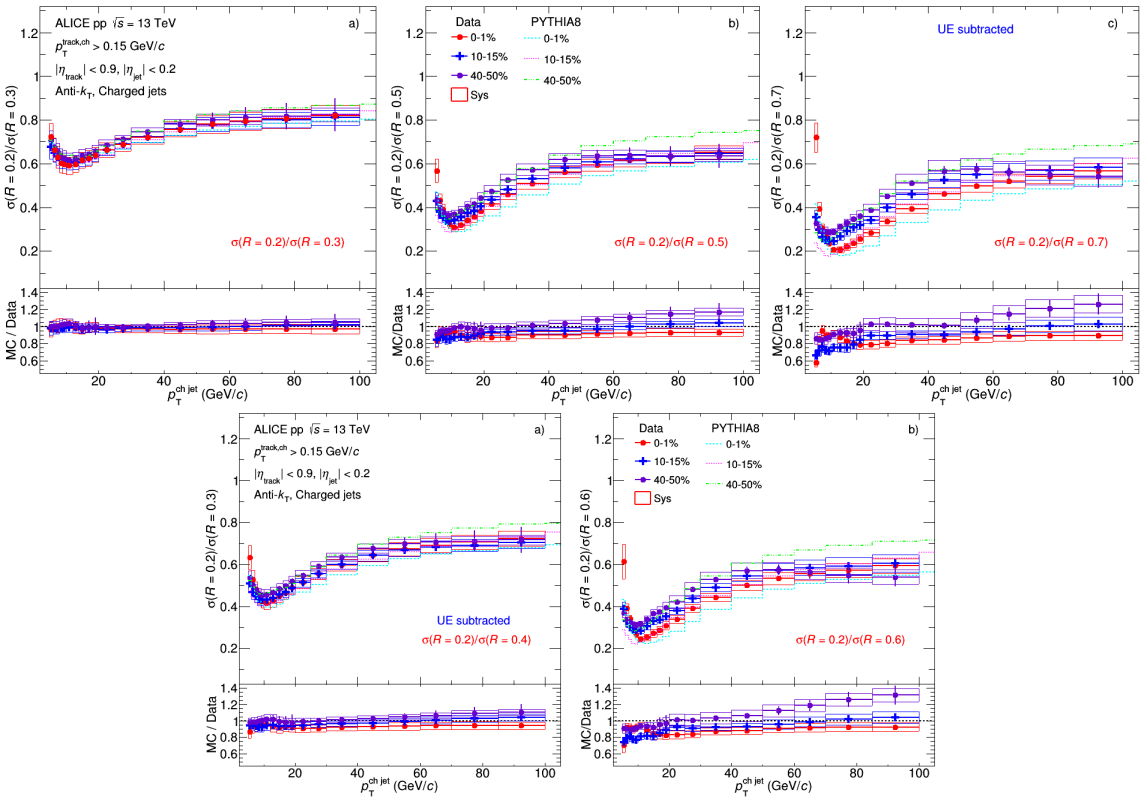

Figure A.9: Comparison the charged jet cross section ratio of $R = 0.2$ to $R = X$ for three different multiplicity bins with the results of PYTHIA8 simulation using SPD tracklets estimator.

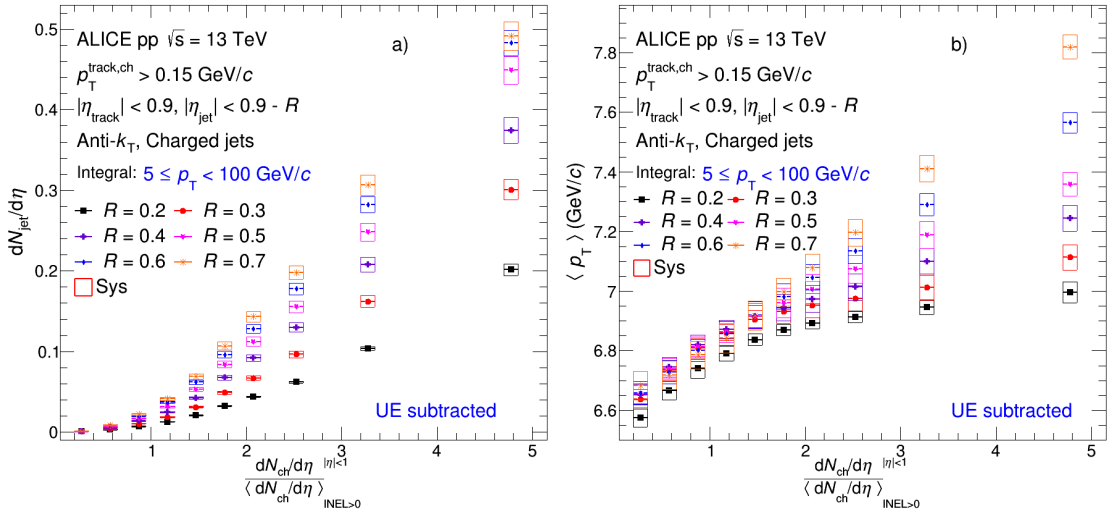

Figure A.10: Integrated and mean jet production vs multiplicity distributions for $R = 0.2 - 0.7$ using SPD tracklets estimator

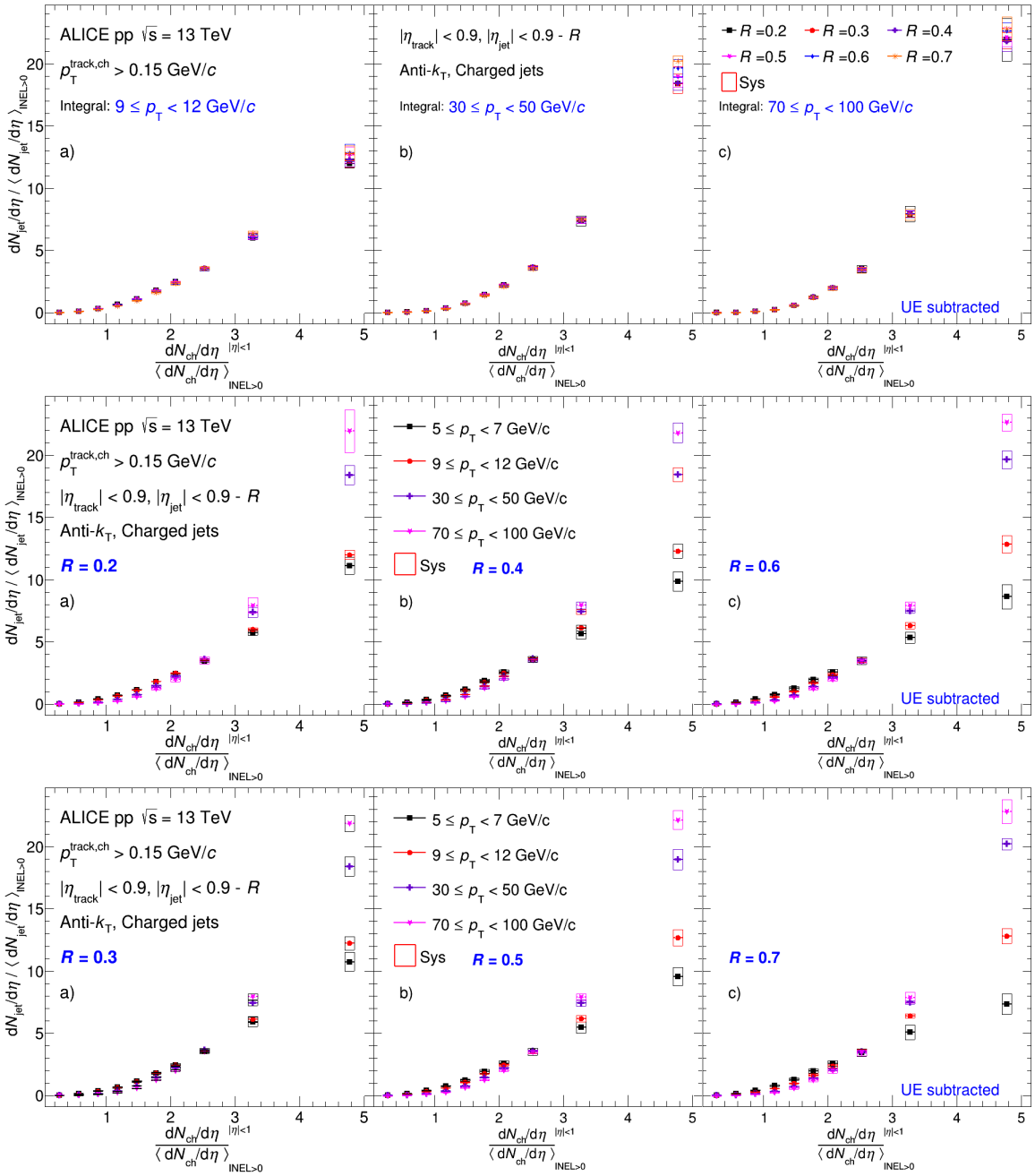

Figure A.11: Integrated Jet production ratio vs multiplicity distributions for $R = 0.2 - 0.7$ using SPD tracklets estimator

After obtaining yield results of jets using the event selection based on SPD tracklets at midrapidity and on V0 amplitude at forward rapidity for different jet resolution parameters in pp collisions at $\sqrt{s}$ = 13 TeV, we compare these results under the same percentile intervals, as depicted in Fig. A.12. We observe significant differences between the two results. However, upon comparing the integral results of jet production and production ratios (multiplicity classes over MB) in Fig. A.13, namely, the normalized jet production and production ratios as a function of the normalized charged-particle pseudorapidity density at midrapidity ($\langle \mathrm{d}N_{\mathrm{ch}}/\mathrm{d}\eta \rangle_{|\eta|<1}$), we find that the two results are essentially consistent, falling within the same curve within uncertainties. Both show an increase in jet yield with increasing multiplicity between using V0M and SPD estimators.

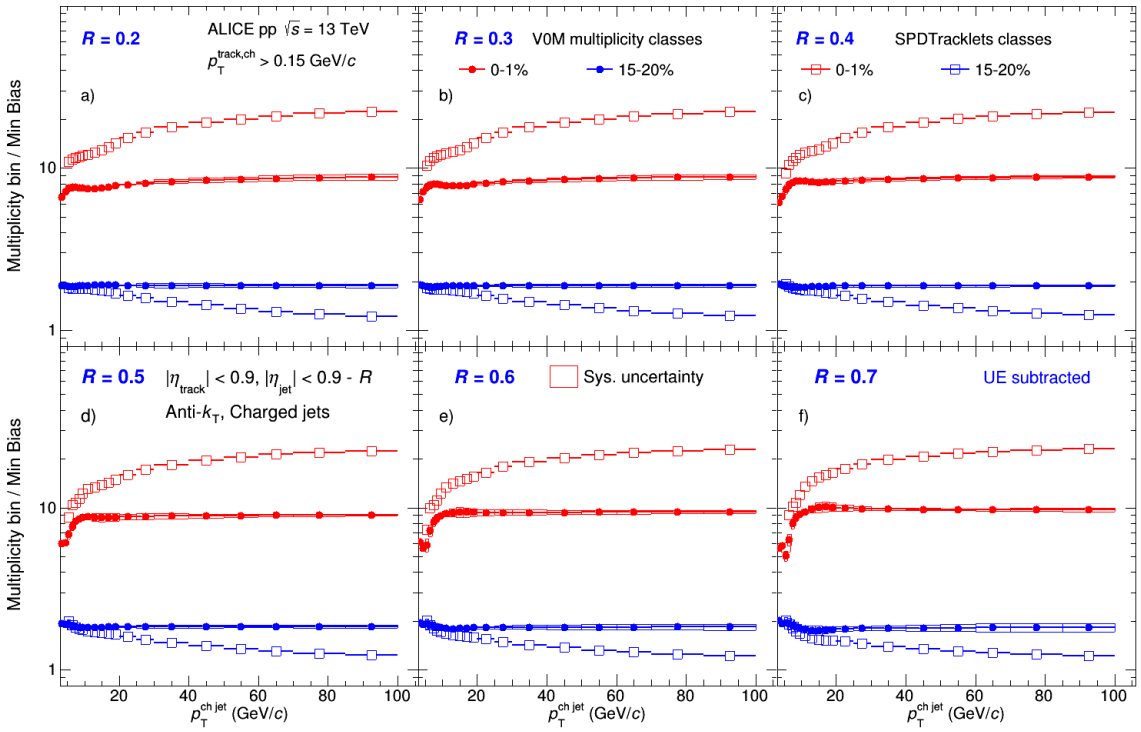

Figure A.12: Comparison of jet production ratio between using V0M (full marker) and SPD tracklets (open marker) multiplicity estimators.

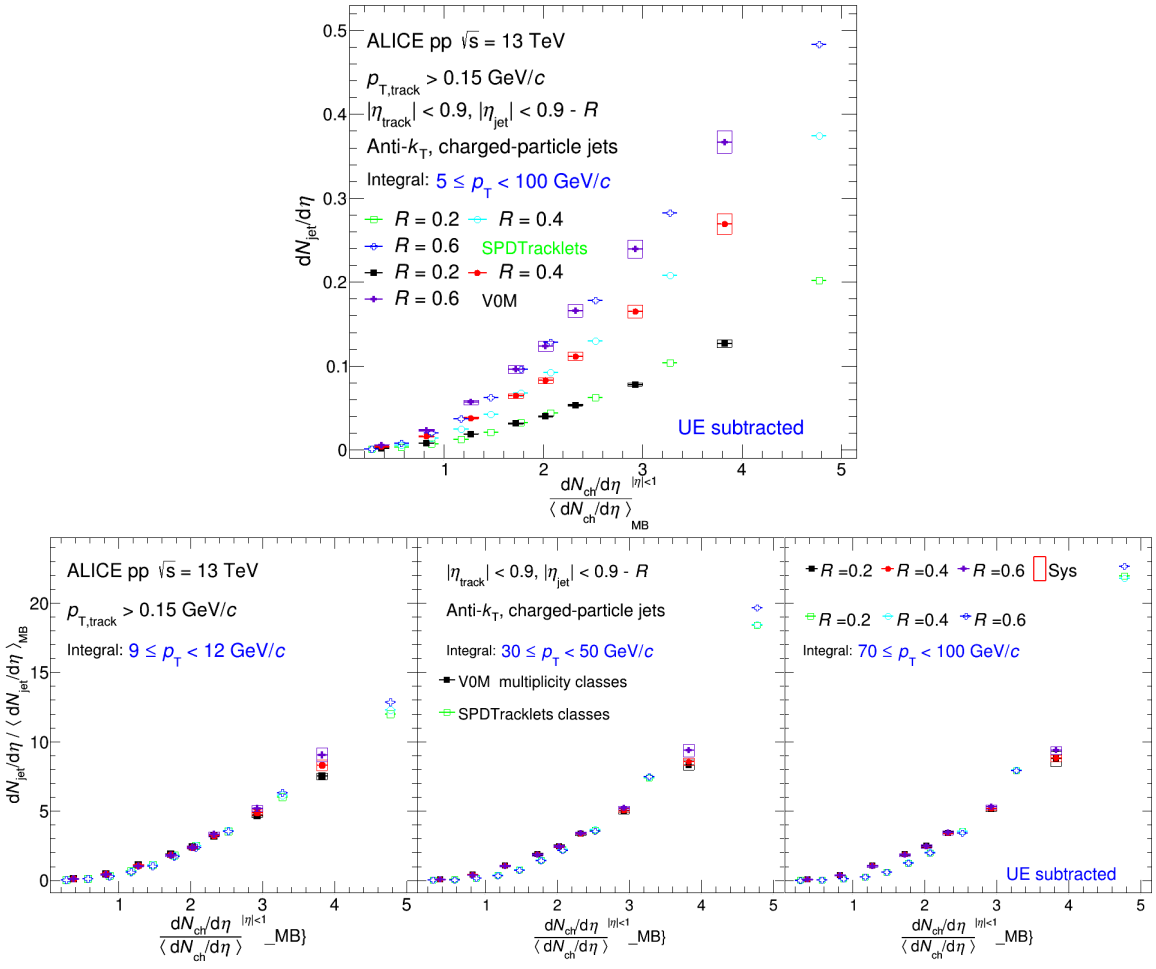

Figure A.13: Comparison of integrated jet production and production ratio between using V0M (full marker) and SPD tracklets (open marker) multiplicity estimators.

A.3 H-jet results with $\mathrm{TT}_{\mathrm{ref}} = \mathrm{TT}\{8, 9\}$ and $\mathrm{TT}_{\mathrm{sig}} = \mathrm{TT}\{20, 50\}$

Figure A.14 displays fully-corrected recoil jet spectra as a function of $p_{\mathrm{T,ch\ jet}}$ for $R = 0.2, 0.4, 0.5$ using $\mathrm{TT}_{\mathrm{sig}} = \mathrm{TT}\{20, 50\}$ and $\mathrm{TT}_{\mathrm{ref}} = \mathrm{TT}\{8, 9\}$. The comparison of the unfolded results to the MC generator level is presented in the bottom panels. The results demonstrate consistency with PYTHIA8 across the entire jet p_{T} range, indicating that PYTHIA8 well describes recoil jet production.

The conclusions of the measurement were verified with different choices of reference TT, and the results were displayed as a function of recoil jet $p_{\mathrm{T,ch\ jet}}$ in Fig. A.15. Qualitatively consistent trends from $I_{\mathrm{AA}}(p_{\mathrm{T,ch\ jet}})$ were observed as a function of $p_{\mathrm{T,ch\ jet}}$, with a suppression in the yield at intermediate $p_{\mathrm{T,ch\ jet}}$ and a rising trend towards higher $p_{\mathrm{T,ch\ jet}}$. As mentioned in the main text, due to the different reference, it is not claimed that these distributions should be quantitatively consistent.

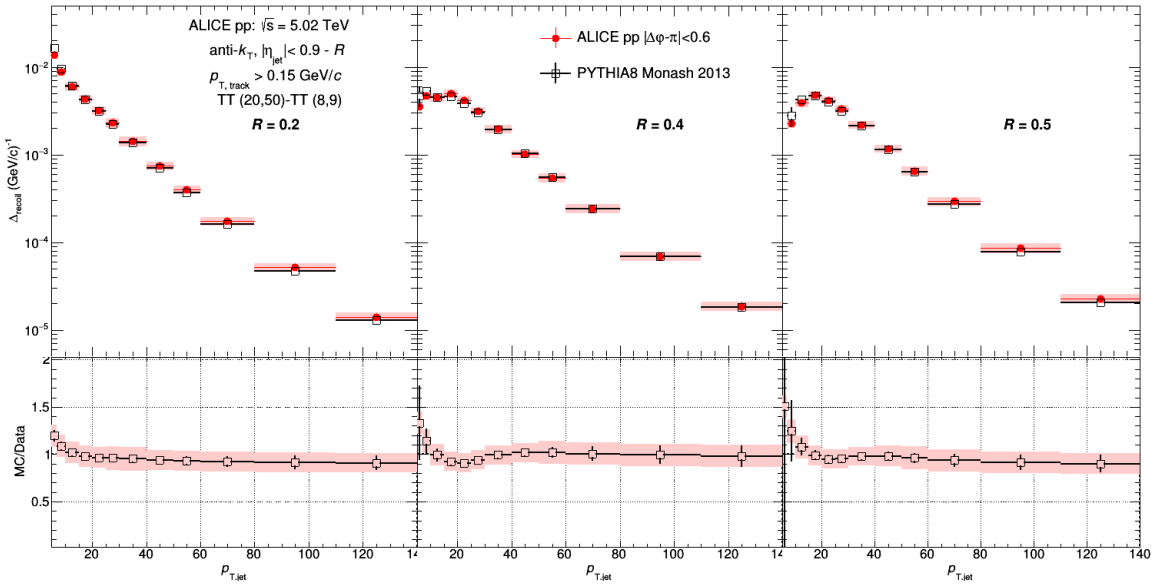

Figure A.14: Corrected $\Delta_{\mathrm{recoil}}(p_{\mathrm{T,ch\ jet}})$ distributions measured in $\mathrm{TT}\{20, 50\} - \mathrm{TT}\{8, 9\}$ for $R = 0.2$ (left), 0.4 (middle), and 0.5 (right) in pp collisions at $\sqrt{s} = 5.02$ TeV, compared to PYTHIA8 calculation.

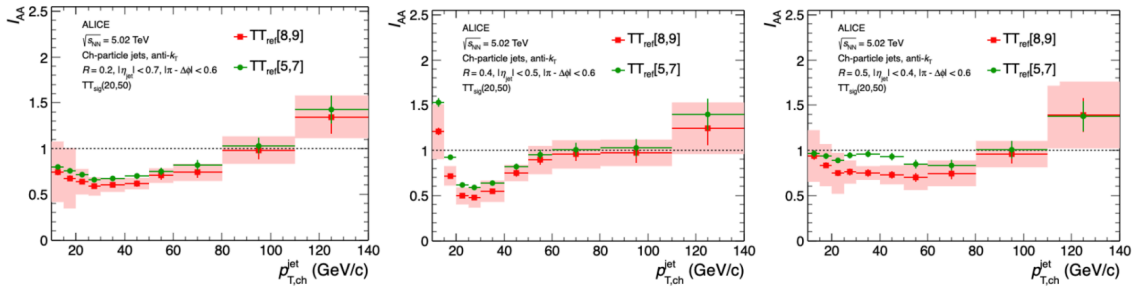

Figure A.15: Comparison of $I_{AA}(p_{T,ch\ jet})$ from TT{20, 50} – TT{5, 7} and TT{20, 50} – TT{8, 9} measured for $R = 0.2$ (top), 0.4 (middle), and 0.5 (bottom) in central Pb–Pb and pp collisions.

Appendix B Introduction à la version française de la thèse de doctorat

B.1 Introduction et objectifs de la thèse

Les recherches sur les collisions d'ions lourds (HI) à des énergies ultra-relativistes explorent les propriétés de la matière nucléaire en interaction forte dans des conditions extrêmes de haute densité d'énergie et de température. Le Plasma Quark-Gluon (QGP), qui est un état chaud et dense de matière déconfinée, est produit dans les collisions HI [243]. Étudier la matière QGP au Large Hadron Collider (LHC) et au Relativistic Heavy-Ion Collider (RHIC) améliore notre compréhension de la chromodynamique quantique (QCD), la théorie de l'interaction forte. Un jet est un émission collimatée de particules provenant de partons initialement créés par diffusion dure au début des collisions. Dans les collisions pp, les mesures de production de jets fournissent des tests rigoureux des calculs QCD perturbatifs d' ordre supérieur. Dans les collisions noyau–noyau, les partons durs créés traversent le milieu QGP et interagissent avec lui. Cette interaction redistribue l'énergie dans la gerbe, menant à une diminution de la production des hadrons et des jets à haute p_{T}, à la modification de la sous-structure du jet, et à l'émergence de l'acoplanarité induite par le milieu ("jet quenching") [244].

Au cours de la dernière décennie, l'étude des petits systèmes a suscité un intérêt croissant en tant que champ de recherche à part entière. En particulier, des effets similaires à ceux présents dans les collisions d'ions lourds ont été observés dans les collisions pp et p–Pb de haute multiplicité où la formation d'un QGP n'était pas attendue. Cela inclut, par exemple, les corrélations angulaires à longue portée [122] et l'augmentation des rapports de production baryon/méson à un moment transverse intermédiaire p_{T} (2–6 GeV/c) [130], qui est qualitativement similaire à celle observée dans les collisions Pb–Pb. Un autre exemple est l'augmentation continue du rapport des hadrons étranges aux hadrons non étranges en fonction de la densité de multiplicité des particules chargées de faible multiplicité pp à haute multiplicité p–Pb jusqu'à atteindre finalement les valeurs observées dans les collisions Pb–Pb [73]. Ces découvertes suggèrent l'existence possible d'un mécanisme sous-jacent commun qui déterminerait la composition chimique des particules produites des petits aux grands systèmes de collision. Par conséquent, nous aimerions rechercher l'effet d'jet-quenching avec la précision actuelle dans les systèmes de collision de petite taille à haute multiplicité et expliquer ces effets semblables au QGP. Pour approfondir notre compréhension des mécanismes en jeu dans les collisions de haute multiplicité de petits systèmes, la dépendance en multiplicité de la production de jets chargés a été étudiée dans les collisions pp à $\sqrt{s}$ = 13 TeV par ALICE.

L'jet-quenching est une conséquence nécessaire de la formation du QGP dans les collisions d'ions lourds. Plusieurs signatures communes de l'suppression des jets sont la déflexion angulaire des jets et la modification de la sous-structure des jets observées dans les collisions d'ions lourds par rapport aux collisions pp. La mesure des jets reconstruits dans les collisions d'ions lourds est un défi en raison du bruit de fond important et non uniforme. Les études initiales de l'jet-quenching ont donc utilisé la production de hadrons à haute-p_{T} et les corrélations [218–220], qui sont plus facilement mesurables avec une haute précision dans un tel environnement. Une compréhension plus approfondie des mécanismes sous-jacents à l'suppression des jets et de la réponse du QGP au passage de partons énergétiques nécessite des mesures incorporant des jets reconstruits. Des progrès significatifs ont été réalisés au cours de la dernière décennie dans la mesure des jets dans les collisions d'ions lourds en termes de production de jets inclusifs, de corrélations di-jet, et d'observables de coïncidence déclencheur-jet [15, 82, 198, 221, 222]. Les études de modèles incorporent à la fois des observables fondées sur des jets reconstruits et des observables fondées sur des hadrons de haut p_{T}, pour une étude plus complète de l'jet-quenching [223, 224]. Nous rapportons de nouvelles mesures de la distribution semi-inclusive des jets de particules chargées, dit "de recul" (par rapport à un hadron chargé de haut p_{T}) ("h+jet") [15, 82] dans les collisions pp et Pb–Pb centrales $\sqrt{s_{\mathrm{NN}}}$ = 5.02 TeV.

Les quarks lourds (charme et beauté) sont principalement produits lors des diffusions dures au stade initial d'une collision, avant la formation du QGP, et leur production thermique dans le QGP est négligeable. Ils traversent le milieu et perdent une partie de leur énergie via des processus collisionnels et radiatifs [234]. Par conséquent, les quarks lourds sont des sondes tomographiques idéales du QGP, permettant l'extraction des propriétés de transport du milieu [235]. Les études sur la production de jets à saveur lourde (jet–$\mathrm{D}^0/\mathrm{D}^+/\Lambda_c^+$) dans les collisions pp peuvent imposer des contraintes supplémentaires sur le mécanisme de perte d'énergie des quarks lourds et les propriétés du milieu car elles fournissent un aperçu de la manière dont l'énergie est perdue et dissipée dans le milieu. Les études de faisabilité sur l'identification et les mesures de marquage des jets de quarks charmés ont été abordées. Le rapport de production Λ_c^+/D^0 sera calculé pour enquêter sur les mécanismes de hadronisation du quark de charme en mésons et baryons.

B.2 Cadre de la thèse

Le premier chapitre 1 de cette thèse présente la physique qui motive le programme scientifique ALICE et donne un aperçu concis des bases de la physique nucléaire et de la physique des particules à haute énergie. Nous commençons par décrire les particules fondamentales du modèle standard et leurs interactions. Nous décrivons ensuite les caractéristiques spécifiques de ces particules et les propriétés

qui les définissent. Nous poursuivons par une introduction concise à la chromodynamique quantique (QCD), en mettant l'accent sur deux aspects clés de la QCD : le confinement des quarks et la liberté asymptotique. Nous approfondissons le concept d'une nouvelle matière QCD déconfinée connue sous le nom de plasma quark-gluon et l'utilisation de jets pour en apprendre davantage à son sujet. Ensuite, nous développons les principales caractéristiques des collisions d'ions lourds, leur évolution spatio-temporelle et les principales variables expérimentales. Enfin, nous présentons les sondes QGP dans les collisions d'ions lourds et les comportements de type QGP observés dans les petits systèmes, en mettant l'accent sur l'effet d'jet-quenching dans les sondes dures associées aux jets qui sont l'objet principal de cette thèse.

Le Chapitre 2 présente brièvement un aperçu du Grand Collisionneur de Hadrons (LHC), soulignant ses principales caractéristiques et les expériences associées. En particulier, l'expérience ALICE est dédiée au programme d'ions lourds pour l'investigation du QGP. Les données utilisées pour les analyses présentées dans cette thèse ont été collectées par les détecteurs d' ALICE. Une description détaillée des divers sous-systèmes d'ALICE sera présentée, en particulier ceux pertinents pour nos analyses, incluant VZER0 (V0), le Système de Trajectographie Interne (ITS), la Chambre de Projection Temporelle (TPC) et le Temps de Vol (TOF). De plus, une brève introduction au cadre hors ligne d'ALICE est fournie pour comprendre le mode opératoire d'AliPhysics. Étant donné l'importance des simulations Monte Carlo (MC) utilisant divers modèles (PYTHIA, POWHEG, JETSCAPE, JEWEL et les calculs du Hybrid Model), nous présentons également une introduction concise aux principes fondamentaux de l' environnement logiciel.

L'analyse des jets est intrinsèquement complexe, impliquant diverses étapes telles que la définition, la reconstruction, l'application de coupures et les techniques de correction. Ces facteurs contribuent à l'ambiguïté entourant le concept de jet. Au final, on doit se contenter du fait que l'on définit d'une certaine manière ce qu'est un jet. Cependant, la principale contrainte est de s'assurer que le jet résultant présente autant de propriétés que possible cohérentes avec les objets physiques conceptuels issus des diffusions de partons durs, tout en garantissant la comparabilité avec d'autres mesures. Le Chapitre 3 fournit un aperçu complet des techniques et algorithmes fondamentaux utilisés dans notre analyse de données. Suite à une discussion sur les bases de la reconstruction de trajectoires et de la reconstruction de jets, nous explorons la méthodologie de la soustraction du bruit de fond. Par la suite, nous décrivons la technique fondamentale de correction par "dépliement" telle qu'appliquée aux mesures de jets.

Le Chapitre 4 détaille les mesures de production de jets de particules chargées dépendantes de la multiplicité dans les collisions pp à $\sqrt{s}$ = 13 TeV avec ALICE au LHC, dans le but d'investiguer les ef-

fets d'jet-quenching dans les événements à haute multiplicité créés dans de petits systèmes de collision. Les stratégies d'analyse incluent la sélection de l'échantillon de données, la sélection des événements, la catégorisation de la multiplicité, la reconstruction des trajectoires et des jets, la soustraction du fond, l'introduction des fluctuations de fond, l'application des corrections par "dépliement", les calculs d'incertitude systématique, et la discussion des résultats physiques finaux. Les informations de base sur la sélection des événements, la reconstruction des trajectoires et des jets, la soustraction du bruit de fond des jets, et le dépliement sont présentées dans le Chapitre 3, tandis que d'autres détails de l'analyse sont élaborés dans ce chapitre.

Le Chapitre 5 détaille les mesures des corrélations hadron-jet dans les collisions pp à $\sqrt{s} = 5.02$ TeV avec ALICE, servant à tester les calculs pQCD et fournissant une référence pour les mêmes mesures dans les collisions d'ions lourds. Comme pour l'étude précédente des jets dépendant de la multiplicité, la stratégie d'analyse pour la corrélation h+jet comprend les étapes suivantes : sélection des échantillons de données expérimentales, sélection des événements, reconstruction des trajectoires, sélection des événements de trajectoire déclencheuse, reconstruction des jets, soustraction du fond, corrélations hadron-jet, correction par "dépliement", calcul de l'incertitude systématique et discussion des résultats physiques.

Le Chapitre 6 montre certains progrès dans les corrélations azimutales entre les jets de particules chargées et les hadrons de saveur lourde dans les collisions pp à $\sqrt{s} = 13$ TeV. La stratégie d'analyse est brièvement décrite ainsi que les graphiques de performance de base obtenus jusqu'à présent. Cette étude vise à mesurer la distribution radiale des particules accompagnant le jet par rapport à l'axe du jet et le rapport baryon à méson pour les distributions de particules radiales des mésons D et des baryons Λ_c^+. Les étapes clés de cette analyse incluent l'extraction des signaux des particules à saveur lourde en utilisant des méthodes d'apprentissage automatique et l'application de corrélations d'événements mixtes.

Le Chapitre 7 discute des principaux résultats physiques et des perspectives pour les mesures futures. Les notes correspondantes en français seront disponibles sur B.4.

B.3 Principaux résultats

La dépendance en multiplicité de la production de jets

Les productions de jet mesurés dans différents intervalles de multiplicité V0M en fonction du p_{T} du jet pour différents paramètres de résolution R variant de 0.2 à 0.7 dans des collisions pp à $\sqrt{s} = 13$ TeV sont présentés dans la Fig. 4.46. Il existe une dépendance de multiplicité des productions de jet, avec des

productions de jet plus élevés (plus faibles) observés dans des classes de multiplicité plus élevées (plus faibles). Pour mieux étudier cette dépendance de multiplicité, les spectres de jets mesurés dans diverses classes de multiplicité, rapportés à celui correspondant aux événements MB (Fig. 4.42) sont présentés dans la Fig. 4.47. la production de jets de particules chargées dans la classe de multiplicité d'événements la plus élevée (0–1%) est environ 10 fois plus élevé que dans le cas MB, indépendamment du paramètre de résolution du jet R, alors que dans la classe d'événements la plus basse (60–100%), elle ne représente qu'environ 10% du production MB. De plus, ce rapport dépend faiblement de p_{T}, sauf dans la région de p_{T} très basse. Ceci indique que la production de jets change avec l'activité de l'événement, mais que la pente du spectre reste similaire à celle mesurée dans les événements MB.

Les productions des jets intégrés surp_{T} ($5 \leq p_{\mathrm{T}} < 100\ \mathrm{GeV}/c$) et le moment transverse moyen des jets de particules chargées en fonction de la multiplicité auto-normalisée des particules chargées, $\langle \mathrm{d}N_{\mathrm{ch}}/\mathrm{d}\eta \rangle_{|\eta|<1}$, sont représentés sur la Fig. 4.51 pour différents paramètres de résolution R de 0.2 à 0.7. Les productions des jets et le p_{T} moyen du jet augmentent avec la multiplicité, l'augmentation est plus évidente lorsque R est plus grand. Les jets avec $R = 0.2$ montrent une très faible dépendance de leur $\langle p_{\mathrm{T}} \rangle$ sur la multiplicité, indiquant que les jets reconstruits avec de petits rayons sont dominés par la particule principale à l'intérieur du jet.

La Fig. 4.52 présente les rapports de production intégral des jets dans différents poucentages de multiplicité par rapport aux événements MB, en fonction de la multiplicité auto-normalisée des particules chargées. Les rapports sont indiqués pour quatre fourchettes de p_{T} jet sélectionnées ($5 \leq p_{\mathrm{T,jet}}^{\mathrm{ch}} < 7$ GeV/c, $9 \leq p_{\mathrm{T,jet}}^{\mathrm{ch}} < 12$ GeV/c, $30 \leq p_{\mathrm{T,jet}}^{\mathrm{ch}} < 50$ GeV/c, et $70 \leq p_{\mathrm{T,jet}}^{\mathrm{ch}} < 100$ GeV/c), et pour les paramètres de résolution $R = 0.2$ - 0.7. Les rapports de production des jets augmentent avec la multiplicité pour tous les paramètres de résolution et les intervalles p_{T}. Aucune dépendance significative des productions de jet avec le paramètre de résolution de jet R n'est observée.

Pour explorer la dépendance en p_{T} de la production de jet normalisée en fonction de la multiplicité auto-normalisée des particules chargées, la Fig. 4.53 montre les productions de jet auto-normalisés en fonction de la multiplicité auto-normalisée dans quatre intervalles de jet p_{T} sélectionnés pour le paramètre de résolution $R = 0.2 - 0.7$, les panneaux du haut représentent $R = 0.2, 0.4, 0.6$, les panneaux du bas représentent $R = 0.3, 0.5, 0.7$. Les prédictions de PYTHIA8 sont également comparées aux données.

Nous avons également effectué la même analyse en utilisant l'estimateur de multiplicité SPD à mi-rapidité comme vérification croisée, obtenant le production du jet en fonction de la multiplicité avec la sélection d'événements basée sur les tracklets SPD à mi-rapidité dans les collisions pp à $\sqrt{s} = 13$ TeV,

comme présenté dans le chapitre A.2 de l'appendice. Fig. A.13 montre le production du jet et les rapports de production (classes de multiplicité sur MB) en fonction de la densité de pseudorapidité normalisée des particules chargées à mi-rapidité, $\langle \mathrm{d}N_{\mathrm{ch}}/\mathrm{d}\eta \rangle_{|\eta|<1}$, la sélection de l'événement étant basée sur l'amplitude V0 à la rapidité avant (marqueurs pleins) et sur les tracklets SPD à la mi-rapidité (marqueurs ouverts). Les résultats des deux méthodes de sélection des événements sont en accord avec l'incertitude.

Les rapports de production de jets mesurés à mi-rapidité augmentent avec la multiplicité d'une manière similaire aux résultats présentés dans des publications antérieures pour les particules identifiées lors de l'utilisation d'estimateurs de multiplicité vers l'avant ou à mi-rapidité [215–217]. L'augmentation est plus faible pour le jet le plus faible p_{T} dans l'intervalle de multiplicité le plus élevé. En général, les simulations de PYTHIA8 prédisent la tendance globale à l'augmentation, mais la magnitude absolue est surestimée par le MC de PYTHIA8, en particulier dans l'intervalle de multiplicité le plus élevé.

Recoil-jet $\Delta_{\mathrm{recoil}}(p_{\mathrm{T,ch\ jet}}, \Delta\varphi)$ résultats

Les panneaux supérieurs de la Fig. 5.45 montrent les distributions $\Delta_{\mathrm{recoil}}(p_{\mathrm{T,ch\ jet}})$ entièrement corrigées pour $R = 0.2$ 0.4, et 0.5 mesurées dans des collisions pp à $\sqrt{s} = 5.02$ TeV, ainsi qu'une comparaison avec des modèles de calcul basés sur PYTHIA8 Monash 2013 tune [33, 34], JEWEL (vide) [32, 79], JETSCAPE (vide) [170], et POWHEG [168]. La Fig. 5.45, dans les panneaux inférieurs, montre le rapport des distributions dans les panneaux supérieurs à l'ajustement d'une fonction aux données, pour supprimer les fluctuations dans les données à des fins de comparaison. La fonction ajustée est cohérente avec la construction précédente de l'a priori (Section 5.6.2). La même procédure de lissage est utilisée dans les panneaux inférieurs des Figs. 5.48.

Les calculs de PYTHIA8 et de JETSCAPE sont en accord avec les données dans les limites des incertitudes expérimentales sur l'ensemble de la gamme $p_{\mathrm{T,ch\ jet}}$. Ces calculs sont liés, puisque JETSCAPE utilise PYTHIA8 pour la génération de processus durs et la fragmentation des cordes, avec des procédures indépendantes pour la douche de partons à l'état final et l'hadronisation. Ces processus indépendants devraient cependant avoir peu d'effet sur la distribution des jets. Les calculs POWHEG décrivent également bien les données sur l'ensemble de la gamme $p_{\mathrm{T,ch\ jet}}$. Le calcul JEWEL ne décrit pas bien la dépendance en $p_{\mathrm{T,ch\ jet}}$ de $\Delta_{\mathrm{recoil}}(p_{\mathrm{T,ch\ jet}})$ surestimant les données pour $p_{\mathrm{T,ch\ jet}} > 30$ GeV/c, avec ~40% de désaccord à $p_{\mathrm{T,ch\ jet}}$ élevé.

La Fig 5.48 montre les distributions corrigées de $\Delta_{\mathrm{recoil}}(\Delta\varphi)$ pour $R = 0.2$, 0.4, et 0.5 mesurées dans les

collisions pp à $\sqrt{s}$ = 5.02 TeV dans différentes tranches de $p_{\mathrm{T,ch\ jet}}$, ainsi que des comparaisons avec les calculs théoriques. Le calcul de JETSCAPE est en accord avec les données à l'intérieur des incertitudes dans tous les panneaux. Les autres calculs sont également en accord avec les données, à l'exception de $\Delta\varphi \lesssim 2.5$ dans les intervalles $p_{\mathrm{T,ch\ jet}} > 30$ GeV/c pour $R = 0.2$ (PYTHIA8, POWHEG, JEWEL), et $p_{\mathrm{T,ch\ jet}} > 50$ GeV/c pour $R = 0.5$ (POWHEG, JEWEL). Ces données de pp fournissent la référence pour la comparaison avec les mêmes distributions mesurées dans les collisions Pb–Pb, afin d'explorer les effets induits par le milieu.

La modification du production induite par le milieu est mesurée par $I_{\mathrm{AA}}(p_{\mathrm{T,ch\ jet}}) = \Delta_{\mathrm{recoil}}(\mathrm{Pb–Pb})/\Delta_{\mathrm{recoil}}(\mathrm{pp})$, le rapport des distributions $\Delta_{\mathrm{recoil}}(p_{\mathrm{T,ch\ jet}})$ mesurées dans les collisions Pb–Pb et pp La Fig. 5.49 montre $I_{\mathrm{AA}}(p_{\mathrm{T,ch\ jet}})$ en utilisant les mesures de $\Delta_{\mathrm{recoil}}(p_{\mathrm{T,ch\ jet}})$ dans les collisions pp comme référence. Les distributions de $I_{\mathrm{AA}}(p_{\mathrm{T,ch\ jet}})$ sont très dépendantes de $p_{\mathrm{T,ch\ jet}}$ et de R. Pour $p_{\mathrm{T,ch\ jet}} < 20$ GeV/c, $I_{\mathrm{AA}}(p_{\mathrm{T,ch\ jet}})$ augmente au-dessus de l'unité ou est cohérent avec l'unité pour tous les R. Pour $R = 0.2$ et 0.4, $I_{\mathrm{AA}}(p_{\mathrm{T,ch\ jet}})$ est inférieur à l'unité dans la région $20 < p_{\mathrm{T,ch\ jet}} < 60$ GeV/c, ce qui correspond à une suppression du production induite par le milieu en raison de la perte d'énergie, qui augmente lorsque $p_{\mathrm{T,ch\ jet}}$ est plus grand. En revanche, $I_{\mathrm{AA}}(p_{\mathrm{T,ch\ jet}})$ pour $R = 0.5$ est cohérent avec l'unité dans la plage $7 < p_{\mathrm{T,ch\ jet}} < 110$ GeV/c, ce qui indique que l'échelle angulaire de la perte d'énergie induite par le milieu est inférieure à 0.5 rad. Des mesures de $I_{\mathrm{AA}}(p_{\mathrm{T,ch\ jet}})$ pour des collisions centrales Au–Au à $\sqrt{s_{\mathrm{NN}}}$ = 200 GeV avec des déclenchements directs de photons et π^0 ont été récemment rapportées [221, 232], avec une observation similaire d'une suppression moindre pour $R = 0.5$ que pour $R = 0.2$, indiquant également une échelle angulaire similaire de redistribution de l'énergie du jet due à l'suppression aux énergies des collisions RHIC.

JETSCAPE décrit le plus précisément l'ampleur et la dépendance en $p_{\mathrm{T,ch\ jet}}$ de $I_{\mathrm{AA}}(p_{\mathrm{T,ch\ jet}})$ dans la gamme $p_{\mathrm{T,ch\ jet}} > 20$ GeV/c pour $R = 0.2$ et $R = 0.4$, tandis que JEWEL le décrit le plus précisément dans la même région $p_{\mathrm{T,ch\ jet}}$ pour $R = 0.5$. La tendance à la hausse des données vers un faible $p_{\mathrm{T,ch\ jet}}$ pour $R = 0.4$ et $p_{\mathrm{T,ch\ jet}} < 20$ GeV/c est décrite à la fois par le modèle hybride et par JEWEL, mais seulement avec l'inclusion des effets de réponse moyenne. Ces modèles ne décrivent cependant pas la tendance plus plate observée pour $R = 0.5$.

Les figures 5.50, 5.51, et 5.52, panneaux supérieurs, montrent les distributions de $\Delta_{\mathrm{recoil}}(\Delta\varphi)$ (acoplanarité) mesurées dans différents intervalles de $p_{\mathrm{T,ch\ jet}}$ $[10, 20]$, $[20, 30]$, $[30, 50]$, $[50, 100]$ GeV/c pour les collisions pp et Pb–Pb Les panneaux inférieurs montrent leur rapport, $I_{\mathrm{AA}}(\Delta\varphi)$, pour R = 0.2, 0.4, et 0.5, respectivement. Les principales conclusions physiques de ces résultats, y compris la discussion phénoménologique et les comparaisons de modèles, sont discutées ci-dessous.

La suppression de $I_{\mathrm{AA}}(\Delta\varphi)$ en dessous de l'unité peut être observée dans certaines régions de $p_{\mathrm{T,ch\ jet}}$, en accord avec la suppression du production dans la Fig. 5.49. Dans la gamme $p_{\mathrm{T,ch\ jet}} > 10$ GeV/c pour $R = 0.2$, et dans la gamme $p_{\mathrm{T,ch\ jet}} > 20$ GeV/c pour $R = 0.4$ et $R = 0.5$, la forme des distributions Pb–Pb $\Delta_{\mathrm{recoil}}(\Delta\varphi)$ est cohérente avec celle des distributions pp, ce qui correspond à aucun élargissement significatif de l'acoplanarité dans le milieu dans les limites des incertitudes expérimentales. En revanche, une augmentation significative de $I_{\mathrm{AA}}(\Delta\varphi)$ à des valeurs de $\Delta\varphi$ éloignées de π est observée dans la région $10 < p_{\mathrm{T,ch\ jet}} < 20$ GeV/c pour $R = 0.4$ et 0.5, ce qui correspond à un élargissement de la distribution d'acoplanarité induit par le milieu. À savoir, l'élargissement de l'acoplanarité induit par le milieu n'est observé que dans la plage $10 < p_{\mathrm{T,ch\ jet}} < 20$ GeV/c, et uniquement pour $R = 0.4$ et 0.5. La valeur de $I_{\mathrm{AA}}(\Delta\varphi)$ est soit cohérente avec l'unité, soit supprimée à des valeurs de $p_{\mathrm{T,ch\ jet}}$ plus élevées pour $R = 0.4$ et 0.5, et pour toutes les valeurs de $p_{\mathrm{T,jet}}$ mesurées pour $R = 0.2$.

Les figures 5.50, 5.51, et 5.52 comparent également les $I_{\mathrm{AA}}(\Delta\varphi)$ mesurées aux calculs théoriques. Le modèle JEWEL (recoils on) décrit le mieux les données sur toute la gamme R et $p_{\mathrm{T,ch\ jet}}$, y compris l'élargissement azimutal significatif pour les faibles $p_{\mathrm{T,ch\ jet}}$ et les grands R. Cependant, aucun des modèles considérés ne décrit avec succès l'ensemble des données mesurées.

Une mesure des di-jets énergétiques dans les collisions Pb–Pb à $\sqrt{s_{\mathrm{NN}}} = 2.76$ TeV a également révélé un élargissement et un adoucissement significatifs de la structure du jet de recul [233]. Ces mesures, les résultats de cette analyse, ainsi que les mesures de la production et de la sous-structure des jets, sondent chacun un aspect différent de l'interaction entre le jet et le milieu. Un modèle de jet-quenching réussi doit décrire correctement cet ensemble complet de données. Une analyse globale est nécessaire pour déterminer si une description totalement cohérente de toutes ces données peut être obtenue par un choix approprié des paramètres du modèle, ou si les mécanismes d'jet-quenching encodés dans le modèle peuvent être exclus par une comparaison complète avec les données d'suppression des jets multi-messagers.

B.4 Conclusions et perspectives

Les sections efficaces de production de jets de particules chargées inclusives mesurées avec un moment transverse de 5 GeV/c à 140 GeV/c dans des collisions pp à $\sqrt{s} = 13$ TeV ont été présentées. Les mesures ont été effectuées à l'aide de l'algorithme de recherche de jet anti-k_{T} avec différents paramètres de résolution R variant de 0.2 à 0.7 et la plage de pseudorapidité $|\eta_{\mathrm{jet}}| < 0.9 - R$. Les sections efficaces de jets de particules chargées inclusives ont été comparées aux calculs pQCD LO PYTHIA et NLO POWHEG. Comme prévu, un meilleur accord entre les données et les MC est observé pour les prédictions NLO,

bien que la prédiction NLO surestime le production du jet en dessous de 20 GeV/c. Les rapports de sections croisées pour différents paramètres de résolution ont également été étudiés. Ces rapports augmentent avec le p_{T} du jet et saturent à l'extrémité supérieure de la gamme en p_{T} du jet, ce qui indique une information de collimation plus forte pour les jets à fort impulsion.

La dépendance en multiplicité de la production de jets en utilisant différents paramètres de résolution a également été étudiée en utilisant l'estimateur de multiplicité V0. Un production de jet plus élevé (plus faible) est observé dans les classes de multiplicité plus élevées (plus faibles). La production de jets dans les différents intervalles de multiplicité par rapport à la MB dépend faiblement des paramètres de résolution des jets. En outre, les productions de jet auto-normalisés et la valeur moyenne du jet en fonction de la multiplicité auto-normalisée des particules chargées ont été mesurés. Les productions intégrés des jets et $\langle p_{\mathrm{T}} \rangle$ dans l'intervalle p_{T} intégré entre 5 et 100 GeV/c augmentent avec la multiplicité auto-normalisée des particules chargées. Aucune dépendance forte du p_{T} du jet et du paramètre de résolution R n'est observée, sauf à faible moment transverse dans l'intervalle de pourcentage de multiplicité le plus élevé. Nous avons également effectué la même analyse en utilisant l'estimateur de multiplicité SPD à mi-rapidité, obtenant que le production du jet augmente également avec la multiplicité, et les résultats entre les estimateurs de multiplicité V0 et SPD sont généralement cohérents à l'intérieur de l'incertitude. Une dépendance de multiplicité similaire a également été signalée pour les mésons D prompts dans les collisions p–Pb à $\sqrt{s_{\mathrm{NN}}} = 5.02$ TeV et la production J/ψ non prompte (provenant des désintégrations de hadrons B) dans les collisions pp à $\sqrt{s} = 7$ TeV lors de l'utilisation d'un estimateur de multiplicité direct. Les générateurs d'événements MC actuels ne peuvent que prédire la tendance à la hausse mais ne peuvent pas décrire les productions absolus, en particulier dans la classe de multiplicité la plus élevée.

Les mesures effectuées dans un petit système et présentées dans cette analyse permettent de mieux comprendre l'interaction entre la production de particules molles et les processus durs. Des comparaisons détaillées entre les modèles et les données permettront d'élucider la relation entre les mécanismes de production de jets et les événements de haute multiplicité dans les petits systèmes, en particulier aux énergies du LHC.

Les mesures des distributions semi-inclusives des jets de particules chargées reculant à partir d'un déclencheur de hadrons des jets (de particules chargées) de recul par rapport à un hadron "déclencheur" dans les collisions pp à $\sqrt{s} = 5.02$ TeV, sont effectuées en utilisant les grands échantillons de données enregistrés avec le détecteur ALICE au cours du cycle 2 du LHC. Les résultats sont présentés en fonction de $p_{\mathrm{T,ch\ jet}}$, l'impulsion transverse du jet de recul, et de $\Delta\varphi$, la séparation azimutale entre le déclencheur et le jet de recul. Une méthode statistique, guidée par les données, développée précédemment par la

collaboration ALICE, est utilisée pour atténuer le bruit de fond non corrélé dans les collisions Pb–Pb centrales, ce qui permet de mesurer l'jet-quenching du jet dans une région cinématique jusqu'alors inexplorée par les jets reconstruits au LHC, y compris à faible $p_{\mathrm{T,ch\ jet}} \sim 10$ GeV/c avec le paramètre de résolution du jet $R = 0.5$. Les phénomènes observés explorent plusieurs aspects différents de la production de jets dans les collisions pp et sont comparés aux collisions Pb–Pb.

Les ditributions en $p_{\mathrm{T,ch\ jet}}$ et les distributions azimutales mesurées dans les collisions pp fournissent une référence précise pour explorer les modifications de la production des jets induites par le milieu dans les collisions Pb–Pb centrales, et sont bien décrites par les calculs basés sur la pQCD sur l'ensemble des plages mesurées. Le rapport entre le production des jets de recul dans les collisions pp pour $R = 0.2$ et celui pour $R = 0.4$ ou 0.5 est inférieur à l'unité à p_{T} élevé, ce qui reflète le profil transversal bien établi de l'énergie au sein d'un jet dans le vide. Cependant, on observe que ce rapport augmente lorsque $p_{\mathrm{T,ch\ jet}}$ est inférieur à la valeur de $p_{\mathrm{T}}^{\mathrm{trig}}$, le p_{T} du hadron déclencheur, ce qui contraste fortement avec le comportement d'un rapport similaire mesuré pour les sections transversales de jet inclusives. Les deux séries de mesures sont bien décrites par les calculs de pQCD, ce qui suggère que ces effets opposés peuvent provenir de différents mécanismes de production de jets, en particulier la suppression des processus d'ordre principal pour la population semi-inclusive de jets de recul par rapport à un hadron de p_{T} élevé, dans lequel $p_{\mathrm{T}}^{\mathrm{trig}}$ fournit une échelle supplémentaire de fragmentation.

Les valeurs mesurées de $I_{\mathrm{AA}}(p_{\mathrm{T,ch\ jet}})$, le rapport du production des jets de recul pour les collisions Pb–Pb et pp pour le même R de jet en fonction de $p_{\mathrm{T,ch\ jet}}$, dépendent de $p_{\mathrm{T,ch\ jet}}$ et de R. Pour $R = 0.5$, le rapport est cohérent avec l'unité dans les limites des incertitudes sur toute la gamme mesurée, ce qui indique que les modifications du jet induites par le milieu, telles que sondées par cette observable, sont largement limitées à des échelles angulaires inférieures à 0.5 radians. Le rapport entre le production du jet de recul dans les collisions Pb–Pb pour $R = 0.2$ et celui pour $R = 0.4$ ou 0.5 est inférieur à celui des collisions pp à $p_{\mathrm{T,ch\ jet}}$ intermédiaire, ce qui indique un élargissement intra-jet induit par le milieu à cette échelle angulaire.

Pour $R = 0.2$ et 0.4, la valeur de $I_{\mathrm{AA}}(p_{\mathrm{T,ch\ jet}})$ est inférieure à l'unité à $p_{\mathrm{T,ch\ jet}}$ intermédiaire, et augmente jusqu'à l'unité à la fois à $p_{\mathrm{T,ch\ jet}}$ inférieur et à $p_{\mathrm{T,ch\ jet}}$ supérieur. Pour $R = 0.4$, $I_{\mathrm{AA}}(p_{\mathrm{T,ch\ jet}})$ dépasse l'unité à la plus faible valeur de $p_{\mathrm{T,ch\ jet}}$ rapportée ici. La comparaison avec les modèles indique que le comportement à faible $p_{\mathrm{T,ch\ jet}}$ peut être dû à la récupération de l'énergie perdue dans le milieu par des jets à $p_{\mathrm{T,ch\ jet}}$ plus élevé qui sont également corrélés avec le déclencheur. Le comportement à haut niveau d'énergie peut provenir de l'interaction entre la perte d'énergie due à l'jet-quenching et le biais géométrique induit par l'utilisation d'un déclencheur hadronique.

Les valeurs mesurées de $I_{AA}(\Delta\varphi)$, le rapport du production de recul pour les collisions Pb–Pb et pp pour le même R de jet en fonction de $\Delta\varphi$, fournissent la première mesure d'un élargissement significatif de l'acoplanarité du jet dans les collisions Pb–Pb pour R = 0.4 et 0.5 à faible $p_{T,ch\ jet}$.

Les modèles de calcul actuels, qui intègrent l'extinction du jet, ne reproduisent pas toutes ces observations. Les développements ultérieurs de la modélisation, et leur comparaison avec ces données et d'autres similaires, promettent une nouvelle compréhension significative des mécanismes régissant le transport d'énergie et la dynamique du QGP. Entre-temps, des mesures plus précises et plus détaillées des profils de jets semi-inclusifs et des sous-structures avec des statistiques plus élevées provenant du Run 3 du LHC devraient être poursuivies pour élucider les origines possibles des résultats physiques obtenus ci-dessus.

Une étude de faisabilité a commencé sur la production de jets de saveur lourde (jet–$D^0/D^+/\Lambda c^+$) dans les collisions pp à $\sqrt{s}$ = 13 TeV sera présentée. La distribution ($\Delta\eta$, $\Delta\phi$) des baryons et des mésons par rapport à la direction du jet déclenché sera calculée pour étudier les mécanismes d'hadronisation.

Contributions on behalf of ALICE Collaboration

List of Publications:

1. **Multiplicity dependence of charged-particle jet production in pp collisions at $\sqrt{s}$ = 13 TeV**

ALICE Collaboration, *Eur. Phys. J. C 82 (2022) 514*

2. **Observation of medium-induced yield enhancement and acoplanarity broadening of low-p_T jets from measurements in pp and central Pb–Pb at $\sqrt{s_{\mathrm{NN}}}$ = 5.02 TeV**

ALICE Collaboration, submitted to arXiv:2308.16131, accepted by *Phys. Rev. Lett*

3. **Measurements of jet quenching using semi-inclusive hadron+jet distributions in pp and central Pb–Pb at $\sqrt{s_{\mathrm{NN}}}$ = 5.02 TeV**

ALICE Collaboration, submitted to arXiv:2308.16128, accepted by *Phys. Rev. C*

Proceedings:

1. **System and event activity dependent inclusive jet production with ALICE**

Yonghzen Hou, *PoS EPS-HEP2019 (2020) 278*

2. **Observation of medium-induced yield enhancement and acoplanarity broadening of low-p_T jets in pp and central Pb–Pb at $\sqrt{s_{\mathrm{NN}}}$ = 5.02 TeV**

Yonghzen Hou, *PoS(HardProbes2023)137*

Conference talks:

1. **Observation of medium-induced yield enhancement and acoplanarity broadening via h-jet correlations with ALICE**

QPT 2023, Dec 14-19, 2023, Zhuhai, China

2. **Study of jet energy redistribution and acoplanarity broadening measurements in Pb–Pb collisions with ALICE**

EPS-HEP 2023, Aug 21-25, 2023, Hamburg, Germany

3. **Observation of medium-induced yield enhancement and acoplanarity broadening of low-p_T jets in pp and central Pb–Pb at $\sqrt{s_{\mathrm{NN}}}$ = 5.02 TeV**

Hard Probes 2023, Mar 26-31, 2023, Aschaffenburg, Germany

4. **Observation of jet broadening acoplanarity in pp and Pb–Pb collisions at 5.02 TeV**

CLHCP 2022, Nov 23-27, 2022, Nanjing, China (online)

5. **Jet acoplanarity measurements via hadron+jet correlations in pp and Pb–Pb collisions**
Hot Quarks 2022, Oct 11-17, 2022, Dao House, Estes Park, Colorado, USA (online)

6. **Semi-inclusive jet acoplanarity measurements via h+jet correlations in pp and Pb–Pb collisions with ALICE**
ICHEP 2022, Jul 6-13, 2022, Bologna, Italy

7. **Multiplicity dependence of charged-particle jet production in pp collisions at 13 TeV with ALICE at the LHC**
Rencontres QGP France 2022, May 2-5, 2022, Tour, France

8. **Measurements of jet quenching using semi-inclusive hadron-jet distributions in pp and Pb–Pb collisions with ALICE**
FCPPL 2021, held remotely on Zoom, Dec 12-16, 2021

9. **Measurement of multiplicity dependence of charged jet production in pp collisions at 13 TeV**
China ALICE Experimental Workshop, Jul 30 to Aug 1, 2021, Guiyang, China

10. **Measurements of jet quenching via h-jet correlations in pp and Pb–Pb collisions with ALICE**
QPT 2021, Guiyang, China

11. **System and event activity dependent inclusive jet production with ALICE**
EPS-HEP 2019, Jul 10-17, Ghent, Belgium

Conference posters:

1. **Semi-inclusive recoil jet measurements via hadron-jet correlations in pp collisions with ALICE**
Quark Matter 2022, 4-10, Apr 2022, KRAKÓW, POLAND (online)

2. **Multiplicity dependent charged particle jet production in pp collisions at 13 TeV with ALICE**
Quark Matter 2019, Nov 3-9, 2019, Wuhan, China

Service work:

1. Beam test data analysis of Circuit Exploratoire 65 nm (CE65) pixel sensor for standard and modified with gap processes

Yongzhen HOU

Study of light and heavy-flavour jet production and correlations with ALICE at the LHC

Abstract

This thesis explored the properties of the quark-gluon plasma (QGP) in heavy-ion collisions, using data from the ALICE experiment at the Large Hadron Collider (LHC). To explore the properties of the QGP, we focused on jet production and correlations, which provide indirect signatures of the medium. We measured jet production in proton-proton (pp) collisions at $\sqrt{s} = 13$ TeV and found that jet production increases with event multiplicity. We also investigated "h+jet" correlations between high-p_{T} hadrons and back-to-back jets in pp and Pb-Pb collisions at $\sqrt{s_{\mathrm{NN}}} = 5.02$ TeV, revealing QGP-induced jet modifications such as energy loss and medium-induced acoplanarity broadening. Additionally, we examined heavy-flavor quark jets, produced in hard scatterings, as probes of the QGP. The feasibility of identifying and tagging charm quark jets was also explored, helping to understand heavy-quark energy loss mechanisms and medium properties.

Keywords : Quark gluon plasma; Heavy-ion; ALICE; Hadron; Jets; Energy loss; Broadening ; Jet quenching; Heavy quarks

Résumé

Cette thèse a exploré les propriétés du plasma de quarks et de gluons (QGP) dans les collisions d'ions lourds, en utilisant les données de l'expérience ALICE (A Large Hadron Collider Experiment) au Grand Collisionneur de Hadrons (LHC). Afin d'explorer les propriétés du QGP, nous nous sommes concentrés sur la production de jets et les corrélations, qui fournissent des signatures indirectes du milieu Nous avons mesuré la production de jets dans les collisions proton-proton (pp) à $\sqrt{s} = 13$ TeV, et nous avons observé que cette production augmente avec la multiplicité des événements. Nous avons également étudié les corrélations "h+jet" entre les hadrons de haut p_{T} et les jets dos-à-dos dans les collisions pp et Pb-Pb à $\sqrt{s_{\mathrm{NN}}} = 5.02$ TeV. Les études de corrélations ont indiqué révélant des modifications des jets induites par le QGP, telles que des pertes d'énergie et un élargissement de l'acoplanarité induite par le milieu. En plus, les jets de quarks de saveur lourde, qui se produit lors de diffusions dures, ont été traités comme des sondes du QGP. La faisabilité de l'identification et du marquage des jets de quarks charmés a également été explorée, contribuant à une meilleure compréhension des mécanismes de perte d'énergie des quarks lourds et des propriétés du milieu.

Mots clés : Plasma de quarks et de gluons; Ions lourds; ALICE; Hadron; Jets; Élargissement; Jet quenching; Quarks lourds